UNIVERSITY OF CALIFORNIA

Santa Barbara

CATECHOL-CATION SYNERGY IN WET ADHESIVE MATERIALS

A dissertation submitted in partial satisfaction of the

requirements for the degree of Doctor of Philosophy

in Chemistry

by

Gregory Peter Maier

Committee in charge:

Professor Alison Butler

Professor J. Herbert Waite

Professor R. Daniel Little

Professor Song-I Han

September 2017

The dissertation of Gregory Peter Maier is approved:

_____

J. Herbert Waite

_____

R. Daniel Little

_____

Song-I Han

_____

Alison Butler, Committee Chair

August 2017

Catechol-Cation Synergy in Wet Adhesive Materials

ACKNOWLEDGEMENTS

My experience in graduate school has had a profound impact on me both personally and professionally. I would like to thank my advisor, Professor Alison Butler, for guiding me through this transformative process. Her support, dedication, and encouragement were unwavering and I consider myself lucky to have been a part of her research group. I would also like to thank my committee members Songi Han, Dan Little, and especially Herb Waite for their guidance in my research.

I've been lucky to have been involved in several fulfilling collaborations. Mike Rapp from Jacob Israelachvili's lab at UC Santa Barbara and I have been partners in research for the majority of my time in graduate school and much of this dissertation would not have been possible without him. Additionally, my current and former group members helped make a positive, fun, and engaging work environment. In particular, Robert Lewis has always been helpful with organic synthesis advise and has always been a great friend.

Thank you to my family for guiding me to where I am today and to my amazing girlfriend Kate Hawley and friend Johnny Kessenich, whose willingness to move to Santa Barbara has truly made the last 5 years some of the best in my life.

VITA OF GREORY PETER MAIER

August 2017

EDUCATION

Doctor of Philosophy, Chemistry, August 2017
University of California, Santa Barbara, CA

Bachelor of Arts, Honors in Chemistry with Minor in Earth Science,
May 2009, Vassar College, Poughkeepsie, NY

RESEARCH EXPERIENCE

September 2011 – Present	Graduate Student Researcher, University of California, Santa Barbara, CA
August 2009 – June 2011	Research Assistant, Channing Laboratory, Harvard Medical School, Boston, MA
June 2007 – August 2009	Environmental Chemist, Alpha Woods Hole Laboratories, Westborough, MA
September 2007 – May 2009	Research Assistant, Vassar College, Poughkeepsie, NY

PUBLICATIONS

Greg P. Maier and Alison Butler. Siderophores and Mussel Foot Proteins: The Role of Catechol, Cations, and Metal Coordination in Surface Adhesion. *J. Biol. Inorg. Chem.*, **2017**, 22, 739-749.

Michael V. Rapp*, Greg P. Maier*, Howard A. Dobbs, Nicholas J. Higdon, J. Herbert Waite, Alison Butler, Jacob N. Israelachili. Defining the Catechol-Cation Synergy for Enhanced Wet Adhesion to Mineral Surfaces. *J. Am. Chem. Soc.* **2016**, 138, 9013−9016. **These authors contributed equally.*

Greg P. Maier*, Michael V. Rapp*, J. Herbert Waite, Jacob N. Israelachvili, Alison Butler. Adaptive synergy between catechol and lysine promotes wet adhesion by surface salt displacement. *Science*. **2015**, 349, 628-632. **These authors contributed equally.*

MANUSCRIPTS IN PREPARATION

Greg P. Maier, Chris Bernt, Alison Butler. Catechol Autoxidation: Consideration to the Design of Wet Adhesives. *Manuscript in preparation.*

POSTER PRESENTATIONS

Greg P. Maier, Michael V. Rapp, J. Herbert Waite, Jacob N. Israelachvili, and Alison. Butler. Siderophore-Inspired Wet Adhesion: Oxidation Resistance and Catechol-Lysine Synergy. Poster presentation delivered at the Materials Research Outreach Program, University of California, Santa Barbara, CA, February, 2015.

Greg P. Maier, Michael V. Rapp, Jacob N. Israelachvili, and Alison Butler. Adhesion and Oxidation Resistance of Catecholate Siderophores. Poster presentation at the Bioinspired Materials Gordon Research Seminar, Sunday River Resort, Bethel, ME, June, 2014.

CERTIFICATES, POSITIONS, AND AWARDS

Graduate Program in Management Practice Certificate, Technology Management Program, University of California, Santa Barbara, CA, June 2017

Vice President of Budget and Finance, Graduate Students Association, University of California, Santa Barbara, 2015-2016

Chemistry Department Graduate Student Safety Committee Representative, University of California, Santa Barbara, 2012-2014

Special Services to the Department Award, Department of Chemistry and Biochemistry, University of California, Santa Barbara, 2013

Lead Teaching Assistant and Outstanding Teaching Assistant Award, Department of Chemistry and Biochemistry, University of California, Santa Barbara, 2012-2013

ABSTRACT

Catechol-Cation Synergy in Wet Adhesive Materials

By

Gregory Peter Maier

In physiological fluids and seawater, adhesion of synthetic polymers to solid surfaces is impaired by high salt, pH, and hydration. However, mussels have evolved effective strategies for wet adhesion despite these impediments. Inspection of mussel foot proteins (Mfps) provides insights into adhesive adaptations. Catecholic Dopa (3,4-dihydroxyphenylalanine) and lysine residues are present in high mole percent in the interfacial Mfps. The siderophore cyclic trichrysobactin also contains high mole percent of catechol and lysine and serves as a simplified mimic of Mfps.

This work is focused on use of Mfp-mimetic siderophores and synthetic siderophore analogs as model systems for dissecting the chemical and physical interactions that enable wet adhesion. Variation in number and identity of functional groups appended to the synthetic siderophore analogs allows identification of the specific contributions of those functional groups to wet adhesion. Both catechol and amine functional groups are critical to strong wet adhesion. The primary amine of lysine and catechol cooperatively displace interfacial hydration and bind to the underlying substrate. Variation in the amine identity

as well as the amine to catechol ratio within siderophore analogs also has a significant impact on wet adhesive performance.

Catechol undergoes a pH-dependent autoxidation in which higher pH leads to faster oxidation by dioxygen. This oxidation abolishes all adhesion of Mfps to mica by pH 7.5, yet many applications of synthetic wet adhesives require adhesion at physiological or oceanic pH. A better understanding of catechol redox chemistry is critical to the design of wet adhesives. To this end, the pH-dependent autoxidation of catechol and substituted catechols was investigated and results are consistent with a mechanism in which O_2 oxidizes both the mono-deprotonated and di-deprotonated catechol. A linear Hammett correlation for the pH-independent second order rate constants for catechol autoxidation indicates that catechols become resistant to autoxidation when functionalized with electron withdrawing groups and more susceptible to autoxidation when functionalized with electron donating groups. Analysis of substituent effects through Hammett correlation allows for selection of functionalized catechols with redox properties ideally suited for a given application.

TABLE OF CONTENTS

LIST OF FIGURES

LIST OF TABLES

LIST OF SCHEMES

LIST OF ABBREVIATIONS

2,3-DHBA – 2,3-dihydroxybenzoic acid

3,4-DHBA – 3,4-dihydroxybenzoic acid

Ac – acetyl

AFM – atomic force microscope

Arg – arginine

Bn - benzyl

Boc – tert-butyloxycarbonyl

CAC – critical adsorption concentration

Cat^{-}– mono-deprotonated catechol

Cat^{2-}– doubly deprotonated catechol

CAS – chrome azurol sulfonate

Cbz – carboxybenzyl

CTC – cyclic trichrysobactin

Dab – diaminobutyric acid

DCC – dicyclohexylcarbodiimide

DCHU – dicyclohexylurea

DCM – dichloromethane

DMSO – dimethylsulfoxide

Dopa – 3,4-dihydroxy-L-phenylalanine

D_T – hardwall thickness

ESI MS – electrospray ionization mass spectrometry

Et_3N - triethylamine

HMBC – heteronuclear multiple bond correlation

HSQC – heteronuclear single quantum correlation

Lys – lysine

Mfp – mussel foot protein

NHS – N-hydroxysuccinimide

p-Me – 4-methylcatechol

p-Et – 4-ethylcatechol

p-H – Catechol

p-Cl – 4-Chlorocatechol

p-COOH – 3,4-dihydroxybenzoic acid

Pd/C – palladium on carbon

PDMS - polydimethylsulfoxide

PEG – polyethylene glycol

RP-HPLC – reverse phase high performance liquid chromatography

SAM – self-assembled monolayer

Ser - serine

SFA – surface forces apparatus

TAC – Tren-Arg-Cam

TC – Tren-Cam

TDC – Tren-Dab-Cam

TEBMA – 2,4,6-triethyl-1,3,5-benzenetrimethylamine

TFA – trifluoroacetic acid

THF - tetrahydrofuran

$TL^{Ac}C$ – Tren-Lys^{Ac}-Cam

TLB – Tren-Lys-Bam

TLC – Tren-Lys-Cam

TLLC – Tren-Lys-Lys-Cam

TLP – Tren-Lys-Pam

TLWC – Tren-Lys-Trp-Cam

TREN – tris(2-aminoethyl)amine

I. SIDEROPHORES AND MUSSEL FOOT PROTEINS: THE ROLE OF CATECHOL, CATIONS, AND METAL COORDINATION IS SURFACE ADHESION

Parts or sections of this chapter were reprinted with permission from Springer-Verlag from: Greg P. Maier and Alison Butler. Siderophores and Mussel Foot Proteins: The Role of Catechol, Cations, and Metal Coordination in Surface Adhesion. *J. Biol. Inorg. Chem.*, 2017,

1.1 Catechols in Nature

Catechols are biologically active functional groups found in animals, plants and microbes (Figure 1.1). It its simplest form, the catechol 1,2-dihydroxybenzene, is present in some organisms, although derivatized forms of 1,2-dihydroxybenzene form the basis of most biologically significant catechol compounds. The distinguishing side chain of the amino acid L-Dopa is 3,4-dihydroxy-L-phenylalanine (Figure 1.1), formed in proteins by the posttranslational hydroxylation of tyrosine. The most common catechol in microbial siderophores, which are compounds produced by bacteria to facilitate sequestration and uptake of Fe(III), is 2,3-dihydroxybenzoic acid (2,3-DHBA; Figure 1.1). This catechol is derived from chorismate, which originates via the shikimic acid pathway. Enterobactin, produced by many enteric bacteria, including *E. coli*, is one of the most well known 2,3-DHBA containing siderophores (Figure 1.2), although 3,4-dihydroxybenzoic acid (3,4-DHBA) has been identified in some siderophores, such as petrobactin from *Marinobacter hydrocarbonoclasticus* [1] *and Bacillus anthracis* [2].

Catechols are also present as catecholamines in neurotransmitters, including dopamine, epinephrine and norepinephrine, as well as in polymerized forms of dopamine, such as the skin pigment melanin (Figure. 1). Other well-known catechols include catechins, members of the flavin-3-ol-class of plant secondary metabolites, isolated from a variety of plants including tea, as well as urushiol, a long-chain alkyl catechol, which is the skin-irritating agent in the poison ivy plant. Humboldt squid beaks contain extensive histidyl-dopa crosslinks that are formed as a result of Dopa oxidation [3]. The sandcastle worm *Phragmatopoma californica* secretes a protein-based cement to construct tunnels with exogenous mineral particles [4]. Catechol oxidation within the cement initiates the formation of 5-S-cysteinyl-Dopa crosslinks, facilitating the curing process [4].

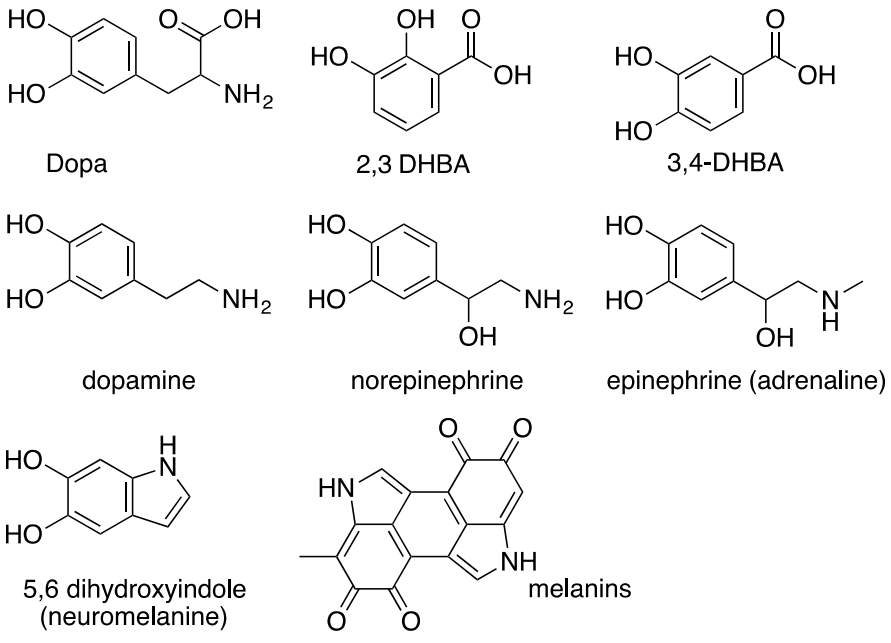

Figure 1.1. Structures of biologically derived catechols.

1.2 Iron Coordination by Biological Catechols

1.2.1 Catechol Siderophores

Enterobactin, salmochelin, cyclic trichrysobactin (CTC), and bacillibactin are all tris-catecholate siderophores with a tri-ester macrolactone core (Figure 1.2). Enterobactin—a natural product of enteric and pathogenic bacteria such as *E. coli*—is the cyclic trimer of 2,3-dihydroxybenzoyl-L-serine (Figure 1.2) [5]. Salmochelin, isolated from *Salmonella enterica* and uropathogenic *E. Coli*, retains the structure of enterobactin although with the addition of glucose at the C-5 position on up to two of the catechol rings [6]. Cyclic trichrysobactin derived from the plant pathogen *Dickeya chrysanthemi* contains the triserine lactone scaffold of enterobactin although with a D-Lys spacer inserted between L-Ser and 2,3-DHBA [7]. Bacillibactin, produced by *Bacillus subtilis* and other *Bacilli* species, is based on the lactone of tris-L-threonine with elongated catechol-terminated arms containing a glycine spacer (Figure 1.2) [8]. These are just a few examples of the tris-catechol siderophores based on a tris-L-Ser or L-Thr macrolactone scaffold.

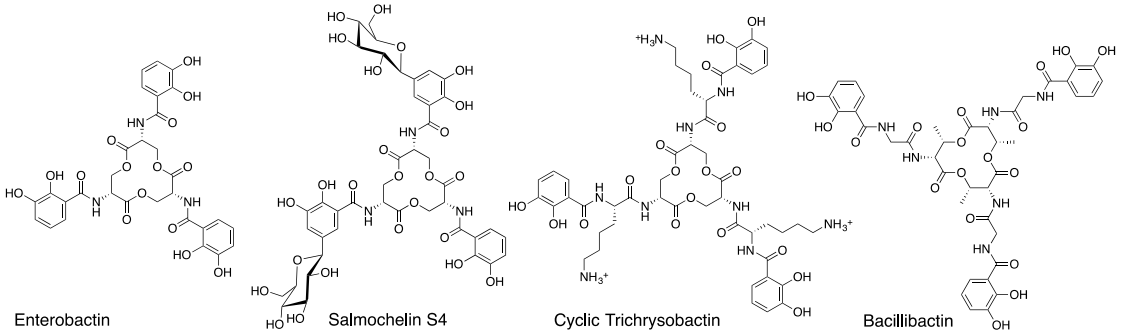

Figure 1.2. Structures of enterobactin, salmochelin S4, cyclic trichrysobactin, and bacillibactin

Tris-catecholate siderophores coordinate iron(III) with particularly high affinity [9, 10]. The proton-independent stability constants for Fe(enterobactin)$^{3-}$ and Fe(bacillibactin)$^{3-}$ are 10^{49} [11] and $10^{47.6}$ [8], respectively. High-resolution X-ray crystal structures for these siderophore complexes are surprisingly rare. The only X-ray crystal structure of a discrete metal-enterobactin complex is of vanadium(IV)-enterobactin, [V(enterobactin)]$^{2-}$, which reveals a Δ-configuration at the metal center, and lacks a characteristic V(IV) oxo group [12, 13]. The circular dichroism spectrum of [Fe(III)(enterobactin)]$^{3-}$ is also consistent with the Δ-configuration [13], as is the Fe(III) complex of linear enterobactin [14]. Interestingly, the presence of a glycine spacer and a tris-L-Thr lactone core in bacillibactin [15] promotes the Λ-configuration [16]. The Fe(III) complexes of cyclic trichrysobactin with a D-Lys spacer and tri-vanchrobactin with a D-Arg spacer have the Λ-configuration, as well [7, 17].

Under physiological conditions, enterobactin coordinates Fe(III) with the three bidentate catecholate groups [18, 19]. At lower pH, however, tris catecholate coordination shifts to tris salicylate coordination, which is induced by protonation of the meta catechol hydroxyl groups. Thus in the salicylate binding mode, Fe(III) is coordinated by the amide oxygen and the ortho hydroxyl oxygen of 2,3-DHBA [20, 21].

The ester linkages in enterobactin, salmochelin, cyclic-trichrysobactin and bacillibactin are quite susceptible to hydrolysis, producing the linear tris catechol form, the dimer fragments (e.g., bis-(2,3-dihydroxybenzoyl-L-Ser) for enterobactin), and the monomers (e.g., 2,3-DHBA-L-Ser of enterobactin, 2,3-DHBA-D-Lys-L-Ser of trichrysobactin, etc). Chrysobactin, 2,3-DHBA-D-Lys-L-Ser [22, 23], and vanchrobactin, 2,3-DHBA-D-Arg-L-Ser [24, 25], were originally reported as a monocatechol siderophores. The pK_a values for the first

catechol hydroxyl of chrysobactin and vanchrobactin are substantially lower than that of catechol due to an intramolecular hydrogen bond between the deprotonated ortho hydroxyl and the proton on the adjacent amide nitrogen [25] (Table 1.1). The logβ_3 stability constants for Fe(III) complexes of chrysobactin, vanchrobactin, catechol, and N,N-dimethyl-2,3-dihydroxybenzamide are surprisingly not exactly parallel to either the 1st or 2nd pKa of the substituted catechols (Table 1.1) [25].

Table 1.1. pKa values and logβ_3 stability constants of selected catechol compounds.

Catechol	COOH pK_a	1st Catechol pK_a	2nd Catechol pK_a	Amine pK_a	logβ_3	Ref.
chrysobactin	3.17	6.73	10.61	12.1	40.2	[23]
vanchrobactin	3.2	6.79	11.8	13.6	42.7	[24]
catechol	—	9.32	13.05	—	44.6	[24]
N,N-dimethyl-2,3-dihydroxybenzamide	—	8.42	12.1	—	40.24	[10]

Catechol in chrysobactin (i.e., 2,3-DHBA-D-Lys-L-Ser) has been shown to coordinate Fe(III) as mono, bis, and tris complexes, depending on pH (Figure 1.3) [10, 23, 24]. The pH dependence of binding stoichiometry of chrysobactin in four-fold excess over Fe(III) reveals that tris catecholate coordination dominates at pH > 6.1, bis catecholate coordination at pH 6.1 > pH > 4.4, and mono catecholate coordination at pH < 4.4 (Figure 1.3).

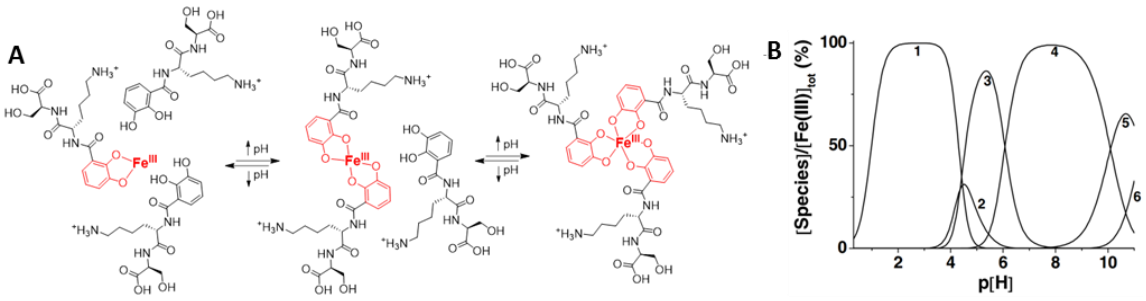

Figure 1.3. pH dependence of Fe(III) coordination by the catechol in chrysobactin. (A) Mono-catechol complexation is favored at low pH and tris-catechol complexation favored at high pH. (B) Distribution diagram of Fe(III)-chrysobactin (1) Fe(III)-chrysobactinH_2^{2+}; (2) Fe(III)-chrysobactin$_2H_3$; (3) Fe(III)-chrysobactin$_2H_2^-$; (4) Fe(III)-chrysobactin$_3H_3^{3-}$; (5) Fe(III)-chrysobactin$_3H_2^{4-}$; (6) Fe(III)-chrysobactin$_3H_5$-. Conditions: 4 mM chrysobactin; 1.0 mM $Fe(ClO_4)_3$; I = 0.1 M ($NaClO_4$); 25°C. Figure 1.3 (B) was reproduced from [23].

While 2,3-DHBA is the predominant type of catechol in siderophores, variation in the nature of the catechol does affect Fe(III)-catechol speciation, such as for Dopa, a 3,4-dihydroxy catechol. In a Dopa-functionalized polyethylene glycol (PEG) polymer, tris catecholate coordination dominates at pH > 9.1 (with Dopa in three-fold excess over $FeCl_3$), bis at 9.1 > pH > 5.6, and mono at pH < 5.6 (Figure 1.4) [26, 27]. Thus tris-catechol Fe(III) complexation is favored for 2,3-DHBA-type catechols at a lower pH than the 3,4-dihydroxy catechol in Dopa. Nitration of Dopa further impacts the binding stoichiometry. 4-Nitro-Dopa in the functionalized polyethylene glycol (PEG) polymer forms hydrogels at pH 9 which contain largely tris-coordinate crosslinks, whereas the non-nitrated Dopa derivative is predominantly bis-coordinate [28].

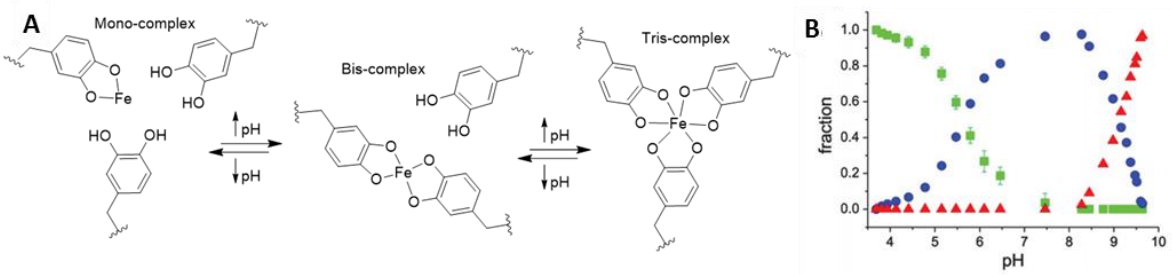

Figure 1.4. Fe(III) coordination to Dopa. (A) Fe(III)-Dopa coordination is pH-dependent, with mono-complexation favored at low pH and tris-complexation favored at high pH. (B) Dopa-modified polyethylene glycol (PEG-$Dopa_4$, 10 kDa PEG core) in solution with $FeCl_3$ (Dopa:Fe(III) ratio = 3:1) shows a pH dependence in the relative fraction of mono- (green), bis- (blue), and tris-catechol-Fe(III) (red) complexes. Figure 1.4 was adapted from [26].

1.2.2 Dopa in Marine Mussel Foot Proteins

Mussels adhere to rocks in the intertidal zone through a radial array of adhesive plaques that are tethered to the body of the mussel by protein-rich threads. The adhesive plaques and threads comprise what is known as the byssus. The plaques contain many different mussel foot proteins (Mfps; Figure 1.5) and Dopa is found in unusual abundance in many of these Mfps. Mfp-3 and Mfp-5 are surface priming proteins that interact directly with the target substrate and prepare it for subsequent deposition of other Mfps. The two main types of Mfp-3 are Mfp-3 fast and Mfp-3 slow [29, 30]. These variants are named for their relative mobility on acetic acid urea polyacrylamide gels [29]. The adhesive properties of Mfp-3 fast [31-33] have been well researched compared to Mfp-3 slow and subsequent sections will therefore focus on Mfp-3 fast. Mfp-3 fast and Mfp-5 contain the highest mol % Dopa at 20 and 30 mol %, respectively [34]. Mfp-5 also has 19.5 mol % Lys and 3.1 mol % Arg and HydroxyArg residues, while Mfp-3 fast has 15.0 mol % Lys and 9.5 mol % Arg and

HydroxyArg [35]. Dopa contributes to adhesive plaque performance through interfacial surface priming interactions in the case of Mfp-3 and Mfp-5—described further, below—and through metal coordination, as seen in Mfp-1 and Mfp-2 [36-39].

Raman microscopy shows Dopa coordination to Fe(III) throughout the plaque with a predominance occurring in the outer cuticle and less near the interface between the plaque and the substrate [40]. Mfp-1 is a coating protein that forms the cuticle of the byssal plaque and thread (Figure 1.5) [39, 41, 42]. Two variants of Mfp-1 exist and differ based on the extent of posttranslational hydroxylation of tyrosine to Dopa [38]. The Mfp-1 variant with higher Dopa content is found as hard granules with a high density of Fe(III)-Dopa coordination, as confirmed by Raman microscopy [38]. The Mfp-1 variant with relatively less Dopa forms the protein matrix that surrounds the granules and has a lower density of Fe(III)-Dopa coordination [38]. The high Fe(III)-Dopa crosslink density of the granules imparts hardness, while the low Fe(III)-Dopa crosslink density of the surrounding protein matrix allows for extensibility [38]. Additionally, these hard Fe(III)-Dopa crosslinked granules enable high cuticle failure strains by hindering crack propagation [38]. When the cuticle is strained microcracks form preferentially within the softer surrounding protein matrix and these cracks extend until obstructed by a harder, more highly crosslinked granule [38, 39, 41]. The importance of Fe(III) to the mechanical properties of the cuticle has been confirmed through EDTA treatment. Raman spectra of EDTA-treated cuticles show significant reduction in Fe(III)-Dopa resonance peaks and the hardness of the EDTA-treated cuticles is reduced by 50% [39]. Reintroduction of Fe(III) to the cuticle is accompanied by recovery of Fe(III)-Dopa resonance peaks in the Raman spectra and

highlights the reversible nature of Fe(III)-Dopa crosslinking [39, 43, 44]. Recent nanoindentation results suggest granules are softer than the surrounding matrix (unpublished data from the lab of J. Herbert Waite, UC Santa Barbara). As a result, the preceding discussion on Mfp-1 chemistry and mechanical properties awaits clarification from continuing experiments.

Mfp-2, located within the central bulk of the plaque (Figure 1.5), is the most abundant Mfp, and contains only 5 mol% Dopa [40]. Mfp-2 is an important structural component of the plaque and therefore must interact strongly with itself to ensure strong cohesion within the bulk of the plaque. Fe(III) addition induces strong crosslinking within Mfp-2 [40]. Additionally, mixtures of purified Mfp-2 and Fe(III) precipitated at pH 8 show a resonance Raman signal characteristic of tris Dopa coordination to Fe(III) [40]. The prevalence of Fe(III)-Dopa complexation within Mfp-1 and Mfp-2 contribute to the structural integrity of the adhesive plaques and enable their unique mechanical properties. Dopa in other Mfps (considered below) is utilized for interfacial interactions.

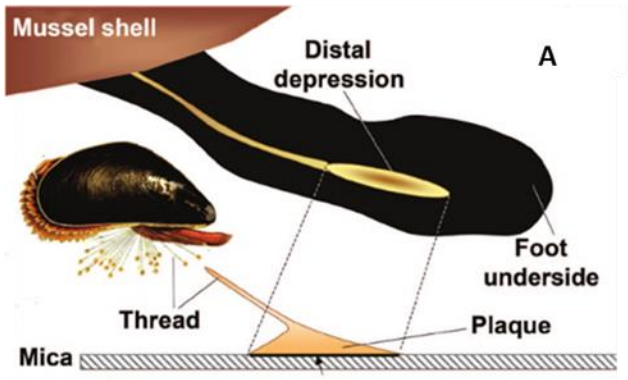

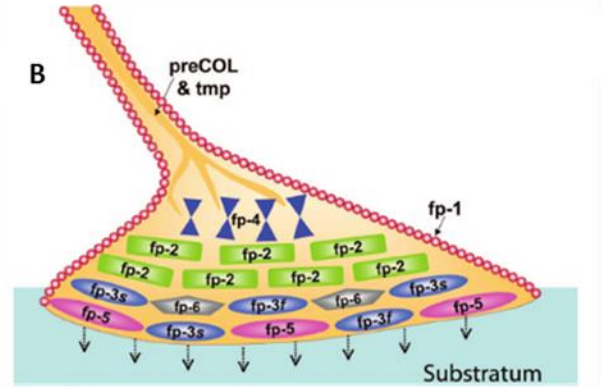

C

Mfp	Dopa %	Lys %	Arg/HyArg %
Mfp-1	15	19.4	1
Mfp-2	5	16.9	9.3
Mfp-3 fast	20	15	9.5
Mfp-5	30	19.5	3.1

Figure 1.5. Byssal plaque of the marine mussel. (A) Adhesive plaques are secreted by the mussel foot into the distal depression. This process is repeated to produce a series of radially distributed proteinaceous adhesive plaques and tethers collectively known as the byssus. (B) The relative location of several mussel foot proteins within the adhesive plaque. Mfp-1 is the surface-coating cuticle of the plaque and thread. Mfp-2 is a cohesive structural protein within the plaque. Mfp-3 and Mfp-5 are deposited onto the substratum as a surface-priming layer. C. Dopa, Lys, and Arg + Arg-OH content of selected Mfps. Figure 1.5 was adapted and developed from [45].

1.3 Surface Interactions of Catechol

1.3.1 Catechol Interactions on Mica

Mica—a hydrophilic, negatively charged aluminosilicate mineral—is representative of rocks found in the marine environment. Water and hydrated cations form a tightly bound hydration layer on mica [46]. This hydration layer obstructs the interaction between an adhesive material and the underlying surface which is required for sturdy wet adhesion. Wet adhesive proteins such as surface priming Mfp-3 and Mfp-5 are capable of displacing this hydration layer, enabling strong adhesive interactions underwater.

The Surface Forces Apparatus (SFA) is ideally suited to investigations of adhesive materials on a mica surface in water, and therefore has been extensively utilized in characterization of wet adhesive properties of Mfps [29, 33-35, 47, 48], as well as other compounds, including catechols [49-51]. The geometry of the catechol group is particularly well suited for binding interactions in mica. The hydroxyl spacing on the catechol moiety (~0.29 nm) is commensurate with the spacing of the hydrogen-bond accepting oxygens on the mica surface (0.28 nm) [32, 52]. Several catechol-containing adhesive materials have been compared to their phenol-containing analogs and the switch from the bidentate interaction of catechol to the monodentate interaction of phenol results in a significant decrease in measured adhesion forces [49, 53]. According to Bell theory ($\tau = \tau_0 e^{-E/kT}$), the bidentate hydrogen bonding of catechol to mica (-E = ~28 kT) would have a binding lifetime (τ) that is 10^6 times longer than the monodentate form (-E = ~14 kT) [31, 32, 54].

The interfacial surface priming adhesive proteins—Mfp-3 and Mfp-5—are relatively low molecular weight, intrinsically unstructured, and adsorb quickly and reversibly to an array of wet surfaces with diverse chemical and physical properties [35]. SFA adhesion experiments of Mfps on mica surfaces show maximum adhesion at or below pH 3.3. This correlates with the low pH deposition environment in the distal depression of the mussel foot during plaque formation (Figure 1.5) [55]. Measured adhesive forces of Mfps are considerably lower at pH 5.5 and in most cases adhesion is completely abolished above pH 7.5 [29, 31, 34, 45]. pH-dependent oxidation of Dopa has been implicated in the pH dependence of Mfp adhesion [31, 32, 34]. The Dopaquinone product of Dopa oxidation is incapable of hydrogen bond donation, resulting in a loss of adhesion. One notable strategy to prevent Dopa oxidation while enabling surface adhesion is through boronate-complexed Dopa [56]. The Dopa-boronate complex has a weak stability constant and the negative surface charge of mica at pH 7.5 destabilizes and induces dissociation of the borate ion from the complex, leading to Dopa surface binding [56].

1.3.2 Catechol Interactions on Titania

Adsorption of catechol [57, 58] and adhesion of single Dopa residues [59] and Dopa-containing Mfp-3 [60] to titania has been extensively studied, in part because of the prevalence of titania in medical implants. Density functional theory studies suggests three distinct adsorption modes of catechol to titania, including bidentate H-bonding, monodentate H-bonding combined with a single coordination bond, and bidentate

coordination [57]. These binding modes also likely occur through Dopa in Mfp-3 [60] (Figure 1.6), with the balance of the three interaction modes on titania depending largely on the pH [59, 60]. In acidic conditions the protonated form of the Dopa catechol is favored and this leads to the formation of bidentate hydrogen bonding between Dopa hydroxyls and interfacial oxygen atoms on the titania surface. At elevated pH, fully deprotonated Dopa coordinates to the available interfacial Ti^{IV} sites in a bidentate manner [60]. At intermediate pH, a hybrid of these two binding modes is possible.

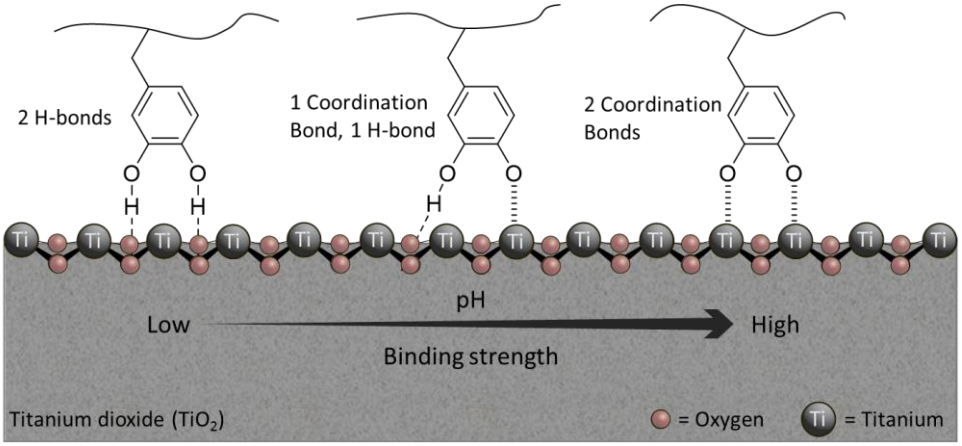

Figure 1.6. Binding modes of Dopa to TiO_2. This simplified TiO_2 surface contains titanium atoms (grey) and oxygen atoms (red). The binding mode of Dopa to TiO_2 is pH dependent with bidentate H-bonding favored below pH 5.5, monodentate H-bonding combined with one coordination bond favored at intermediate pH, and two coordination bonds favored at pH above 7.0. Figure 1.6 was adapted from [60].

Bacterial biofilms readily form on titania-coated surgical implants [61]. Attenuated total reflection infrared spectroscopy (ATR-IR) results show that the siderophores, enterobactin and pyoverdine, may play a key role in biofilm initiation on titania [62, 63]. Pyoverdines, produced by many Pseudomonads including *Pseudomonas aeruginosa*, have dihydroxyquinoline and two hydroxamic acid groups that coordinate iron(III). Apo

pyoverdines may be bound at the cell surface through the outer membrane FpvA receptor protein [64]. Similarly, apo enterobactin can be bound at the cell surface of *E. coli* through association with the FepA receptor [62]. ATR-IR of free enterobactin and pyoverdine in the presence of titania surfaces show characteristic absorption bands of catecholate ligands coordinated to metal ions [62, 63]. ATR-IR spectra retain these characteristic features when wild-type *P. aeruginosa* or *E. coli* cells decorated with their respective siderophores are exposed to titania surfaces [62, 63]. A *P. aeruginosa* mutant was produced that lacks the outer membrane pyoverdine receptor, FpvA, and therefore cannot bind pyoverdine at the cell surface [63]. The characteristic ATR-IR absorption bands for catechol-titania coordination are absent for the mutant *P. aeruginosa*. These results are consistent with siderophore-initiated bacterial cell attachment to titania surfaces. Interestingly, catechol can also be used to prevent bacterial attachment to titania surfaces. Several materials utilize catechol as an anchor for antifouling self-assembled monolayers (SAMs) on titania as well as other metal oxides [65, 66].

1.4 Catechol Oxidation

Catechol undergoes pH-dependent oxidation by dioxygen in aqueous solution, producing quinone and hydrogen peroxide [67, 68]. The reactive semiquinone intermediate and quinone product can undergo secondary reactions, forming crosslinked catechol products through aryl coupling, Michael-type addition, Schiff base reaction, and Strecker degradation [69]. The mechanisms of these reactions have been reviewed previously [69].

The reaction sequence of catechol autoxidation is relevant to understanding the formation and function of many biological materials. These materials include Mfps [31, 45, 52], squid beaks [3], sand castle worm cement [4], and melanins [70]. Additionally, antioxidant tea catechins and neurotransmitters (e.g., dopamine, epinephrine, and norepinephrine) are also classes of catechol-containing small molecules that are susceptible to autoxidation [68, 71-73]. Despite the prevalence of catechol autoxidation, many mechanistic details remain to be elucidated.

The autoxidation of catechol has been investigated electrochemically and by tracking dioxygen concentration in aqueous solution [67, 68, 71, 72, 74, 75]. It is widely accepted that this radical process proceeds through semiquinone and superoxide [68, 71, 75]. However, the lack of agreement on the identity of the initiation reaction of the autoxidation has sparked contrasting interpretations on the mechanism of catechol oxidation by O_2. One interpretation proposes a one-electron oxidation of catechol by dioxygen, involving a direct electron transfer from singlet state catechol to triplet state molecular oxygen [75]. Alternatively, the reaction may begin with the conproportionation of catechol and *o*-quinone to form two equivalents of semiquinone [68]. The more reactive semiquinone can then be oxidized by dioxygen, forming superoxide and quinone. These reactions are summarized in Figure 1.7.

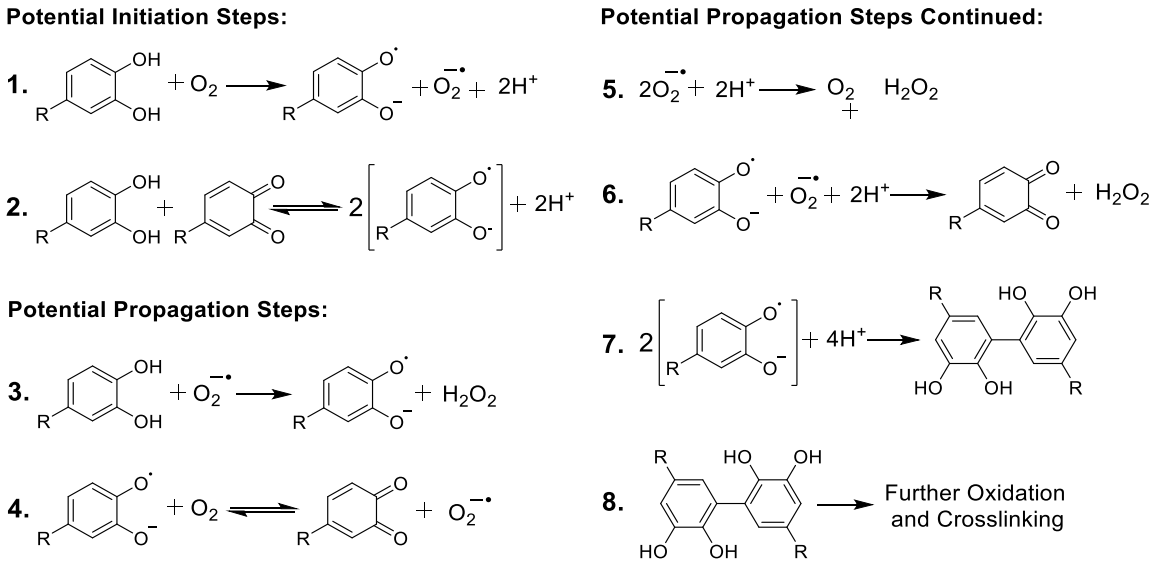

Figure 1.7. Potential catechol autoxidation reactions. Catechol autoxidation is initiated either by direct electron transfer from catechol to dioxygen to form semiquinone and superoxide or by the conproportionation of catechol and quinone to form semiquinone. Catechol autoxidation is propagated by steps involving the superoxide or semiquinone radicals. The protonation state of semiquinone is uncertain and reactions shown here involving semiquinone are balanced assuming a deprotonated hydroxyl.

The rate of autoxidation of catechol-containing small molecules increases with increasing pH [67, 71, 72, 76-78]. Autoxidation also depends on the nature of the catechol (e.g., 2,3-dihydroxy versus 3,4-dihydroxy catechol), as well as the nature of the substituent groups. A definitive physical organic analysis of aqueous catechol oxidation by dioxygen under physiological relevant conditions is needed to fully understand the natural system and for development of new wet adhesive materials.

1.4.1 Oxidation of Catechols by Fe(III) in Mussel Plaques

Oxidation of catechol, Dopa, and several other 3,4-dihydroxy catechols by Fe(III) occurs in aqueous acidic solution (0.01-1M H^+) forming quinone and two equivalents of Fe(II) [79-81]. A semiquinone radical intermediate is formed during the rate-determining step, which is subsequently oxidized to quinone by a second equivalent of Fe(III) [80] (Figure 1.8).

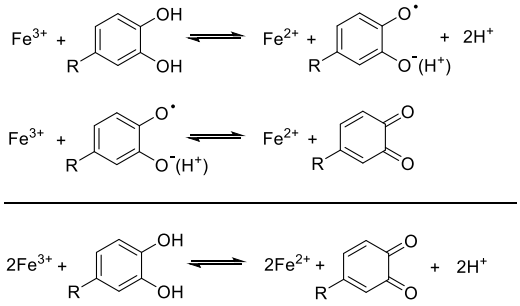

Figure 1.8. Redox reactions between iron(III) and catechol in aqueous acidic media. The protonation state of semiquinone is uncertain and reactions shown here involving semiquinone are balanced assuming a deprotonated hydroxyl.

In addition to Fe(III)-Dopa crosslinking in the mussel plaques described above, Fe(III)-induced oxidation and aryl crosslinking of the 3,4-dihydroxy catechol in Dopa is implicated in the curing process of mussel adhesive plaques [82-85]. Purified Mfp-1 and Mfp-2 precipitate upon addition of Fe(III) at pH 1.5. Analysis of the precipitate reveals the presence of radical species by EPR from high spin Fe(III) and an organic radical [84], presumably Dopa-semiquinone, which readily undergoes aryl coupling [69]. EPR signals are absent in the Fe(III)-free form of Mfp-1 and Mfp-2, suggesting that Dopa-semiquinone appears as a result of Fe(III) addition [84]. Dopa-containing small molecules and model

peptides also form covalently crosslinked aryl dimers at pH 2 in the presence of Fe(III) [85]. Fe(III)-dependent dimer formation decreases with increasing pH. Dimerization occurs most readily at pH 2, can be detected at pH 5, and is absent at pH 7 and 9, where Fe(III) coordination is favored over Fe(III) induced oxidation [85]. A Dopa autoxidation product was observed at pH 9 in the absence of Fe(III) and this product is not detected in the presence of Fe(III), demonstrating that Fe(III) coordination protects Dopa against autoxidation [85].

Collectively, these results imply that a significant number of Fe(III)-induced covalent crosslinks may initially form within the Mfps in the plaque in the low pH environment of the distal depression before mussel foot removal allows equilibration to oceanic pH. The pH increase favors Fe(III) coordination to Dopa, which protects the catechol group against oxidation and adds an additional layer of crosslinking in the cured plaque.

2,3-DHBA in siderophores and analogs coordinated to Fe(III) in physiological conditions (near neutral pH and higher) is stabilized against catechol oxidation. However in strongly acidic solution (1 M H^+), Fe(III) catalyzes oxidation of 2,3-DHBA [86]. Thus, 2,3-DHBA behaves similarly to Dopa, although the pH range is shifted, and at physiological pH little if any oxidation of 2,3-DHBA and aryl crosslinking occurs.

1.5 Conclusion

The impressive range of catechol chemical reactivity and physicochemical interactions enable its inclusion in a wide range of natural materials, including neurotransmitters,

catechins, melanin, bacterial siderophores, and mussel adhesive plaques among others. Fe(III) coordination is especially important in bacterial siderophores—in which catechol binds Fe(III) with exceptionally high affinity—and for mussel adhesive plaques—where Fe(III) coordination to Dopa and Fe(III)-induced oxidation of Dopa forms crosslinks that are essential to plaque cohesion. Catechol in siderophore analogs and Mfps is also a key contributor to energetic adhesive interactions on wet surfaces. Parsing catechol interactions in natural adhesive materials aids in the understanding of these complex systems and as a result new synthetic materials are incorporating catechol [47, 84, 87-98] and utilizing its impressive range of chemical reactivity and physicochemical interactions for adhesive and other interactions.

1.6 References

1 Hickford SJH, Kupper FC, Zhang GP, Carrano CJ, Blunt JW and Butler A (2004) Journal of Natural Products 67:1897-1899

2 Pfleger BF, Lee JY, Somu RV, Aldrich CC, Hanna PC and Sherman DH (2007) Biochemistry 46:4147-4157

3 Miserez A, Schneberk T, Chengjun S, Frank CW and Waite JH (2008) Science 319:1816-1819

4 Zhao H, Sun C, Stewart RJ and Waite JH (2005) J Biol Chem 280:42938-42944

5 Raymond KN, Dertz EA and Kim SS (2003) Proc Natl Acad Sci U S A 100:3584-3588

6 Reichert J, Sakaitani M and Walsh CT (1992) Protein Sci 1:549-556

7 Sandy M and Butler A (2011) J Nat Prod 74:1207-1212

8 Dertz EA, Xu J, Stintzi A and Raymond KN (2006) J Am Chem Soc 128:22-23

9 Avdeef A, Sofen SR, Bregante TL and Raymond KN (1978) J Am Chem Soc 100:5362-5370

10 Harris WR, Carrano CJ, Cooper SR, Sofen SR, Avdeef AE, McArdle JV and Raymond KN (1979) J Am Chem Soc 101:6097-6104

11 Loomis LD and Raymond KN (1990) Inorg Chem 30:906-911

12 Karpishin TB and Raymond KN (1992) Angew Chem Int Ed Engl 31:466-468

13 Karpishin TB, Dewey TM and Raymond KN (1993) J Am Chem Soc 115:1842-1851

14 Scarrow RC, Ecker DJ, Ng C, Liu S and Raymond KN (1991) Inorg Chem 30:900-906

15 Bluhm ME, Kim SS, Dertz EA and Raymond KN (2002) J Am Chem Soc 124:2436-2437

16 Abergel RJ, Zawadzka AM, Hoette TM and Raymond KN (2009) Journal of the American Chemical Society 131:12682-12692

17 Sandy M, Han A, Blunt J, Munro M, Haygood M and Butler A (2010) Journal of Natural Products 73:1038-1043

18 Butler A and Theisen RM (2010) Coord Chem Rev 254:288-296

19 Sandy M and Butler A (2009) Chem Rev 109:4580-4595

20 Abergel RJ, Warner JA, Shuh DK and Raymond KN (2006) J Am Chem Soc 128:8920-8931

21 Cohen SM and Raymond KN (2000) Inorg Chem 39:3624-3631

22 Persmark M, Expert D and Neilands JB (1989) J Biol Chem 264:3187-3193

23 Tomisic V, Blanc S, Elhabiri M, Expert D and Albrecht-Gary A-M (2008) Inorg Chem 47:9419-9430

24 Soengas RG, Anta C, Espada A, Paz V, Ares IR, Balado M, Rodríguez J, Lemos ML and Jiménez C (2006) Tetrahedron Letters 47:7113-7116

25 Iglesias E, Brandariz I, Jimenez C and Soengas RG (2011) Metallomics 3:521-528

26 Holten-Andersen N, Harrington MJ, Birkedal H, Lee BP, Messersmith PB, Lee KY and Waite JH (2011) Proc Natl Acad Sci U S A 108:2651-2655

27 Sever MJ and Wilker JJ (2004) Dalton Trans, doi 10.1039/B315811J:1061-1072

28 Menyo MS, Hawker CJ and Waite JH (2013) Soft Matter 9

29 Wei W, Yu J, Broomell C, Israelachvili JN and Waite JH (2013) J Am Chem Soc 135:377-383

30 Zhao H, Robertson NB, Jewhurst SA and Waite JH (2006) J Biol Chem 281:11090-11096

31 Yu J, Wei W, Danner E, Israelachvili JN and Waite JH (2011) Adv Mater 23:2362-2366

32 Yu J, Wei W, Danner E, Ashley RK, Israelachvili JN and Waite JH (2011) Nat Chem Biol 7:588-590

33 Lin Q, Gourdon D, Sun C, Holten-Andersen N, Anderson T, Waite JH and Israelachvili JN (2007) Proc Natl Acad Sci U S A 104:3782-3786

34 Danner EW, Kan Y, Hammer MU, Israelachvili JN and Waite JH (2012) Biochemistry 51:6511-6518

35 Lu Q, Danner E, Waite JH, Israelachvili JN, Zeng H and Hwang DS (2013) J R Soc Interface 10:20120759

36 Wilker JJ (2010) Angew Chem Int Ed Engl 49:8076-8078

37 Wilker JJ (2010) Curr Opin Chem Biol 14:276-283

38 Harrington MJ, Masic A, Holten-Andersen N, Waite JH and Fratzl P (2010) Science 328:216-220

39 Holten-Andersen N, Mates TE, Toprak MS, Stucky GD, Zok FW and Waite JH (2008) Langmuir 25:3323-3326

40 Hwang DS, Zeng H, Masic A, Harrington MJ, Israelachvili JN and Waite JH (2010) J Biol Chem 285:25850-25858

41 Holten-Andersen N, Fantner GE, Hohlbauch S, Waite JH and Zok FW (2007) Nat Mater 6:669-672

42 Taylor SW, Luther III GW and Waite JH (1994) Inorg Chem 33:5819-5824

43 Werneke SW, Swann C, Farquharson LA, Hamilton KS and Smith AM (2007) J Exp Biol 210:2137-2145

44 Vaccaro E and Waite JH (2001) Biomacromolecules 2:906-911

45 Nicklisch SC and Waite JH (2012) Biofouling 28:865-877

46 Israelachvili JN and Wennerstrom H (1996) Nature 379:219-225

47 Lee BP, Messersmith PB, Israelachvili JN and Waite JH (2011) Annu Rev Mater Res 41:99-132

48 Hwang DS, Wei W, Rodriguez-Martinez NR, Danner E and Waite JH (2013) In: H. Zeng (ed) Polymer adhesion, friction,a nd lubrication. John Wiley & Sons, Inc., Hoboken, NJ,

49 Maier GP, Rapp MV, Waite JH, Israelachvili JN and Butler A (2015) Science 349:628-632

50 Rapp MV, Maier GP, Dobbs HA, Higdon NJ, Waite JH, Butler A and Israelachvili JN (2016) J Am Chem Soc 138:9013-9016

51 Ahn BK, Das S, Linstadt R, Kaufman Y, Martinez-Rodriguez NR, Mirshafian R, Kesselman E, Talmon Y, Lipshutz BH, Israelachvili JN and Waite JH (2015) Nat Commun 6:8663

52 Wilker JJ (2011) Nat Chem Biol 7:579-580

53 Wei W, Yu J, Gebbie MA, Tan Y, Martinez Rodriguez NR, Israelachvili JN and Waite JH (2015) Langmuir 31:1105-1112

54 Israelachvili J (2011) Intermolecular and surface forces. Elsevier Inc.,

55 Martinez Rodriguez NR, Das S, Kaufman Y, Israelachvili JN and Waite JH (2015) Biofouling 31:221-227

56 Kan Y, Danner EW, Israelachvili JN, Chen Y and Waite JH (2014) PLoS One 9:e108869

57 Terranova U and Bowler DR (2010) j phys Chem C 114:6491-6495

58 Liu Y, Dadap JI, Zimdars D and Eisenthal KB (1999) J Phys Chem B 103:2480-2486

59 Lee H, Scherer NF and Messersmith PB (2006) Proc Natl Acad Sci U S A 103:12999-13003

60 Yu J, Wei W, Menyo MS, Masic A, Waite JH and Israelachvili JN (2013) Biomacromolecules 14:1072-1077

61 Costerton J, Stewart P and Greenberg E (1999) Science 284:1318-1322

62 Upritchard HG, Yang J, Bremer PJ, Lamont IL and McQuillan AJ (2011) Langmuir 27:10587-10596

63 Upritchard HG, Yang J, Bremer PJ, Lamont IL and McQuillan AJ (2007) Langmuir 23:7189-7195

64 Schalk IJ, Hennard C, Dugave C, Poole K, Abdallah MA and Pattus F (2001) Mol Microbiol 39:351-360

65 Lau KH, Ren C, Sileika TS, Park SH, Szleifer I and Messersmith PB (2012) Langmuir 28:16099-16107

66 Kang T, Oh DX, Heo J, Lee HK, Choy S, Hawker CJ and Hwang DS (2015) ACS Appl Mater Interfaces 7:24656-24662

67 Joslyn MA and Branch GEK (1935) J Am Chem Soc 57:1779-1785

68 Li G, Zhang H, Sader F, Vadhavkar N and Njus D (2007) Biochemistry 46:6978-6983

69 Yang J, Cohen Stuart MA and Kamperman M (2014) Chem Soc Rev 43:8271-8298

70 Felix CC and Sealy RC (1981) J Photochem Photobiol 34:423-429

71 Mochizuki M, Yamazaki S, Kano K and Ikeda T (2002) Biochim Biophys Acta 1569:35-44

72 Roginsky V and Alegria AE (2005) J Agric Food Chem 53:4529-4535

73 Roginsky V, Barsukova TK, Bruchelt G and Stegmann HB (1997) Z Naturforsch 53:380-390

74 Nematollahi D, Taherpour A, Jameh-Bozorghi S, Mansouri A and Dadpou B (2010) Int J Electrochem Sci 5:867-879

75 Shendrik AN, Odaryuk ID, Kanibolotska LV, Kalinichenko EA, Tsyapalo AS, Beznos VV and Kanibolotsky AL (2012) International Journal of Chemical Kinetics 44:414-422

76 Heacock RA (1959) Chem Rev 59:181-237

77 Bors W, Saran M, Michel C, Lengfelder E, Fuchs C and Spottl R (1975) Int J Radiat Biol Relat Stud Phys Chem Med 28:353-371

78 Bors W, Michel C, Manfred S and Lengfelder E (1978) Biochim Biophys Acta 540:162-172

79 Mentasti E and Pelizzetti E (1973) J Chem Soc Dalton Trans:2605

80 Mentasti E, Pelizzetti E and Saini G (1973) J Chem Soc Dalton Trans:2609-2614

81 Mentasti E, Pelizzetti E and Baiocchi C (1976) J Inorg Nucl Chem 38:2017-2021

82 Burzio LA and Waite JH (2000) Biochemistry 39:11147-11153

83 Miaoer Y, Hwang JW and Deming TJ (1999) J Am Chem Soc 121:5825-5826

84 Sever MJ, Weisser JT, Monahan J, Srinivasan S and Wilker JJ (2004) Angew Chem Int Ed Engl 43:448-450

85 Fullenkamp DE, Barrett DG, Miller DR, Kurutz JW and Messersmith PB (2014) RSC Adv 4:25127-25134

86 Xu J and Jordan RB (1988) Inorg Chem 27:4563-4566

87 Matos-Perez CR and Wilker JJ (2012) Macromolecules 45:6634-6639

88 Matos-Perez CR, White JD and Wilker JJ (2012) J Am Chem Soc 134:9498-9505

89 Lee H, Dellatore SM, Miller WM and Messersmith PB (2007) Science 318:426-430

90 Kim BJ, Oh DX, Kim S, Seo JH, Hwang DS, Masic A, Han DK and Cha HJ (2014) Biomacromolecules 15:1579-1585

91 Cencer M, Murley M, Liu Y and Lee BP (2015) Biomacromolecules 16:404-410

92 Cencer M, Liu Y, Winter A, Murley M, Meng H and Lee BP (2014) Biomacromolecules 15:2861-2869

93 Barrett DG, Bushnell GG and Messersmith PB (2013) Adv Healthc Mater 2:745-755

94 Lee J, Yang SH, Hong SP, Hong D, Lee H, Lee HY, Kim YG and Choi IS (2013) Macromol Rapid Commun 34:1351-1356

95 Yang SH, Kang SM, Lee KB, Chung TD, Lee H and Choi IS (2011) J Am Chem Soc 133:2795-2797

96 Sedo J, Saiz-Poseu J, Busque F and Ruiz-Molina D (2013) Adv Mater 25:653-701

97 White JD and Wilker JJ (2011) Macromolecules 44:5085-5088

98 Brubaker CE, Kissler H, Wang LJ, Kaufman DB and Messersmith PB (2010) Biomaterials 31:420-427

II. ADAPTIVE SYNERGY BETWEEN CATECHOL AND LYSINE PROMOTES WET ADHESION BY SURFACE SALT DISPLACEMENT

Parts of sections of this chapter were taken with permission from: Greg P. Maier*, Michael V. Rapp*, J. Herbert Waite, Jacob N. Israelachvili, Alison Butler. Adaptive synergy between catechol and lysine promotes wet adhesion by surface salt displacement. *Science*. 2015, 349, 628-632.

2.1 Introduction

The biomimetic approach to wet adhesive design has long utilized marine mussels as a source of inspiration. Mussels attach to wet surfaces using an array of proteins in the form of adhesive plaques and tethers (Figure 1.5) [1, 2]. Mfp-3 and mfp-5 are deposited first as a primer to condition the target surface and enable other Mfps to adhere [3]. These proteins are able to displace hydration layers, which are present at virtually all underwater mineral surfaces, and form strong adhesive interactions with the underlying surface [4].

The 30 mol % Dopa in Mfp-5 is exceptionally high and the highest among Mfps [5]. Atomic force microscope (AFM) experiments showing strong and reversible bidentate coordination and hydrogen bonds between Dopa and mineral oxide surfaces rationalized its importance in wet adhesion and its presence in surface priming Mfps [6]. Mfp-5 also contains 19.5 mol % Lys [7]; however, the significance of cationic residues in wet adhesion is

* These authors contributed equally to this work.

poorly understood compared to Dopa. The abundance and proximity of Dopa and Lys residues in Mfp-5 suggest a synergistic interaction with respect to wet adhesion [4].

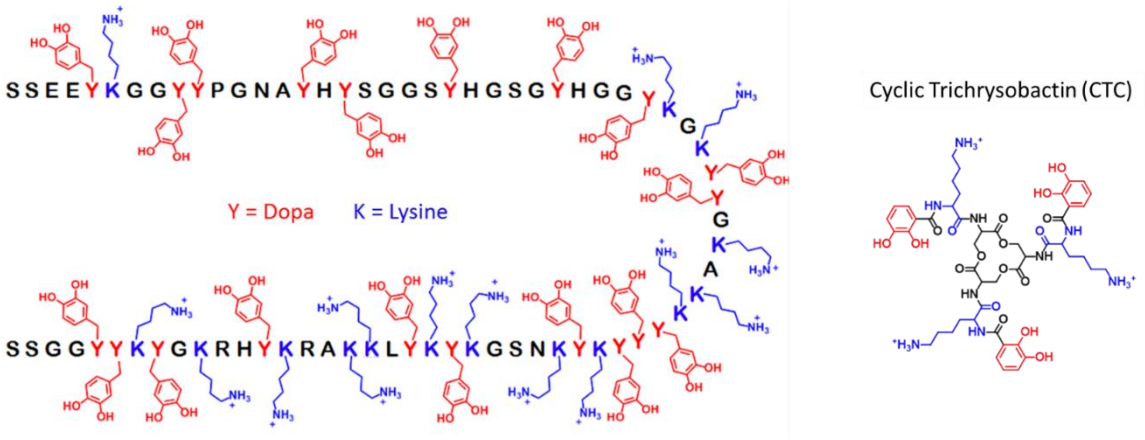

Figure 2.1. Amino acid sequence of Mfp-5 and structure of CTC

The abundance and proximity of catechol and Lys in CTC parallels Mfp-5 (Figure 2.1) [5]. However, the mass of Mfp-5 is ten times the mass of CTC [4]. The smaller siderophore has relaxed steric constraints when adsorbed to a surface and the simpler siderophore structure allows for more straightforward interpretation of the adhesive mechanisms. Additionally, synthetic analogs of CTC based on the tris(2-aminoethyl)amine (TREN) scaffold are stable over a broad pH range compared to the tri-serine lactone core of the natural siderophore [8] and provide a synthetically tractable platform to explore nanoscale wet adhesion mechanisms.

2.2 Statement of Chapter Objectives and Results Summary

The purpose of this study was to determine the contribution of both catechol and Lys to wet adhesion by comparing adhesive characteristics of a suite of six synthetic siderophore analogs using the SFA. Tren-Lys-Cam (TLC, Figure 2.9) and Tren-Dab-Cam (TDC, Figure 2.10) retain both catechol and amine functionalities seen in CTC and differ from eachother only in the length on the primary amine. Tren-Lys-Pam (TLP, Figure 2.11) and Tren-Lys-Bam (TLB, Figure 2.12) retain Lys and compromise the catechol functionality through removal of one or both hydroxyls. Tren-Lys^{Ac}-Cam (TL^{Ac}C, Figure 2.13) and Tren-Cam (TC, Figure 2.14) retain catechol but remove the amine functionality by acetylation to remove the charge or by completely removing the Lys residues. Collectively, the results reveal a maximum adhesion only when both catechol and cation (Lys or diaminobutyric acid (Dab)) are present. Additionally, siderophore analogs penetrate the hydration layer and adsorb to the mica surface only when the amine cations remain intact.

2.3 Experimental

2.3.1 Materials

2,3-dihydroxybenzoic acid (2,3-DHBA), catechol, 3,4-dihydroxybenzoic acid (3,4- DHBA), dicyclohexylcarbodiimide (DCC), and tris(2-aminoethyl)amine (TREN) were purchased from Aldrich. 4-methylcatechol (4-MC) was purchased from Acros Organics. Benzyl bromide, palladium on carbon, and benzoic acid were purchased from Alfa Aesar. N-

hydroxysuccinimide (NHS) was purchased from Fluka. Triethylamine, sodium phosphate dibasic, potassium hydroxide, and trifluoroacetic acid (TFA) were purchased from Fisher. 3-hydroxybenzoic acid was purchased from TCI. CAPSO buffer was purchased from Research Organics. Phosphate buffer was purchased from Fisher. H-Lys(Z)-OH, H-Dab(Boc)-H, and H-Lys(Ac)-OH were purchased from Bachem. Unless otherwise stated, all chemicals were used as received without further purification or modification.

2.3.2 Cyclic Trichrysobactin Isolation and Purification

A single colony of *Dickeya chrysanthemi* EC16 was inoculated into 200 mL of Difco LB Millar media. This started culture was grown overnight at 37°C on an orbital shaker (180 rpm). 5 ml of the started culture was inoculated into 2 L of pH 7.4 low-iron minimal nutrient medium containing NaCl (0.1 M), glycerol (0.041 M), citric acid (0.0238 M), NH_4Cl (0.02 M), Na_2HPO_4 (0.02 M), KCl (0.01 M), and $MgSO_4$ (0.0008 M) in iron-free Erlenmeyer flasks (4 L). Cultures were shaken at 180 rpm until reaching the early stationary growth phase (48 h). Liquid chrome azurol sulfonate (CAS) was used to indicate the presence of iron(III)-binding ligands. Cells were pelleted by centrifugation (6000 rpm, 30 min). The supernatant was decanted and shaken with 100 g/L Amberlite XAD-2 resin (Supelco) for 3 h at 120 rpm. The supernatant was removed by filtration and the XAD resin was transferred to a glass chromatography column (2 cm i.d.) and washed with 2 L doubly deionized H_2O. Siderophores were eluted with MeOH until CAS no longer indicated the presence of iron(III)-binding ligands and the MeOH eluent was concentrated under vacuum.

Siderophores were purified with reverse phase high performance liquid chromatography (RP-HPLC) on a prep-scale C_4 column (22 mm i.d., 250 mm length, Vydac) using a gradient from 90% doubly deionized H_2O (0.05 % TFA) and 10 % MeOH (0.05 % TFA) to 50 % doubly deionized H_2O (0.05 % TFA) and 50 % MeOH (0.05 % TFA) over 40 minutes. The eluent was continuously monitored at 215 nm and fractions were collected manually then concentrated under vacuum. CTC was identified using electrospray ionization mass spectrometry (ESI-MS) and the manually collected fraction containing CTC was ultrapurified by RP-HPLC using the method previously described. The ultrapure CTC fraction was lyophilized and stored at -20°C.

Cyclic Trichrysobactin: white powder; UV (MOPS pH 7) λ_{max} 330 nm; ^{1}H NMR data; ESI MS *m/z* 1054.46 $[M + H]^+$.

2.3.3 Siderophore Analog Synthesis

The triserine lactone scaffold of CTC hydrolyzes under acidic conditions [8]. To increase stability across a broad pH range a synthetic analog of CTC was synthesized, replacing the triserine lactone with a TREN core [9-12]. Five additional siderophore analogs were also synthesized. The structures of these six siderophore analogs are shown in Figure 2.8.

2.3.3.1 Synthesis and purification of Tren-Lys-Cam

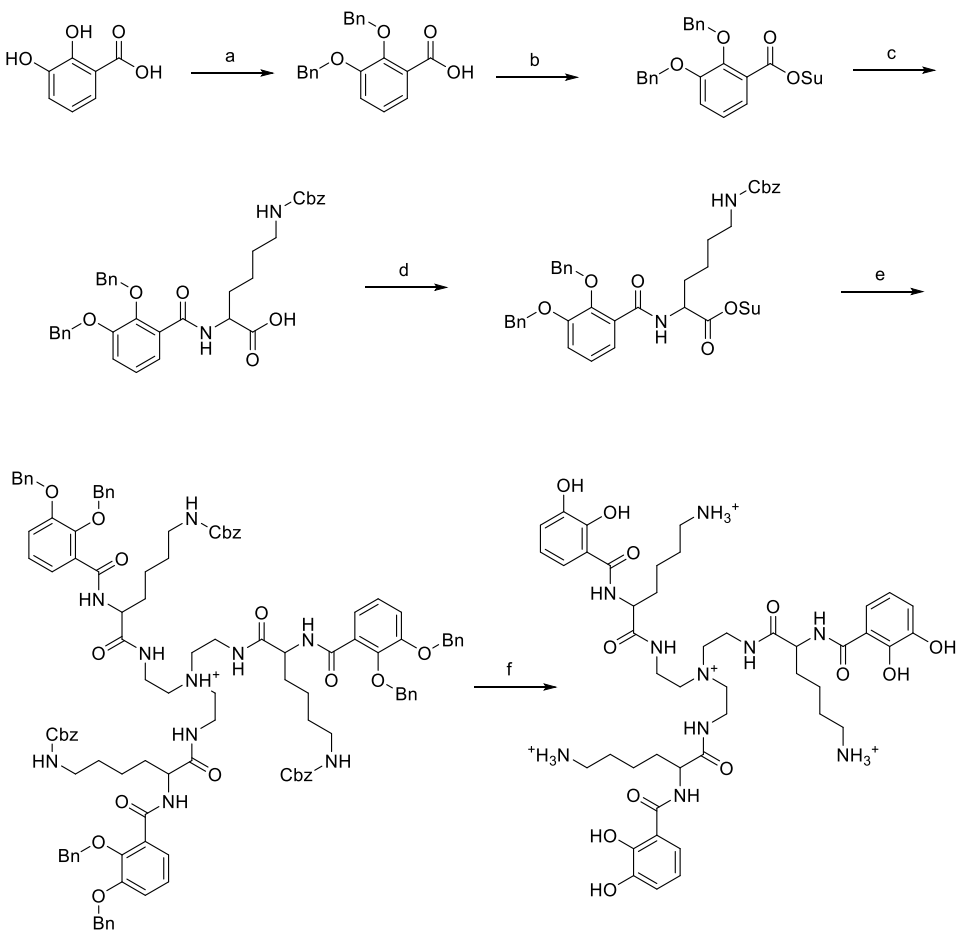

Figure 2.2. Synthesis scheme for TLC.

Step a: 1 equivalent of 2,3-DHBA and 12 equivalents of KOH were dissolved in dimethylsulfoxide (DMSO) and stirred for 15 minutes. 5 equivalents of benzyl bromide were added and the reaction was stirred overnight at room temperature. The reaction products were diluted with H_2O and extracted 3X with ethyl acetate, washed with brine, dried with anhydrous $MgSO_4$, and the solvent was removed under vacuum. Reaction products were analyzed using ESI-MS.

Step b: 1 equivalent of benzyl protected 2,3-dihydroxybenzoic acid (Bn-2,3-DHBA) and 1 equivalent of N-hydroxysuccinimide (NHS) were dissolved in anhydrous THF under nitrogen. 1 equivalent of dicyclohexylcarbodiimide (DCC) was then dissolved separately in anhydrous tetrahydrofuran (THF) under nitrogen and added dropwise to the initial solution over several minutes. The reaction was stirred for 4 h at room temperature. Solvent was removed under vacuum and the residue was dissolved in ethyl acetate. The solid dicyclohexylurea (DCHU) byproduct was removed by filtration and the remaining solvent was removed under vacuum. Reaction products were analyzed using ESI-MS.

Step c: 1 equivalent of Nε-benzyloxycarbonyl-L-lysine (H-Lys(Cbz)-OH) was dissolved in 70% THF in H_2O using heat and sonication. Subsequently, 4 equivalents of triethylamine (Et_3N) was dissolved in the solution. 1 equivalent of NHS activated Bn-2,3-DHBA (Bn-2,3-DHBA-OSu) was dissolved separately in THF and added to the Et_3N solution and stirred overnight at room temperature. The THF portion of the solvent was removed under vacuum and the remaining aqueous layer was acidified to pH 1-2 with 1 M HCl. The acidified aqueous layer was extracted 3X with ethyl acetate, washed with brine, dried with anhydrous $MgSO_4$, and the solvent was removed under vacuum. Reaction products were analyzed using ESI-MS.

Step d: 1 equivalent of Bn-2,3-DHBA-Lys(Cbz)-OH and 1 equivalent of NHS were dissolved in anhydrous THF under nitrogen. 1 equivalent of DCC was then dissolved separately in anhydrous THF under nitrogen and added dropwise to the initial solution over several minutes. The reaction was stirred overnight at room temperature. Solvent was removed under vacuum and the residue was dissolved in ethyl acetate. The solid DCHU byproduct

was removed by filtration and the remaining solvent was removed under vacuum. Reaction products were analyzed using ESI-MS.

Step e: 3.3 equivalents of Bn-2,3-DHBA-Lys(Cbz)-OSu was dissolved in dry dichloromethane (DCM) under nitrogen. 6 equivalents of Et_3N and 1 equivalent of TREN were then dissolved separately in dry DCM under nitrogen and added dropwise to the initial solution over several minutes and stirred overnight at room temperature. Any precipitates were removed via filtration and the filtrate was washed with brine, dried with $MgSO_4$, and the solvent was removed under vacuum. Reaction products were analyzed using ESI-MS.

Step f: 1 equivalent of Tren[Bn-2,3-DHBA-Lys(Cbz)]$_3$ was dissolved in 3% acetic acid in ethanol under nitrogen. 0.25 equivalents of 10 wt. % palladium on carbon (Pd/C) was added to the solution and the atmosphere was exchanged to H_2. The solution was stirred overnight and filtered to remove Pd/C. Reaction products were analyzed using ESI-MS.

TLC was purified with RP-HPLC on a prep-scale C_4 column (22 mm i.d., 250 mm length, Vydac) using a gradient from 100% doubly deionized H_2O (0.05 % TFA) to 25 % doubly deionized H_2O (0.05 % TFA) and 75 % MeOH (0.05 % TFA) over 10 minutes. The column was exchanged back to 100% H_2O (0.05% TFA) over the next 10 minutes. The eluent was continuously monitored at 215 nm and fractions were collected manually then concentrated under vacuum. TLC was identified using ESI-MS and the fraction containing TLC was ultrapurified by RP-HPLC using the method previously described. The ultrapure TLC fraction was lyophilized and stored at -20°C.

Tren-Lys-Cam: white powder; ^1H, ^{13}C, 2D NMR data; ESI-MS *m/z* 939.5 $[M + H]^+$.

2.3.3.2 Synthesis and purification of Tren-Dab-Cam

The synthesis for TDC follows the same procedure as the synthesis of TLC with the exception of using Nγ-*tert*-butyloxycarbonyl-L-2,4-diaminobutyric acid (H-Dab(Boc)-OH) in place of H-Lys(Cbz)-OH. An additional final step was performed to remove the Boc protecting group. The product of step f was dissolved in 50% TFA in DCM at room temperature and stirred for 2 hours. TDC was purified with RP-HPLC on a prep-scale C_4 column (22 mm i.d., 250 mm length, Vydac) using a gradient from 100% doubly deionized H_2O (0.05 % TFA) to 60 % doubly deionized H_2O (0.05 % TFA) and 40 % MeOH (0.05 % TFA) over 10 minutes. The column was exchanged back to 100% H_2O (0.05% TFA) over the next 10 minutes. The eluent was continuously monitored at 215 nm and fractions were collected then concentrated under vacuum. TDC was identified using ESI-MS and the manually collected fraction containing TDC was ultrapurified by RP-HPLC using the method previously described. The ultrapure TDC fraction was lyophilized and stored at -20°C.

Tren-Dab-Cam: white powder; ^{1}H, ^{13}C, NMR data; ESI-MS *m/z* 855.31 $[M + H]^+$.

2.3.3.3 Synthesis and purification of Tren-Lys-Pam

The synthesis for TLP follows the same procedure as the synthesis of TLC with the exception of using 3-hydroxybenzoic acid in place of 2,3-dihydroxybenzoic acid. TLP was purified with RP-HPLC on a prep-scale C_4 column (22 mm i.d., 250 mm length, Vydac) using a gradient from 100% doubly deionized H_2O (0.05 % TFA) to 25 % doubly deionized H_2O (0.05

% TFA) and 40 % MeOH (0.05 % TFA) over 15 minutes. The column was exchanged back to 100% H_2O (0.05% TFA) over the next 10 minutes. The eluent was continuously monitored at 215 nm and fractions were collected manually then concentrated under vacuum. TLP was identified using ESI-MS and the manually collected fraction containing TLP was ultrapurified by RP-HPLC using the method previously described. The ultrapure TLP fraction was lyophilized and stored at -20°C.

Tren-Lys-Pam: white powder; ^{1}H, ^{13}C, NMR data; ESI-MS *m/z* 891.47 $[M + H]^+$.

2.3.3.4 Synthesis and purification of Tren-Lys-Bam

The synthesis for TLB follows the same procedure as the synthesis of TLC with the exception of using benzoic acid in place of 2,3-DHBA, which obviates step a and allows the synthesis to begin directly with step b. TLB was purified with RP-HPLC on a prep-scale C_4 column (22 mm i.d., 250 mm length, Vydac) using a gradient from 100% doubly deionized H_2O (0.05 % TFA) to 25 % doubly deionized H_2O (0.05 % TFA) and 40 % MeOH (0.05 % TFA) over 15 minutes. The column was exchanged back to 100% H_2O (0.05% TFA) over the next 10 minutes. The column was exchanged back to 100% H_2O (0.05% TFA) over the next 10 minutes. The eluent was continuously monitored at 215 nm and fractions were collected manually then concentrated under vacuum. TLB was identified using ESI-MS and the manually collected fraction containing TLB was ultrapurified by RP-HPLC using the method previously described. The ultrapure TLB fraction was lyophilized and stored at -20°C.

Tren-Lys-Bam: white powder; ^{1}H, ^{13}C, NMR data; ESI-MS *m/z* 843.53 $[M + H]^+$.

2.3.3.5 Synthesis and purification of Tren-Lys^{Ac}-Cam

The synthesis for TL^{Ac}C follows the same procedure as the synthesis of TLC with the exception of using Nε-acetyl-L-lysine (H-Lys(Ac)-OH) in place of Nε-benzyloxycarbonyl-L-lysine (H-Lys(Cbz)-OH). TL^{Ac}C was purified with RP-HPLC on a prep-scale C_4 column (22 mm i.d., 250 mm length, Vydac) using a gradient from 100% doubly deionized H_2O (0.05 % TFA) to 25 % doubly deionized H_2O (0.05 % TFA) and 40 % MeOH (0.05 % TFA) over 15 minutes. The column was exchanged back to 100% H_2O (0.05% TFA) over the next 10 minutes. The eluent was continuously monitored at 215 nm and relevant fractions were concentrated under vacuum. TL^{Ac}C was identified using ESI-MS and the fraction containing TL^{Ac}C was ultrapurified by RP-HPLC using the same method. The ultrapure TL^{Ac}C fraction was lyophilized and stored at -20°C.

Tren-Lys^{Ac}-Cam: white powder; ^{1}H, ^{13}C, NMR data; ESI-MS *m/z* 1065.44 $[M + H]^+$.

2.3.3.6 Synthesis and purification of Tren-Cam

The synthesis for TC follows the same procedure as the synthesis of TLC with the exception of omitting steps c and d. TC was purified with RP-HPLC on a prep-scale C_4 column (22 mm i.d., 250 mm length, Vydac) using a gradient from 100% doubly deionized H_2O (0.05 % TFA) to 25 % doubly deionized H_2O (0.05 % TFA) and 40 % MeOH (0.05 % TFA) over 15 minutes. The column was exchanged back to 100% H_2O (0.05% TFA) over the next 10 minutes. The eluent was continuously monitored at 215 nm and fractions were collected

manually then concentrated under vacuum. TC was identified using ESI-MS and the manually collected fraction containing TC was ultrapurified by RP-HPLC using the method previously described. The ultrapure TC fraction was lyophilized and stored at -20°C.

Tren-Cam: white powder; ^{1}H, ^{13}C, 2D NMR data; ESI-MS *m/z* 555.2 $[M + H]^{+}$.

2.3.4 Surface Forces Apparatus Technique and Measurements

SFA measurements were performed by Michael V. Rapp in the research lab of Professor Jacob Israelachvili at UC Santa Barbara. Details on the SFA instrument and experimental methods have been published elsewhere [4, 13, 14]. For each experiment, mica surfaces are fixed to perpendicular cylinders in the SFA. Forces recorded during experiments are normalized by the radius of these cylinders to account for small differences in mica-mica contact area between experiments. A 50 µL drop of buffer was injected between the two freshly cleaved mica surfaces. Force-distance measurements for the buffer were determined for each experiment to ensure contaminant free surfaces. In these experiments, the surfaces were brought together in buffer at a constant speed and held in contact under load for a certain amount of time. The surfaces were then pulled apart at a constant rate. The adhesive/repulsive forces as well as the distance between the surfaces were continuously measured and recorded throughout the experiment. Subsequently, 10 µL of a siderophore or siderophore analog solution in buffer was injected into the gap solution at the interface between the two mica surfaces. Siderophores or siderophore

analogs were allowed to adsorb to the mica surfaces for 20 minutes prior to a second force-distance measurement.

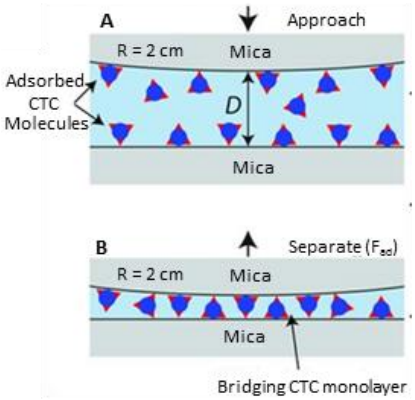

Figure 2.3. SFA experimental procedure. (A) Prior to the approach of the mica surfaces, CTC or a siderophore analog were allowed to adsorb to the mica surfaces. (B) The adsorbed molecules were compressed into a monolayer (as shown here for CTC) or a multilayer and held under force for a certain amount of time before the surfaces are separated. Figure 2.3 was produced by Michael V. Rapp in the research lab of Professor Jacob Israelachvili at UC Santa Barbara.

2.4 Results

2.4.1 Cyclic Trichrysobactin Isolation and Purification

Dickeya chrysanthemi was grown in low-iron media to promote the production of cyclic trichrysobactin, which was isolated from the cell-free supernatant by adsorption onto Amberlite XAD-2 resin, elution with methanol, solvent exchange into H_2O, and purified by RP-HPLC. The HPLC chromatogram contains several iron(III)-binding ligands, all of which gave a positive CAS assay response [15]. However, only CTC was of interest and therefore only this peak was collected, purified, and characterized (Figure 2.4-2.8).

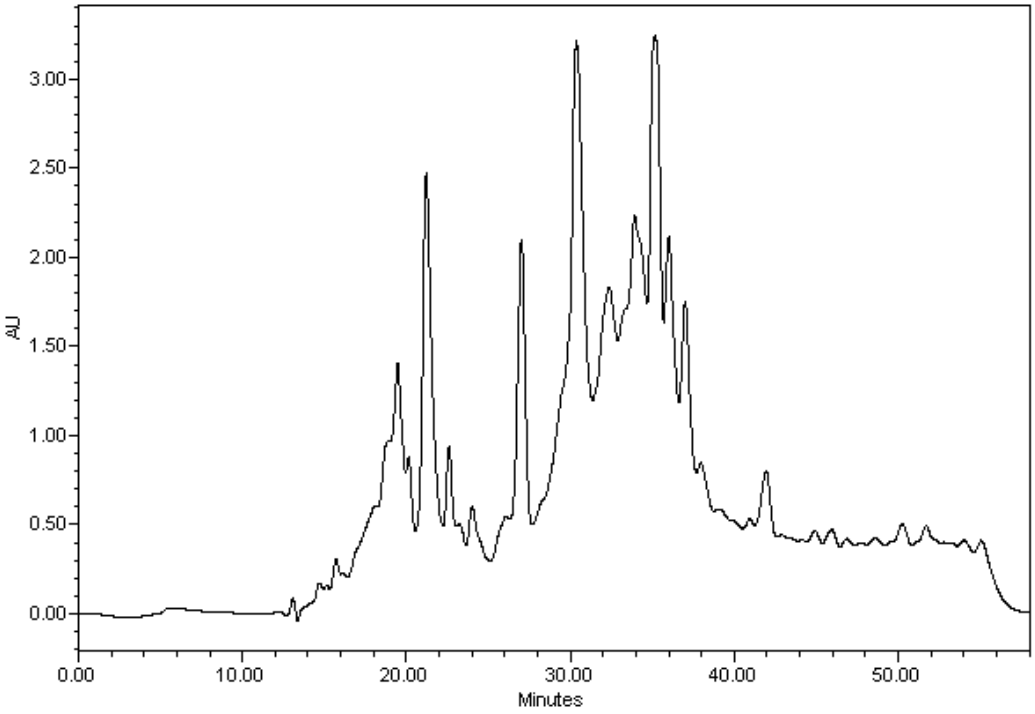

Figure 2.4. RP-HPLC chromatogram of the MeOH XAD-2 extract form *Dickeya Chrysanthemi* culture supernatant. The eluent was monitored at 215 nm.

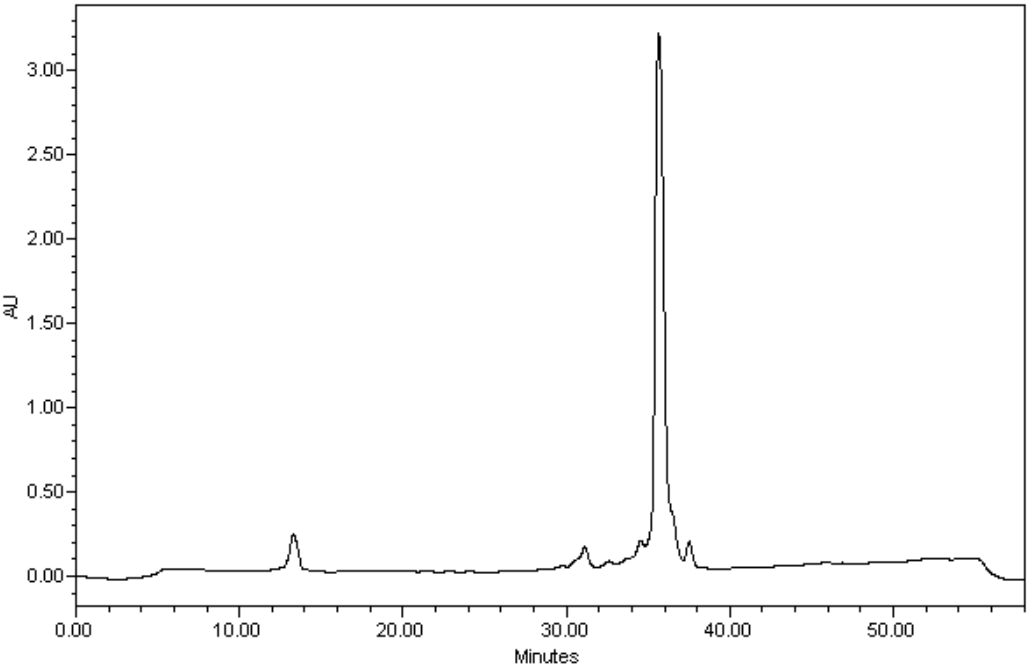

Figure 2.5. RP-HPLC chromatogram for the ultrapurification of CTC. The eluent was monitored at 215 nm.

2.4.2 Cyclic Trichrysobactin Characterization

2.4.2.1 Cyclic Trichrysobactin Mass Spectrometry

ESI mass spectrometry yields two parent ions with *m/z* of 1054.47 $[M + H]^+$ and 527.73 $[M + 2H]^+$ for CTC (Figure 2.6 and 2.7). ESI tandem mass spectrometry (ESI MS/MS) reveals multiple fragments consistent with the structure of CTC. The loss of 2,3-DHBA corresponds to *m/z* of 918.31, the loss of 2,3-DHB-Lys corresponds to *m/z* of 790.40, the loss of 2,3-DHB-Lys-Ser corresponds to *m/z* of 703.49, the loss of 2,3-DHB-Lys-Ser plus 2,3-DHBA corresponds to *m/z* of 567.66, the loss of 2,3-DHB-Lys-Ser plus 2,3-DHBA-Lys corresponds to *m/z* of 439.70, and the loss of 2,3-DHB-Lys-Ser plus 2,3-DHB-Lys-Ser corresponds to *m/z* of 352.74. Additionally, *m/z* of 256.75 corresponds to the 2,3-DHB-Lys fragment and *m/z* of 129.71 corresponds to the Lys fragment. All of these ESI MS/MS fragments match previously published data for CTC [8].

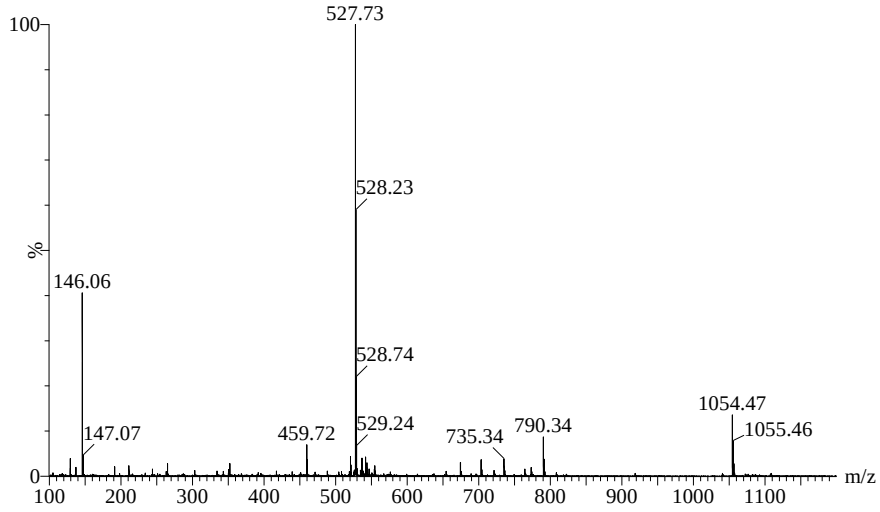

Figure 2.6. ESI-MS of CTC.

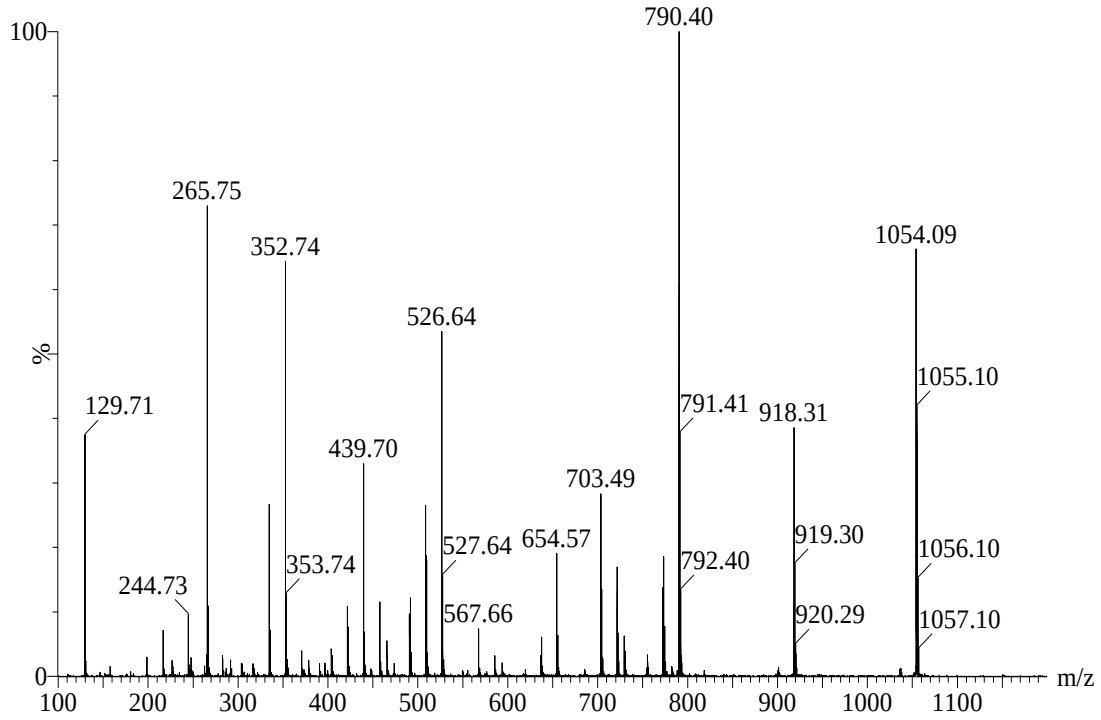

Figure 2.7. ESI-MS/MS of CTC.

2.4.2.2 Cyclic Trichrysobactin NMR Characterization

^{1}H NMR results for CTC show the characteristic aromatic resonances for the 2,3-DHBA moiety: δ_H 7.19 ppm (d, J = 7.8 Hz), 7.01 (d, J = 7.8 HZ), and 6.81 (t, J = 8.0 Hz). The Lys (δ_H 1.21 – 2.85) and Ser (δ_H 4.35) contribute ten methylene protons. Ser (δ_H of 4.85) and Lys (δ_H of 4.94) each contribute a single methine carbon (Figure 2.8). The ^{1}H NMR spectra and resonance annotations for CTC match previously published data [8].

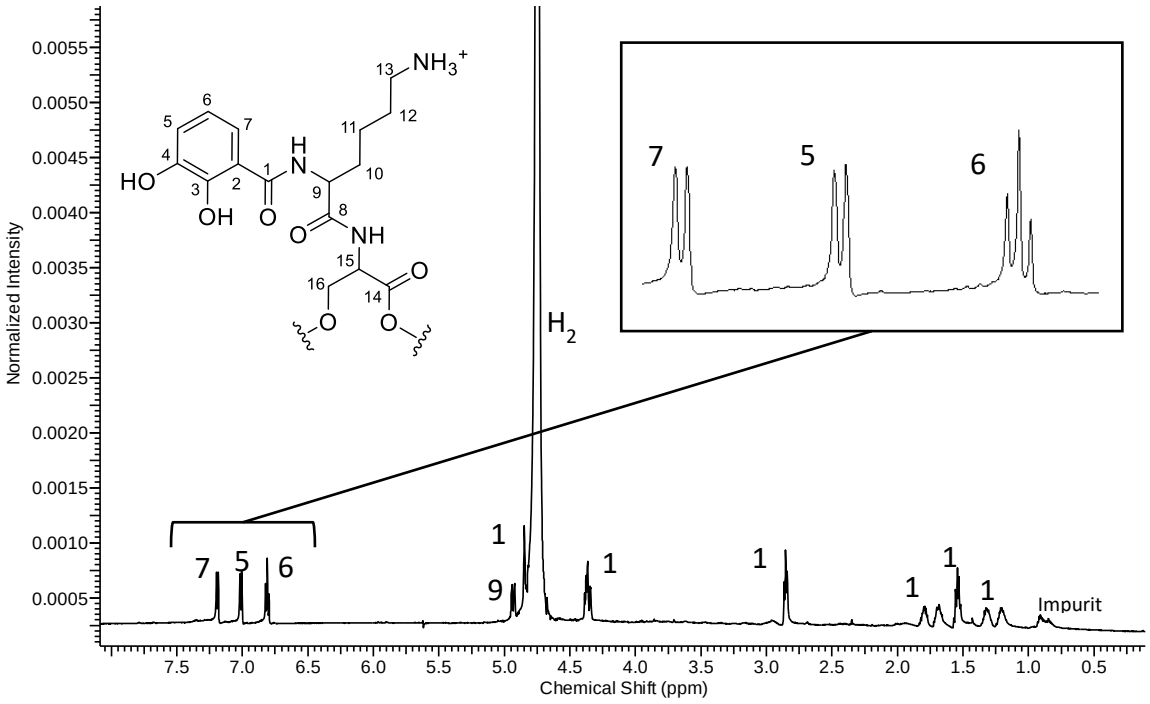

Figure 2.8. ^{1}H NMR (600 MHz) data for CTC in D_2O with enlarged aromatic region.

2.4.3 Siderophore Analog Purification

The instability of the macrolactone scaffold of CTC motivated the synthesis of a more stable siderophore analog built on a TREN core. This provided a platform for investigating wet adhesive mechanisms by variation to the siderophore structure. Six siderophore analogs were synthesized with modified catechol or amine functionalities. TLC (Figure 2.9) and TDC (Figure 2.10) both have intact catechol and a primary amine. The amine in TLC is linked to the molecule by a four-carbon chain whereas the amine in TDC is linked by a two-carbon chain. TLP (Figure 2.11) and TLB (Figure 2.12) both retain the Lys functionality, but compromise catechol. TLP has a single hydroxyl in the 3 position of the aromatic ring and

TLB removes both hydroxyls on the aromatic ring. TL^{Ac}C (Figure 2.13) and TC (Figure 2.14) contain an intact catechol and modify the Lys. Lys is completely absent in TC and the charge on Lys in TL^{Ac}C has been removed through acetylation.

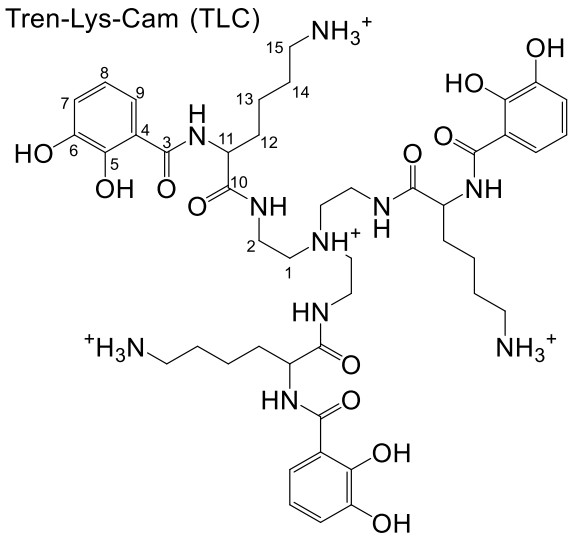

Figure 2.9. Structure of TLC. Numbered carbons correspond to NMR data in Table 2.1.

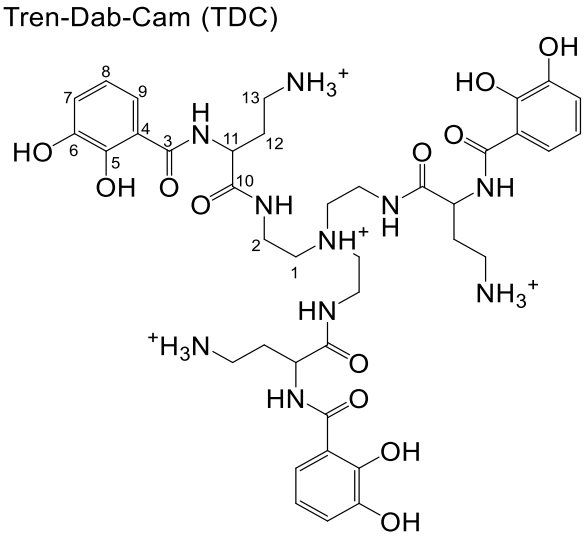

Figure 2.10. Structure of TDC. Numbered carbons correspond to NMR data in Table 2.2.

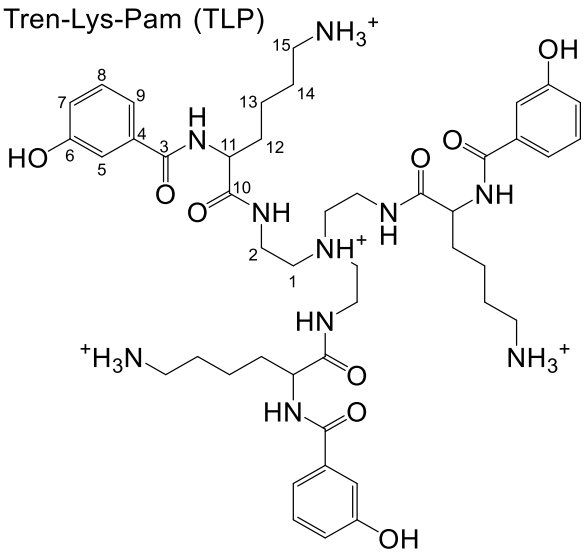

Figure 2.11. Structure of TLP. Numbered carbons correspond to NMR data in Table 2.2.

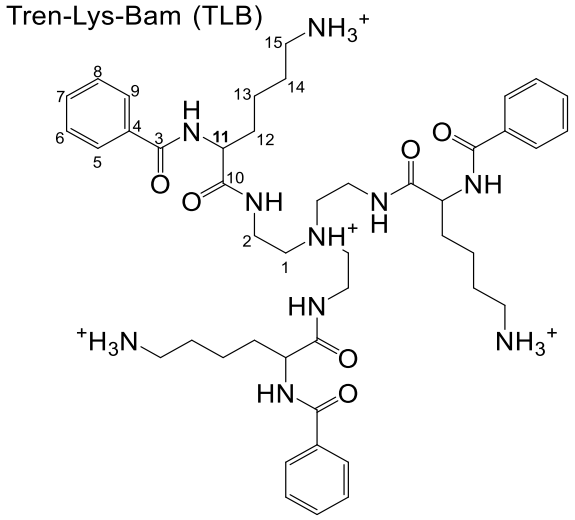

Figure 2.12. Structure of TLB. Numbered carbons correspond to NMR data in Table 2.3.

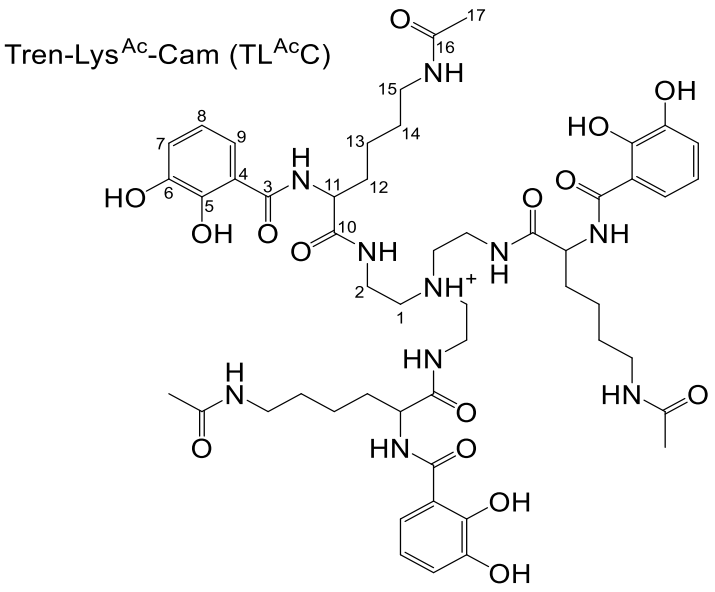

Figure 2.13. Structure of TL^{Ac}C. Numbered carbons correspond to NMR data in Table 2.3.

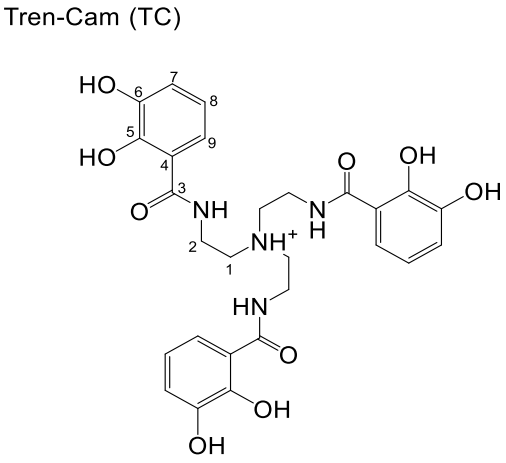

Figure 2.14. Structure of TC. Numbered carbons correspond to NMR data in Table 2.3.

The final hydrogenolysis deprotection step removes up to nine carboxybenzyl and benzyl protecting groups simultaneously. The deprotected amine of Lys can potentially poison the Pd/C catalyst and reduce the yield of the reaction. Due to these factors, several different reaction products are possible and vary between from unreacted starting material, a range of partially deprotected compounds, and the fully deprotected siderophore analog. Siderophores were purified by RP-HPLC. The eluent was monitored at 215 nm and each prominent peak was collected and analyzed by ESI-MS until the desired siderophore analog was identified. Trace impurities remain after the initial RP-HPLC purification. It was therefore necessary to subject siderophore analogs to an additional round of RP-HPLC purification (Figure 2.15) to ensure the high purity required for accurate SFA results.

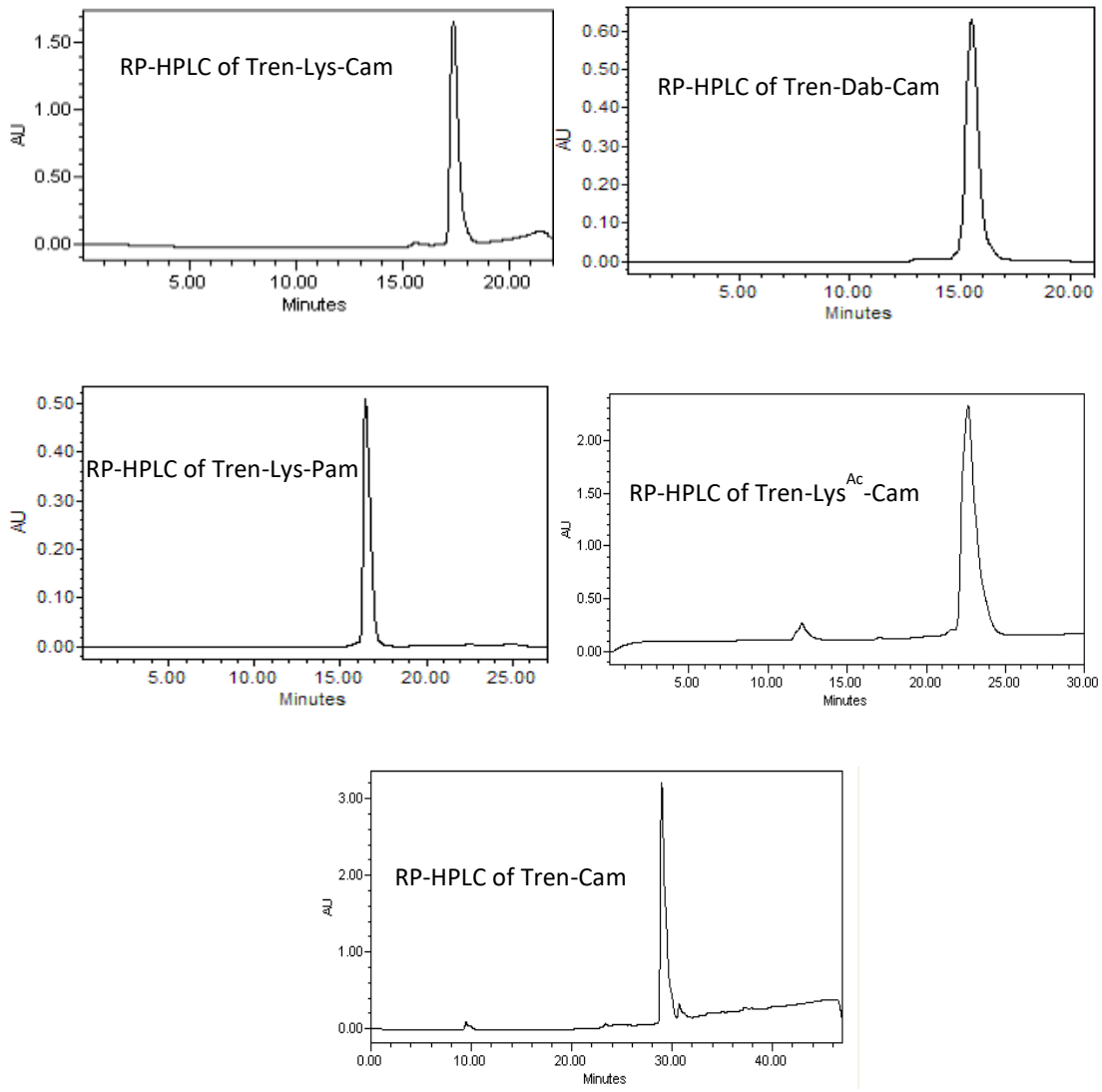

Figure 2.15. RP-HPLC purification of TREN-based siderophore analogs. RP-HPLC was carried out on a C4 preparative column (22 mm i.d., x 250 mm, Vydac). A gradient elution was performed from nanopure H_2O with 0.05% TFA to MeOH with 0.05% TFA. The rate of gradient transition was optimized for each individual compound (section 2.3.2.1 - section 2.3.2.6). The eluent for all RP-HPLC purifications was monitored at 215 nm.

2.4.4 Siderophore Analog Characterization

2.4.4.1 Siderophore Analog Mass Spectrometry

Siderophore analog structures were characterized with ESI-MS and ESI-MS/MS (Table 2.1). Peptides typically fragment at the amide bonds [16] and this behavior is also seen in the siderophore analogs. The fragmentation pattern observed in the ESI-MS/MS spectrum of TLC is consistent with the loss of one or more subunits from one or more of the 2,3-DHBA terminated arms. The fragmentation occurs at the amide bond between the 2,3-DHBA unit and the Lys, at the amide bond between the Lys and the TREN scaffold, and at the central nitrogen of the TREN scaffold. The fragmentation pattern seen for TLC is also seen for each other siderophore analog. The mass differences observed between compounds result from the difference in side chain structure and in the case of TC, amino acid content.

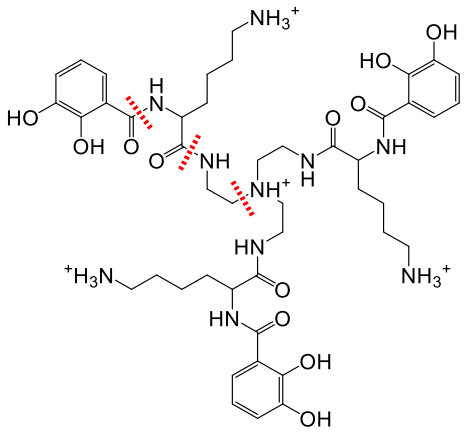

Figure 2.16. ESI-MS Fragmentation of siderophore analogs. Fragmentation typically occurs at amide bonds between the 2,3-DHBA and Lys, at the amide bonds between the Lys and the TREN scaffold, and at the center nitrogen of the TREN scaffold.

Table 2.1. ESI-MS and ESI-MS/MS fragmentation of TREN-based siderophore analogs. See Figures 2.17-2.25 for ESI-MS and ESI-MS/MS spectra.

Tren-Lys-Cam		Tren-Lys^{Ac}-Cam		Tren-Cam	
Fragment	$[M+H]^+$	Fragment	$[M+H]^+$	Fragment	$[M+H]^+$
Parent Ion	939.5	Parent Ion	1065.44	Parent Ion	555.2
loss of DHB	803.48	loss of DHB	929.49	loss of DHB	419.2
loss of DHB-Lys	675.39	loss of DHB-Lys^{Ac}	759.4	loss of DHB-Lys^{Ac}	-
loss of single arm	632.35	loss of single arm	716.35	loss of single arm	376.15
loss of DHB-Lys + DHB	539.38	loss of DHB-Lys^{Ac} + DHB	623.39	loss of DHB-Lys^{Ac} + DHB	-
loss of 2x DHB-Lys	411.28	loss of 2x DHB-Lys^{Ac}	453.26	loss of 2x DHB-Lys^{Ac}	-
single arm	308.16	single arm	350.17	single arm	180.07
DHB-Lys	265.13	DHB-Lys^{Ac}	307.14	DHB-Lys^{Ac}	-
Lys	129.1	Lys^{Ac}	-	Lys^{Ac}	-

Tren-Dab-Cam*		Tren-Lys-Pam*		Tren-Lys-Bam*	
Fragment	$[M+H]^+$	Fragment	$[M+H]^+$	Fragment	$[M+H]^+$
Parent Ion	855.31	Parent Ion	891.47	Parent Ion	843.53
loss of DHB	719.26	loss of Phenol	771.46	loss of Benzyl	739.51
loss of DHB-Dab	619.25	loss of Phenol-Lys	643.37	loss of Benzyl-Lys	611.41
loss of single arm	-	loss of single arm	600.33	loss of single arm	568.37
loss of 2x DHB-Dab	383.19	loss of 2x Phenol-Lys	395.26	loss of 2x Benzyl-Lys	379.29
single arm	-	single arm	292.15	single arm	276.18
DHB-Dab	237.06	Phenol-Lys	249.12	Benzyl-Lys	233.13
Dab	101.06	Lys	129.1	Lys	-

* ESI-MS/MS not available, ESI-MS used

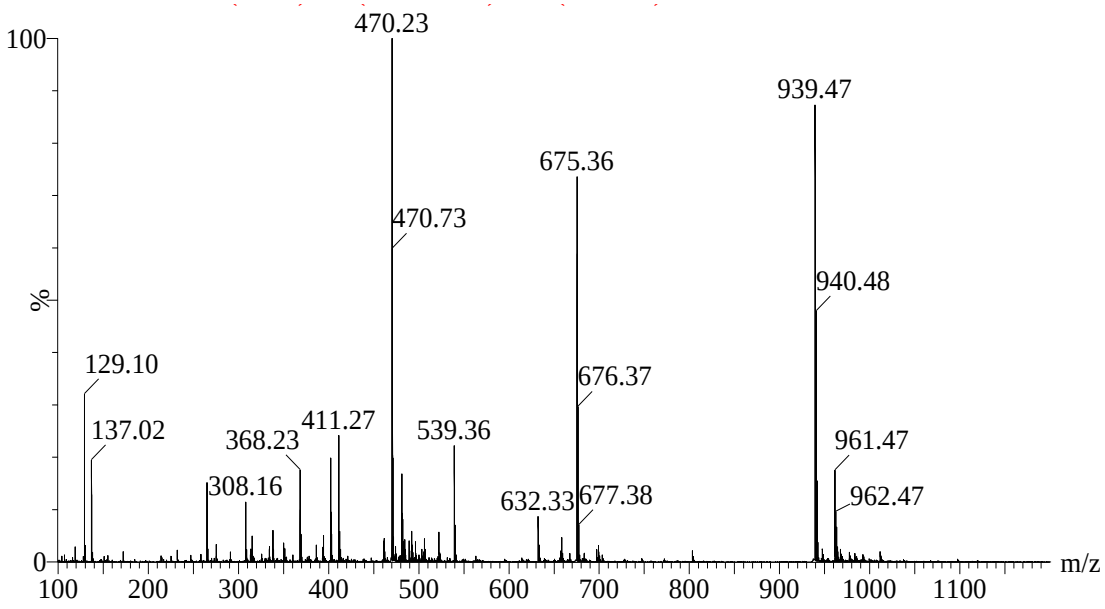

Figure 2.17. ESI-MS of TLC.

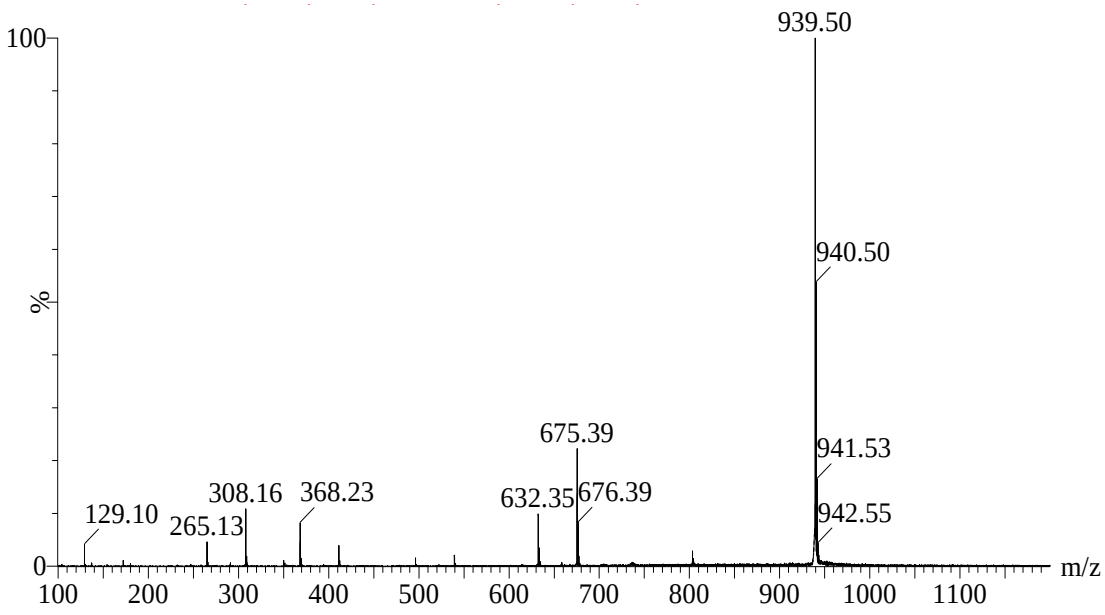

Figure 2.18. ESI-MS/MS of TLC.

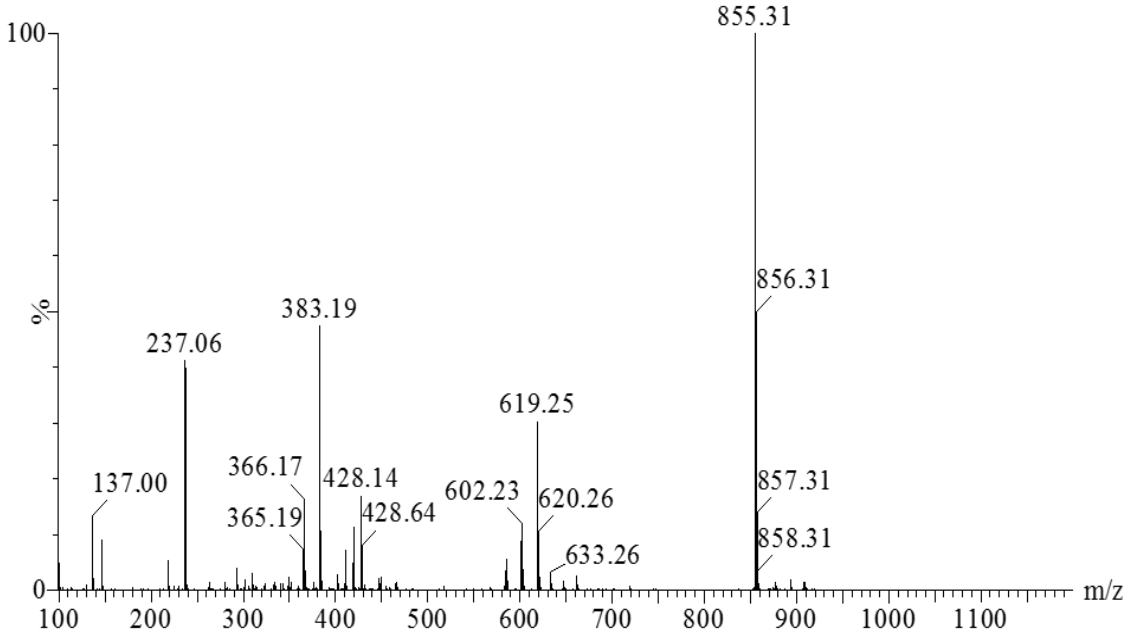

Figure 2.19. ESI-MS of TDC.

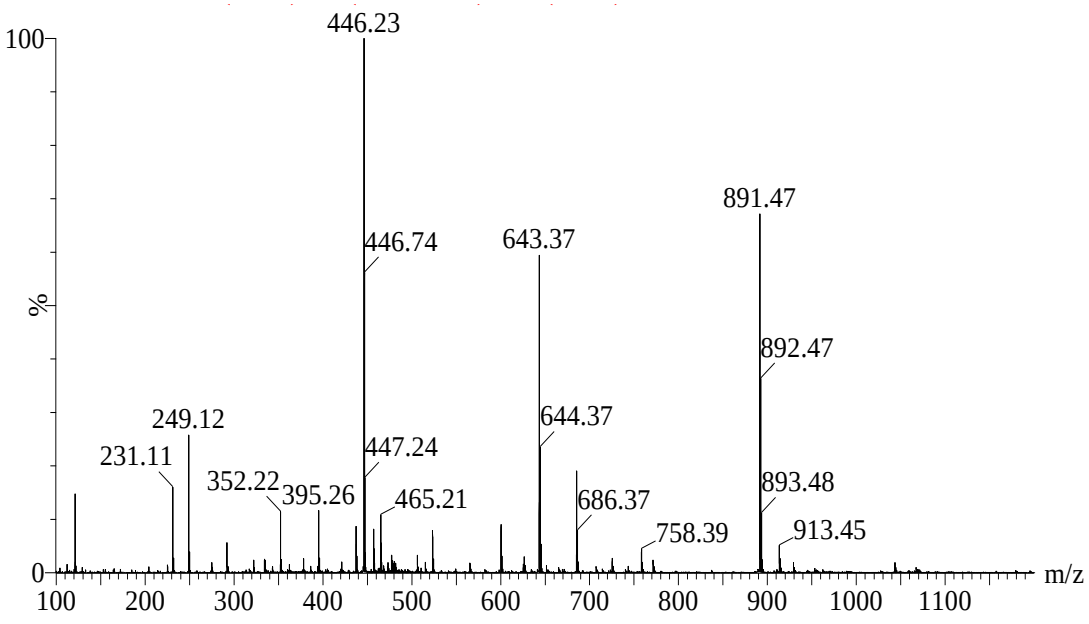

Figure 2.20. ESI-MS of TLP.

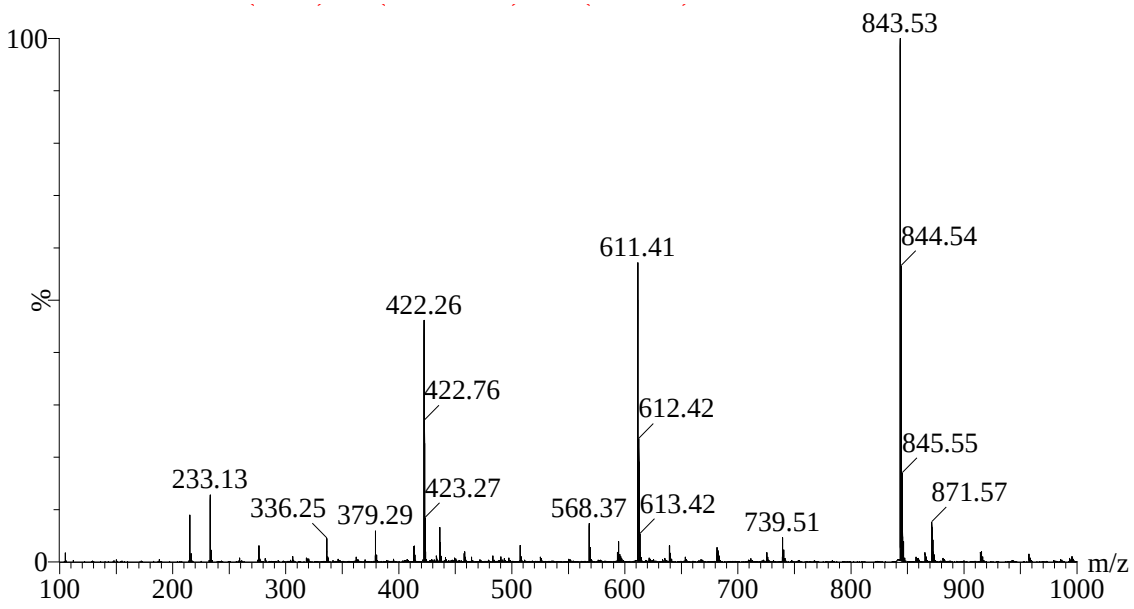

Figure 2.21. ESI-MS of TLB.

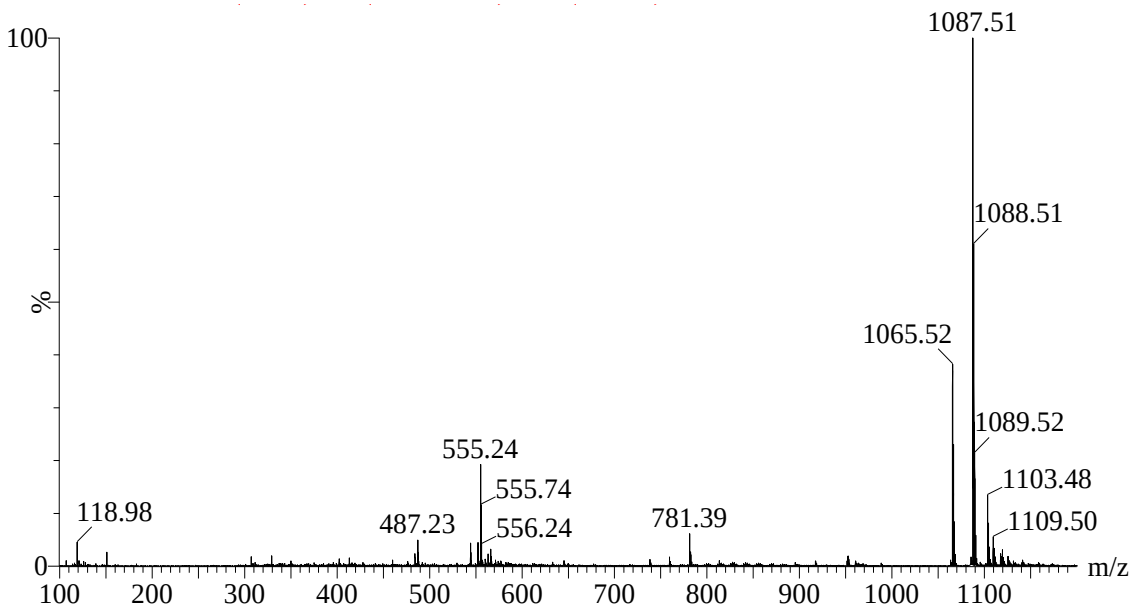

Figure 2.22. ESI-MS of TL^{Ac}C.

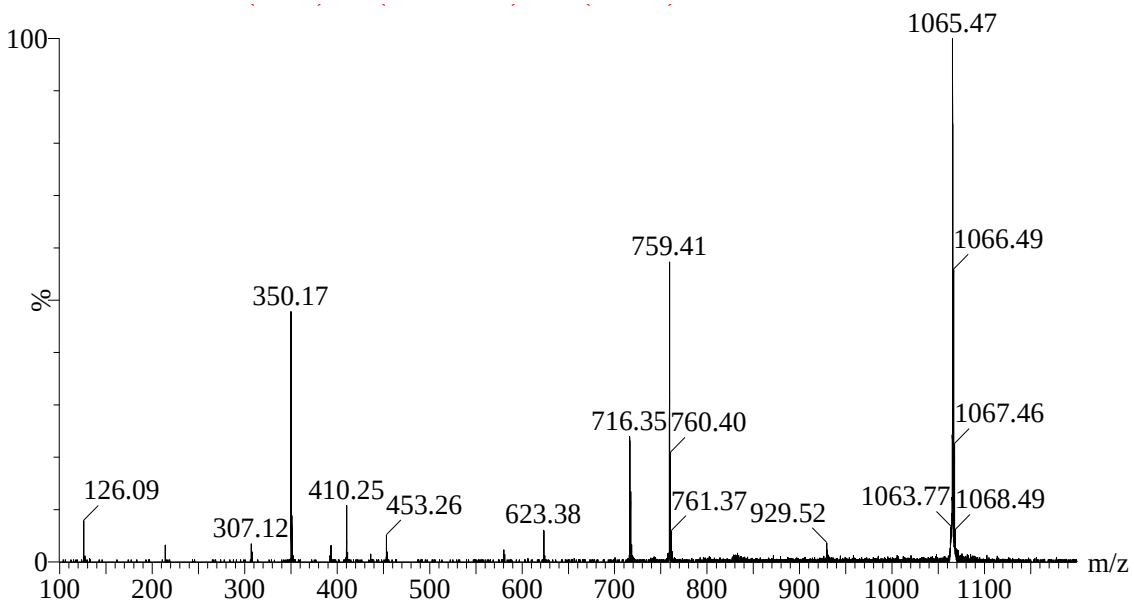

Figure 2.23. ESI-MS/MS of TL^{Ac}C.

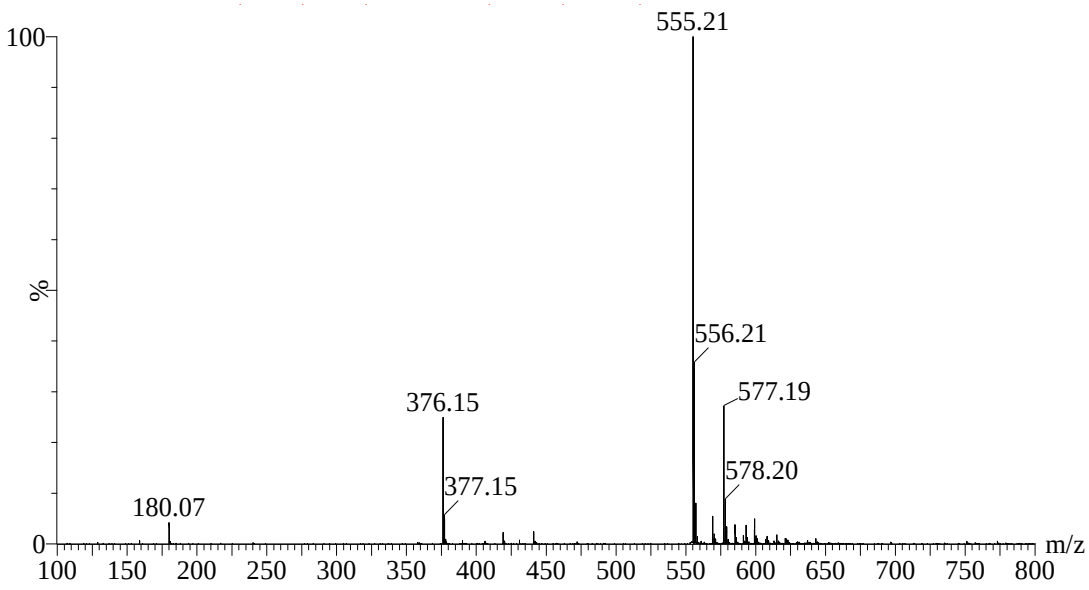

Figure 2.24. ESI-MS of TC.

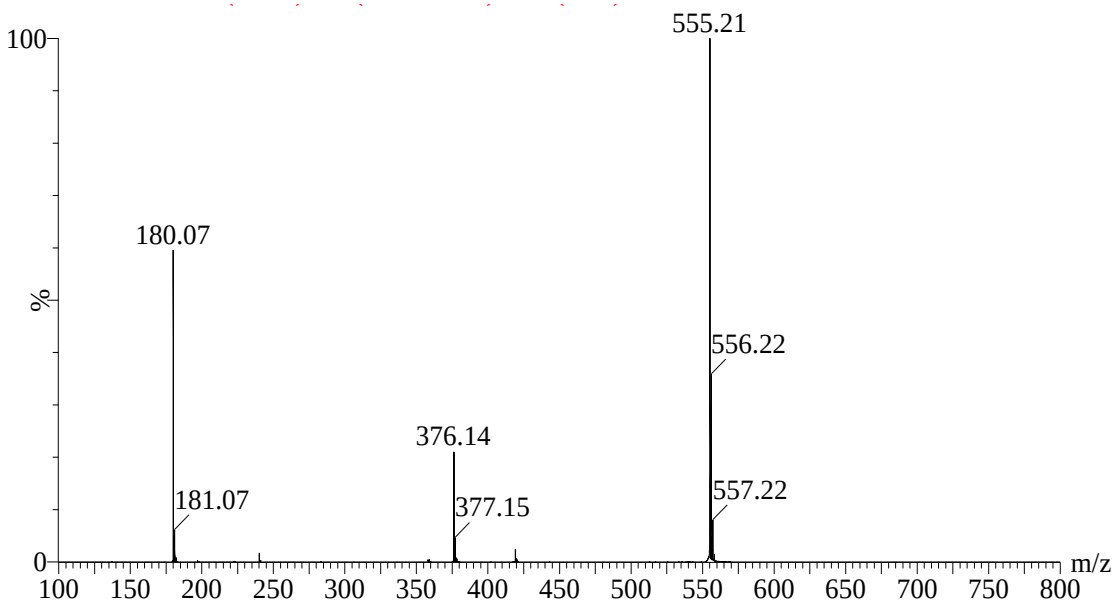

Figure 2.25. ESI-MS/MS of TC.

2.4.4.2 Siderophore Analog NMR Characterization

^{1}H, ^{13}C, and ^{1}H-^{13}C HMBC NMR confirmed the molecular structures suggested from the ESI-MS and ESI-MS/MS fragmentation patterns. ^{1}H and ^{13}C results are summarized in Table 2.2 and Table 2.3. ^{1}H NMR results for TLC show the characteristic aromatic resonances for the 2,3-DHBA moiety (δ_H 6.70, 6.93, and 7.09). The Lys residue (δ_H 1.28 – 2.86) and TREN scaffold (δ_H 3.46, 3.67) contribute twelve methylene protons. Lys has two sets of diastereotopic protons (δ_H 1.28, 1.33 and 1.58, 1.71) that are directly adjacent and one carbon removed from the chiral α carbon. Lys also contributes a single methine carbon (δ_H 4.29). ^{13}C NMR results for TLC shows a single carbonyl carbons (δ_C 168.77). Surprisingly, the carbonyl carbon from the Lys in TLC does not appear in the ^{13}C NMR. However, this carbonyl carbon does appear in the ^{1}H-^{13}C HMBC spectrum (δ_C 172.44). The Lys residue (δ_C

22.44 - 30.64) and TREN scaffold (δ_C 38.53) contribute twelve methylene carbons. The DMSO solvent peak obscures one of the TREN methylene carbons and the terminal methylene carbon on the Lys sidechain. Lys also contributes a single methine carbon (δ_C 52.72). The correlation between the carbonyl carbon of 2,3-DHBA and the α-proton of Lys seen in the ^{1}H-^{13}C HMBC NMR confirms the 2,3-DHBA-Lys sequence in each arm of TLC.

The ^{1}H and ^{13}C NMR characterization for TDC, TL^{Ac}C, TC, TLP, and TLB closely resemble the ^{1}H and ^{13}C NMR data for TLC. Key resonances enable clear distinction between TLC and each other siderophore analog. TDC, TL^{Ac}C, and TC all retain the characteristic aromatic resonances for the 2,3-DHBA moiety. TDC has a primary amine side chain that is two methylene carbons shorter than the carbon chain found in TLC and comparing the total integration of Lys methylene proton resonances to the integration of Dab proton resonances clearly differentiates the two compounds. A large singlet (δ_H 1.76) in the 1H spectra of TL^{Ac}C results from the methyl carbon on the acetylated Lys amine and distinguishes TL^{Ac}C from TLC. TC is also easily distinguished from TLC due to the absence of all Lys resonances. TLP and TLB both lack the characteristic aromatic resonances for the 2,3-DHBA moiety and comparison of the aromatic region between these compounds and TLC enables their identification. TLP has four proton resonances in the aromatic region compared to three proton resonances for TLC. TLB has 5 aromatic protons in three chemically distinct environments. This leads to three resonances in the aromatic region, two of which have double the integration of the third.

Table 2.2. NMR Data for TLC, TDC, and TLP. NMR (^{1}H on a Varian Unity Inova 600 MHz spectrometer and ^{13}C on a Varian Unity Inova 500 MHz spectrometer) was taken in D_2O or DMSO. Numbers correspond to Figures 2.9-2.11. See Figures 2.26-2.29 for spectra.

	Tren-Lys-Cam		Tren-Dab-Cam		Tren-Lys-Pam	
Position	δ_C	δ_H (J in Hz)	δ_C	δ_H (J in Hz)	δ_C	δ_H (J in Hz)
TREN						
1	Obscured by DMSO	3.67, m	Obscured by DMSO	Obscured by Water	Obscured by DMSO	Obscured by Water
2	38.53, CH_2	3.46, m	36.33, CH_2	Obscured by Water	38.49, CH_2	Obscured by Water
DHBA						
3	168.77, C	-	168.370, C	-	166.59, C	-
4	115.67, C	-	115.47, C	-	135.19, C	-
5	148.41, C	-	147.88, C	-	114.46, CH	7.30, s
6	145.90, C	-	145.59, C	-	157.13, C	-
7	118.63, CH	6.93, d (7.31)	118.41, CH	6.95, d (7.49)	117.98, CH	7.35, m
8	118.19, CH	6.70, t (7.74)	118.05, CH	6.71, t (7.65)	129.01, CH	7.23, t (7.65)
9	117.94, CH	7.09, d (7.88)	117.77, CH	7.37, d (8.02)	118.17, CH	6.93, d (7.68)
Lysine						
10	172.44, C	-	172.31, C	-	172.39, C	-
11	52.72, CH	4.29, m	50.28, CH	4.54, m	53.27, CH	4.35, m
12	30.74, CH_2	1.58; 1.71, m	25.25, CH_2	1.96; 2.11, m	30.51, CH_2	1.73; 1.77, m
13	22.44, CH_2	1.28; 1.33, m	29.56, CH_2	2.85, m	22.60, CH_2	1.31; 1.38, m
14	26.48, CH_2	1.57, m	-	-	26.47, CH_2	1.55, m
15	Obscured by DMSO	2.86, t (7.66)	-	-	Obscured by DMSO	2.75, m

Table 2.3. NMR Data for TLB, TL^{Ac}C, and TC, NMR spectra were taken in D_2O or DMSO. Numbers correspond to numbers in Figure 2.12-2.14. See Figures 2.30-2032 for NMR spectra. Characterization data for Tren-Cam matches previously published data [12].

	Tren-Lys-Bam		Tren-Lys^{Ac}-Cam		Tren-Cam	
Position	δ_C	δ_H (J in Hz)	δ_C	δ_H (J in Hz)	δ_C	δ_H (J in Hz)
TREN						
1	Obscured by DMSO	3.62, m	Obscured by DMSO	Obscured by Water	Obscured by DMSO	3.84, m
2	38.66, CH_2	3.47, m	38.74, CH_2	Obscured by Water	Obscured by DMSO	3.69, m
DHBA						
3	166.71, C	-	169.52, C	-	169.86, C	-
4	133.89, C	-	116.17, C	-	115.12, C	-
5	127.61, CH	7.69, d (7.30)	149.08, C	-	148.93, C	-
6	128.17, CH	7.45, t (7.65)	146.49, C	-	146.04, C	-
7	131.41, CH	7.57, t (7.19)	119.28, CH	6.93, d (7.65)	118.85, CH	6.87, d (7.65)
8	128.17, CH	7.45, t (7.65)	118.81, CH	6.70, t (7.18)	118.02, CH	6.57, t (7.43)
9	127.61, CH	7.69, d (7.30)	118.56, CH	7.42, d (7.30)	117.48, CH	6.89, d (7.65)
Lysine						
10	172.54, C	-	169.44, C	-	-	-
11	53.52, CH	4.31, m	53.59, CH	4.40, m	-	-
12	30.68, CH_2	1.72; 1.79, m	31.40, CH_2	1.72, m	-	-
13	22.80, CH_2	1.33; 1.39, m	23.02, CH_2	1.26; 1.32, m	-	-
14	26.67, CH_2	1.60, m	29.27, CH_2	1.37, m	-	-
15	Obscured by DMSO	2.90, t (7.30)	Obscured by DMSO	2.99, m	-	-
16	-	-	169.33, C	-	-	-
17	-	-	23.52, CH_3	1.76, s	-	-

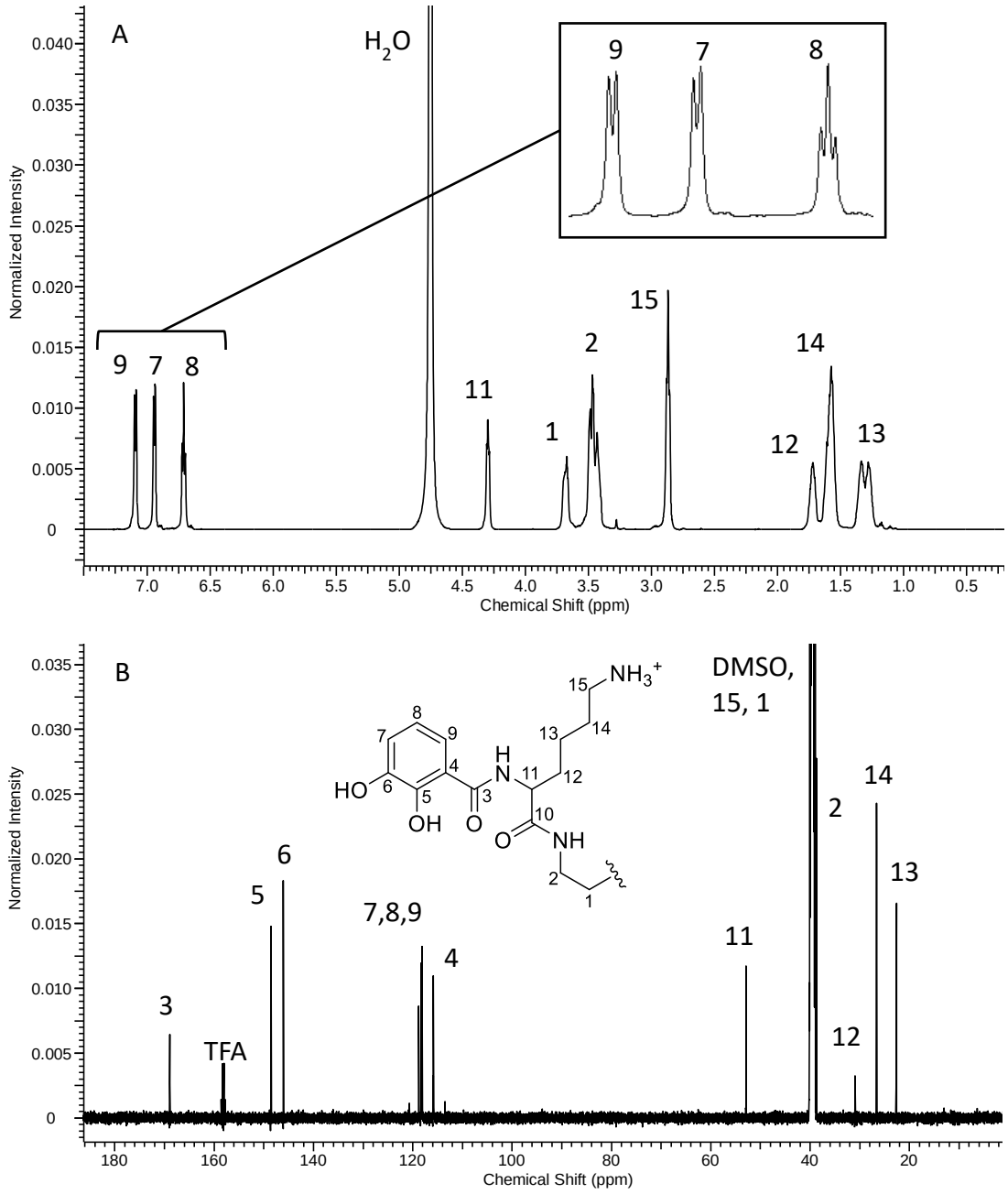

Figure 2.26. NMR data for TLC. (A) ^{1}H NMR Data for TLC. NMR (600 MHz) in D_2O with enlarged aromatic region. (B) ^{13}C NMR Data for TLC. NMR (500 MHz) in DMSO. TFA originates from RP-HPLC purification.

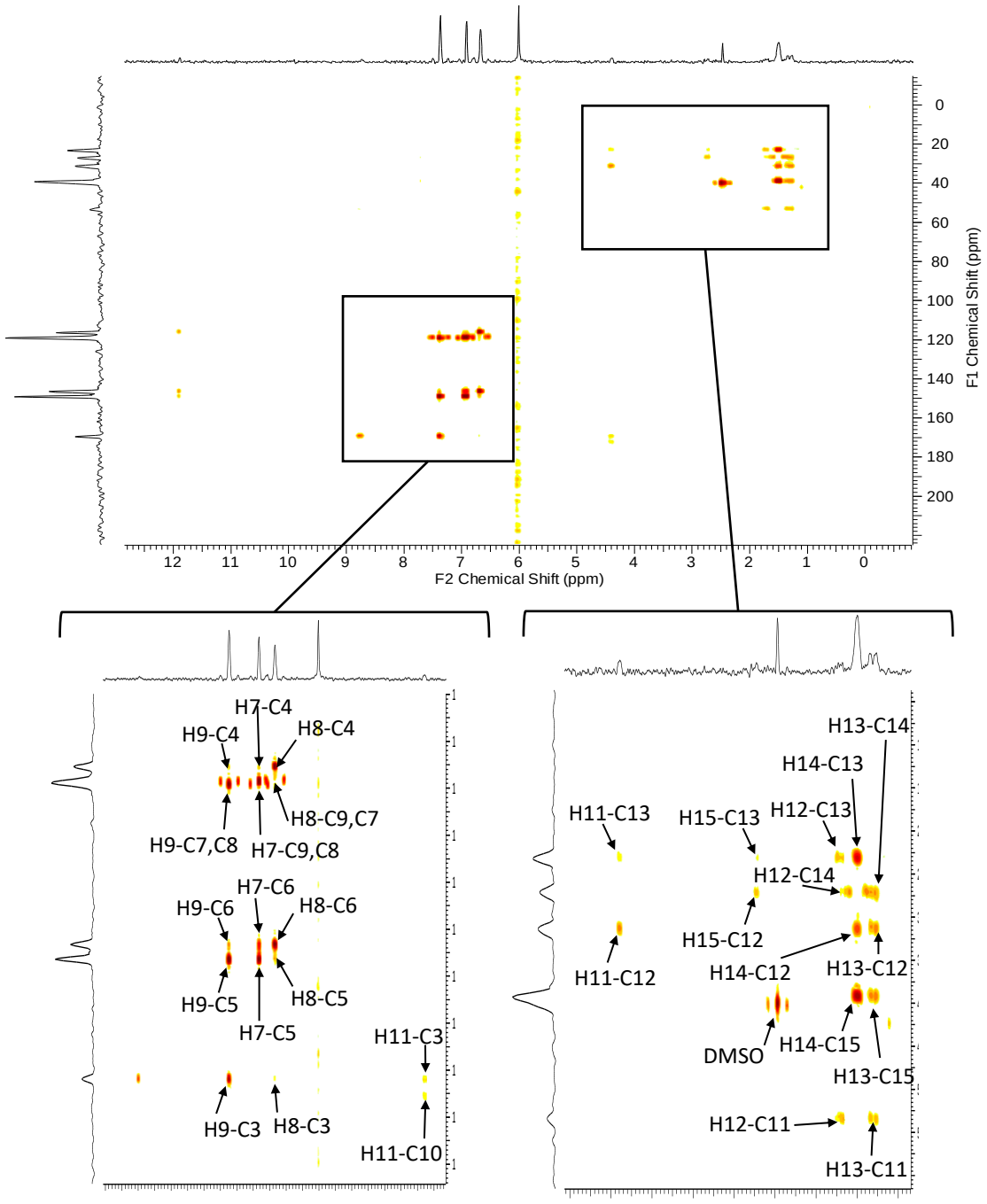

Figure 2.27 ^{1}H-^{13}C HMBC NMR for TLC. NMR (600 MHz) in DMSO. Enlarged Regions of the ^{1}H-^{13}C HMBC NMR for TLC are in bottom panel. The spectrum is annotated with the correlations between specific carbons and hydrogens.

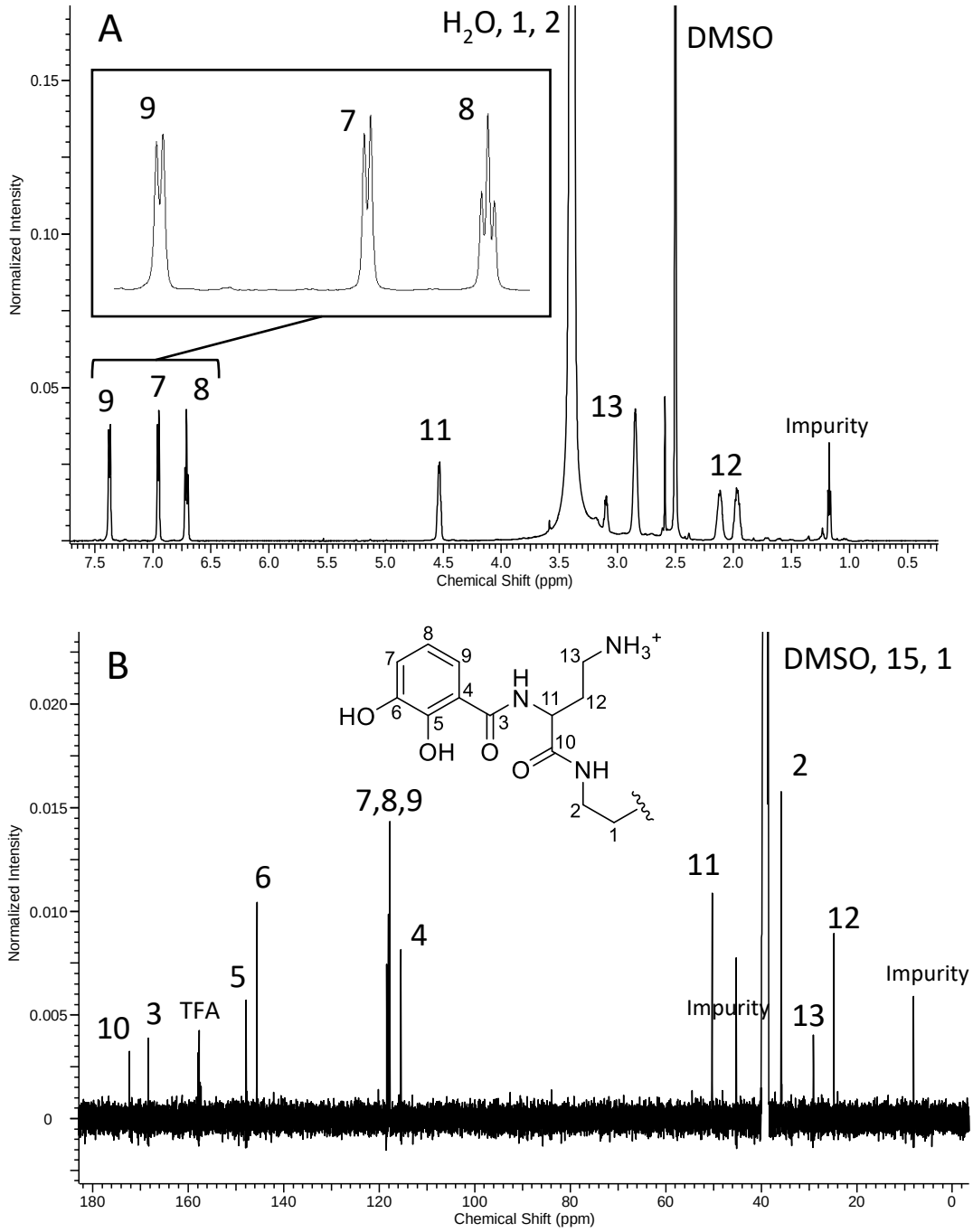

Figure 2.28. NMR data for TDC. (A) ^{1}H NMR Data for TDC. NMR (600 MHz) in DMSO with enlarged aromatic region. (B) ^{13}C NMR Data for TDC. NMR (500 MHz) in DMSO. TFA originates from RP-HPLC purification.

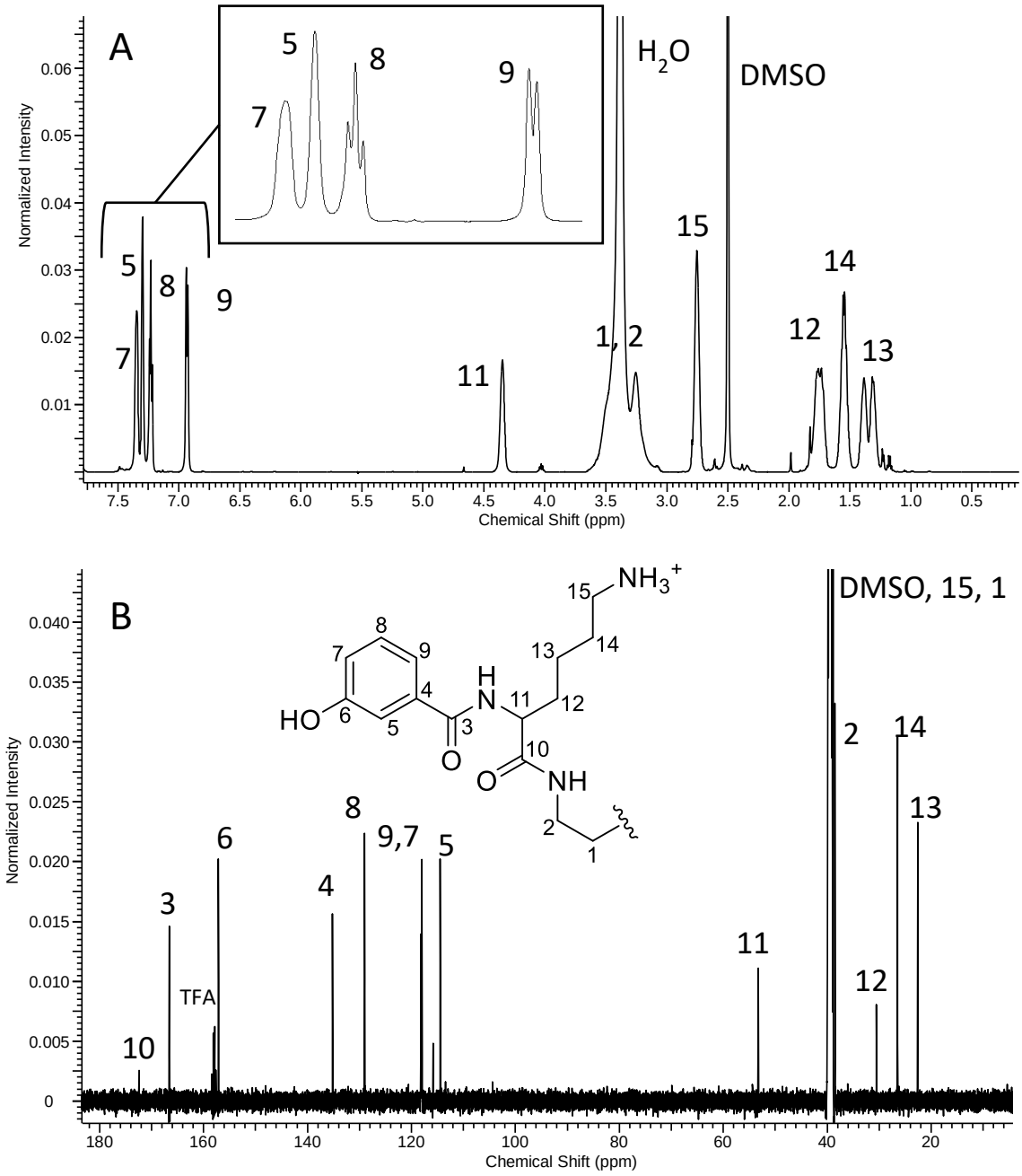

Figure 2.29. NMR data for TLP. (A) ^{1}H NMR Data for TLP. NMR (600 MHz) in DMSO with enlarged aromatic region. (B) ^{13}C NMR Data for TLP. NMR (500 MHz) in DMSO. TFA originates from RP-HPLC purification.

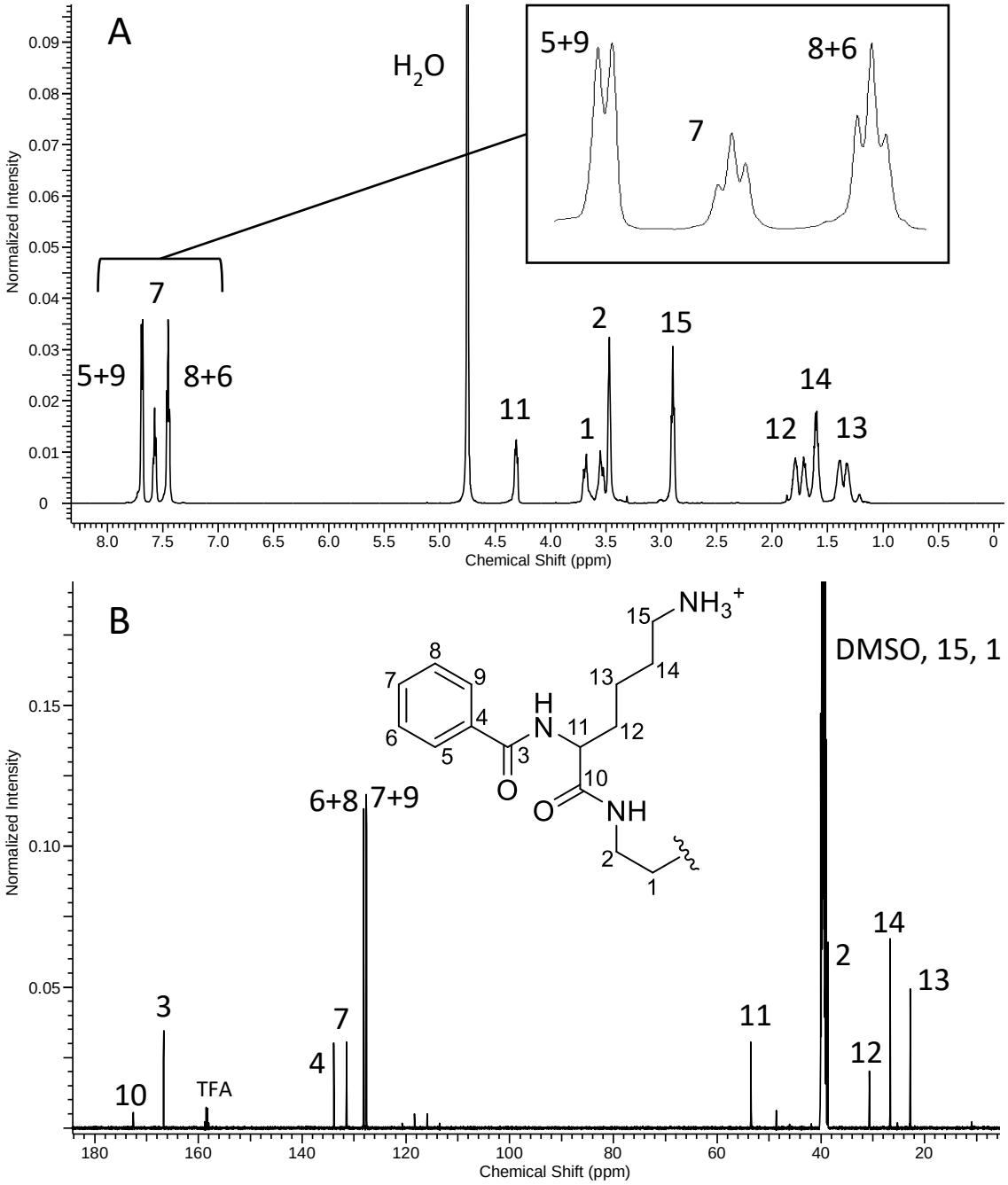

Figure 2.30. NMR data for TLB. (A) ^{1}H NMR Data for TLB. NMR (600 MHz) in D_2O with enlarged aromatic region. (B) ^{13}C NMR Data for TLB. NMR (500 MHz) in DMSO. TFA originates from RP-HPLC purification.

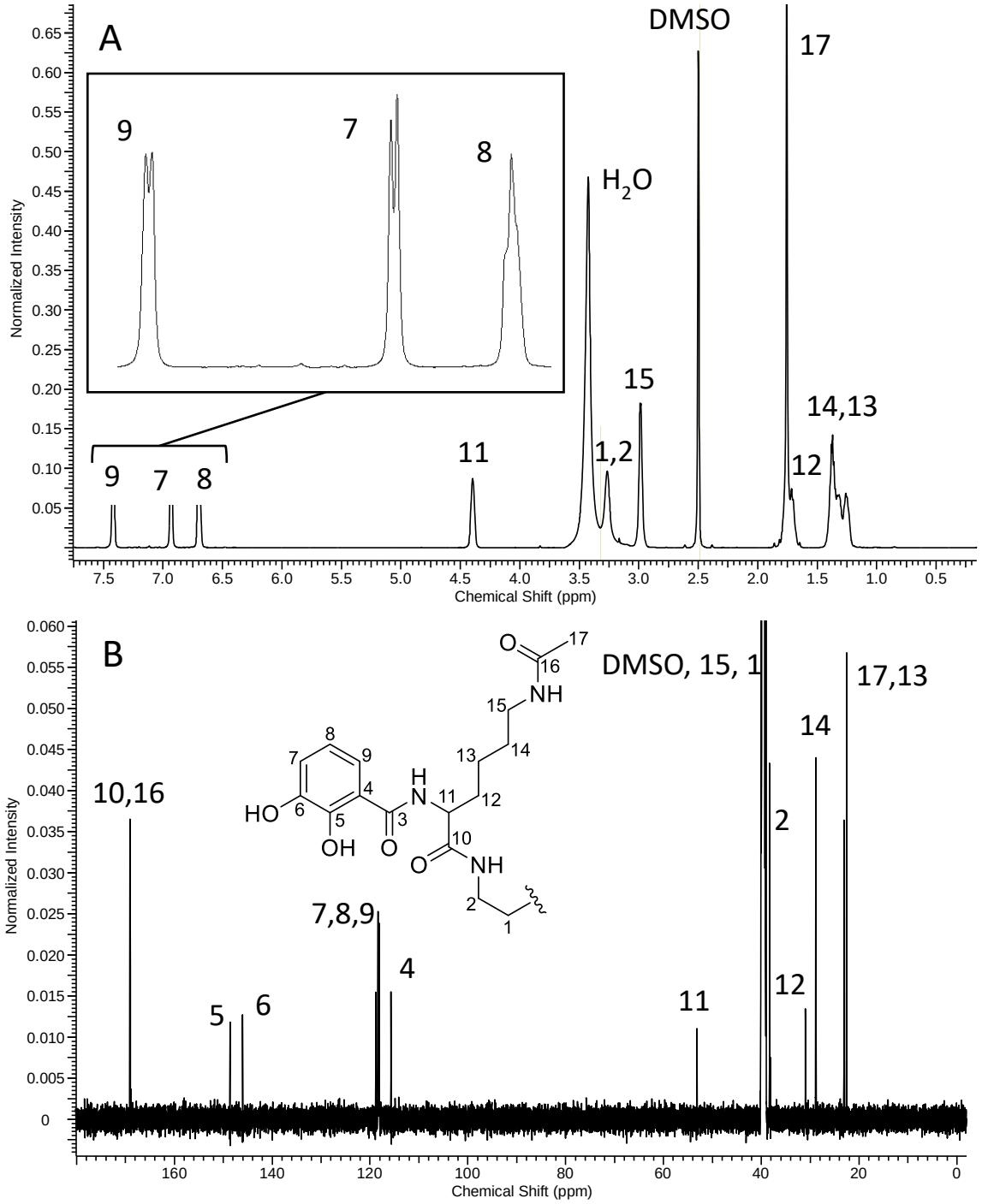

Figure 2.31. NMR data for TL^{Ac}C. (A) ^{1}H NMR Data for TL^{Ac}C. NMR (600 MHz) in DMSO with enlarged aromatic region. (B) ^{13}C NMR Data for TL^{Ac}C. NMR (500 MHz) in DMSO. TFA originates from RP-HPLC purification.

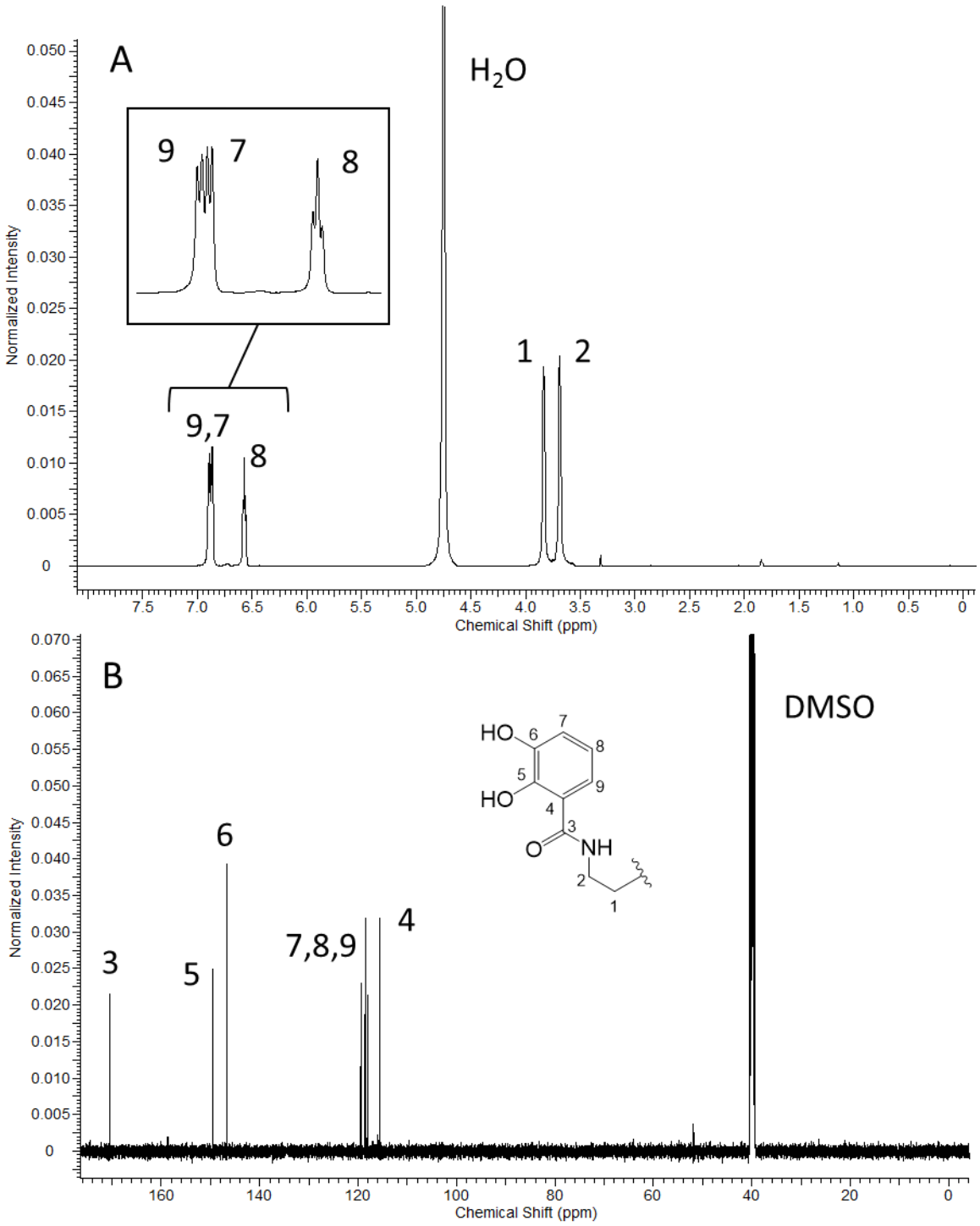

Figure 2.32. NMR data for TC. (A) ^{1}H NMR Data for TC. NMR (600 MHz) in D_2O with enlarged aromatic region. (B) ^{13}C NMR Data for TC. NMR (500 MHz) in DMSO.

2.4.5 Surface Forces Apparatus Adhesion Measurements

Force-distance measurements were taken for the natural siderophore, CTC as well as all six siderophore analogs. The majority of experiments were performed in pH 3.3, 50 mM acetate buffer with 150 mM KNO_3 (Figures 2.35-2.42). The optimal TLC concentration for force-distance measurements was determined to be 20 µM by tracking adhesion versus moles of siderophore analog (three order of magnitude range) in the 50 µl gap solution between the mica surfaces (Figure 2.35). Under-concentrated solutions leave potential adhesion/bridging sites on the mica surface vacant and this results in low adhesion. Conversely, over-adsorption results in a minor decrease in adhesion. The optimal 20 µM siderophore analog concentration was used for all subsequent force-distance measurements. In one series of experiments the pH was raised to 5.5 in 50 mM acetate buffer with 150 mM KNO_3 and again to 7.5 in 50 mM phosphate buffer with 150 mM KNO_3 (Figure 2.36). The low pH solution conditions are consistent with previously published SFA measurements on Mfps and are an approximation of conditions during plaque formation within the distal depression of the mussel foot [17]. Force-distance measurements for CTC were performed at pH 6.7 because acid catalyzed lactone hydrolysis degrades the central scaffold [8], which can prevent adhesive bridging interactions.

In force-distance measurement data the open circles represent data collected as the mica surfaces are brought into contact and solid circles represent data collected as surfaces are pulled apart. By convention, positive values are repulsive forces and negative values are attractive forces. Approaching mica surfaces come into contact, compress the intervening

material, and result in repulsive forces. The point at which added force no longer decreases the distance between the mica surfaces is known as the hardwall thickness (D_T). The surfaces are then pulled apart. If adhesive material is present at the interface and is capable of bridging the two surfaces then attractive forces can be measured. The minimum force/radius value is the maximum adhesion recorded for the material [13].

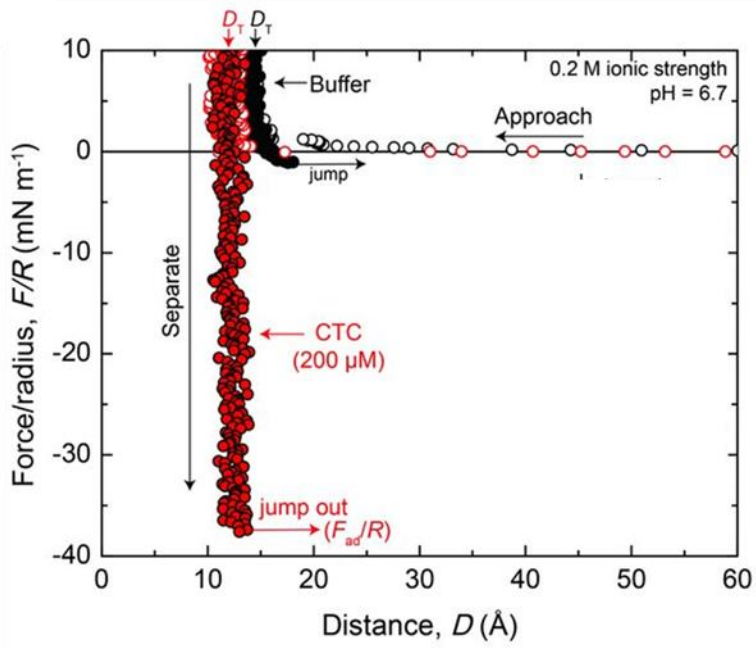

Figure 2.33. Adhesion of CTC. Force-distance measurements were performed in 50 mM phosphate buffer + 150 mM KNO_3 at pH 6.7. The surfaces were left in contact for 10 min before separation.

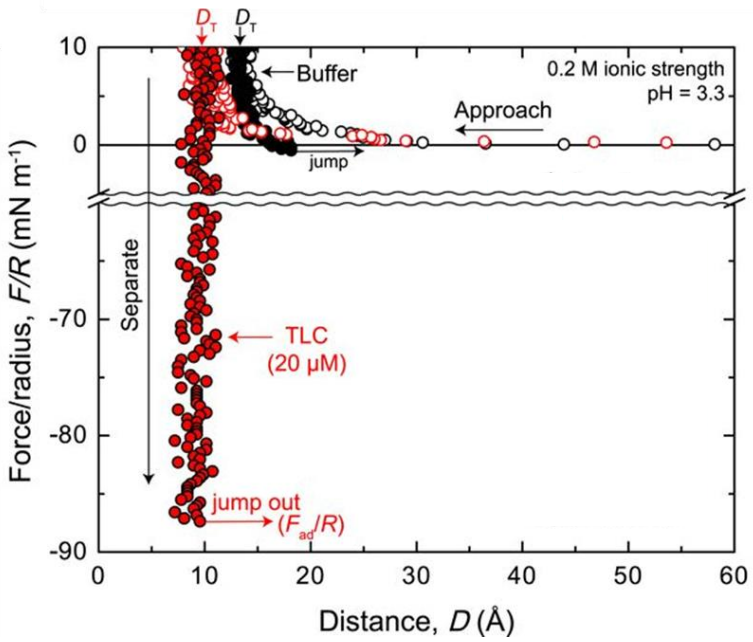

Figure 2.34. Adhesion of TLC. Force-distance measurements were performed in 50 mM acetate buffer with 150 mM KNO_3 at pH 3.3. The surfaces were left in contact for 10 min before separation.

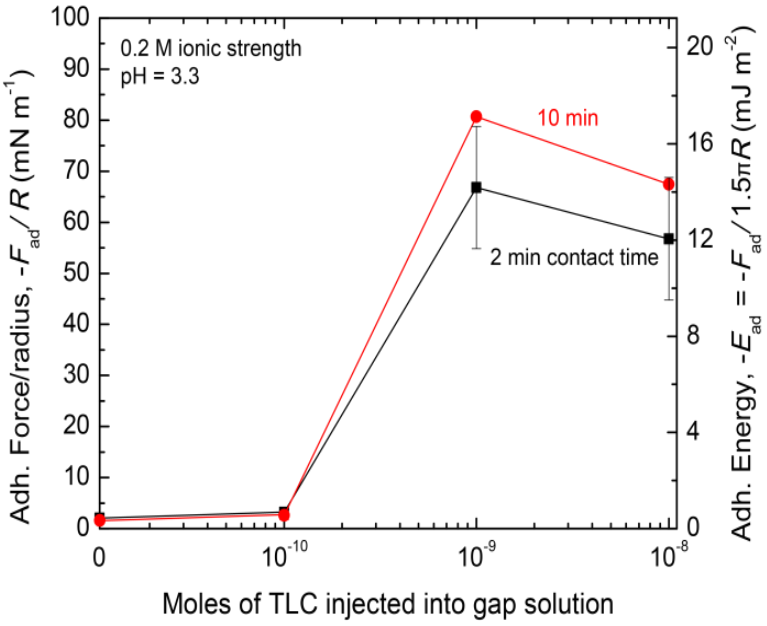

Figure 2.35. Concentration dependence of TLC adhesion. Force-distance measurements were performed in 50 mM acetate buffer with 150 mM KNO_3 at pH 3.3 with varying moles of TLC injected into the 50 μM gap solution between the mica surfaces.

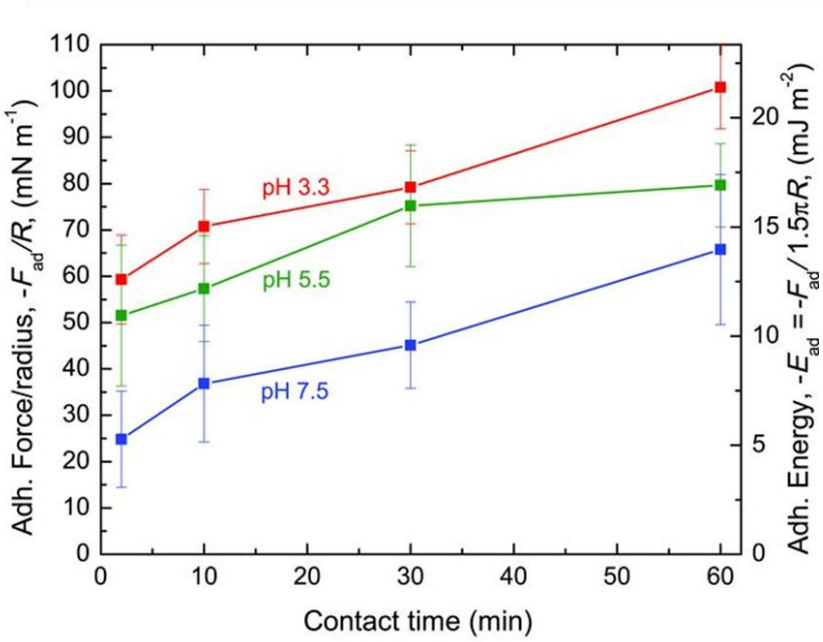

Figure 2.36. pH-dependent adhesion of TLC. pH 3.3 and pH 5.5 experiments were performed in 50 mM acetate with 150 mM KNO_3. pH 7.5 experiments were performed in 50 mM phosphate with 150 mM KNO_3. Error bars represents ± standard deviation.

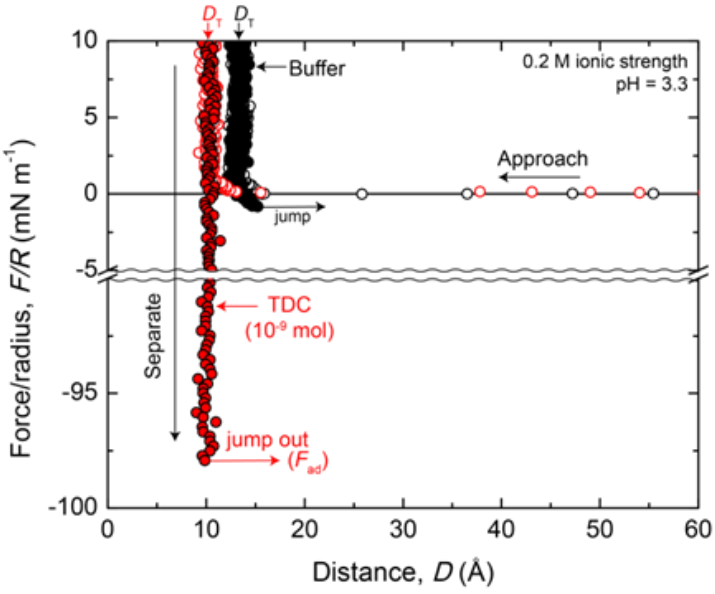

Figure 2.37. Adhesion of TDC. Force-distance measurements were performed in 50 mM acetate buffer with 150 mM KNO_3 at pH 3.3. The surfaces were left in contact for 10 min before separation.

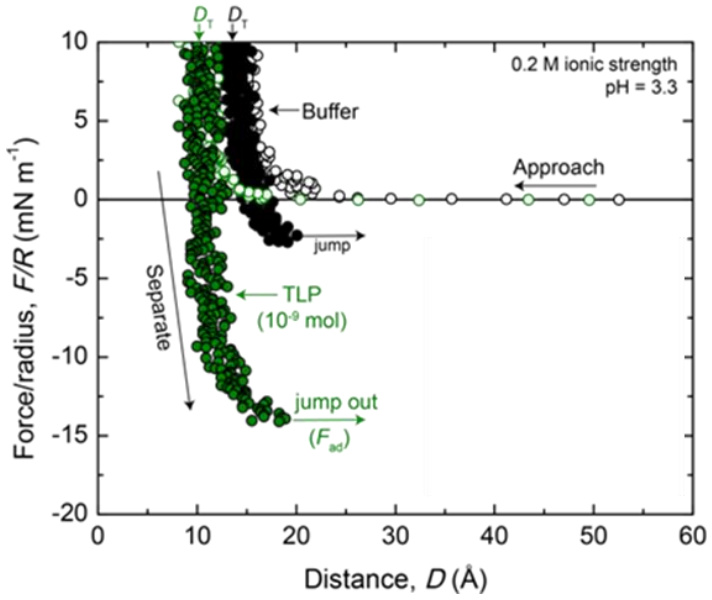

Figure 2.38. Adhesion of TLP. Force-distance measurements were performed in 50 mM acetate buffer with 150 mM KNO_3 at pH 3.3. The surfaces were left in contact for 10 min before separation.

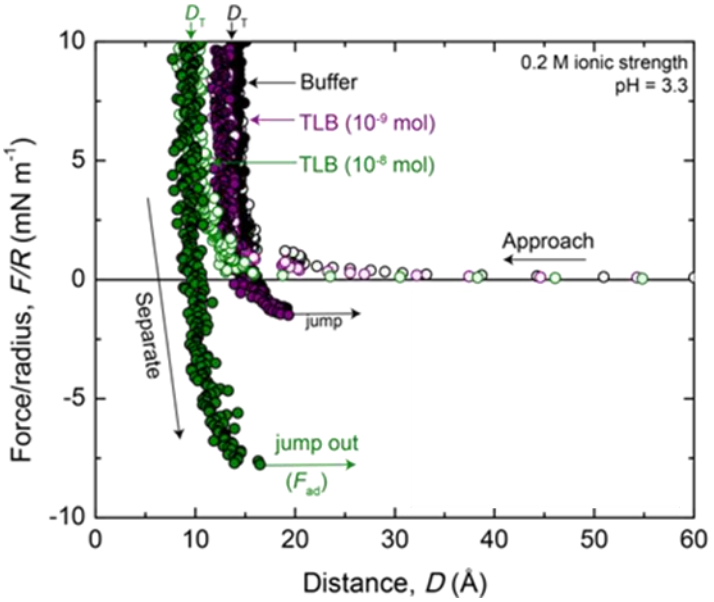

Figure 2.39. Adhesion of TLB. Force-distance measurements were performed in 50 mM acetate buffer with 150 mM KNO_3 at pH 3.3. The surfaces were left in contact for 10 min before separation. When 10^{-9} moles of TLB are injected into the gap solution between the mica surfaces there is no significant adsorption of the siderophore analog onto the mica surfaces. An increase in moles of injected material by an order of magnitude enables adsorption to the surface, decreases the hardwall thickness, and increases the measured adhesion force.

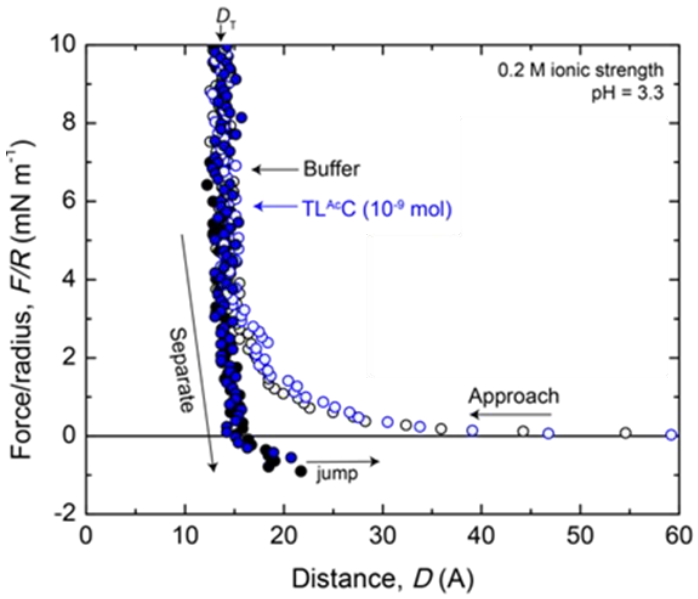

Figure 2.40. Adhesion of TL^{Ac}C. Force-distance measurements were performed in 50 mM acetate buffer with 150 mM KNO_3 at pH 3.3. The surfaces were left in contact for 10 min before separation. TL^{Ac}C does not adsorb significantly to the mica surface, causing results similar to buffer-only experiments.

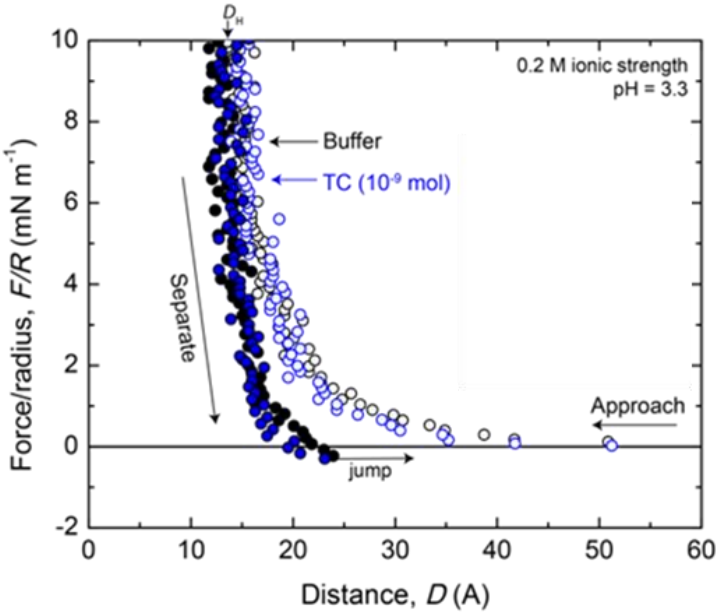

Figure 2.41. Adhesion of TC. Force-distance measurements were performed in 50 mM acetate buffer with 150 mM KNO_3 at pH 3.3. The surfaces were left in contact for 10 min before separation. TC doesn't adsorb significantly to the mica surface, causing results similar to buffer-only experiments.

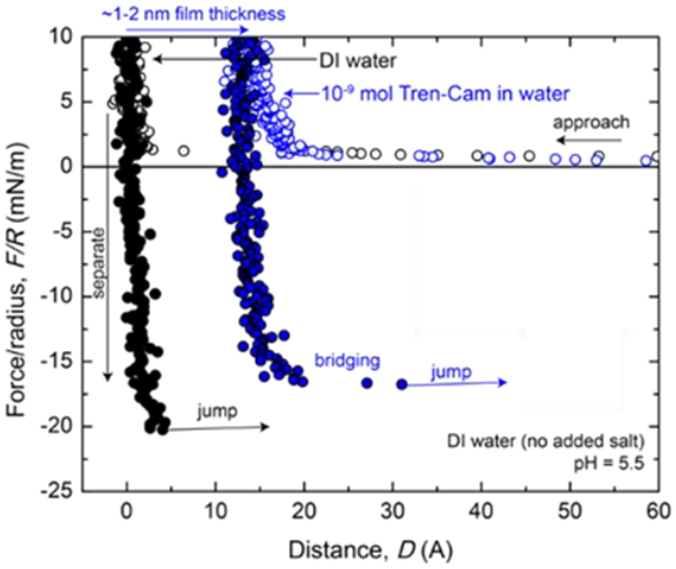

Figure 2.42. Adhesion of TC in doubly deionized H_2O. The force-distance measurement for mica surfaces in doubly deionized H_2O in the absence of TC at pH 5.5 results in moderate adhesion due to van der Waals forces between the surfaces [18]. Addition of TC causes adhesion that is not observed in high salt solutions. The surfaces were left in contact for 10 min before separation.

2.5 Discussion

While it is not possible to decipher the relative contributions of the adhesive forces of cationic amino acids and Dopa in the Mfps, it is possible to do so in small molecules such as certain siderophores and synthetic analogs. The composition of CTC resembles that of adhesive proteins Mfp-3 and Mfp-5 in the proximity and relative ratio of catechol and Lys groups. CTC binds to mica with a significant force of adhesion, F_{ad} of -30 ± 10 mN/m^{-1} at pH 6.7 [4], compared to Mfp-5 at -65 mN/m measured at pH 2.6 [5]. The hydration layer thickness (13 ± 1Å, as measured by the SFA) decreases to 11 ± 1Å upon the addition of CTC, which is consistent with formation of a CTC monolayer bridging the mica surfaces and displacement of the hydration layer [4].

The tri-serine lactone scaffold of CTC readily hydrolyzes under acidic conditions [8]. Synthetic analogs of CTC in which TREN replaces the macrolactone core provide a synthetically tractable platform to investigate specific contributions of catechol and Lys to mica adhesion by variation in the amine and aromatic functionalities (Figure 2.43) [4]. TLC and TDC (Figure 2.43) retain the catechol and amine, although with variation in the length of the amine side chain. These siderophore analogs replicate strong adhesion to mica observed with CTC. TLP and TLB (Figure 2.43) lack catechol but retain Lys. The adhesion energy of TLP and TLB to mica is much weaker than TLC, presumably because the absence of catechol prevents strong adhesion. TC and $TL^{Ac}C$ (Figure 2.43) retain the catechol group, but reduce the molecular charge of the compound from 4+ to 1+ by acetylation or removal of Lys. TC and $TL^{Ac}C$ are unable to displace the hydration layer and exhibit no adhesion despite the presence of intact catechol. Only when both catechol and cationic groups are present do these siderophore analogs display strong adhesion. These observations are consistent with a mechanism whereby the cationic primary amine of Lys is able to disrupt the hydration layer on the mica surface (Figure 2.44). Catechol adheres to the mica surface through bidentate interactions once the hydration layer has been breached (Figure 2.44). Interestingly, TC is able to adhere in buffer-free and salt-free doubly deionized water (Figure 2.42), suggesting that cationic amines are only necessary for adhesion when hydrated salt layers are present at the interface. In the intertidal habitat, the high salt content of the ocean ensures the presence of hydrated cation layers on virtually all mineral surfaces. Cationic Lys may also contribute to adhesion through electrostatic interactions with the negatively charged mica surface [14].

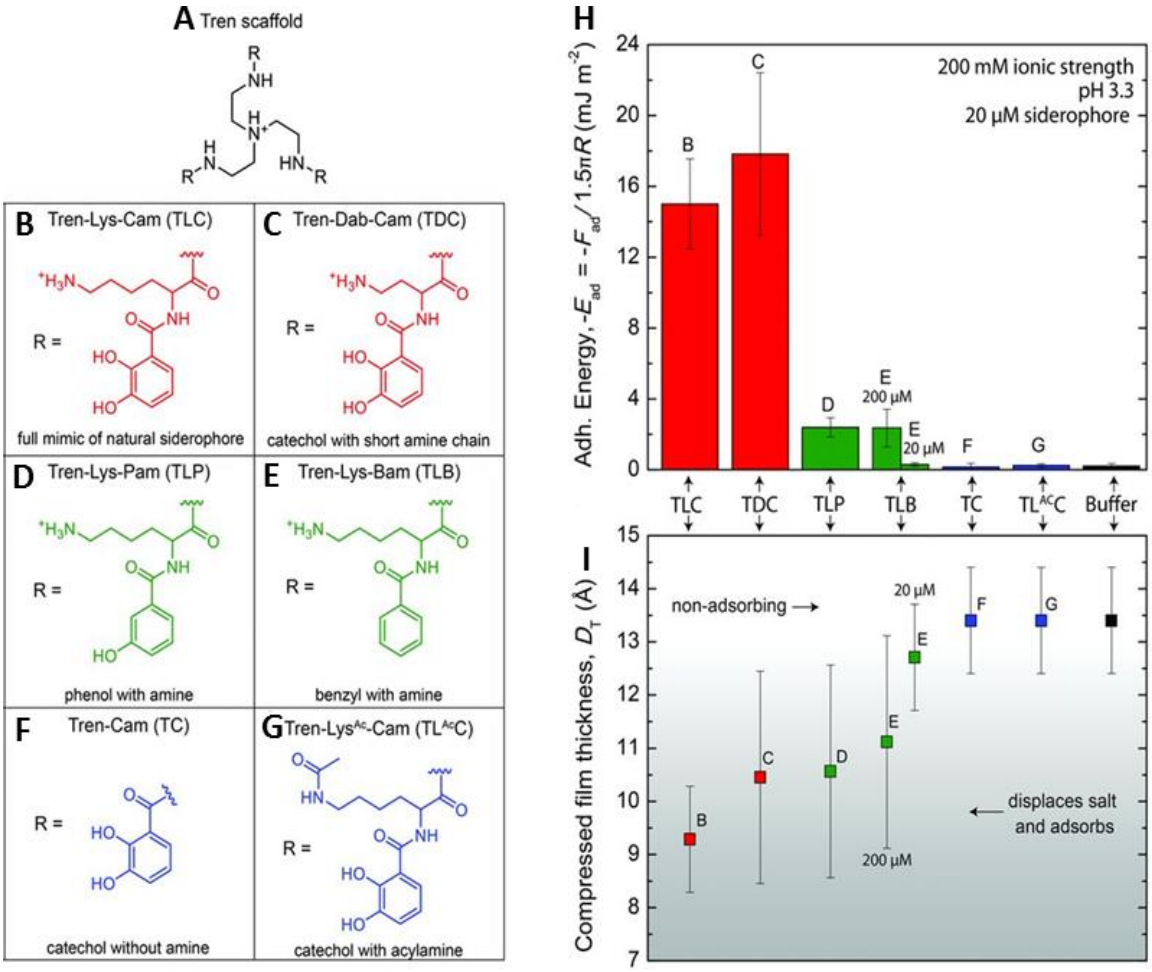

Figure 2.43. The synergy of catechol and cations in siderophore adhesion. (A) Structure of the TREN scaffold. (B to G) The R groups appended to TREN. (H) The average adhesion energy required to separate two mica surfaces adsorbed with 1 nmole of the analog (a 20 µM final concentration in the gap solution, except where indicated at 200 µM) in buffer (50 mM acetate + 150 mM KNO_3) at pH 3.3 after 10 min of contact. (I) Thickness of the siderophore monolayer between two mica surfaces at 10mN/m of compressive load. The film thicknesses correspond with the adhesion energy displayed in H. A decreased film thickness (<12 Å) indicates that siderophore analogs B, C, D, and E (200 µM) displace hydrated salt and adsorb to the mica surface.

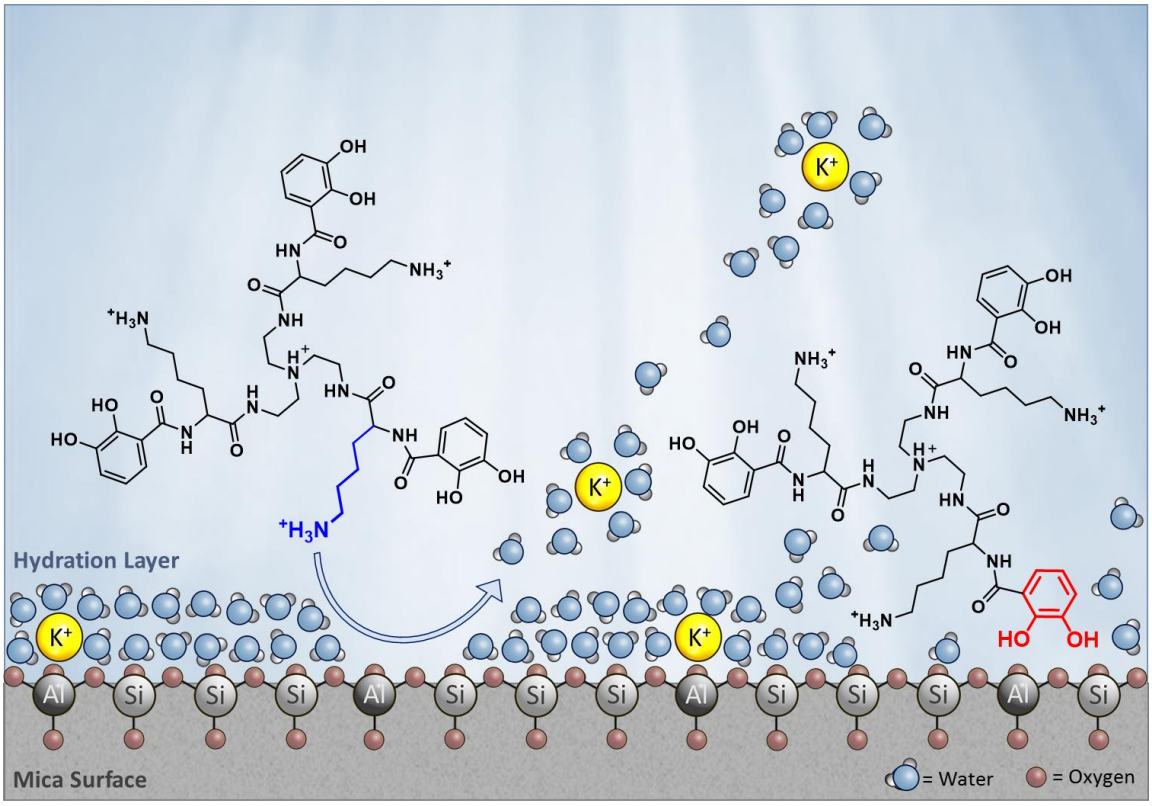

Figure 2.44. TLC at the mica-water interface.

2.6 References

1 Bandara N, Zeng H and Wu J (2013) Journal of Adhesion Science and Technology 27:2139-2162

2 Stewart RJ, Ransom TC and Hlady V (2011) J Polym Sci B Polym Phys 49:757-771

3 Lee BP, Messersmith PB, Israelachvili JN and Waite JH (2011) Annu Rev Mater Res 41:99-132

4 Maier GP, Rapp MV, Waite JH, Israelachvili JN and Butler A (2015) Science 349:628-632

5 Danner EW, Kan Y, Hammer MU, Israelachvili JN and Waite JH (2012) Biochemistry 51:6511-6518

6 Lee H, Scherer NF and Messersmith PB (2006) Proc Natl Acad Sci U S A 103:12999-13003

7 Lu Q, Danner E, Waite JH, Israelachvili JN, Zeng H and Hwang DS (2013) J R Soc Interface 10:20120759

8 Sandy M and Butler A (2011) J Nat Prod 74:1207-1212

9 Persmark M, Expert D and Neilands JB (1989) J Biol Chem 264:3187-3193

10 Lu C, Buyer JS, Okonya JF and Miller MJ (1996) Biometals 9:377-383

11 Imbert D, Thomas F, Baret P, Serratrice G, Gaude D, Pierre J-L and Laulhère J-P (2000) New Journal of Chemistry 24:281-288

12 Rodgers SJ, Lee C, Ng CY and Raymond KN (1987) Inorg Chem 26:1622-1625

13 Israelachvili J, Min Y, Akbulut M, Alig A, Carver G, Greene W, Kristiansen K, Meyer E, Pesika N, Rosenberg K and Zeng H (2010) Reports on Progress in Physics 73:036601

14 Rapp MV, Maier GP, Dobbs HA, Higdon NJ, Waite JH, Butler A and Israelachvili JN (2016) J Am Chem Soc 138:9013-9016

15 Schwyn B and Neilands JB (1987) Anal Biochem 160:47-56

16 Biemann K (1990) Methods in Enzymology 193:455-479

17 Martinez Rodriguez NR, Das S, Kaufman Y, Israelachvili JN and Waite JH (2015) Biofouling 31:221-227

18 Israelachvili JN (2011) Intermolecular and surface forces. Academic Press, San Diego

III. DEFINING THE CATECHOL-CATION SYNERGY FOR ENHANCED WET ADHESION TO MINERAL SURFACES

Parts of sections of this chapter were taken with permission from: Michael V. Rapp*, Greg P. Maier*, Howard A. Dobbs, Nicholas J. Higdon, J. Herbert Waite, Alison Butler, Jacob N. Israelachvili. Defining the catechol-cation synergy for enhanced wet adhesion to mineral surfaces. *J. Am. Chem. Soc.* 2016, 138 (29), 9013-9016.

3.1 Introduction

Catechols and amines account for half of the amino acid side chains in surface priming Mfp-3 fast and Mfp-5 [1, 2] and have been shown to cooperatively displace the interfacial hydration layer and promote adhesion between mica surfaces [3]. Both Mfp-3 fast and Mfp-5 have high mol % Dopa (20 and 30 mol %, respectively) and high mol % cationic residues (24.5 and 22.6 mol %, respectively) [1, 2]. The prominence of basic residues in Mfp-3 fast and Mfp-5 enables electrostatic attraction between the positively charged residues within the protein and a range of negatively charged surfaces, including mica and other mineral oxides found in the mussel's intertidal habitat [4]. Adhesive electrostatic interaction between a single Lys residue and a wet mica surface has also been demonstrated with AFM [5]. Increasing solution pH above the Lys side chain pKa

* These authors contributed equally to this work

significantly reduces adhesion and indicates that adhesion of a single Lys residue to a wet mica surface requires a cationic amine [5].

The identity of the cationic residues in Mfp-3 fast and Mfp-5 differs significantly. Mfp-5 contains almost exclusively Lys with a relatively low mol % Arg (Figure 1.5). The substantial Arg content of Mfp-3 fast (Figure 1.5) implies potential synergy between Arg and catechol, similar to the synergy seen between Lys and catechol observed in CTC and TLC [3]. The abundance and proximity of catechol and Arg in Tren-Arg-Cam (TAC) parallels Mfp-3 fast [6] and serves as a model system for understanding the synergy between Arg and catechol in Mfps (Figure 3.1).

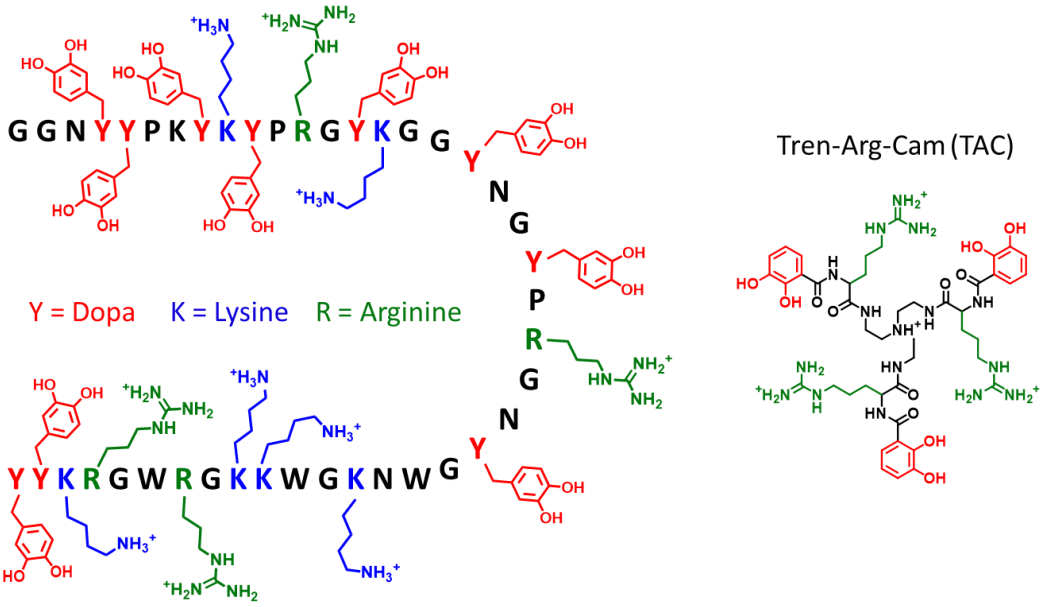

Figure 3.1. Amino acid sequence of Mfp-3 fast and structure of TAC

Nearly all tyrosine residues in Mfp-3 fast are post-translationally modified to Dopa; however, in Mfp-3 slow many tyrosine residues remain unmodified [6]. In addition, Mfp-3 slow contains 15 mol % tryptophan and only 9 mol % cationic residues (Figure 3.2). Hydrophobicity of amino acids is commonly determined through the sign and magnitude of the free energy transfer of the amino acid from pure ethanol to water (ΔG_t) [7]. Trp, Dopa, and Tyr are some of the most hydrophobic amino acids with $\Delta G_{t\text{-}Trp}$ = 3.4 kcal/mol, $\Delta G_{t\text{-}tyrosine}$ = 2.3 kcal/mol, and $\Delta G_{t\text{-}Dopa}$ = 1.8 kcal/mol at 25°C [7]. These hydrophobic residues make up 54 mol% of Mfp-3 slow [6], which suggests the potential for adhesion to hydrophobic surfaces. Gold, in the form of Au (110), is the most hydrophobic metal and Dopa interacts with the gold substrate most prominently via the hydrophobic benzene ring through charge transfer (chemisorption), π electron polarizability (physisorption), or a combination of both [8, 9]. On a polystyrene surface, catechol is capable of hydrophobic interactions as well as well as π-π stacking between the aromatic benzene ring of the catechol and the interfacial phenyl groups [2]. Several Mfps adhere strongly to methyl terminated, hydrophobic self-assembled monolayers (CH_3-SAM), as measured by the SFA [10]. H-bonding, covalent bonding, and coulombic interactions are not possible on the CH_3-SAM. The adhesion derives from interaction between the hydrophobic SAM and the hydrophobic residues within the Mfps.

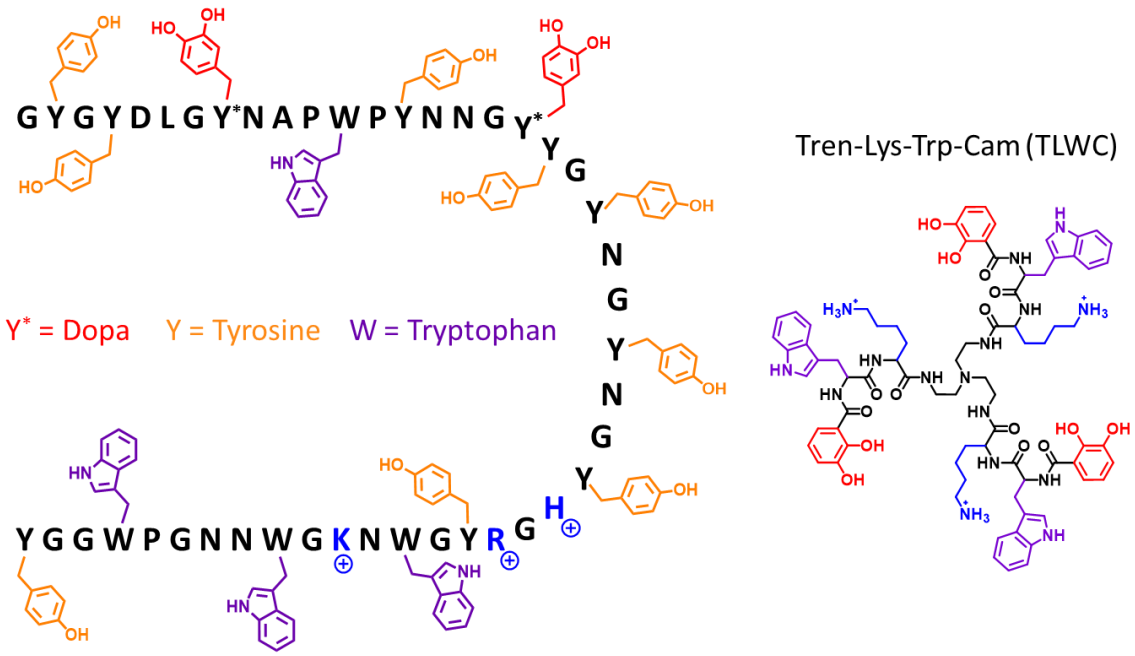

Figure 3.2. Amino acid sequence of Mfp-3 slow and structure of TLWC

3.2 Statement of Chapter Objectives and Results Summary

The purpose of this study was to further define the role of cations in catechol-cation synergy and to examine adhesion of siderophore analogs to hydrophobic surfaces using the SFA. TAC was synthesized to see if the guanidinium cation is able to reproduce the catechol-cation synergy previously observed with primary amines, thereby providing a rationale for the Arg content of Mfps. The results reveal that Arg is capable of interacting synergistically with catechol in wet adhesion, but produces lower adhesion than a primary amine. Tren-Lys-Lys-Cam (TLLC) was synthesized to determine how a higher cation to catechol ratio impacts the adhesion and adsorption properties of the siderophore analog. Doubling the cation content of the siderophore analog decreases the critical adsorption

concentration (CAC) as well as the maximum adhesion. Mixed molecule experiments were performed with catechols and cations in separate molecules to determine if intramolecular proximity is a prerequisite for catechol-cation synergy. These experiments were unable to reproduce the catechol-cation synergy observed when both functional groups are adjacent in the same molecule. Finally, Tren-Lys-Trp-Cam (TLWC) was synthesized to determine the effect of increased hydrophobicity on adhesion to a hydrophobic surface. The presence of the Trp residues in TLWC increased adhesion to a hydrophobic polydimethylsiloxane (PDMS) surface by 25% compared to TLC.

3.3 Experimental

3.3.1 Materials

2,3-dihydroxybenzoic acid (2,3-DHBA), dicyclohexylcarbodiimide (DCC), and tris(2-aminoethyl)amine (TREN) were purchased from Aldrich. Ethanol, THF, trimethylamine (Et3N), potassium hydroxide, trifluoroacetic acid (TFA) and DCM were purchased from Fisher. DMSO and acetic acid were purchased from EMD. Benzyl bromide and palladium on carbon were purchased from Alfa Aesar. N-hydroxysuccinimide (NHS) was purchased from Fluka. H-Lys(Z)-OH and Boc-Arg(Z)2-OSu were purchased from Bachem. Unless otherwise stated, all chemicals were used as received without further purification or modification.

3.3.2 Siderophore Analog Synthesis

The triserine lactone scaffold of CTC hydrolyzes under acidic conditions [11]. To increase stability across a broad pH range a synthetic analog of CTC was made, replacing the triserine lactone with a TREN core [12-14]. Two siderophore analogs were synthesized to examine the role of cations in wet adhesion. The first of these analogs, TAC (Figure 3.5), replaces the Lys of TLC with Arg. The second analog, TLLC (Figure 3.6), extends the catechol terminated arms of TLC with an additional Lys residue. A third siderophore analog was synthesized to examine adhesion to a hydrophobic surface. TLWC (Figure 3.7) inserts a Trp residue between the Lys and 2,3-DHBA of TLC.

3.3.2.1 Synthesis and purification of Tren-Arg-Cam

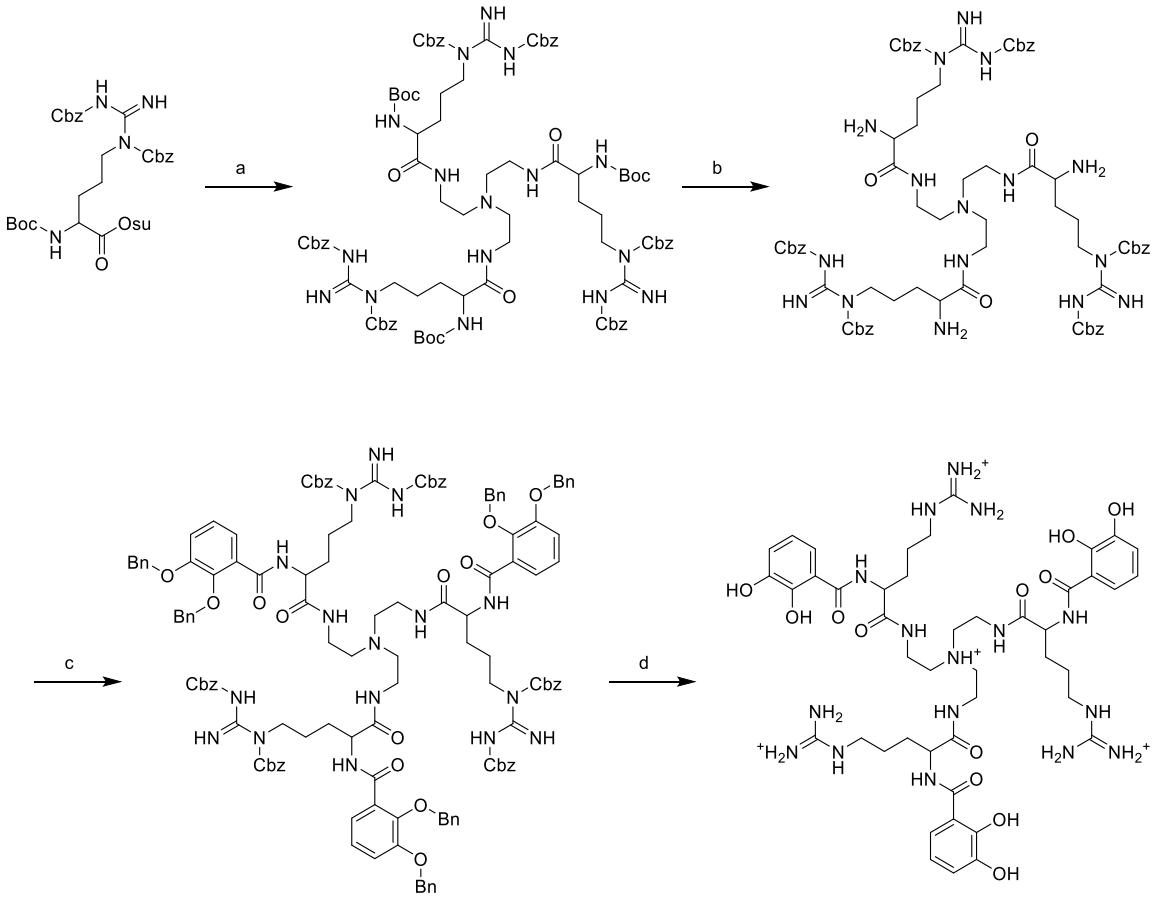

Figure 3.3. Synthesis scheme for TAC.

Step a: 3.3 equivalents of Boc-Arg(Z)$_2$-OSu was dissolved in dry DCM under nitrogen. 6 equivalents of Et_3N and 1 equivalent of TREN were then dissolved separately in dry DCM under nitrogen and added dropwise to the initial solution over several minutes and stirred overnight at room temperature. Any precipitates were removed via filtration and the filtrate was washed with brine, dried with $MgSO_4$, and the solvent was removed under vacuum. Reaction products were analyzed using ESI-MS.

Step b: 1 equivalent of Tren-[Arg(Z)$_2$-Boc]$_3$ was dissolved in DCM. A volume of TFA equal to the volume of DCM used to dissolve Tren-[Arg(Z)$_2$-Boc]$_3$ was added dropwise at room temperature. The reaction was allowed to stir for 2 hours before the solvent and TFA were removed under vacuum. Reaction products were analyzed using ESI-MS.

Step c: 3.3 equivalents of Bn-2,3-DHBA-OSu (see section 2.3.2.1 for synthesis of Bn-2,3-DHBA-OSu) were dissolved in anhydrous THF under nitrogen. 1 equivalent of of Tren-[Arg(Z)$_2$-OH]$_3$ was dissolved separately in anhydrous THF under nitrogen. 6 equivalents of Et_3N were added to the Tren-[Arg(Z)$_2$-OH]$_3$ solution, which was subsequently added dropwise to the initial solution over several minutes. The reaction was stirred under nitrogen at room temperature overnight. Precipitates were removed via filtration and the filtrate was washed with brine, dried with $MgSO_4$, and the solvent was removed under vacuum. Reaction products were analyzed using ESI-MS.

Step d: 1 equivalent of Tren[Bn-2,3-DHB-Arg(Cbz)$_2$]$_3$ was dissolved in 3% acetic acid in ethanol under nitrogen. 0.25 equivalents of 10 wt. % Pd/C was added to the solution and the atmosphere was exchanged to H_2. The solution was stirred overnight, filtered to remove Pd/C, and the solvent was removed under vacuum. Reaction products were analyzed using ESI-MS.

TAC was purified with RP-HPLC on a prep-scale C_4 column (22 mm i.d., 250 mm length, Vydac) using a gradient from 100% doubly deionized H_2O (0.05 % TFA) to 50 % doubly deionized H_2O (0.05 % TFA) and 50 % MeOH (0.05 % TFA) over 15 minutes. The column was exchanged back to 100% H_2O (0.05% TFA) over the next 10 minutes. The eluent was

continuously monitored at 215 nm and fractions were collected manually then concentrated under vacuum. TAC was identified using ESI-MS and the manually collected fractions containing TAC were ultrapurified by RP-HPLC using the method previously described. The ultrapure TAC fraction was lyophilized and stored at -20°C.

Tren-Arg-Cam: white powder; ^{1}H, ^{13}C, 2D NMR data; ESI-MS *m/z* 1023.53 $[M + H]^{+}$.

3.3.2.2 Synthesis and purification of Tren-Lys-Lys-Cam

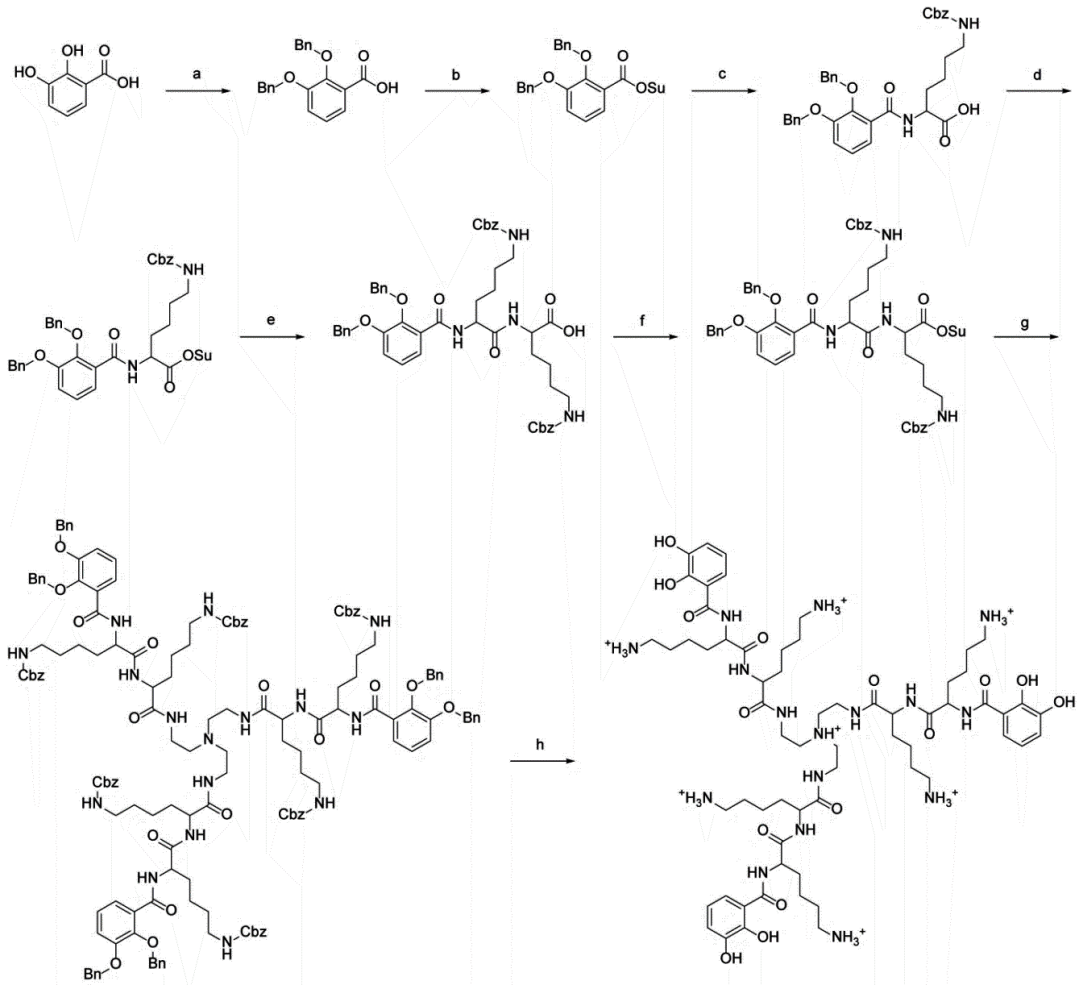

Figure 3.4. Synthesis scheme for TLLC.

Step a-d: Steps a-d in the synthesis of TLLC were done as described in section 2.3.2.1.

Step e: 1 equivalent of Nε-benzyloxycarbonyl-L-lysine (H-Lys(Cbz)-OH) was dissolved in 70% THF in H_2O using heat and sonication. Subsequently, 4 equivalents of Et_3N was dissolved in the solution. 1 equivalent of Bn-2,3-DHBA-Lys(Cbz)-OSu was dissolved separately in THF and added to the Et_3N solution and stirred overnight at room temperature. The THF portion of the solvent was removed under vacuum and the remaining aqueous layer was acidified to pH 1-2 with 1 M HCl. The acidified aqueous layer was extracted 3X with ethyl acetate, washed with brine, dried with anhydrous $MgSO_4$, and the solvent was removed under vacuum. Reaction products were analyzed using ESI-MS.

Step d: 1 equivalent of Bn-2,3-DHBA-Lys(Cbz)-Lys(Cbz)-OH and 1 equivalent of NHS were dissolved in anhydrous THF under nitrogen. 1 equivalent of DCC was then dissolved separately in anhydrous THF under nitrogen and added dropwise to the initial solution over several minutes. The reaction was stirred overnight at room temperature. Solvent was removed under vacuum and the residue was dissolved in ethyl acetate. The solid DCHU byproduct was removed by filtration and the remaining solvent was removed under vacuum. Reaction products were analyzed using ESI-MS.

Step e: 3.3 equivalents of Bn-2,3-DHBA-Lys(Cbz)-Lys(Cbz)-OSu were dissolved in dry DCM under nitrogen. 6 equivalents of Et_3N and 1 equivalent of TREN were then dissolved separately in dry DCM under nitrogen and added dropwise to the initial solution over several minutes and stirred overnight at room temperature. Precipitates were removed via

filtration and the filtrate was washed with brine, dried with $MgSO_4$, and the solvent was removed under vacuum. Reaction products were analyzed using ESI-MS.

Step f: 1 equivalent of Tren[Bn-2,3-DHBA-Lys(Cbz)-Lys(Cbz)]$_3$ was dissolved in 3% acetic acid in ethanol under nitrogen. 0.25 equivalents of 10 wt. % Pd/C were added to the solution and the atmosphere was exchanged to H_2. The solution was stirred overnight, filtered to remove Pd/C, and the solvent was removed under vacuum. Reaction products were analyzed using ESI-MS.

TLLC was purified with RP-HPLC on a prep-scale C_4 column (22 mm i.d., 250 mm length, Vydac) using a gradient from 100% doubly deionized H_2O (0.05 % TFA) to 50 % doubly deionized H_2O (0.05 % TFA) and 50 % MeOH (0.05 % TFA) over 10 minutes. The column was exchanged back to 100% H_2O (0.05% TFA) over the next 10 minutes. The eluent was continuously monitored at 215 nm and fractions were collected manually then concentrated under vacuum. TLLC was identified using ESI-MS and the manually collected fractions containing TLLC were ultrapurified by RP-HPLC using the method previously described. The ultrapure TLLC fraction was lyophilized and stored at -20°C.

Tren-Lys-Lys-Cam: white powder; ^1H, ^{13}C, 2D NMR data; ESI Mass Spec *m/z* 1323.79 $[M + H]^+$.

3.3.2.3 Synthesis and purification of Tren-Lys-Trp-Cam

The synthesis for TLWC follows the same procedure as the synthesis of TLLC with the exception of using tryptophan in place of H-Lys(Cbz)-OH in step c. TLWC was purified with RP-HPLC on a prep-scale C_4 column (22 mm i.d., 250 mm length, Vydac) using a gradient from 100% doubly deionized H_2O (0.05 % TFA) to 20 % doubly deionized H_2O (0.05 % TFA) and 80 % MeOH (0.05 % TFA) over 15 minutes. The column was exchanged back to 100% H_2O (0.05% TFA) over the next 10 minutes. The eluent was continuously monitored at 215 nm and fractions were collected manually then concentrated under vacuum. TLWC was identified using ESI-MS and the manually collected fraction containing TLWC was ultrapurified by RP-HPLC using the method previously described. The ultrapure TLWC fraction was lyophilized and stored at -20°C.

Tren-Lys-Trp-Cam: white powder; ^{1}H, ^{13}C, NMR data; ESI-MS *m/z* 1497.73 $[M + H]^+$.

3.3.3 Surface Forces Apparatus Technique and Measurements

SFA measurements were performed by Michael V. Rapp in the research lab of Professor Jacob Israelachvili at UC Santa Barbara as described in section 2.3.4. Details on the SFA instrument and experimental methods have been published elsewhere [3, 15, 16]. Mixed molecule experiments were performed in which one molecule contained catechol and a different molecule contained at least one cationic group. TC (see section 2.3.2.6 for synthesis details) was the catechol containing component for all experiments and either TLB

(see section 2.3.2.4 for synthesis details) or tetramethylamine, Lys, isopropylamine, analine, 1,3-diaminopropane, diethylenetriamine, TREN, or 2,4,6-triethyl-1,3,5-benzenetrimethylamine (TEBMA) was the cation containing component. Force-distance measurements for the buffer were determined for each experiment to ensure contaminant free surfaces. In these experiments, the surfaces were brought together in buffer at a constant speed and held in contact under load for a certain amount of time. The surfaces were then pulled apart and the adhesive/repulsive forces as well as the distance between the surfaces were continuously measured and recorded. Between 0.1 and 5 mM of the cationic molecule was mixed with 0.02-1 mM Tren-Cam in pH 3.3, 50 mM acetate with 150 mM KNO_3. 10 µL of this solution was injected into the buffer-only solution at the interface between the mica surfaces. Solutions were allowed to equilibrate for 20 minutes prior to a second force-distance measurement.

Asymmetric force-distance measurements were taken for TLC and TLWC. In these experiments, one surface was mica and the other was a PDMS brush film that was covalently grafted to a molecularly smooth gold surface. The surfaces were prepared by Michael V. Rapp in the lab of Professor Jacob Israelachvili at UC Santa Barbara and the method for preparing the hydrophobic PDMS surface has been detailed elsewhere [17, 18]. Briefly, the gold surface was submerged in a 1 mM solution of 11-amino-1-undecanethiol HCl in ethanol, forming a SAM on the gold surface. The SAM coated gold surface was subsequently dried under N_2 and submerged in neat monoglycidyl ether-terminated PDMS (5000 g/mol). Heating to 130°C for 1 hour caused a click reaction between the PDMS epoxide and the SAM terminal amine. Excess unreacted PDMS was removed by cycles of

rinsing and sonicating in toluene, leaving a uniformly dense hydrophobic polymer surface without exposed SAM or gold. The experimental procedure for asymmetric force-distance measurements is the same as the procedure the symmetric mica-mica experiments described in section 2.3.3.

3.4 Results

3.4.1 Siderophore Analog Purification

The final deprotection step in the synthesis of siderophore analogs often contained unreacted starting material and partially deprotected starting material along with the fully deprotected desired product. It is essential to have highly pure material to get accurate SFA data. Each siderophore analog was subjected to an initial round of RP-HPLC purification in which the desired product was isolated from impurities. The eluent was monitored at 215 nm and each prominent peak was collected and analyzed by ESI-MS until the desired siderophore analog was identified. The desired peak in the HPLC spectrum often had slight overlap with impurities of similar retention time. It was therefore necessary to subject the siderophore analog to an additional round of RP-HPLC purification to remove any remaining trace impurities.

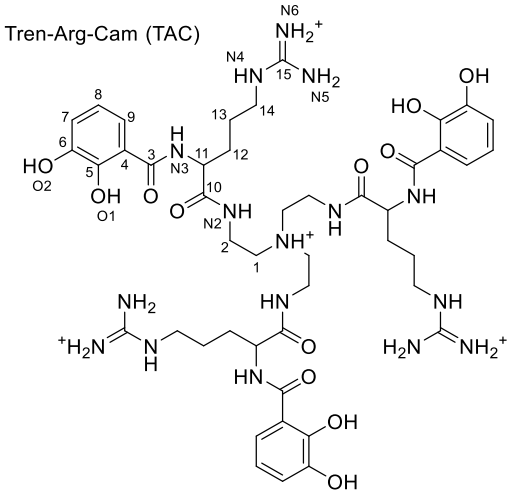

Figure 3.5. Structure of TAC. Numbered carbons correspond to NMR data in Table 3.1.

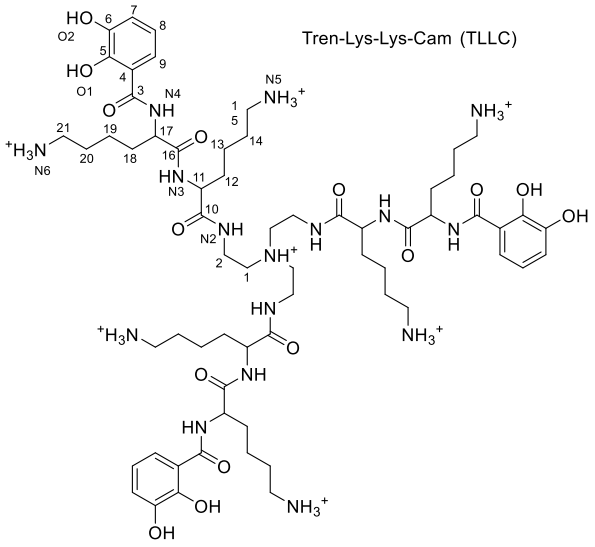

Figure 3.6. Structure of TLLC. Numbered carbons correspond to NMR data in Table 3.1.

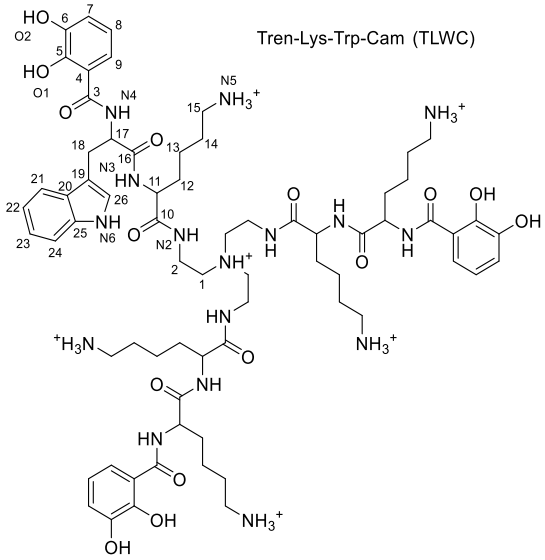

Figure 3.7. Structure of TLWC. Numbered carbons correspond to NMR data in Table 3.1.

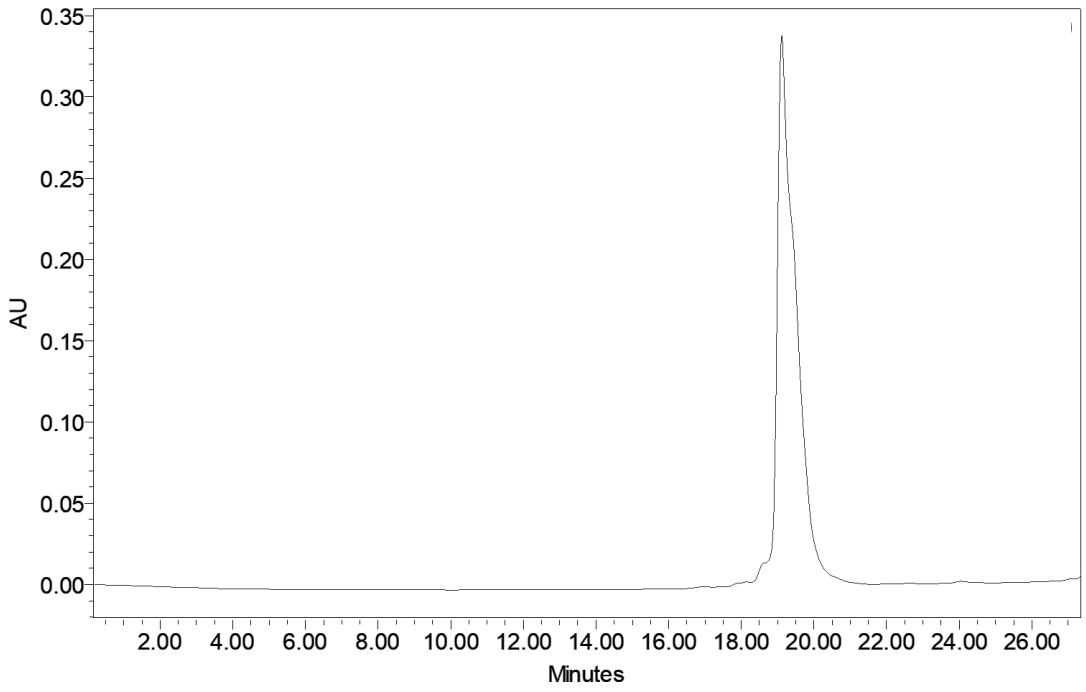

Figure 3.8. Reverse phase HPLC purification for TAC. The eluent was monitored at 215 nm.

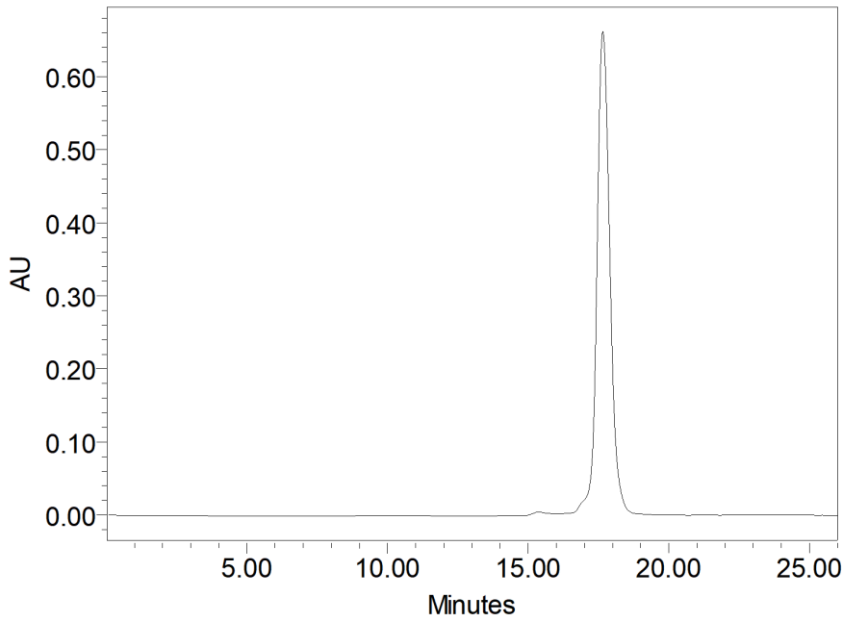

Figure 3.9. Reverse phase HPLC purification for TLLC. The eluent was monitored at 215 nm.

3.4.2. Siderophore Analog Structural Characterization

3.4.2.1 Siderophore Analog Mass Spectrometry

Siderophore analogs were characterized with ESI-MS (Figure 3.10-3.12). TAC shows a parent ion *m/z* of 1023.53 $[M + H]^+$ and 512.25 $(M + 2H)^{2+}$, which is consistent with the expected mass of the compound. TLLC shows the expected parent ions of *m/z* of 1329.79 $[M + H]^+$ and 662.37 $(M + 2H)^{2+}$. ESI-MS for TLLC also shows 2,3-DHB-Lys (*m/z* = 265.12) and Lys (*m/z* 129.1) that result from fragmentation at the amide bond between Lys and TREN as well as the amide bond between 2,3-DHBA and Lys. TLWC shows a parent ion *m/z* of 1497.73 $[M + H]^+$ and 749.35 $(M + 2H)^{2+}$, which is also consistent with the expected mass of the compound.

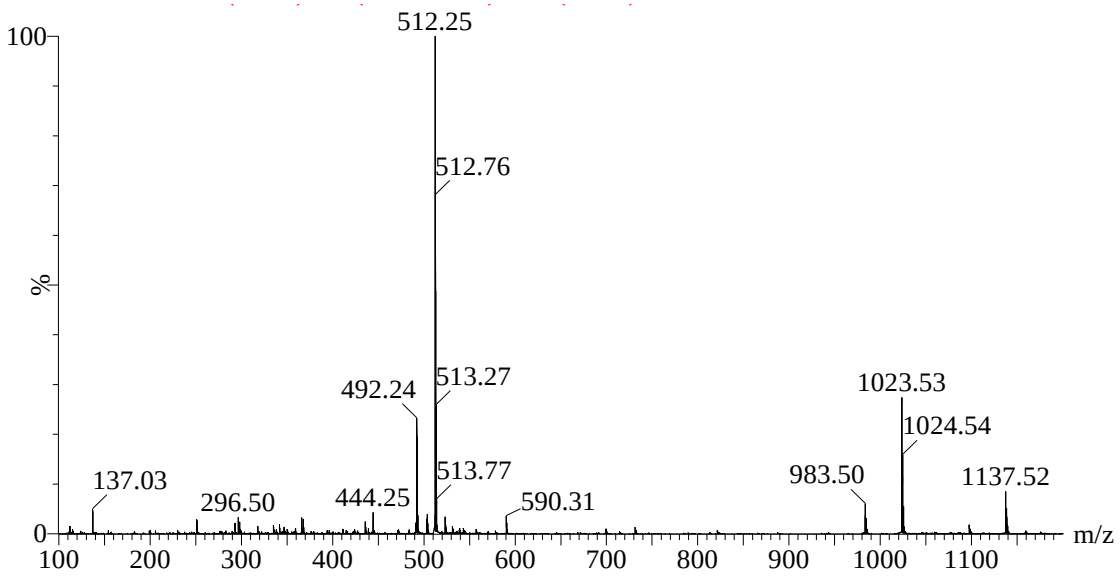

Figure 3.10. ESI-MS for TAC.

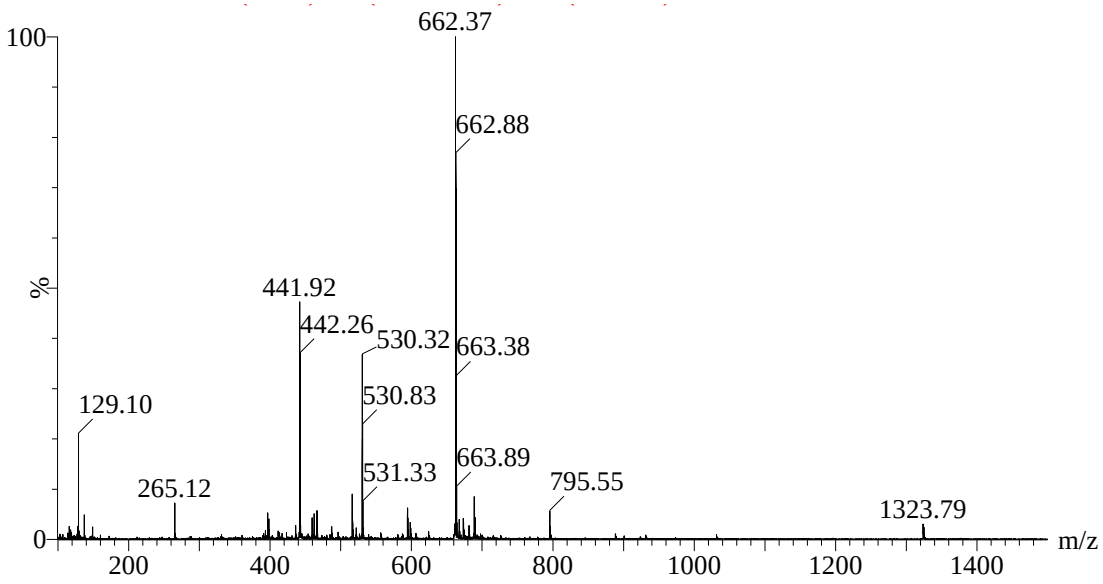

Figure 3.11. ESI-MS for TLLC.

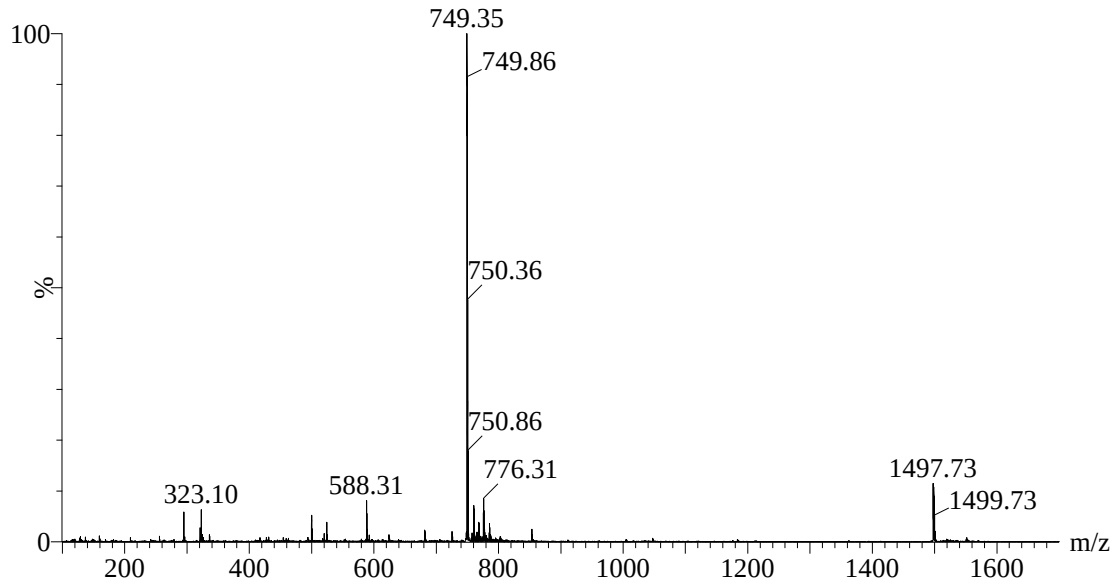

Figure 3.12. ESI-MS for TLWC.

3.4.2.2 Siderophore Analog NMR Characterization

^{1}H, ^{13}C, ^{1}H-^{13}C HMBC and ^{1}H-^{13}C HSQC NMR confirmed the expected molecular structures of TAC, TLLC, and TLWC that were predicted based on ESI-MS results and the synthetic pathway. ^{1}H and ^{13}C results are summarized in Table 3.1. The NMR characterization for TLC (section 2.4.4.2) serves as a useful reference for annotation of TAC, TLLC, and TLWC NMR resonances. TAC, TLLC, and TLWC all retain the characteristic aromatic resonances for the 2,3-DHBA moiety (δ_H 6.85 - 7.39). TAC, TLLC, and TLWC differ from TLC in the number and identity of the amino acids between the central TREN scaffold and the arm terminating 2,3-DHBA moiety. Key resonances resulting from these structural differences enable clear distinction between TLC and these siderophore analogs. TAC has a guanidinium moiety that is connected to the molecule by three methylene carbons rather

than the four methylene carbons that connect the primary amine of Lys to TLC. Comparing the total integration of Lys methylene proton resonances to the integration of Arg methylene proton resonances clearly differentiates the two compounds. Additionally, the guanidinium of TAC has a distinct carbon resonance (δ_C 156.71) that does not appear in TLC. The integration of Lys methylene protons is TLLC is twice the integration of Lys methylene protons in TLC, corroborating the presence of two Lys residues in TLLC compared to a single Lys in TLC. ^{1}H-^{13}C HMBC NMR of TLLC shows a correlation between the carbonyl carbon of 2,3-DHBA and the α-proton of a Lys as well as a correlation between the carbonyl carbon of that same Lys and the α-proton of a second Lys, confirming the presence of two Lys residues. Finally, the presence of Trp in TLWC produces more aromatic proton and carbon resonances than TLC. The resonance produced by the diastereotopic Trp methylene protons (δ_H 3.08 and 3.29) is also instructive in confirming the structure of TLWC.

Table 3.1. NMR data for TAC, TLLC, and TLWC. NMR (^{1}H on a Varian Unity Inova 600 MHz spectrometer and ^{13}C on a Varian Unity Inova 500 MHz spectrometer) was taken in D_2O or DMSO. Numbers correspond to Figure 3.5-3.7. See Figures 3.15-3.18 for NMR spectra.

Position*	δ_C	δ_H (J in Hz)	δ_C	δ_H (J in Hz)	δ_C	δ_H (J in Hz)
TREN						
1	Obscured by DMSO	3.61, m	Obscured by DMSO	Obscured by Water	54.02	3.36, m
2	Obscured by DMSO	3.51, m	Obscured by DMSO	Obscured by Water	35.02	3.16, m
DHBA						
3	168.76, C	-	168.69, C	-	169.9	-
4	115.93, C	-	114.83, C	-	115.1	-
5	148.38, C	-	148.50, C	-	146.5	-
6	146.04, C	-	146.10, C	-	144.3	-
7	118.18, CH	6.98, d (7.8)	118.20, CH	6.95, d (7.8)	119.6	6.85, d (6.6)
8	118.81, CH	6.75, t (7.8)	118.81, CH	6.70, t (7.8)	119	6.59, t (7.2)
9	118.44, CH	7.14, d (8.1)	118.37, CH	7.39, d (7.8)	117.5	6.99, d (8.4)
Lys/Arg/Trp						
10	171.81, C			-	173.8	-
11	52.71, CH	4.38, m	52.48, CH	4.20, m	54.94	4.06, m
12	28.63, CH2	1.83; 1.68, m	31.28, CH2	1.70, m	29.58	1.44; 1.30, m
13	25.31, CH2	1.52; 1.42, m	22.67, CH2	1.34, m	22.23	0.97, m
14	40.39, CH2	3.10, t (6.9)	26.63, CH2	1.53, m	26.15	1.23, m
15	156.71, C	-	38.76, CH_2	2.75, m	38.97	2.65, m
16	-	-	171.54, C	-	174.6	-
17	-	-	53.04, CH	4.48, m	55.73	4.67, m
18	-	-	30.94, CH2	1.70, m	26.45	3.29; 3.08, m
19	-	-	22.33, CH2	1.34, m	108.9	-
20	-	-	26.63, CH2	1.53, m	126.7	-
21	-	-	38.68, CH2	2.75, m	119.3	7.38, d (7.8)
22	-	-	-	-	118.2	6.91, t (6.6)
23	-	-	-	-	121.9	7.05, m
24	-	-	-	-	111.7	7.33, d (7.2)
25	-	-	-	-	136	-
26	-	-	-	-	124.3	7.04, s
Heteroatoms						
O1	-	-	-	11.88, s	-	-
O2	-	-	-	-	-	-
N1	-	-	-	-	-	-
N2	-	-	-	-	-	-
N3	-	-	-	8.17, m	-	-
N4	-	-	-	8.76, m	-	-
N5	-	-	-	7.81, m	-	-
N6	-	-	-	7.81, m	-	-

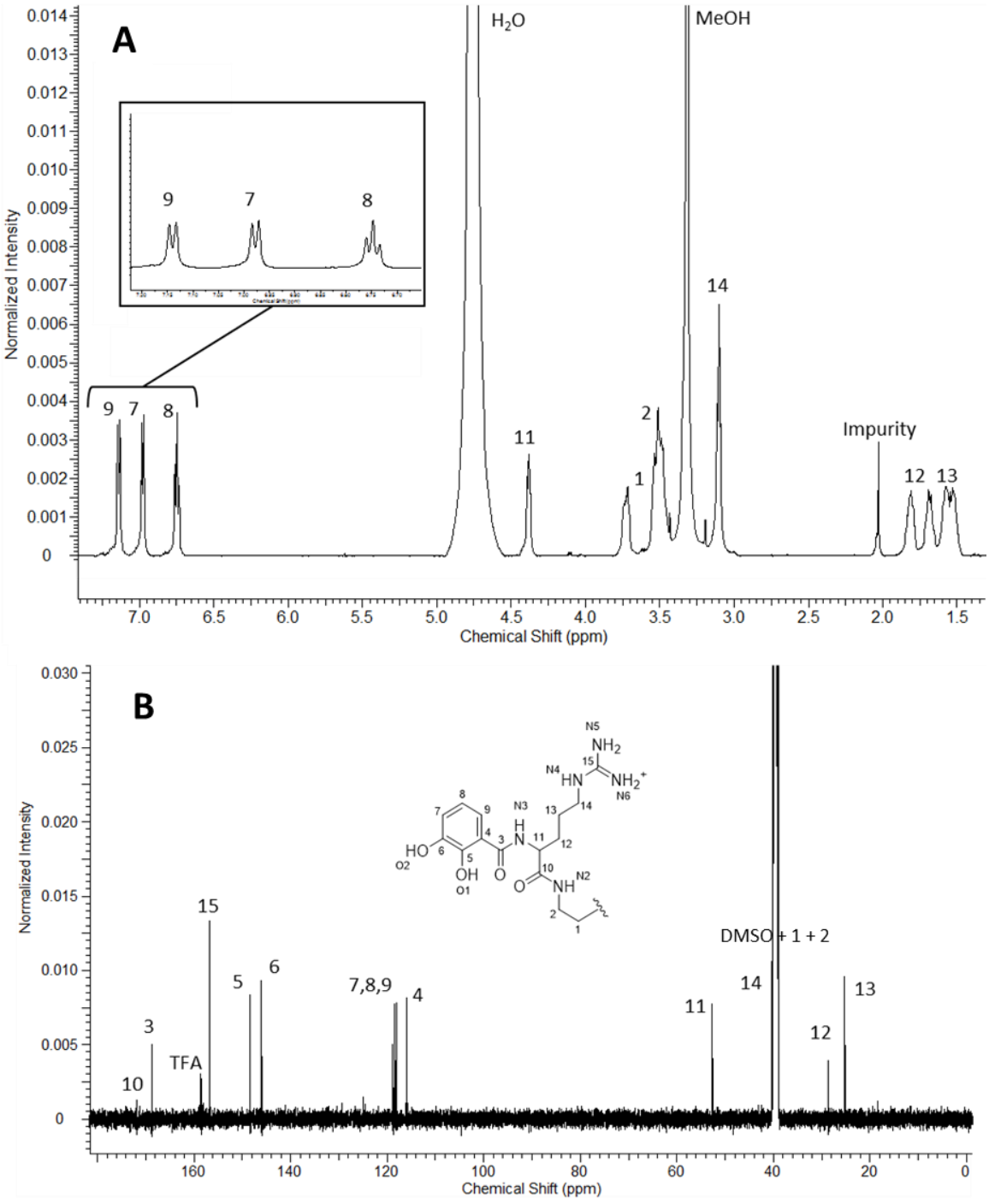

Figure 3.13. NMR data for TAC. (A) ^{1}H NMR Data for TAC. NMR (600 MHz) in D_2O with enlarged aromatic region. (B) ^{13}C NMR Data for TAC. NMR (500 MHz) in DMSO. TFA originates from RP-HPLC purification.

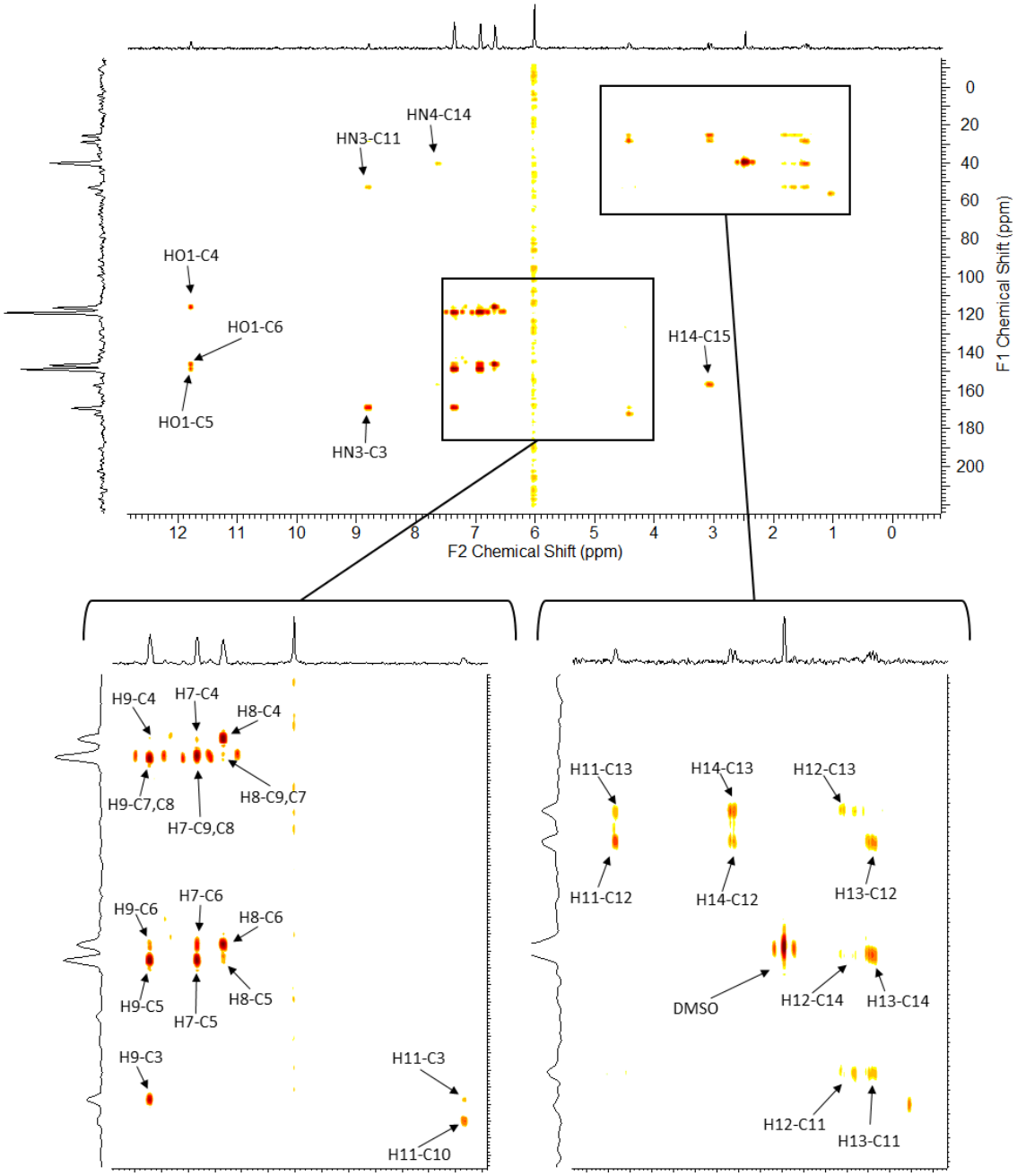

Figure 3.14. ^{1}H-^{13}C HMBC NMR for TAC. NMR (600 MHz) in DMSO. Enlarged Regions of the ^{1}H-^{13}C HMBC NMR for TAC are in bottom panel. The spectrum is annotated with the correlations between specific carbons and hydrogens.

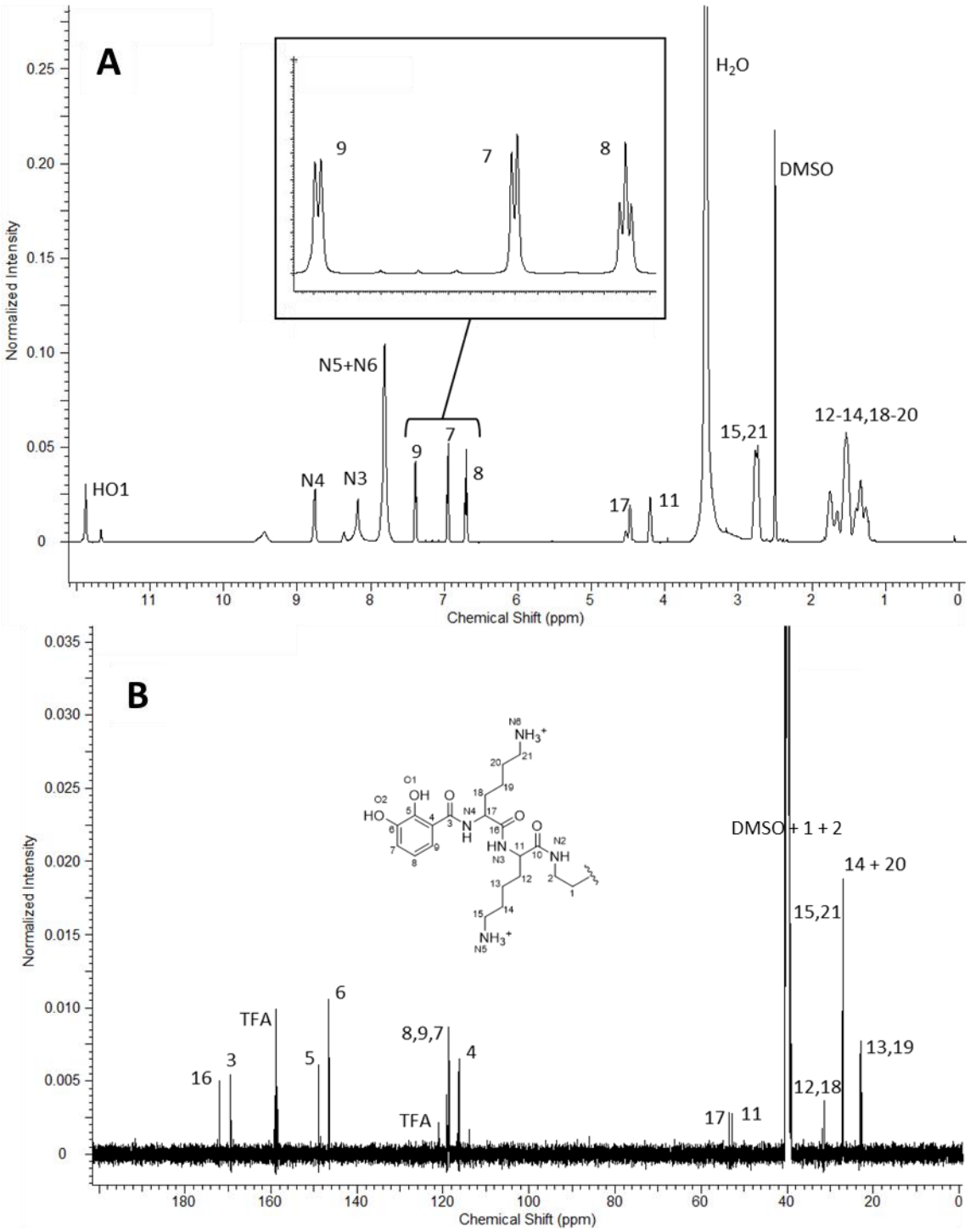

Figure 3.15. NMR data for TLLC. (A) ^{1}H NMR Data for TLLC. NMR (600 MHz) in DMSO with enlarged aromatic region. (B) ^{13}C NMR Data for TLLC. NMR (500 MHz) in DMSO. TFA originates from RP-HPLC purification.

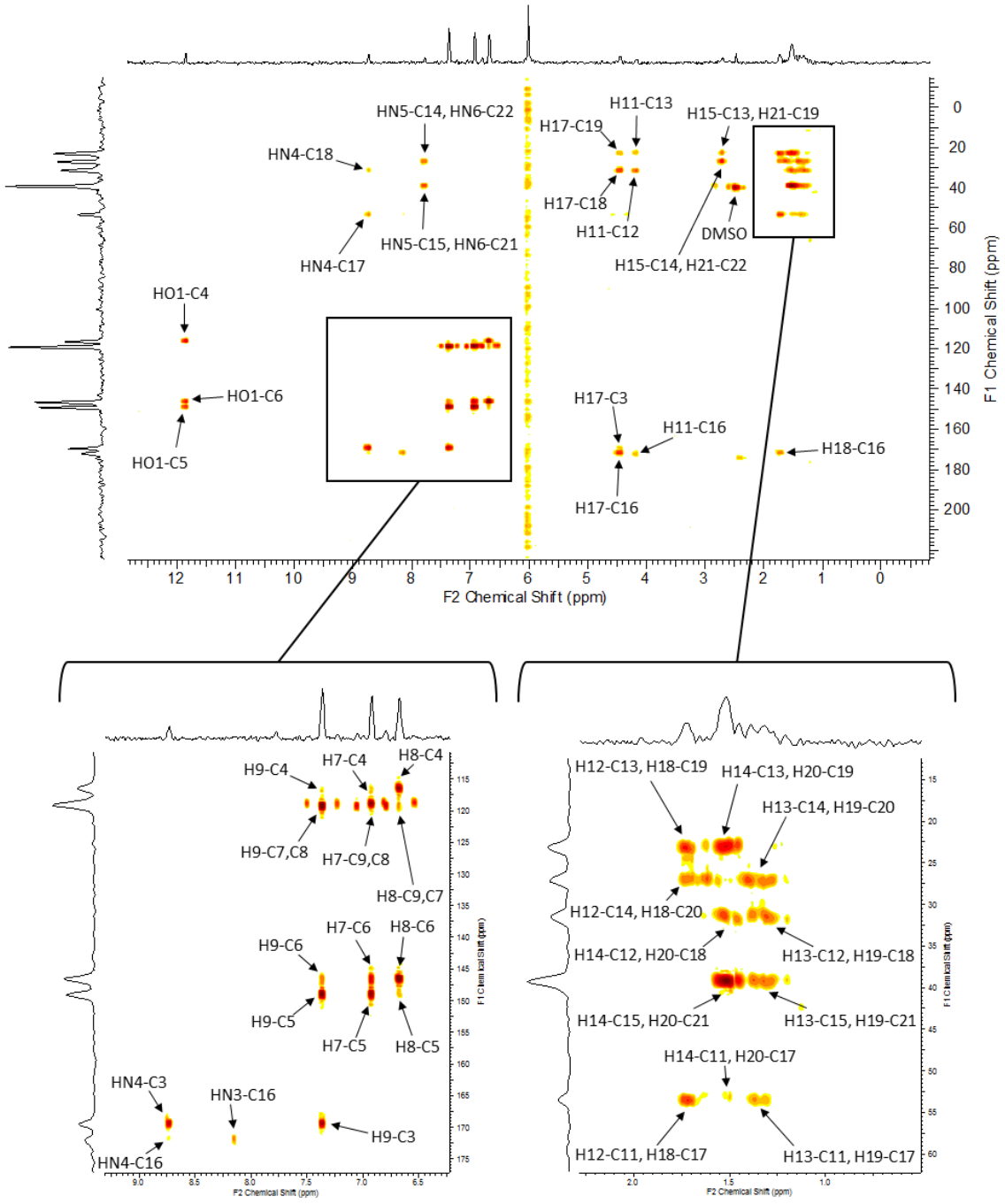

Figure 3.16. ^{1}H-^{13}C HMBC NMR for TLLC. NMR (600 MHz) in DMSO. Enlarged Regions of the ^{1}H-^{13}C HMBC NMR for TLLC are in bottom panel. The spectrum is annotated with the correlations between specific carbons and hydrogens.

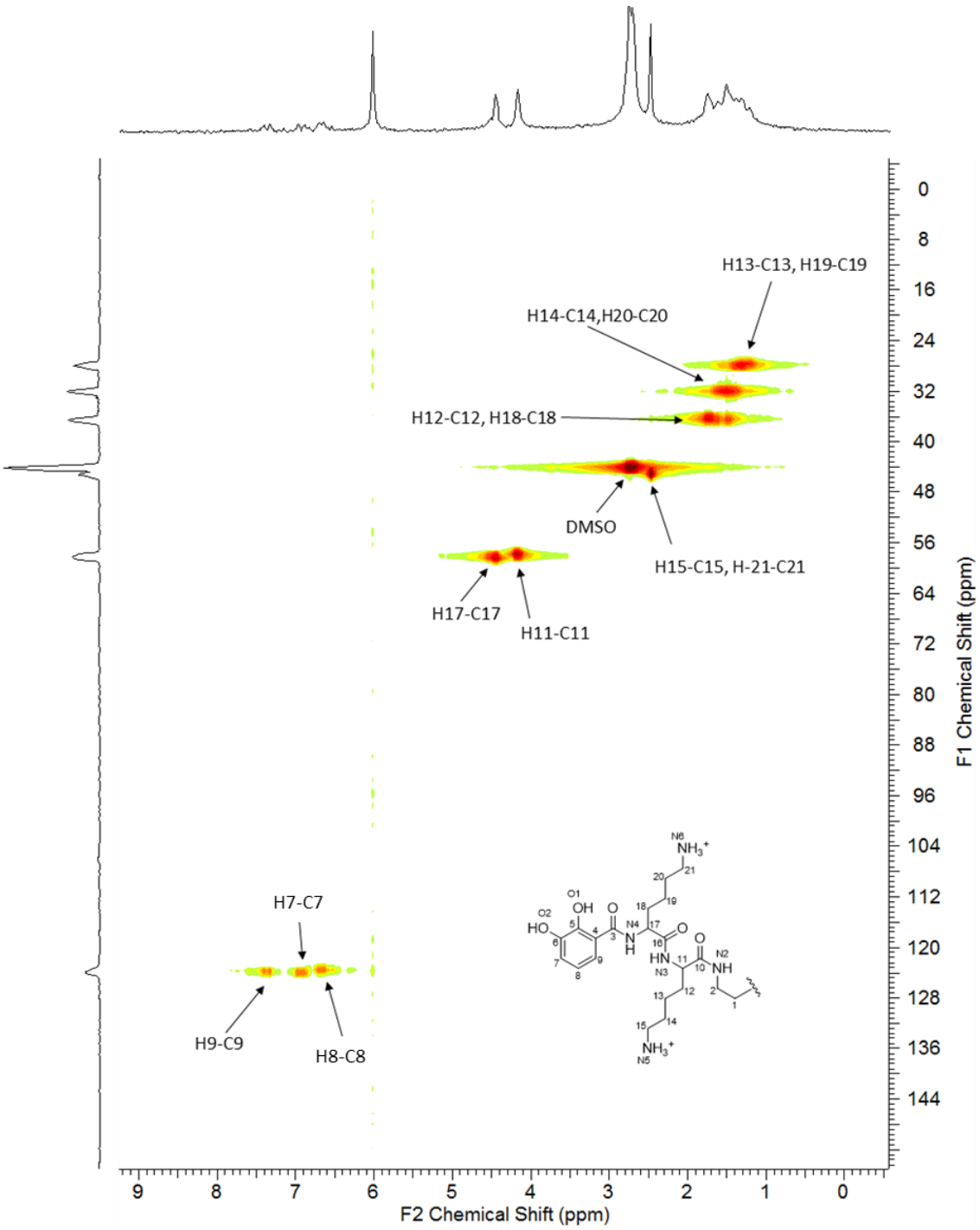

Figure 3.17. ^{1}H-^{13}C heteronuclear single quantum correlation (HSQC) NMR for TLLC. NMR (600 MHz) in DMSO. The spectrum is annotated with the correlations between specific carbons and hydrogens.

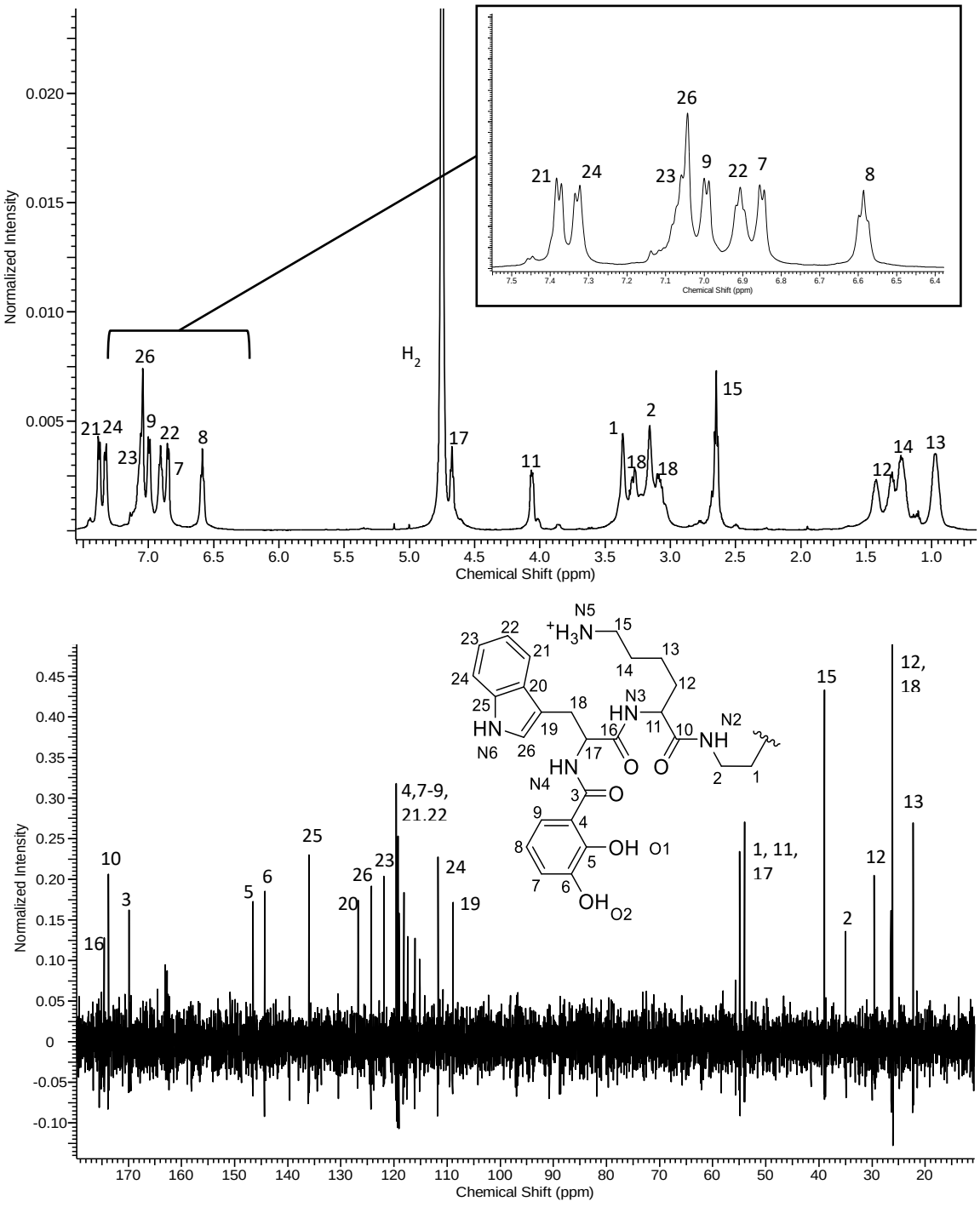

Figure 3.18. NMR data for TLWC. (A) ^{1}H NMR Data for TLWC. NMR (600 MHz) in D_2O with enlarged aromatic region. (B) ^{13}C NMR Data for TLWC. NMR (500 MHz) in D_2O.

3.4.3 Surface Forces Apparatus Adhesion Measurements

Symmetric force-distance measurements were taken for TAC, TLLC, and TLWC. All experiments were performed in pH 3.3, 50 mM acetate buffer with 150 mM KNO_3 (Figures 3.19-3.27). These solution conditions are consistent with previously published SFA measurements on Mfps and are an approximation of conditions during plaque formation within the distal depression of the mussel foot [19]. In force-distance measurement data the open circles represent data collected as the mica surfaces are brought into contact and solid circles represent data collected as surfaces are pulled apart. By convention, positive values are repulsive forces and negative values are attractive forces. Approaching mica surfaces come into contact, compress the intervening material and result in repulsive forces. The point at which added force no longer decreases the distance between the mica surfaces is known as the hardwall thickness. The surfaces are then pulled apart. If adhesive material is present at the interface and is capable of bridging the two surfaces then attractive forces can be measured. The minimum force/radius value is the maximum adhesion recorded for the material [16]. Asymmetric force-distance measurements were taken for TLC and TLWC and the hardwall thickness measured in these experiments is significantly larger than that for the symmetric mica-mica experiments due to the volume occupied by the SAM and PDMS layer on the gold surface.

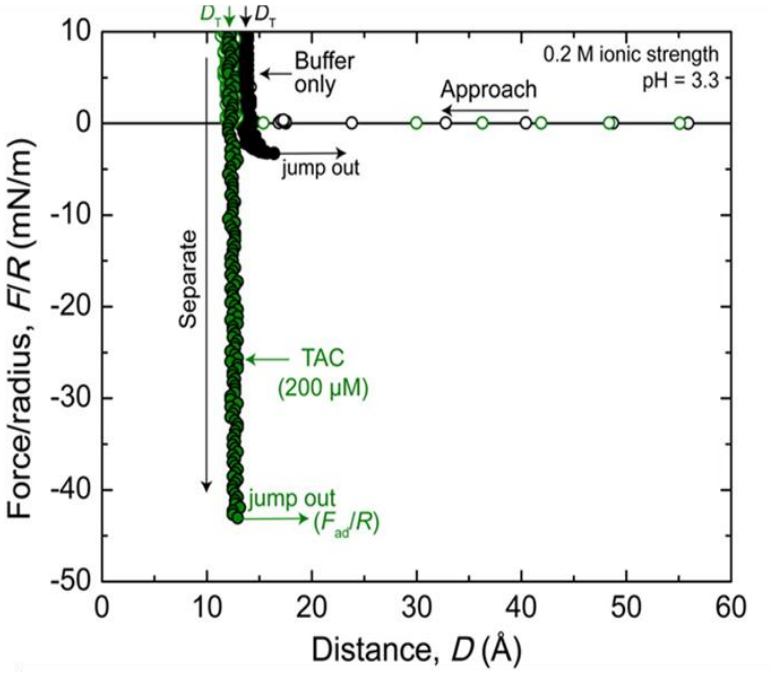

Figure 3.19. Adhesion of TAC. Force-distance measurements were performed in 50 mM acetate buffer + 150 mM KNO_3 at pH 3.3. See Figure 3.5 for structure of TAC.

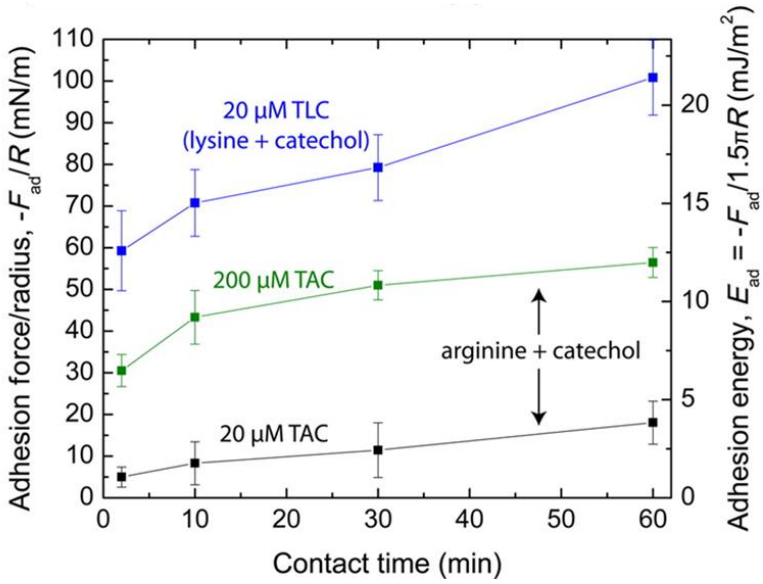

Figure 3.20. Adhesion of TAC vs TLC. Force-distance measurements were performed in 50 mM acetate buffer + 150 mM KNO_3 at pH 3.3 and 20 μM TAC and 200 μM TAC. Increasing the contact time between the surfaces prior to separation increases adhesion. TLC mediates greater adhesion force than TAC.

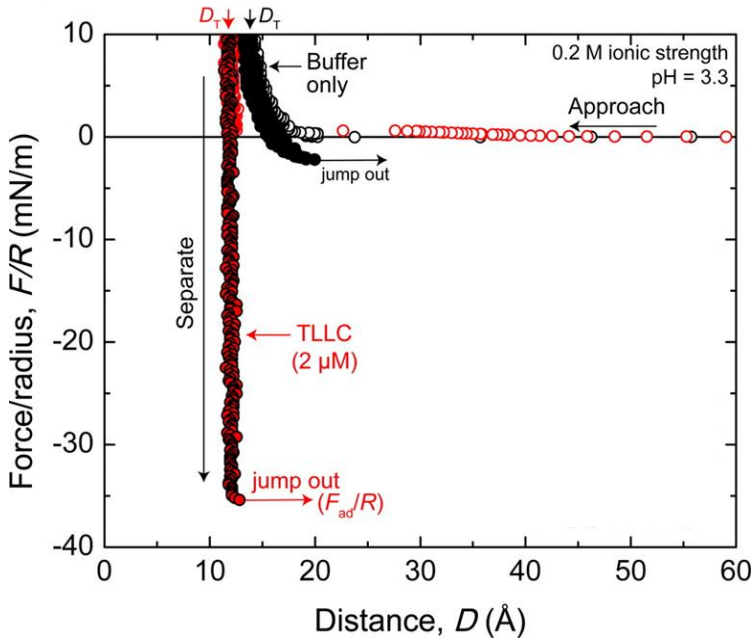

Figure 3.21. Adhesion of TLLC. Force-distance measurements were performed in 50 mM acetate buffer with 150 mM KNO_3 at pH 3.3. The surfaces were left in contact for 10 min before separation. See Figure 3.6 for structure of TLLC.

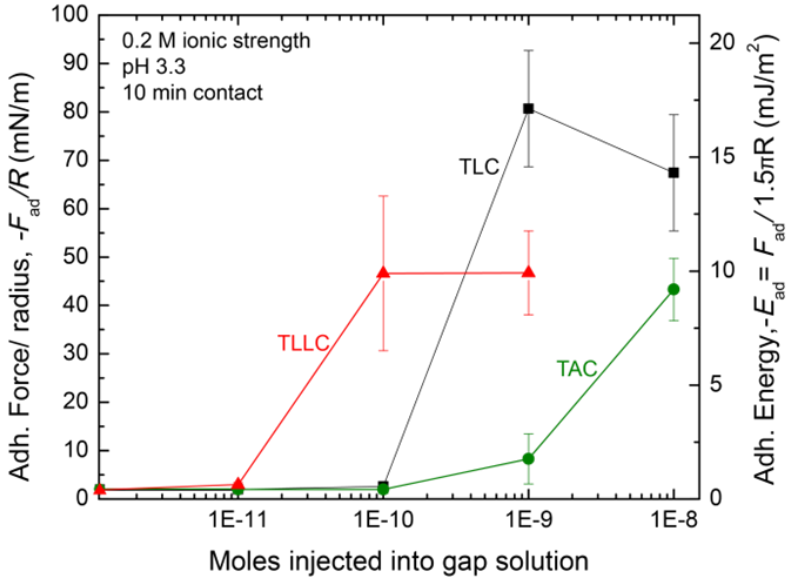

Figure 3.22. Concentration dependence of TLC, TAC, and TLLC adhesion. CAC is dependent on the number and identity of cationic functional groups within the adhesive molecule. Error bars represent one standard deviation.

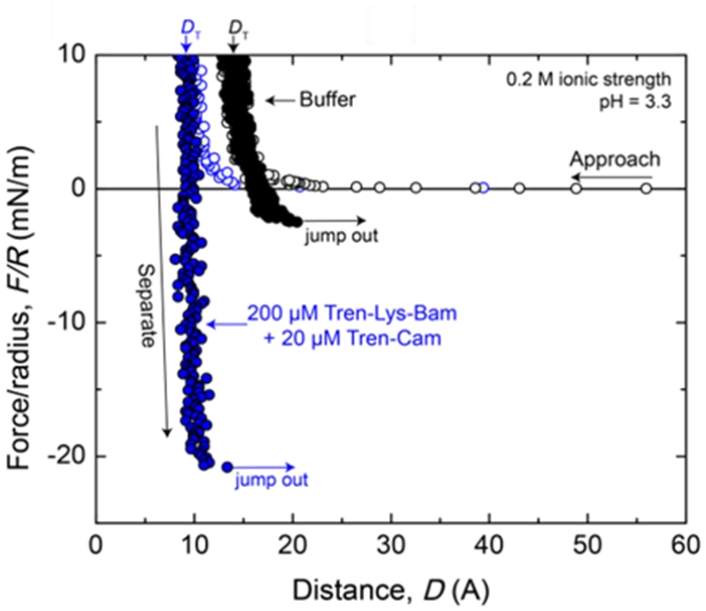

Figure 3.23. Mixed molecule adhesion of TC and TLB. See Figure 2.12 and 2.14 for structures of TLB and TC, respectively.

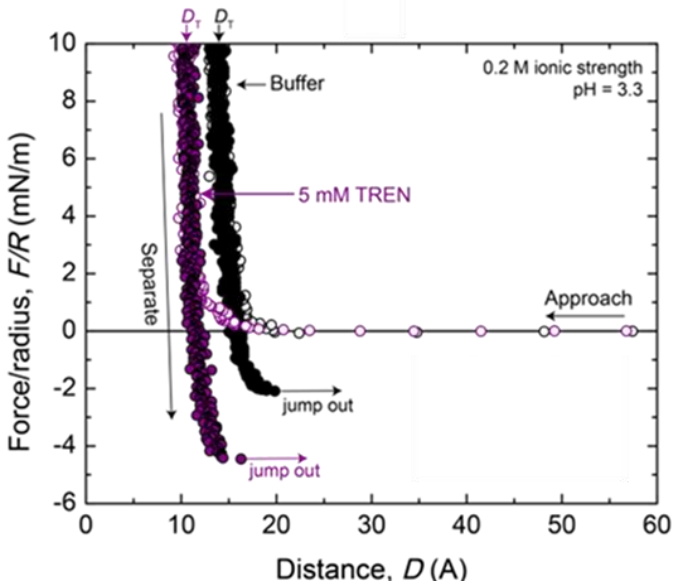

Figure 3.24. Mixed molecule adhesion of TC and TREN. See Figure 2.14 for structure of TC

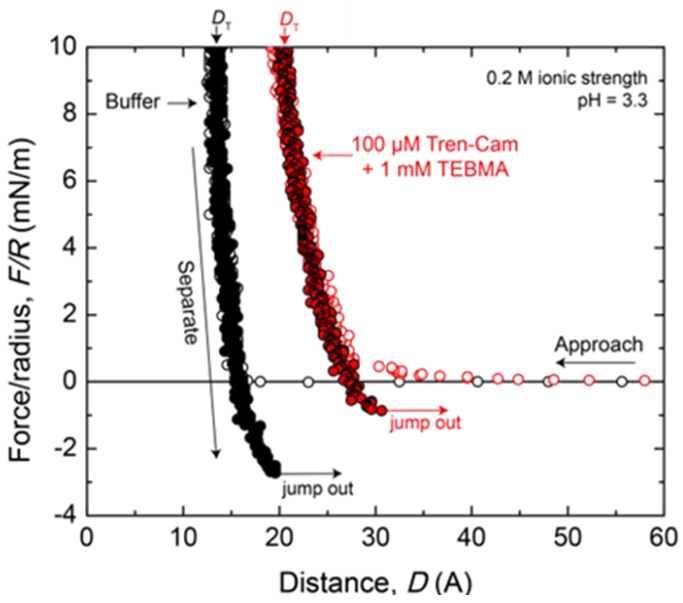

Figure 3.25. Mixed molecule adhesion of TC and TEBMA. See Figure 2.14 for structure of TC.

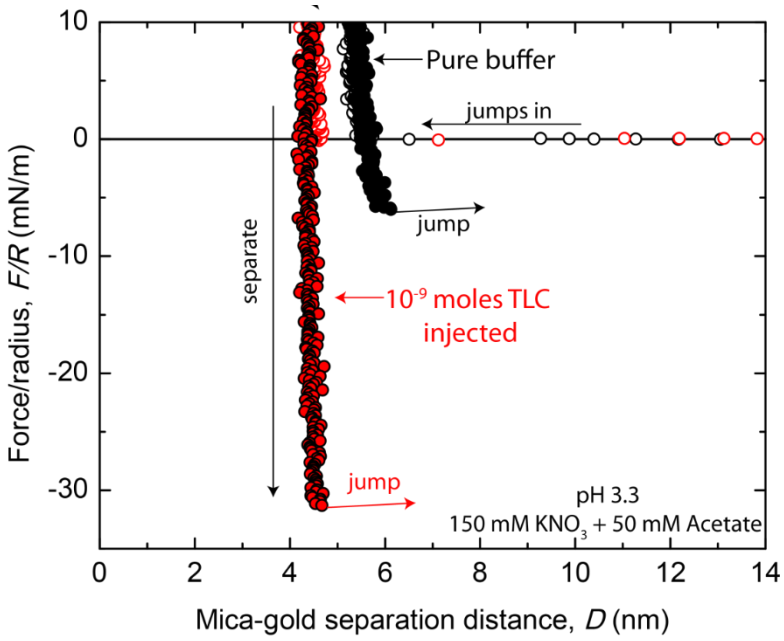

Figure 3.26. Asymmetric adhesion of TLC. Force-distance measurements were performed in 50 mM acetate with 150 mM KNO3 at pH 3.3 between a mica surface and a grafted PDMS surface.

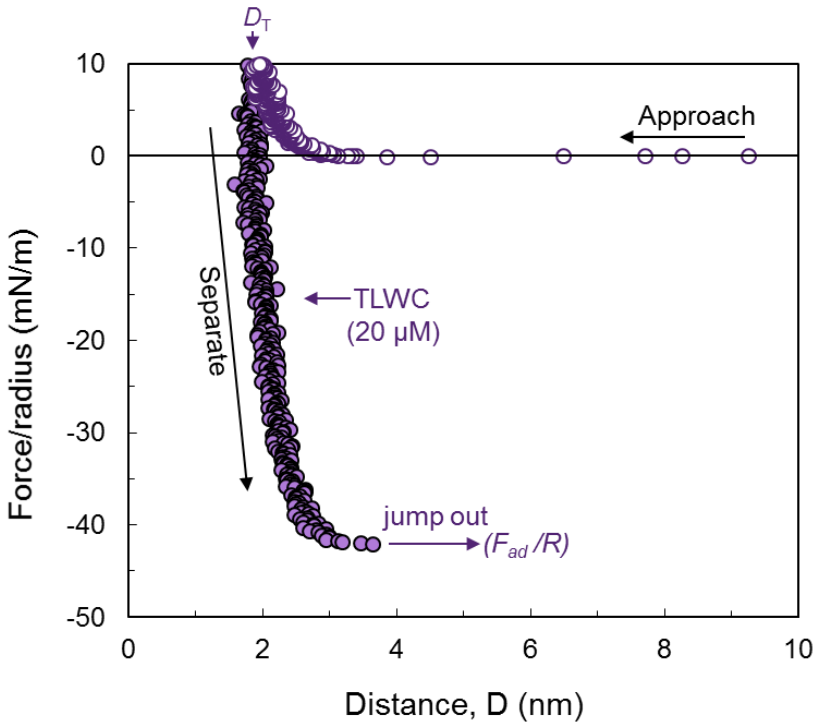

Figure 3.27. Asymmetric adhesion of TLWC. Force-distance measurements were performed in 50 mM acetate with 150 mM KNO3 at pH 3.3 between a mica surface and a grafted PDMS surface.

3.5 Discussion

TAC and TLLC were synthesized to probe the role of cations in wet adhesion [15]. TAC replaces the Lys residue with an Arg and TLLC doubles the ratio of Lys to catechol. Both TAC and TLLC perform similarly to TLC in SFA experiments [3]. All three siderophore analogs are able to displace the hydration layer, form a monolayer between the mica surfaces, and produce strong adhesion. However, TAC produces only 50-60% of the maximum TLC adhesion and has a CAC approximately 10x higher than TLC 9 (Figure 3.22). The guanidinium cation is bulkier and has a delocalized charge that is presumably less effective

than the primary amine of Lys at hydration layer displacement on mica. Similarly, the smaller K^+ cation has a more favorable adsorption free energy on mica than the larger Cs^+ cation [20]. TLLC has a 2:1 Lys to catechol ratio rather than the 1:1 ratio of TLC. Therefore, TLLC will have a lower catechol density per unit area, which may explain in the observed ~50% reduction in adhesion energy compared to TLC. However, the higher electrostatic charge density of TLLC compared to TLC improves its ability to penetrate the hydration layer and lowers the CAC by an order of magnitude (Figure 3.22). It is clear that cationic residues are critical for breaching the hydration layer; however, the role of cations after hydration layer displacement remains uncertain. Given the negative charge of the mica surface, it is likely that the cationic groups contribute to adhesion through Coulombic interactions [5, 21].

Mixtures of two separate molecules—one with only catechol appended to a TREN core (TC) and one with only amines—were subjected to the same experimental conditions used for the other siderophore analog force-distance measurements. Strong adhesion was not measured for any of the mixtures containing TC and a cationic amine compound, indicating that intramolecular proximity is required for catechol-cation synergy. Two highly charged amine compounds, TREN (4+ charge) and TEBMA (3+ charge), breached the hydration layer and adsorbed to the mica surface, but did not product the strong adhesion that results from catechol-cation synergy. The inability of mixtures of singly functionalized molecules to reproduce the catechol-cation synergy and strong adhesion of TLC indicate that the molecular geometry and configurational entropy upon adsorption are important contributors to the surface phenomena of siderophore analogs [22].

The TLWC structure is similar to TLC, but contains a hydrophobic Trp residue between the Lys and catechol. TLWC was synthesized to examine how inclusion of hydrophobic residues impacts adhesion to hydrophobic surfaces. The TLC control was able to produce strong adhesion in the asymmetric force-distance measurements between a mica surface and a grafted hydrophobic PDMS surface. At the mica surface, catechol adheres via bidentate interactions and lysine likely contributes to adhesion through electrostatic interactions (Figure 3.28 C) [2]. These types of adhesive interactions are not available at the PDMS surface and adhesion results from hydrophobic interactions between the surface and hydrophobic functional groups within TLC (Figure 3.28 A) [10, 23]. Similar asymmetric experiments between mica and a hydrophobic CH_3-terminated SAM have been conducted with Mfp-3 [10, 23]. Replica exchange molecular dynamics simulations show that Dopa adopts a parallel orientation with respect to the SAM, exposing the hydrophobic benzene ring to the hydrophobic surface [10, 23]. The catechol group of 2,3-DHBA in TLC potentially adopts a similar orientation at the PDMS surface to maximize hydrophobic interactions (Figure 3.28. A). Additionally, Lys contains a hydrophobic alkyl chain that may also contribute to hydrophobic interactions [24].

The presence of the PDMS surface caused a reduction in adhesion of TLC by ~66% compared to the adhesion measured in the symmetric mica-mica force-distance measurement (Figure 2.34 and 3.26), indicating that TLC adheres more strongly to the mica surface than to the PDMS surface. TLWC also produced strong adhesion in the asymmetric force-distance measurements between a mica surface and a grafted PDMS surface. Trp is the most hydrophobic amino acid [7] and its inclusion in TLWC improved adhesion between

mica and grafted PDMS by 25% compared to TLC (Figure 3.26 and 3.27). These experiments show that surface chemistry is a critical determinant of wet adhesive design and that optimizing the structure of wet adhesive materials to a particular surface can improve performance.

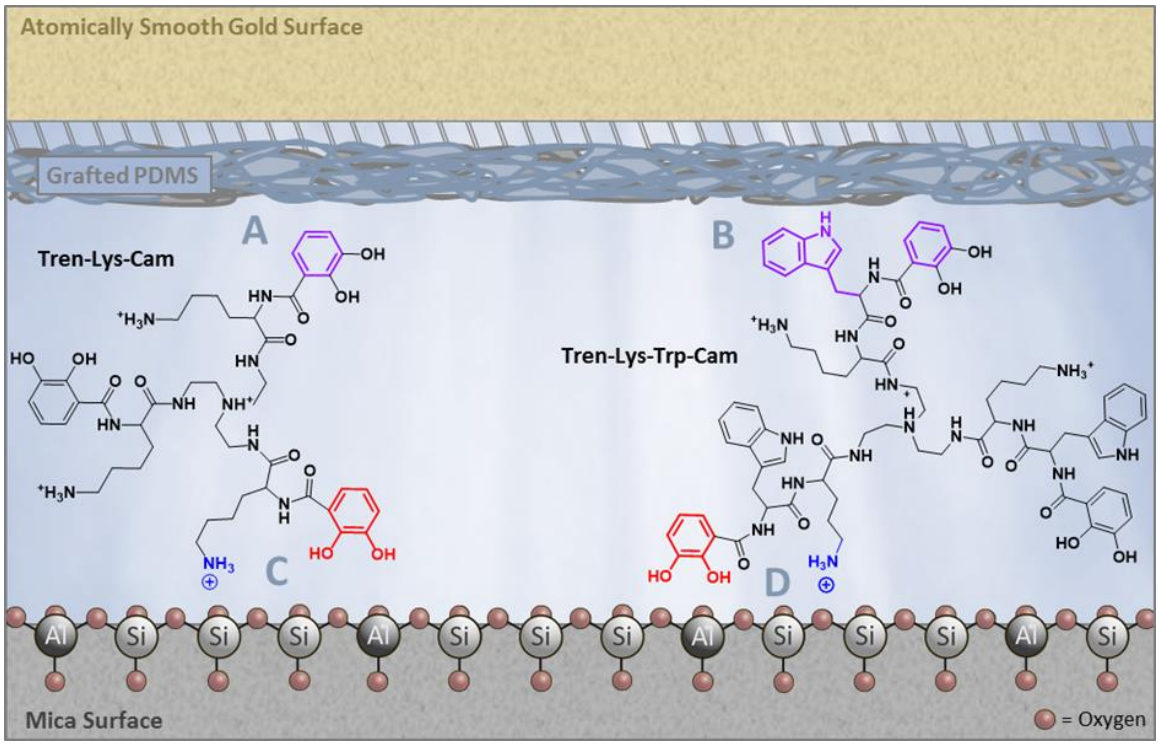

Figure 3.28. Asymmetric Adhesion of Tren-Lys-Cam and Tren-Lys-Trp-Cam. A + B. The hydrophobic functional groups in TLC and TLWC enable adhesion to the grafted PDMS surface. C + D. Catechol and Lys in both TLC and TLWC work synergistically to adhere to the mica surface.

3.6 References

1 Danner EW, Kan Y, Hammer MU, Israelachvili JN and Waite JH (2012) Biochemistry 51:6511-6518

2 Lu Q, Danner E, Waite JH, Israelachvili JN, Zeng H and Hwang DS (2013) J R Soc Interface 10:20120759

3 Maier GP, Rapp MV, Waite JH, Israelachvili JN and Butler A (2015) Science 349:628-632

4 Maier GP and Butler A (2017) J Biol Inorg Chem, doi 10.1007/s00775-017-1451-6

5 Razvag Y, Gutkin V and Reches M (2013) Langmuir 29:10102-10109

6 Wei W, Yu J, Broomell C, Israelachvili JN and Waite JH (2013) J Am Chem Soc 135:377-383

7 Nozaki Y and Tanford C (1971) J Biol Chem 246:2211-2217

8 Weinhold M, Soubatch S, Temirov R, Rohlfing M, Jastorff B, Tautz FS and Doose C (2006) J Phys Chem B 110:23756-23769

9 Ye Q, Zhou F and Liu W (2011) Chem Soc Rev 40:4244-4258

10 Yu J, Kan Y, Rapp M, Danner E, Wei W, Das S, Miller DR, Chen Y, Waite JH and Israelachvili JN (2013) Proc Natl Acad Sci U S A 110:15680-15685

11 Sandy M and Butler A (2011) J Nat Prod 74:1207-1212

12 Persmark M, Expert D and Neilands JB (1989) J Biol Chem 264:3187-3193

13 Lu C, Buyer JS, Okonya JF and Miller MJ (1996) Biometals 9:377-383

14 Rodgers SJ, Lee C, Ng CY and Raymond KN (1987) Inorg Chem 26:1622-1625

15 Rapp MV, Maier GP, Dobbs HA, Higdon NJ, Waite JH, Butler A and Israelachvili JN (2016) J Am Chem Soc 138:9013-9016

16 Israelachvili J, Min Y, Akbulut M, Alig A, Carver G, Greene W, Kristiansen K, Meyer E, Pesika N, Rosenberg K and Zeng H (2010) Reports on Progress in Physics 73:036601

17 Donaldson SH, Jr., Das S, Gebbie MA, Rapp M, Jones LC, Roiter Y, Koenig P, Gizaw Y and Israelachvili J (2013) ACS Nano 7:10094-10104

18 Rapp MV, Donaldson SH, Jr., Gebbie MA, Gizaw Y, Koenig P, Roiter Y and Israelachvili JN (2015) Langmuir 31:8013-8021

19 Martinez Rodriguez NR, Das S, Kaufman Y, Israelachvili JN and Waite JH (2015) Biofouling 31:221-227

20 Pashley RM (1982) Adv Colloid Interface Sci 16:57-62

21 Israelachvili JN (2011) Intermolecular and surface forces. Academic Press, San Diego

22 Baker BG (1966) The Journal of Chemical Physics 45:2694-2697

23 Levine ZA, Rapp M, Wei W, Mullen RG, Wu C, Zerze GH, Mittal J, Waite JH, Israelachvili J and Shea JE (2016) Proc Natl Acad Sci U S A 113:4332-4337

24 Creighton TE (1993) Proteins: Structures and molecular properties. W.H. Freeman, New York

IV. CATECHOL AUTOXIDATION: CONSIDERATION TO THE DESIGN OF WET ADHESIVES

4.1 Introduction

Catechols perform a broad range of functions in natural systems and materials [1, 2]. Catechol is a 1,2-benzenediol and is capable of a remarkable breadth of chemical and physical interactions. The ortho-hydroxyl configuration enables strong coordination to metals, including Fe^{3+}. The coordination of catechol to Fe^{3+} is best exemplified by catecholate siderophores [3-5]. In microbes, siderophores coordinate iron using 2,3-dihydroxybenzoic acid (2,3-DHBA)—a 2,3-dihydroxy catechol. The siderophore enterobactin—a cyclic trimer of 2,3-dihydroxybenzoyl-L-serine—is a natural product of enteric and pathogenic bacteria such as *E. coli* [6]. Under physiological conditions, tris-catecholate siderophores coordinate iron(III) with three bidentate catecholate groups and do so with particularly high affinity [7, 8]. The proton-independent stability constants for Fe(enterobactin)$^{3-}$ is 10^{49} [9]. While 2,3-DHBA is the predominant type of catechol in siderophores, variation in the nature of the catechol has been observed in the siderophore petrobactin, which employs two 3,4-DHBA moieties, as well as the α-hydroxy carboxylate of citric acid for Fe^{3+} coordination [10, 11].

The ortho-hydroxyl configuration that so effectively coordinates Fe^{3+} is also critical for adhesion to a variety of surfaces with disparate properties [12, 13]. Mussel foot proteins

(Mfps) utilize catechol-containing Dopa, 3,4-dihydroxyphenylalanine, for adhesion to wet and fouled surfaces in the wave-swept intertidal zone [14]. Redox chemistry has important consequences on function for catechols within Mfps. Catechol undergoes a pH-dependent oxidation by O_2 in aqueous solution in which higher pH promotes faster rates of oxidation [15-19]. Despite the prevalence of catechol autoxidation in nature, many mechanistic details remain to be elucidated. It is widely accepted that this radical process proceeds through semiquinone and superoxide intermediates before producing *o*-quinone and hydrogen peroxide [16, 17, 20, 21]. Both the semiquinone intermediate and quinone product can form irreversible covalent crosslinks through aryl-aryl coupling or Michael addition reactions, respectively (Figure 4.1) [22]. Oxidation of Dopa to Dopa-semiquinone and Dopa-quinone in Mfps induces crosslinking within the bulk of the adhesive plaque, providing cohesive strength to the material [23].

Hardening of insect cuticles and squid beaks also depends on catechol oxidation and subsequent crosslinking. Catechol-containing small molecules—dopamine, N-acetyl-dopamine and N-β-alanyl-dopamine—diffuse within the proteins in the nascent insect exoskeleton, oxidize to *o*-quinone, and form covalent crosslinks between proteins, imparting mechanical strength to the natural material [24-26]. Similarly, sclerotized squid beak formation relies on diffusion of 4-methylcatechol throughout the chitin-protein matrix where it oxidizes and forms covalent crosslinks with histidine residues in adjacent proteins [27]. Oxidation of Dopa residues and subsequent crosslinking between Dopa-quinone and histidine residues also contributes to the hardening of squid beaks [28].

A consequence of Dopa oxidation is the conversion of the vicinal hydroxyls to carbonyls [15]. Dopa-quinone cannot adhere to hydrogen-bond-accepting surfaces such as mica or other mineral oxides because the carbonyls of Dopa-quinone cannot donate hydrogen bonds. At the interface between the adhesive plaque and a mineral oxide surface oxidation prevents adhesion [20, 29]. The use of Dopa for both interfacial adhesion and internal cohesion within mussel adhesive plaques requires precise spatial and temporal control of redox chemistry. The mussel has evolved a series of strategies including antioxidant proteins that are co-deposited with interfacial adhesive proteins and a precisely controlled protein deposition environment to control catechol redox chemistry [30-32].

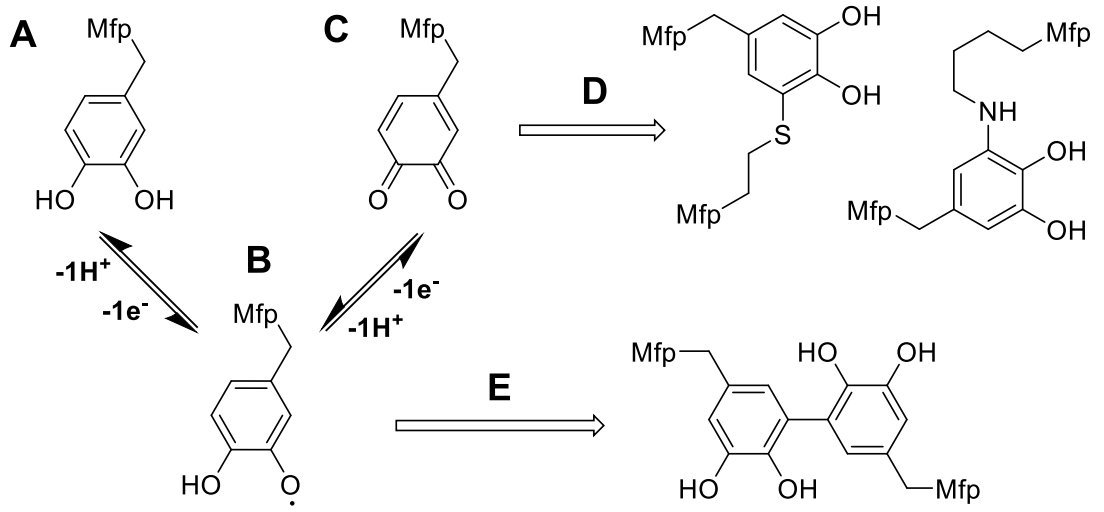

Figure 4.1. Catechol Oxidation in Mussel Foot Proteins. (A) The vicinal hydroxyl groups of Dopa are capable of bidentate hydrogen bonding with hydrogen bond accepting surfaces such as mica or other mineral oxides. (B) Dopa is oxidized to Dopa-quinone in a pH-dependent process that consumes dissolved O_2 and proceeds through a Dopa-semiquinone intermediate. (C) Dopa-quinone cannot act as a hydrogen bond donor to mineral oxide surfaces, effectively eliminating adhesion to mica or other mineral oxides. (D) Dopa-quinone can participate in Michael addition reactions with lysine and cysteine residues to form covalent crosslinks. (E) Dopa-semiquinone forms aryl-aryl crosslinking. Each of these crosslinking reactions is accompanied by the conversion of the carbonyls back to hydroxyl groups. These newly formed catechol-containing compounds are susceptible to subsequent autoxidation and crosslinking.

4.2 Statement of Chapter Objectives and Results Summary

The diverse natural uses for catechol has inspired the inclusion of catechol in many synthetic functional materials [1, 2]. A better understanding of catechol redox chemistry is critical to the design of wet adhesives and other catechol-containing functional materials. The purpose of this study was to investigate aspects of the mechanism of catechol oxidation by dioxygen, including the effect of pH and substituents on catechol autoxidation. The results are consistent with a mechanism for pH-dependent catechol autoxidation in which higher pH leads to faster autoxidation and in which the monoanion and dianion are oxidized by O_2. Autoxidation kinetics depend on the nature of the catechol (e.g., 2,3-dihydroxy versus 3,4-dihydroxy catechol), as well as the nature of the substituent groups. A linear Hammett correlation for the pH-independent second-order rate constants for catechol autoxidation indicates that the autoxidation mechanism is consistent throughout the substituents investigated and that catechols functionalized with electron withdrawing groups are more resistant to autoxidation.

4.3. Experimental

4.3.1 Materials

All aqueous solutions were made using ultrapure water with resistivity of 18.2 MΩ-cm (Barnstead Nanopure II). Catechol, 4-methylcatechol, 2,3-dihydroxybenzoic acid (DHBA), 3,4-DHBA, 4-ethylcatechol, and 4-chlorocatechol were purchased from Sigma-Aldrich. The

purity of purchased catechols was checked by ^{1}H and ^{13}C NMR (Varian Unity Inova 600 MHz spectrometer). Sodium phosphate dibasic, sulfuric acid, and tricine were purchased from Fisher. CAPSO was purchased from Research Organics Inc. CAPS was purchased from Chem IMPEX International Inc. Chelex-100 resin was purchased from Bio-Rad. All materials were used as received unless otherwise stated.

4.3.2. Synthesis, Characterization, and Purification of 5-Sulfo-2,3-DHBA

5-Sulfo-2,3-DHBA was synthesized based on previously published procedures [33]. 2,3-DHBA was dissolved in excess concentrated sulfuric acid and allowed to stir at 80°C for 1 hour. The reaction was then allowed to stir at room temperature for 8 hours and solvent was removed under vacuum.

5-Sulfo-2,3-DHBA was subjected to an initial round of RP-HPLC purification in which the desired product was isolated from impurities. The eluent was monitored at 215 nm and each prominent peak was collected and analyzed by ESI-MS until the desired product was identified. The desired peak in the HPLC spectrum had slight overlap with impurities of similar retention time. It was therefore necessary to subject the siderophore analog to an additional round of RP-HPLC purification to remove any remaining trace impurities (Figure 4.8). The expected structure of 5-Sulfo-2,3-DHBA was confirmed with ^{1}H and ^{13}C NMR (Varian Unity Inova 600 MHz spectrometer).

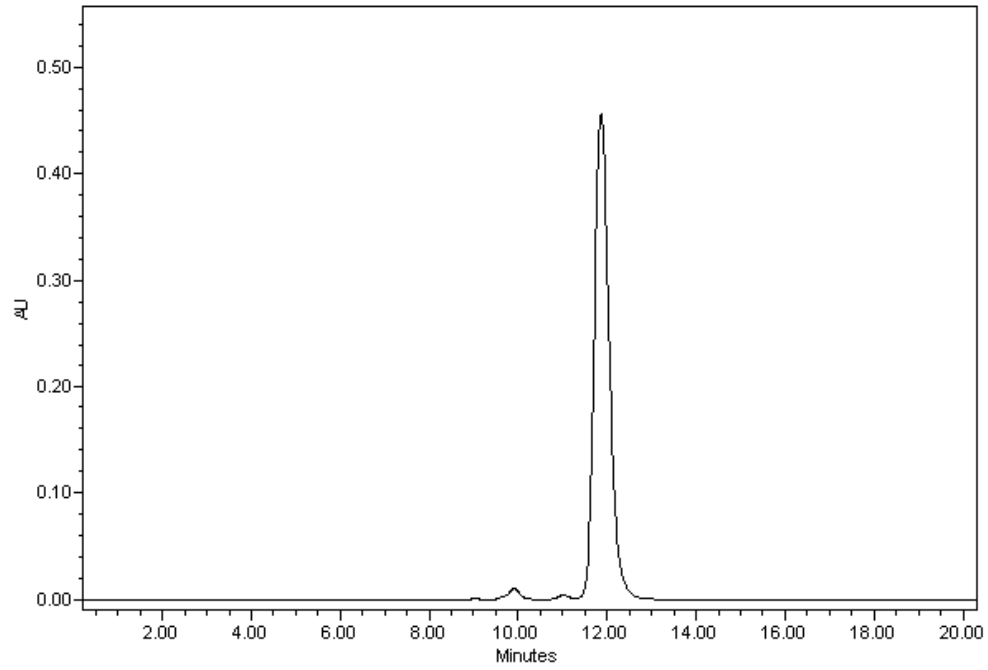

Figure 4.2. Reverse phase HPLC purification for 5-Sulfo-2,3-DHBA. The eluent was monitored at 215 nm.

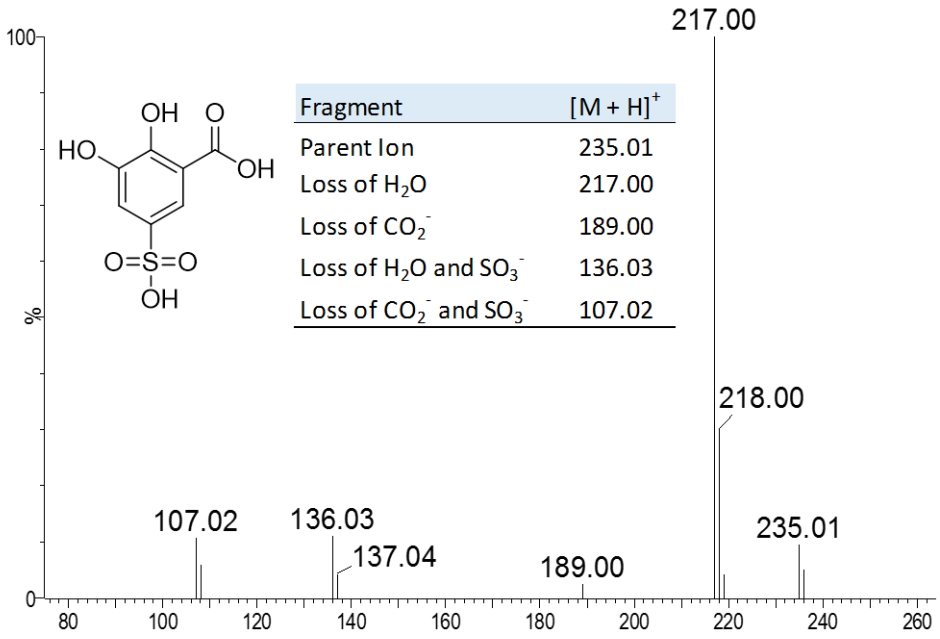

Figure 4.3. ESI Mass Spectrometry of 5-Sulfo-2,3-DHBA. Data was collected on a XEVO G2-XS TOF Mass Spectrometer and the parent ion and fragmentations are listed.

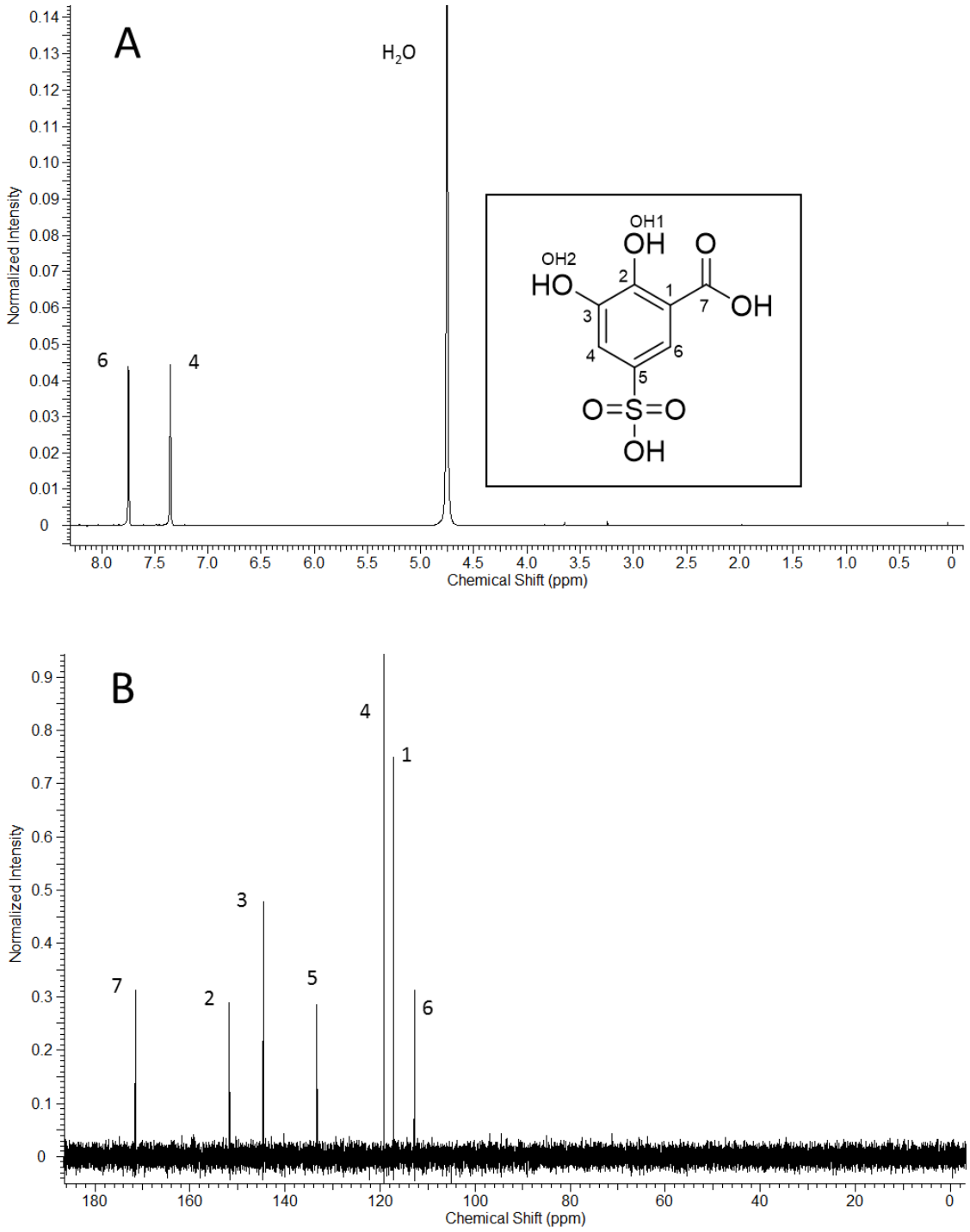

Figure 4.4. NMR Spectra of 5-Sulfo-2,3-DHBA. (A) ^{1}H NMR (600 MHz) data for 5-sulfo-2,3-DHBA in DMSO with enlarged aromatic region. (B) ^{13}C NMR (600 MHz) data for 5-sulfo-2,3-DHBA in DMSO.

4.3.3 Oxidation Kinetics:

A 5300 Biological Oxygen Monitor (Yellow Springs Instruments) equipped with a Clark-type oxygen electrode was used to monitor the catechol oxidation kinetics through the consumption of dissolved O_2. Buffer solutions were held at 29.5˚C ± 0.01 and bubbled with compressed air for at least 10 minutes to equilibrate to the same starting concentration of dissolved O_2 for all experiments. Trace metal was removed from buffers with Chelex 100 resin (100-200 mesh, sodium form, Bio-Rad). The water-jacketed reaction chamber was filled with 3 ml of buffer solution and held at 29.5˚C ± 0.01. The reaction chamber was sealed with the Clark-type oxygen electrode—eliminating the headspace by expelling air through the narrow injection port—and allowed to equilibrate for 5 – 10 minutes prior to each experiment. The reactions were initiated by injection of 10 µl of catechol or a functionalized catechol solution with a glass capillary tube and the percent O_2 remaining in solution was recorded as a function of time for either 5 or 10 minutes. All catechol solutions were prepared in 0.5 M HCl immediately prior to each experiment to prevent any catechol oxidation prior to reaction initiation. Ethanol was used in combination with 0.5 M HCl to improve solubility if necessary. Phosphate buffer was used for pH 6.0, 7.0, 7.5, 8.0, 11.5, and 12.0. Tricine buffer was used for pH 8.5. CAPSO buffer was used for pH 9.0, 9.5, and 10.0. CAPS buffer was used for pH 10.5 and 11.0. The buffer concentration was 50 mM for all experiments.

The percent O_2 remaining in the reaction solution was corrected for the baseline measurement of the Clark-type oxygen electrode (Figure 4.11) and then converted to O_2

concentration in solution by utilizing previously published O_2 solubility data [34]. The concentration of O_2 in air-saturated water is 223 µM at 29.5 ˚C. The catechol concentrations used were high enough to ensure pseudo first-order reaction conditions with catechol in excess of O_2 for all experiments.

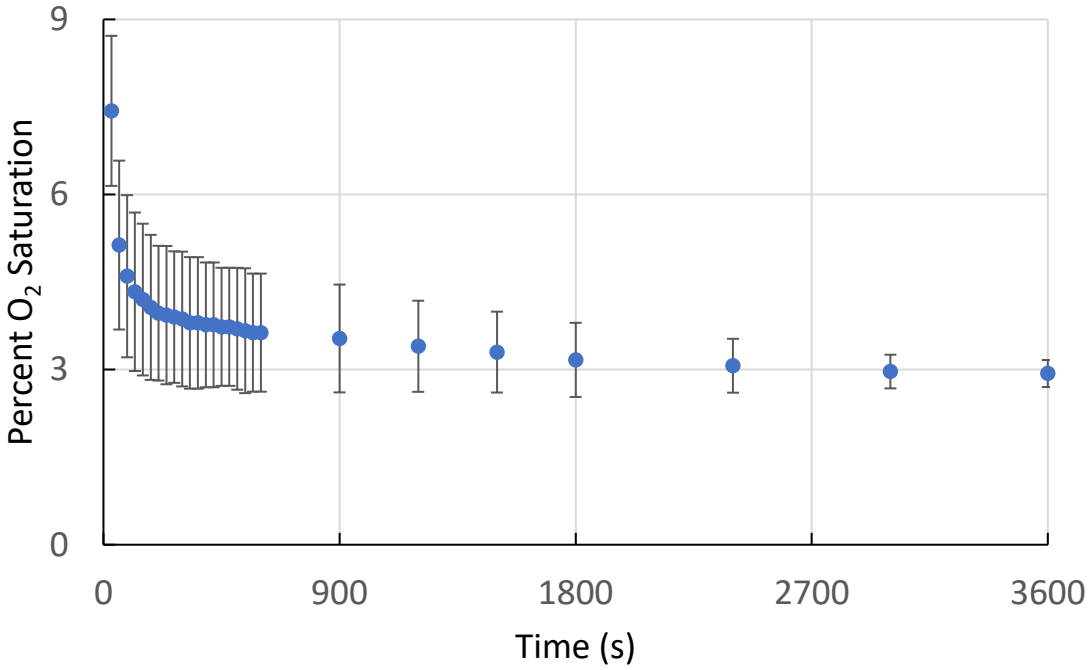

Figure 4.5. Minimum Percent O_2 Saturation Measurement for Clark-type Electrode. The minimum percent O_2 saturation for the Clark-type oxygen electrode was determined by removing all dissolved oxygen from the system. Dissolved O_2 was removed via the oxidation of 16.6 mM catechol at pH 12.0 in 50 mM phosphate buffer at 29.5°C. The high pH and high concentration of catechol were chosen to promote fast oxidation and ensure complete removal of dissolved O_2. The baseline reading was determined to be 2.9% ± 0.2% O_2 saturation after all O_2 was removed from the reaction solution. All O_2 saturation measurements were adjusted based on the baseline reading of 2.9% according to the following formula: Corrected % O_2 Saturation = 100 – (% O_2 Consumed * 1.0298)

4.3.4 Potentiometric Titration

Potentiometric titrations were performed to determine the pK_{a1} and pK_{a2} of 4-ethylcatechol using a Hanna Instruments HI2002-01 pH meter. The electrode was calibrated as previously described [35, 36]. Titrations were carried out in jacketed three-necked titration vessels at 25.0 ± 0.1 °C. Solutions were degassed with Ascarite-scrubbed argon and kept under a positive pressure of argon to prevent autoxidation. Standardized NaOH (0.0982 M) was incrementally added to a solution of 10 mM 4-ethylcatechol in 0.1 M NaCl background electrolyte. Acid dissociation constants were determined from the nonlinear refinement of the potentiometric titration data using Hyperquad2008 software (Figure 4.18) [37]. The pK_{a1} and pK_{a2} of 4-ethylcatechol are listed in Table 4.2.

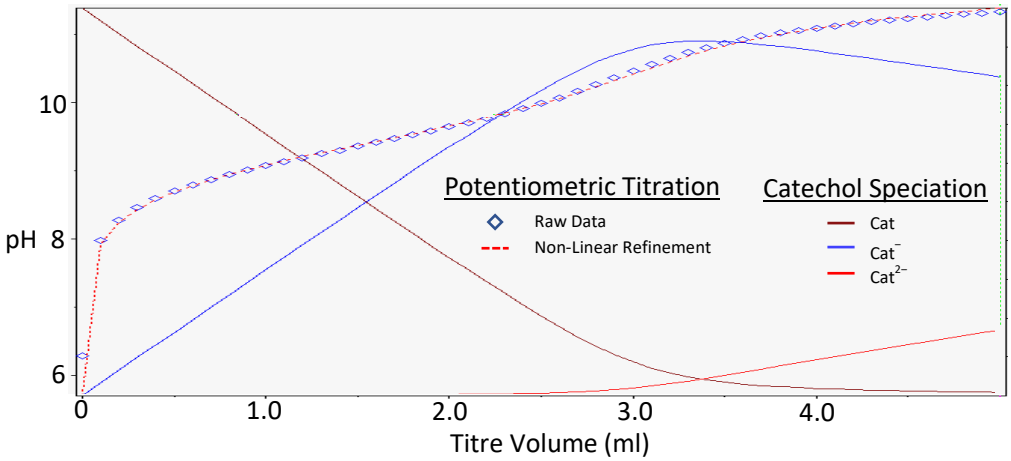

Figure 4.6. Potentiometric Titration and Speciation Diagram for 4-Ethylcatechol. The dashed red line corresponds to the Hyperquad2008 calculated non-linear fit. The relative concentrations of Cat, Cat^{-}, and Cat^{2-} were calculated by Hyperquad2008. The potentiometric titration of 4-ethylcatechol was done in triplicate. The average and standard deviation for the three experiments are shown in Table 4.2.

4.4 Results

4.4.1 Catechol Autoxidation: Order with Respect to O_2.

The kinetics of oxidation of catechol by O_2, under pseudo first-order conditions, with catechol in excess of O_2, was monitored by a Clark-type oxygen electrode in buffered aqueous solution as a function of $[O_2]$ from 1.76 x 10^{-4} M to 1.06 x 10^{-3} M (Figure 4.14). A plot of ln[initial rate] from the slopes of Figure 4.14 versus ln$[O_2]$ is linear with a slope of 0.96 ± 0.02, indicating that the rate of catechol autoxidation is first-order in O_2 (Figure 4.15).

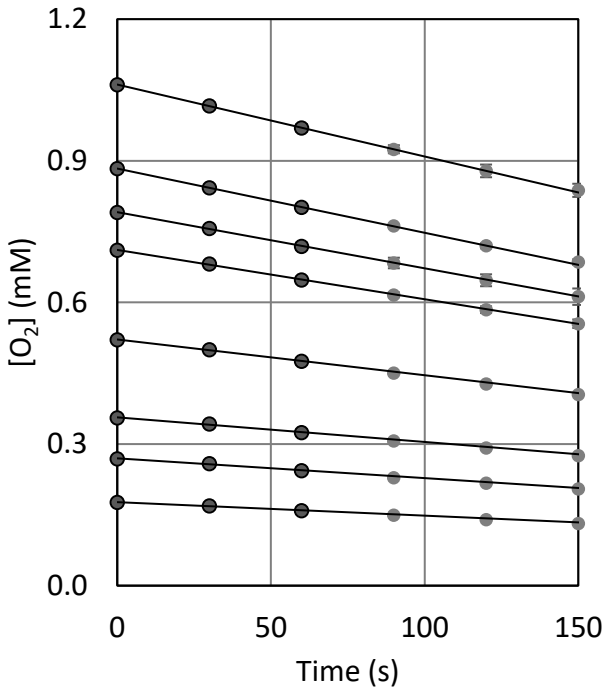

Figure 4.7. Dependence of rate of catechol oxidation on O_2 concentration. Reactions were carried out under pseudo first-order conditions in 50 mM phosphate buffer pH 8.5, at 29.5°C with 13.3 mM catechol, which is in excess of $[O_2]$. Each reaction at a defined initial O_2 concentration was carried out in triplicate. The initial O_2 concentrations were 1.06 mM, 0.883 mM, 0.790 mM, 0.710 mM, 0.521 mM, 0.356 mM, 0.269 mM, and 0.176 mM, as listed from top to bottom. The best fit lines were determined over the first 60 seconds of reaction (i.e., the first three data points of each kinetic run), which corresponds to no more than 10% consumption of $[O_2]$.

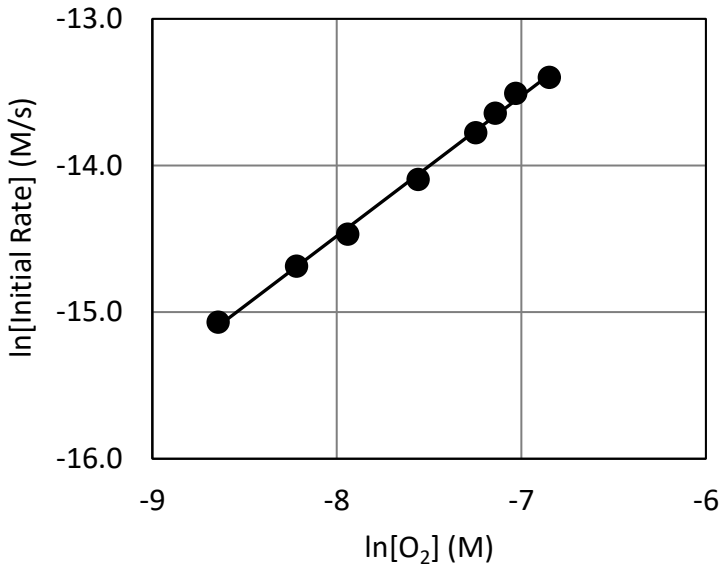

Figure 4.8. Catechol Autoxidation: Order with Respect to O_2. The plot of ln[initial rate] from the slopes of Figure 4.14 versus ln[O_2], is linear with a slope of 0.96 ± 0.02, indicating that the rate of catechol autoxidation is first-order in O_2.

4.4.2 Catechol Autoxidation: Effect of Catechol Concentration at pH 7.0

The kinetics of oxidation of catechol by O_2, under pseudo first-order conditions, with catechol in excess of O_2, was monitored by a Clark-type oxygen electrode in buffered aqueous solution as a function of [Catechol] from 1.66 x 10^{-2} M to 4.98 x 10^{-2} M (Figure 4.12). A plot of ln[initial rate] from the slopes of Figure 4.12 versus ln[Catechol] is linear with a slope of 1.00 ± 0.06, indicating that the rate of catechol autoxidation is first-order in catechol (Figure 4.13).

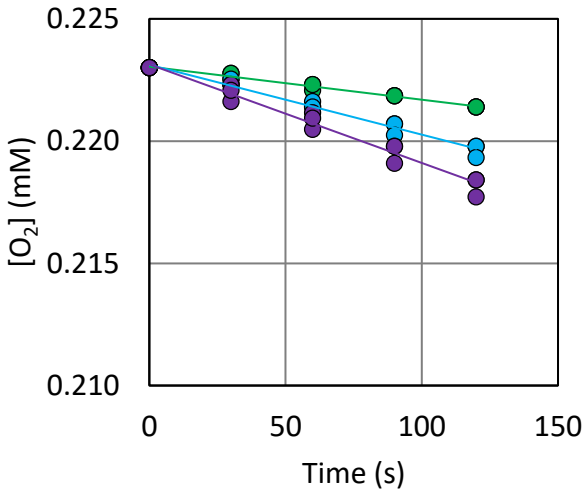

Figure 4.9. Dependence of rate of catechol oxidation on catechol concentration. Reactions were carried out under pseudo first-order conditions in 50 mM phosphate buffer pH 7.0, at 29.5°C with variable catechol concentration, which is in excess of $[O_2]$. Each reaction at a defined catechol concentration was carried out in triplicate. The initial catechol concentrations were 16.6 mM, 33.2 mM, and 49.8 mM, as listed from top to bottom. The best fit lines were determined over the first 120 seconds of reaction (i.e., the first five data points), which corresponds to less than 10% consumption of $[O_2]$.

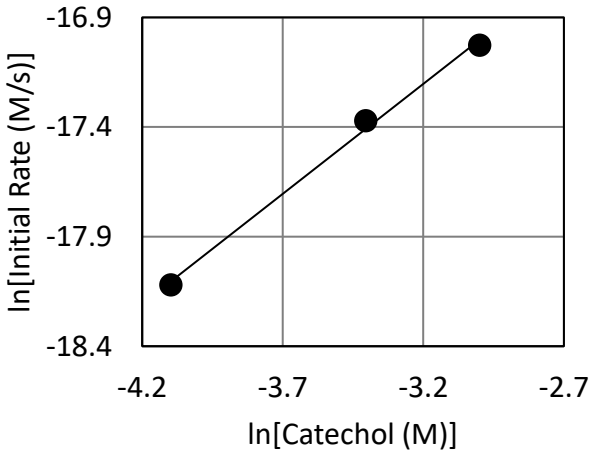

Figure 4.10. Catechol Autoxidation: Order with Respect to Catechol. The plot of ln[initial rate] from the slopes of Figure 4.12 versus ln[Catechol], is linear with a slope of 1.00 ± 0.06 and an R2 = 0.996, indicating that the rate of catechol autoxidation is first-order in O_2.

4.4.3 Catechol Autoxidation versus pH and Catechol Concentration.

The pseudo first-order rate constant for the autoxidation of catechol was obtained with Dynafit software (version 4.04.087, Biokin Ltd.) from the initial rate of O_2 consumption, under pseudo first-order conditions, in which the catechol concentration was in excess of O_2. Disproportionation of the superoxide intermediate produces O_2 [38] and could lead to slight non-linearity of $\ln[O_2]$ versus time plots (Appendix A.1-A.7). Therefore, only the initial linear portion of the $\ln[O_2]$ versus time plot was considered in determining pseudo first-order rate constants. This initial linear portion was converted to a plot of $[O_2]$ versus time before Dynafit software, version 4.05.087 (Biokin Ltd.), was used to determine the pseudo first-order rate constants by non-linear least squares analysis (Table 4.1, Appendix A.1).

Table 4.1. Kinetics Data Summary for Catechol Oxidation by O_2. See Appendix A.1 for supporting data.

pH	Conc. (mM)	Pseudo 1st Order k_{obs} (s^{-1})	Standard Error	R^2	2nd Order k_{obs} ($M^{-1}s^{-1}$)	Avg. 2nd Order k_{obs} ($M^{-1}s^{-1}$)	Standard Deviation
7	16.6	6.05E-05	5.50E-07	0.975	3.64E-03	3.96E-03	2.83E-04
	33.2	1.39E-04	1.60E-06	0.965	4.19E-03		
	49.8	2.02E-04	1.70E-06	0.963	4.06E-03		
7.5	9.96	1.69E-04	1.60E-06	0.94	1.69E-02	1.49E-02	2.00E-03
	23.3	3.44E-04	2.50E-06	0.986	1.48E-02		
	33.2	4.30E-04	3.50E-06	0.995	1.29E-02		
8	6.64	4.44E-04	1.70E-06	0.998	6.68E-02	6.59E-02	1.99E-03
	13.3	8.96E-04	5.20E-06	0.993	6.73E-02		
	19.9	1.27E-03	5.30E-06	0.998	6.37E-02		
8.5	3.32	7.34E-04	5.80E-06	0.985	2.21E-01	2.17E-01	4.32E-03
	6.64	1.44E-03	1.60E-05	0.963	2.16E-01		
	9.96	2.12E-03	1.30E-05	0.987	2.13E-01		
9	3.32	2.11E-03	5.30E-06	0.983	6.36E-01	5.79E-01	6.71E-02
	3.32	2.12E-03	5.30E-06	0.994	6.39E-01		
	4.98	2.63E-03	5.20E-06	0.999	5.28E-01		
	6.64	3.42E-03	1.40E-05	0.996	5.15E-01		

The oxidation of catechol is strongly pH-dependent over the pH range investigated, with the pseudo first-order rate constant increasing linearly with catechol concentration for a given pH (Figure 4.16). To obtain the observed second-order rate constant at a given pH, the pseudo first-order rate constants measured at that pH were divided by the catechol concentration and averaged (Table 4.1). The observed second-order rate constants show a strong pH-dependence, with a significantly greater rate constant at pH 9.0 compared to pH 7.0. This pH-dependence is consistent with previous results of catechol-containing compounds in which higher pH led to faster rates of oxidation [16-18].

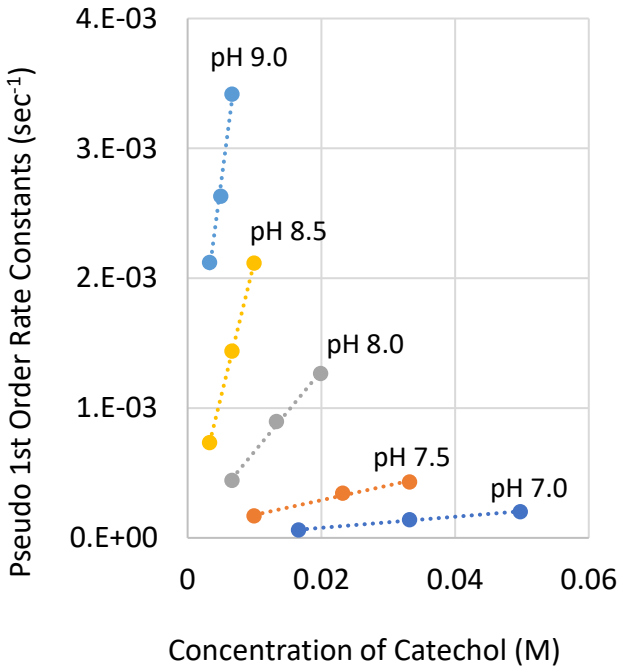

Figure 4.11. Concentration and pH-Dependence of Catechol Autoxidation. The kinetics of O_2 consumption in the presence of catechol was carried out in triplicate for each catechol concentration at the specified pH values. All reactions were run at 29.5°C in 50 mM Chelex-treated buffer.

The plot of the observed second-order rate constant (Table 4.1) versus [H+] in Figure 4.17 was found to fit to a mechanism incorporating both mono-deprotonated catechol (Cat^{-}) and di-deprotonated catechol (Cat^{2-}) species in which both species are oxidized by O_2 (Scheme 4.1). The fit of observed second-order rate constants versus [H+] (Figure 4.17) was done using Igor Pro 7 software (WaveMetrics, Inc.).

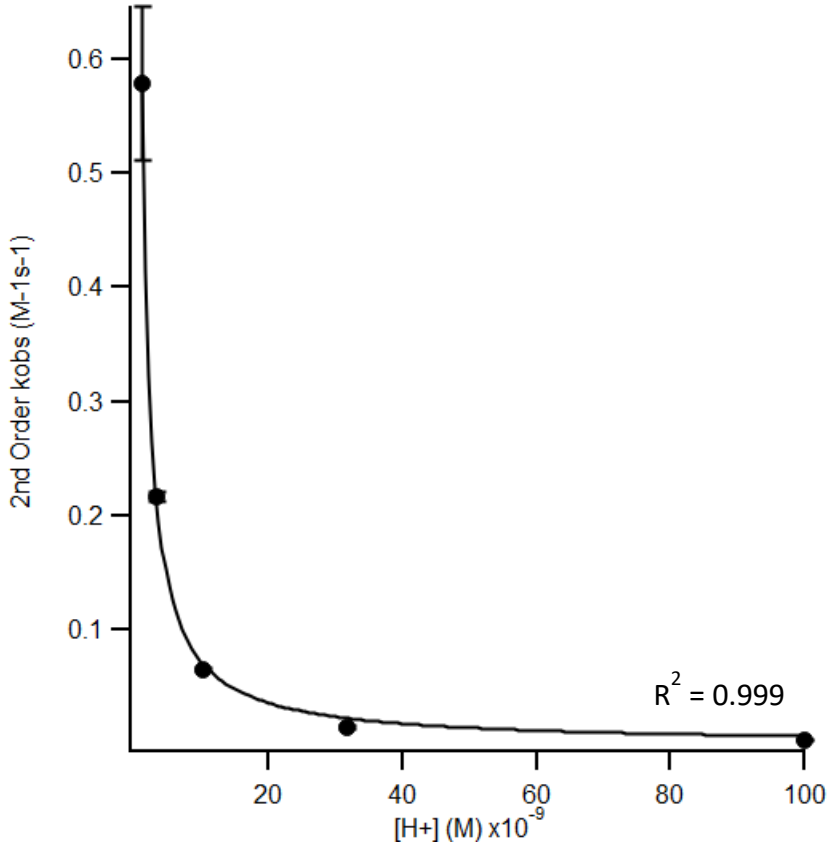

Figure 4.12. Observed Second-Order Rate Constants versus $[H^+]$ for Catechol Autoxidation. Igor Pro 7 was used to fit Eqn. (1) to the plot of second-order rate constant for the oxidation of catechol by O_2 versus $[H^+]$ using non-linear least squares analysis. This analysis provides the fit pK_{a1}, fit pK_{a2}, k_1, and k_2 values in Table 4.2. See Table 4.1 for observed second-order rate constants.

Scheme 4.1. Proposed Mechanism for the pH-Dependent Oxidation of Catechol by O_2.

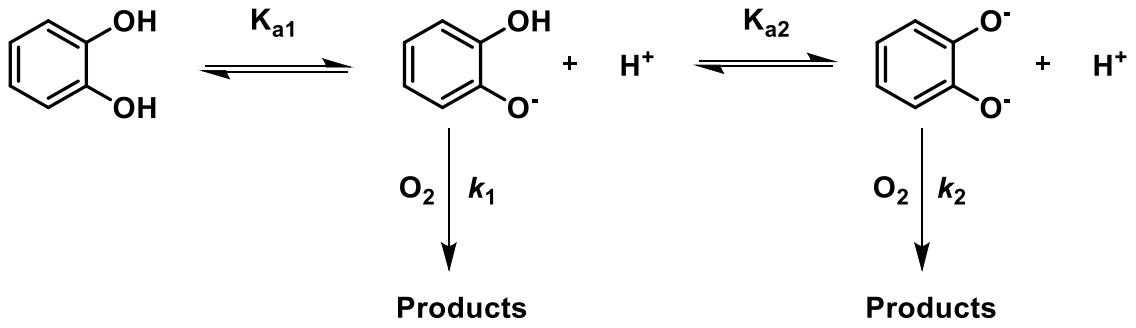

The expression for k_{obs} derived from Scheme 4.1 is

$$k_{obs} = \frac{K_1(k_1[H^+]+k_2K_2)}{([H^+]^2+K_1[H^+]+K_1K_2)} \quad (1)$$

where k_1 is the pH-independent second-order rate constant for the reaction of Cat^- with O_2, k_2 is the pH-independent second-order rate constant for the reaction of Cat^{2-} with O_2, K_1 is the first acid dissociation constant, and K_2 is the second acid dissociation constant of catechol. The catechol pK_a values predicted by the fit (pK_{a1}, 9.49; pK_{a2}, 13.03) are in agreement with average literature pK_a values (Table 4.2). The pH-independent second-order rate constant for the oxidation of Cat^{2-} (i.e., k_2) is about three orders of magnitude larger than the pH-independent second-order rate constant for the oxidation of Cat^- by O_2 (k_1) (Table 4.2), indicating even small amounts of Cat^{2-} may dominate the rate of the reaction.

Table 4.2. Kinetic Parameters for the Autoxidation of Substituted Catechols.

Compound	4-Methyl-catechol	4-Ethyl-catechol	Catechol	4-Chloro-catechol	3,4-DHBA	2,3-DHBA
Experimental pH	6.0-8.0	6.5-8.0	7.0-9.0	7.0-8.5	9.0-10.5	10.0-12.0
k_1 ($M^{-1}s^{-1}$)	8.81	3.09	2.27	0.65	0.04	0.19
k_2 ($M^{-1}s^{-1}$)	55778	12176	1670	1266	64.7	16.3
Fit pK_{a1}	9.60	9.54	9.49	8.83	8.26	10.73
Fit pK_{a2}	12.54	12.17	13.03	12.16	12.55	13.00
Substituent	p-Me	p-Et	p-H	p-Cl	p-COOH	-
σ+	-0.31	-0.3	0	0.11	0.42	-
Avg. Lit. pK_{a1}	9.59 ± 0.12	9.41 ± 0.02	9.34 ± 0.10	8.57 ± 0.12	8.74 ± 0.10	10.04 ± 0.13
Avg. Lit. pK_{a2}	12.54 ± 0.56	12.08 ± 0.03	13.03 ± 0.41	12.16 ± 0.55	12.55 ± 0.58	-
pK_a Refs.	[39-42]	this work	[7, 43-47]	[40, 48-50]	[42, 43, 51-53]	[7, 53]

Literature pK_a values are the average and standard deviation from multiple literature sources. Literature pKa values were not available for 4-ethylcatechol. 4-Ethylcatechol pK_a values were determined experimentally by potentiometric titration (Figure 4.18). The values for k_1, k_2, pk_{a1}, and pk_{a2} were determined by the non-linear least squares fit of Eqn. (1) to plots of observed second-order rate constant versus $[H^+]$ for each substituted catechol (Figure 4.25). pK_{a1} refers to the first hydroxyl pK_a and pK_{a2} refers to the second hydroxyl pK_a. The values for σ+ were taken from [54].

4.4.4 Substituent Effects in Catechol Autoxidation

The effect of catechol substituents in the 4-position of the aromatic ring on the rate of catechol autoxidation was investigated for both electron donating alkyl groups (methyl, and ethyl) and electron withdrawing groups (chloro and carboxyl). The rate of oxidation of the

substituted catechol compounds by O_2 was also investigated as a function of pH and the concentration of the substituted catechol (Tables 4.3, Appendix A.2-A.7). Like catechol, plots of the observed second-order rate constant versus $[H^+]$ for the substituted catechols (Figure 4.25) were fit to Eqn. (1).

Oxidation reactions in which 4-tert-butylcatechol is oxidized by O_2 were also attempted. However, 4-tert-butylcatechol has low solubility and mixing within the reaction solution was clearly visible for several minutes upon initiation of the autoxidation reaction. This long mixing time prevented meaningful analysis of the rate data and therefore the results of 4-tert-butylcatechol autoxidation were not included.

For all of these substituted catechols, the second-order rate constants for the autoxidation of substituted Cat^{2-} (k_2) are several orders of magnitude larger than the second-order rate constants for the autoxidation of substituted Cat^- (k_1), as was also observed for the oxidation of unsubstituted catechol. The predicted pK_a values determined from the fit of Eqn. (1) to the second-order rate constant versus $[H^+]$ plots (Figure 4.25) are generally in agreement with the average literature pK_a values (Table 4.2). The O_2 consumption data for catechol and substituted catechols supports a mechanism in which the pH-dependence of autoxidation is primarily determined by the pK_a values of the hydroxyl groups.

Table 4.3. Kinetics Data Summary for p-Me, p-Et, and p-Cl. See Appendix A.2-A.4 for supporting data

Compound	pH	Conc. (mM)	Pseudo 1st Order k_{obs} (sec^{-1})	Stadnard Error	R^2	2nd Order k_{obs} ($M^{-1}s^{-1}$)	Average 2nd Order k_{obs} ($M^{-1}s^{-1}$)	Standard Deviation
4-Methylcatechol	6.0	13.3	8.79E-05	7.6E-07	0.955	6.61E-03	5.54E-03	9.51E-04
(p-Me)		26.6	1.39E-04	8.8E-07	0.984	5.23E-03		
		39.9	1.91E-04	1.9E-06	0.986	4.79E-03		
	7.0	13.3	7.06E-04	6.0E-06	0.996	5.31E-02	4.78E-02	4.75E-03
		19.9	9.24E-04	7.6E-06	0.991	4.64E-02		
		26.6	1.17E-03	1.0E-05	0.995	4.39E-02		
	7.5	6.64	2.74E-04	2.4E-06	0.965	4.13E-02	8.27E-02	3.59E-02
		9.96	1.03E-03	6.3E-06	0.996	1.03E-01		
		13.3	1.38E-03	9.2E-06	0.996	1.04E-01		
	8.0	3.32	7.61E-04	3.7E-06	0.992	2.29E-01	2.52E-01	2.54E-02
		6.64	1.65E-03	6.6E-06	0.997	2.48E-01		
		13.3	3.72E-03	3.0E-05	0.995	2.80E-01		
	9.0	3.32	1.68E-02	1.4E-04	0.997	5.05E+00	5.05E+00	
4-Ethylcatechol	6.5	16.6	1.52E-04	1.1E-06	0.966	9.16E-03	7.52E-03	1.52E-03
(p-Et)		33.2	2.41E-04	4.4E-06	0.980	7.26E-03		
		49.8	3.06E-04	1.9E-06	0.967	6.14E-03		
	7.0	16.6	3.65E-04	2.0E-06	0.988	2.20E-02	1.79E-02	3.89E-03
		33.2	5.75E-04	3.0E-06	0.988	1.73E-02		
		49.8	7.10E-04	3.6E-06	0.984	1.43E-02		
	7.5	9.96	5.59E-04	2.3E-06	0.993	5.61E-02	4.99E-02	8.42E-03
		16.6	8.83E-04	3.7E-06	0.996	5.32E-02		
		33.2	1.34E-03	4.5E-06	0.985	4.03E-02		
	8.0	3.32	4.24E-04	1.8E-06	0.986	1.28E-01	1.10E-01	1.56E-02
		9.96	1.05E-03	2.3E-06	0.999	1.06E-01		
		16.6	1.62E-03	8.2E-06	0.998	9.75E-02		
	9.0	3.32	8.35E-03	5.3E-05	0.997	2.52E+00	2.52E+00	
4-Chlorocatechol	7.0	16.6	3.13E-04	8.5E-07	0.997	1.89E-02	1.78E-02	1.10E-03
(p-Cl)		23.3	3.89E-04	1.7E-06	0.978	1.67E-02		
		33.2	5.95E-04	5.3E-06	0.986	1.79E-02		
	7.5	9.96	4.80E-04	3.6E-06	0.968	4.82E-02	4.70E-02	1.63E-03
		16.6	7.92E-04	4.6E-06	0.995	4.77E-02		
		23.3	1.05E-03	5.0E-06	0.999	4.51E-02		
	8.0	9.96	1.00E-03	2.6E-06	0.999	1.00E-01	9.49E-02	5.40E-03
		16.6	1.57E-03	6.4E-06	0.997	9.46E-02		
		23.3	2.09E-03	1.2E-05	0.996	8.96E-02		
	8.5	3.32	9.57E-04	4.4E-06	0.995	2.88E-01	2.91E-01	5.18E-03
		6.64	1.91E-03	5.5E-06	0.999	2.88E-01		
		9.96	2.96E-03	8.3E-06	0.999	2.97E-01		
	9.0	3.32	3.01E-03	1.1E-04	0.976	9.07E-01	9.07E-01	

Table 4.3 Continued. Kinetics Data Summary for p-COOH, 2,3-DHBA, and 5-Sulfo-2,3-DHBA. See Appendix A.5-A.7 for supporting data.

Compound	pH	Conc. (mM)	Pseudo 1st Order k_{obs} (sec^{-1})	Standard Error	R^2	2nd Order k_{obs} ($M^{-1}s^{-1}$)	Average 2nd Order k_{obs} ($M^{-1}s^{-1}$)	Standard Deviation
3,4-DHBA (p-COOH)	9.0	3.32	9.67E-05	3.8E-07	0.995	2.91E-02	2.94E-02	3.59E-03
		4.98	1.29E-04	7.7E-07	0.930	2.60E-02		
		6.64	2.20E-04	3.2E-06	0.925	3.31E-02		
	9.5	3.32	6.19E-04	1.9E-06	0.995	1.86E-01	1.54E-01	3.11E-02
		4.98	7.48E-04	5.7E-06	0.971	1.50E-01		
		6.64	8.26E-04	2.7E-06	0.995	1.24E-01		
	10.0	3.32	5.84E-04	1.7E-05	0.996	1.76E-01	1.55E-01	1.96E-02
		4.98	6.85E-04	2.3E-06	0.989	1.38E-01		
		6.64	9.97E-04	1.6E-05	0.939	1.50E-01		
	10.5	3.32	2.30E-03	3.4E-05	0.946	6.93E-01	6.20E-01	8.07E-02
		4.98	3.15E-03	3.2E-05	0.994	6.33E-01		
		6.64	3.54E-03	4.1E-05	0.995	5.33E-01		
2,3-DHBA	10.0	6.64	7.64E-05	1.5E-06	0.915	1.15E-02	1.14E-02	3.32E-04
		9.96	1.17E-04	1.2E-06	0.966	1.17E-02		
		13.3	1.48E-04	2.9E-06	0.935	1.11E-02		
	11.0	3.32	3.00E-04	5.5E-06	0.912	9.04E-02	8.68E-02	7.00E-03
		4.98	4.55E-04	7.3E-06	0.909	9.14E-02		
		6.64	5.23E-04	6.7E-06	0.952	7.88E-02		
	11.5	3.32	3.29E-03	3.0E-05	0.989	9.91E-01	7.76E-01	1.88E-01
		4.98	3.47E-03	3.0E-05	0.967	6.97E-01		
		6.64	4.26E-03	6.0E-05	0.928	6.42E-01		
	12.0	3.32	5.10E-03	9.0E-05	0.977	1.54E+00	1.54E+00	2.31E-02
		4.15	6.51E-03	9.5E-05	0.974	1.57E+00		
		4.98	7.59E-03	1.1E-04	0.991	1.52E+00		
5-Sulfo-2,3-DHBA	12.0	3.32	7.76E-05	4.9E-06	0.996	2.34E-02	1.18E-02	1.02E-02
		13.3	9.79E-05	3.2E-06	0.999	7.36E-03		
		26.6	1.21E-04	3.5E-06	0.999	4.55E-03		

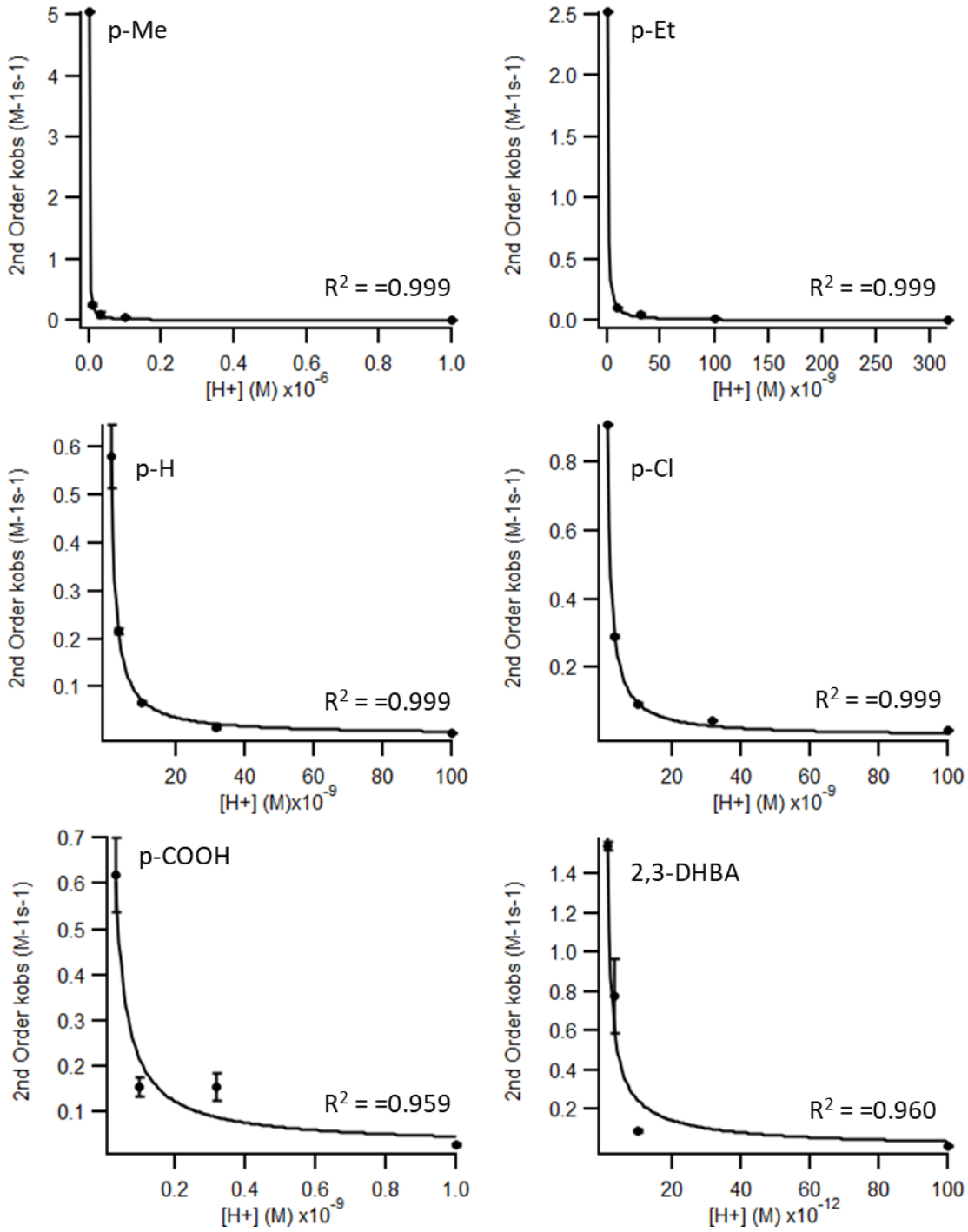

Figure 4.13. Observed Second-Order Rate Constants versus $[H^+]$ for the Oxidation of Catechol and Substituted Catechol by O_2. Igor Pro 7 (Wavemetrics Inc.) was used to fit Eqn. (1) to the plot of observed second-order rate constant for the oxidation of catechol or substituted catechol by O_2 versus $[H^+]$ using non-linear least squares analysis. This analysis provides the fit pK_{a1}, fit pK_{a2}, k_1, and k_2 values in Table 4.2. See Table 4.1 and Table 4.3 for observed second-order rate constants.

The pH-independent second-order rate constant for the oxidation of Cat^{-}, k_1, and the pH-independent second-order rate constant for the oxidation of Cat^{2-}, k_2, both show a strong dependence on the nature of the catechol substituent. Hammett correlations have been used to analyze the effect of substituents on the reactivity of compounds in a wide range of organic and biological reactions [54-56]. The substituent constant $\sigma+$ has been effective in correlating many radical reactions of organic compounds [55]. A plot of $\log(k_{1,X}/k_{1,H})$ versus $\sigma+$ is linear with a $\rho+$ value of -2.84 (Figure 4.26), where $k_{1,H}$ is the pH-independent second-order rate constant of Cat^{-} and $k_{1,X}$ is the pH-independent second-order rate constant of substituted Cat^{-} (Table 4.2). The plot of $\log(k_{2,X}/k_{2,H})$ versus $\sigma+$ is also linear with a $\rho+$ value of -3.55 (Figure 4.26), where $k_{2,H}$ is the pH-independent second-order rate constant of Cat^{2-} and $k_{2,X}$ is the pH-independent second-order rate constant of substituted Cat^{2-} (Table 4.2). These second-order rate constants were obtained from the fit of Eqn. (1) to plots of observed second-order rate constant versus $[H^{+}]$ (Figure 4.25).

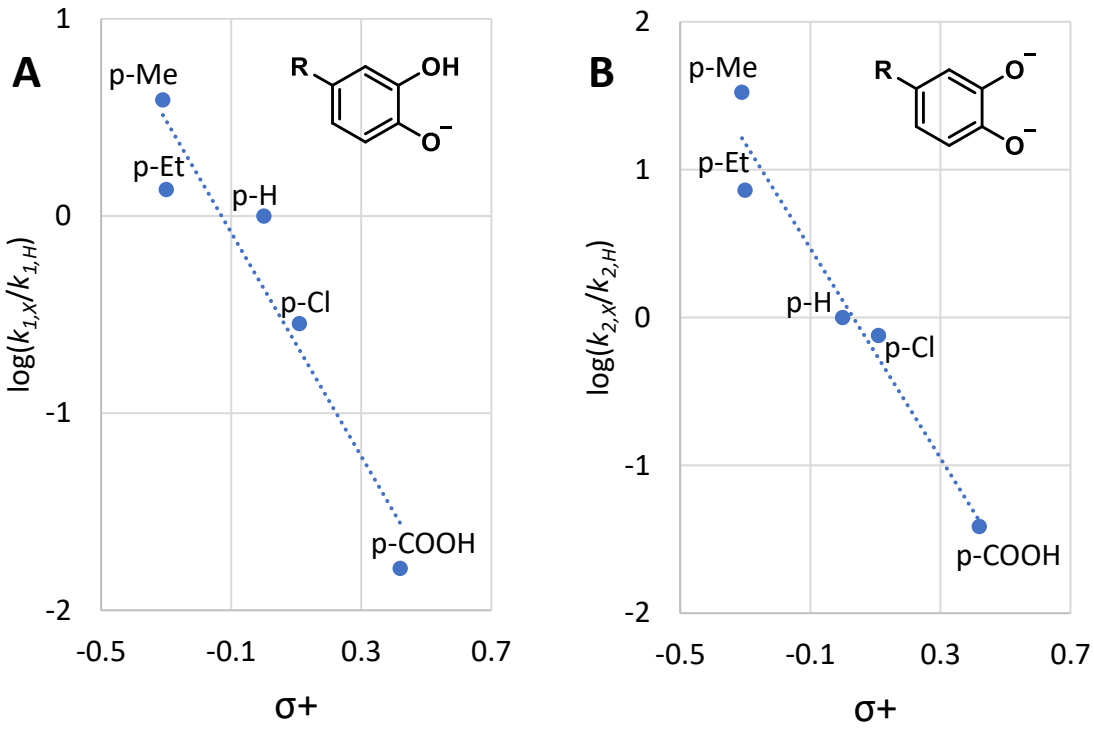

Figure 4.14. Hammett Correlation for the Autoxidation of Substituted Catechol. (A) The Hammett correlation for the autoxidation of substituted Cat^{-} is a plot of $\log(k_{1,H}/k_{1,X})$ versus the substituent constant $\sigma+$ that is linear with a slope of -2.85 and a R^2 of 0.90. (B) The Hammett correlation for the autoxidation of substituted Cat^{2-} is a plot of $\log(k_{2,H}/k_{2,X})$ versus the substituent constant $\sigma+$ that is linear with a slope of -3.55 and a R^2 of 0.95. Data points are labeled as follows: p-Me is 4-methylcatechol, p-Et is 4-ethylcatechol, p-H is catechol, p-Cl is 4-chlorocatechol, and p-COOH is 3,4-DHBA.

The linearity of the Hammett correlation implies each substituted catechol autoxidizes via the same mechanism [56-58]. The negative $\rho+$ value suggests that electron withdrawing groups sequester electron density away from the hydroxyls and aromatic ring through induction, field effects, and/or resonance [56], hindering the initial oxidation of catechol and reduction of O_2. Conversely, electron donating groups provide additional electron density to the aromatic ring of catechol, increasing the autoxidation rate. Interestingly, the Hammett plot for the autoxidation of substituted Cat^{2-} has a $\rho+$ that is greater than the $\rho+$

from the Hammett plot for the autoxidation of substituted Cat^{-}, indicating that Cat^{2-} is more susceptible to substituent effects than Cat^{-}.

4.4.5 Autoxidation of 2,3-DHBA

The substituent constant *σ+* only applies to para-substituents and therefore 2,3-DHBA and 5-sulfo-2,3-DHBA cannot be included in the Hammett correlation [59]. A selection of substituted catechols was chosen to qualitatively illustrate the impact of changing the position and number of substituents on catechol autoxidation kinetics (Figure 4.27).

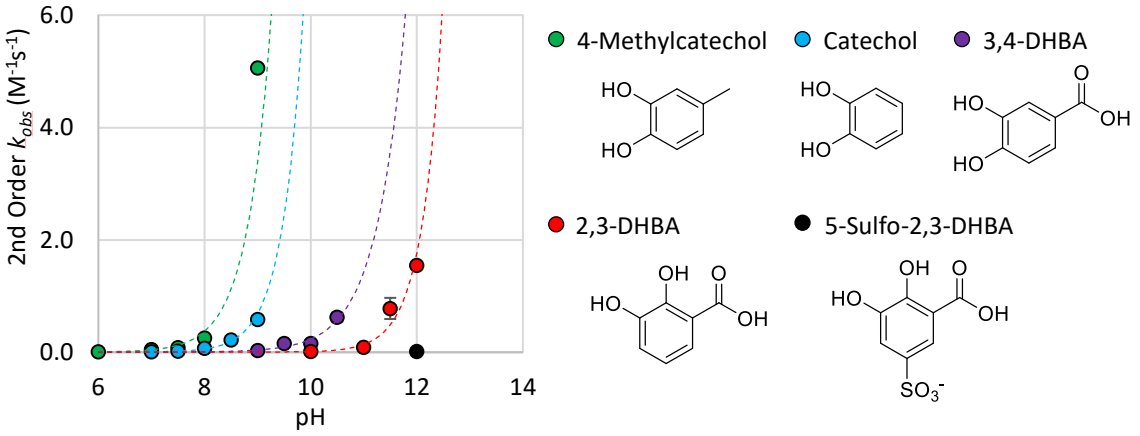

Figure 4.15. Effect of Number and Position of Substituents on Catechol Autoxidation. The observed second-order rate constant was plotted versus pH for catechol and a selection of substituted catechols. The plots were fit with an exponential regression.

The trend in autoxidation kinetics over 4-methylcatechol, catechol, and 3,4-DHBA correlates with the electron donating or withdrawing nature of the substituent (Figure 4.27). However, the difference in autoxidation kinetics between 3,4-DHBA and 2,3-DHBA cannot be solely explained by the strength of the electron withdrawing group. Variation of the substituent position on the aromatic ring will produce different field, inductive, and resonance effects [56]. Also, the proximity of the 2-hydroxyl to the carbonyl in 2,3-DHBA allows for the formation of an intramolecular hydrogen bond. IR experiments on salicylic acid have confirmed the presence of this type of intramolecular hydrogen bond [60, 61] and these intramolecular hydrogen bonds have also been proposed to exist in the siderophore, enterobactin [6].

Hydrogen bonding can have a significant impact on oxidizability. Density functional theory calculations show that a single hydrogen bond between a water molecule or amino acid and plastoquinone increases the reduction potential by ~100-200 mV [62]. For 2,3-DHBA, intramolecular hydrogen bonding raises pK_{a1} to 10.04—compared to 8.74 for 3,4-DHBA—and reduces the autoxidation rate. Sulfonation of 2,3-DHBA in the 5-position on the aromatic ring adds an additional electron withdrawing group and the sum of the electron withdrawing effects suppresses autoxidation to such an extent that it is barely detectable at pH 12.0 (Figure 4.27).

4.5 Discussion

4.5.1 pH Dependence of Catechol Autoxidation

The pH-dependence of catechol autoxidation correlates with the pK_a values of catechol. While the neutral catechol compound is not particularly reactive with O_2, Cat^{-}, and to a greater extent Cat^{2-}, are susceptible to oxidation by O_2. This reactivity is consistent with the fit of the kinetic data to the mechanism in Scheme 4.1.

At neutral and moderately basic pH conditions, the fits of Eqn. (1) yielded high correlation coefficients and fit pK_a values in agreement with average literature pK_a values. The fit of Eqn. (1) for catechol and substituted catechol autoxidation data suggests that at neutral and moderately basic conditions the pH-dependence of autoxidation is primarily determined as described in Scheme 4.1.

4.5.2 Substituent Effect in Catechol Autoxidation and the Design of Wet Adhesives

Catechol is a hydrogen bond donor and imparts adhesive capabilities to a range of natural and synthetic materials [1, 2, 63]. On the other hand, the corresponding orthoquinone is reactive and capable of forming covalent crosslinks that improve cohesion within materials [22]. Depending on the intended application of a catechol-containing compound, either interfacial adhesion or internal cohesion may be the desired role for the

catechol. It is therefore of interest to understand how to influence catechol autoxidation kinetics through substituent effects.

4-Methylcatechol is a mimic of the Dopa present in mussel foot proteins (Mfps), given the same 3,4-dihydroxy orientation and the electron donating alkyl group. Neither Dopa nor dopamine could be investigated directly because the Dopa-quinone and dopamine-quinone oxidation products both undergo an intramolecular cyclization reaction with the amine substituent. The cyclization reaction converts the quinone moiety back to its initial catechol form, which is then susceptible to subsequent oxidation. In proteins, the amine substituent of Dopa is part of the peptide backbone and does not undergo cyclization with Dopa-quinone. Therefore, 4-methylcatechol is a better small molecule mimic for the oxidation of Dopa in proteins than the Dopa monomer or dopamine.

2,3-DHBA shares the same 2,3 hydroxyl positioning and adjacent carbonyl found in many siderophores [6, 64]. Comparison of the autoxidation of 4-methylcatechol and 2,3-DHBA (Figure 4.27) shows that 2,3-DHBA is more oxidation resistant than the Dopa-mimetic 4-methylcatechol. Enhancing the oxidation resistance of catechol through electron withdrawing groups has been shown to dramatically improve the interfacial interactions of wet adhesives at elevated pH [65]. Siderophore analogs—containing a 2,3-dihydroxy catechol with an electron withdrawing amide—strongly adhere to mica in the pH 3.3-7.5 range (Figure 2.36), significantly outperforming their Dopa-containing Mfp counterparts at near-neutral pH and confirming that the adhesive capability of catechol extends beyond Dopa [65, 66].

Catechol must resist oxidation and remain in a fully protonated form to maximize bidentate interfacial interactions. As predicted by Bell Theory, the bidentate hydrogen bonds that form between catechol and a mineral oxide surface will have a lifetime that is 10^6 times longer than the singly deprotonated, monodentate form of catechol [29, 31]. Electron withdrawing groups lead to slower catechol autoxidation kinetics, but typically also reduce the first hydroxyl pK_a of catechol [54, 56]. To maximize adhesive interfacial interactions, care must be taken to select an electron withdrawing group that significantly reduces catechol autoxidation kinetics, yet retains a pK_{a1} higher than the pH conditions of the intended application. Interactions between cysteine and lysine or arginine lower the pK_a of cysteine in NrdH-redoxins [67]. Context-dependent factors may also influence the pK_a of catechol and should be considered when designing catechol-containing functional materials.

Cohesive strength within mussel adhesive plaques results in part from oxidation-induced Dopa crosslinking [15, 22, 31]. The use of Dopa in mussel adhesive plaques for both interfacial adhesion and internal cohesion requires precise spatial and temporal control of catechol redox chemistry during plaque deposition and maturation. Reproduction of this precise redox control in a synthetic wet adhesive is a seemingly intractable obstacle. Use of separate strategies for interfacial adhesion and internal cohesion that can be independently optimized may simplify wet adhesive design. One such strategy for interfacial adhesion is the use of oxidation resistant catechol (i.e. catechol functionalized with an electron withdrawing group) as the adhesive moiety. Conversely, cohesion via crosslinking of catechol oxidation products can be promoted through use of

catechol functionalized with an electron donating group. Analysis of substituent effects through Hammett correlation and the pH-dependence of catechol autoxidation allows for selection of functionalized catechols with redox properties optimized for a given application at a given pH.

4.6 References

1 Sedo J, Saiz-Poseu J, Busque F and Ruiz-Molina D (2013) Adv Mater 25:653-701

2 Lee BP, Messersmith PB, Israelachvili JN and Waite JH (2011) Annu Rev Mater Res 41:99-132

3 Butler A and Theisen RM (2010) Coord Chem Rev 254:288-296

4 Vraspir JM and Butler A (2009) Ann Rev Mar Sci 1:43-63

5 Sandy M and Butler A (2009) Chem Rev 109:4580-4595

6 Raymond KN, Dertz EA and Kim SS (2003) Proc Natl Acad Sci U S A 100:3584-3588

7 Avdeef A, Sofen SR, Bregante TL and Raymond KN (1978) J Am Chem Soc 100:5362-5370

8 Harris WR, Carrano CJ, Cooper SR, Sofen SR, Avdeef AE, McArdle JV and Raymond KN (1979) J Am Chem Soc 101:6097-6104

9 Loomis LD and Raymond KN (1990) Inorg Chem 30:906-911

10 Hickford SJH, Kupper FC, Zhang G, Carrano CJ, Blunt JW and Butler A (2004) J Nat Prod 67:1897-1899

11 Pfleger BF, Lee JY, Somu RV, Aldrich CC, Hanna PC and Sherman DH (2007) Biochemistry 46:4147-4157

12 Israelachvili JN (2011) Intermolecular and surface forces. Academic Press, San Diego

13 Lu Q, Danner E, Waite JH, Israelachvili JN, Zeng H and Hwang DS (2013) J R Soc Interface 10:20120759

14 Hwang DS, Wei W, Rodriguez-Martinez NR, Danner E and Waite JH (2013) In: H. Zeng (ed) Polymer adhesion, friction,a nd lubrication. John Wiley & Sons, Inc., Hoboken, NJ,

15 Maier GP and Butler A (2017) J Biol Inorg Chem, doi 10.1007/s00775-017-1451-6

16 Mochizuki M, Yamazaki S, Kano K and Ikeda T (2002) Biochim Biophys Acta 1569:35-44

17 Roginsky V and Barsukova T (2000) Journal of the Chemical Society, Perkin Transactions 2, doi 10.1039/b000538j:1575-1582

18 Tratnyek P and Hologne J (1991) Environ Sci Technol 25:1596-1604

19 Joslyn MA and Branch GEK (1935) J Am Chem Soc 57:1779-1785

20 Nicklisch SC and Waite JH (2012) Biofouling 28:865-877

21 Li G, Zhang H, Sader F, Vadhavkar N and Njus D (2007) Biochemistry 46:6978-6983

22 Yang J, Cohen Stuart MA and Kamperman M (2014) Chem Soc Rev 43:8271-8298

23 Hwang DS, Zeng H, Masic A, Harrington MJ, Israelachvili JN and Waite JH (2010) J Biol Chem 285:25850-25858

24 Andersen SO (2010) Insect Biochem Mol Biol 40:166-178

25 Hopkins TL, Morgan TD, Aso Y and Kramer KL (1982) Science 217:364-366

26 Lee K, Prajatelistia E, Hwang DS and Lee H (2015) Chemistry of Materials 27:6478-6481

27 Miserez A, Rubin D and Waite JH (2010) J Biol Chem 285:38115-38124

28 Miserez A, Schneberk T, Chengjun S, Frank CW and Waite JH (2008) Science 319:1816-1819

29 Yu J, Wei W, Danner E, Israelachvili JN and Waite JH (2011) Adv Mater 23:2362-2366

30 Nicklisch SC, Das S, Martinez Rodriguez NR, Waite JH and Israelachvili JN (2013) Biotechnol Prog 29:1587-1593

31 Yu J, Wei W, Danner E, Ashley RK, Israelachvili JN and Waite JH (2011) Nat Chem Biol 7:588-590

32 Martinez Rodriguez NR, Das S, Kaufman Y, Israelachvili JN and Waite JH (2015) Biofouling 31:221-227

33 Sundeen J, Zahler R and Jendrzejewski S (1991) In: USPTO (ed). US5030724 A,

34 (1958) Handbook of chemistry and physics. Chemical Rubber Pub. Co., Cleveland

35 Zane HK and Butler A (2013) J Nat Prod 76:648-654

36 Gans P and O'Sullivan B (2000) Talanta 51:33-37

37 Gans P, Sabatini A and Vacca A (1996) Talanta 43:1739-1753

38 Bielski B and Allen A (1977) J Phys Chem 81:1048-1050

39 Sunkel J and Staude H (1968) Ber Bunsenges Phys Chem 72:567-573

40 Ackerman G, Hesse D and Volland P (1970) Z Anorg Allg Chem 377:92-99

41 Harada H (1969) Nippon Kagaku Zasshi 90:267-271

42 Slabbert N (1977) Tetrahedron 33:821-824

43 Athavale V, Prabhu L and Vartak D (1966) J Inorg Nucl Chem 28:1237-1249

44 Bartusek M and Zelinka J (1967) Collect Czech Chem Commun 32:992-1005

45 Perrin D (1958) Nature 182:741-742

46 Timberlake C (1957) J Chem Soc:4987-4993

47 Tyson CA and Martell AE (1972) J Am Chem Soc 94:939-945

48 Pichet P and Benoit R (1967) Inorg Chem 6:1505-1509

49 Murakami Y and Tokunaga M (1964) Bull Soc Chem Jpn 37:1562-1563

50 Jameson R and Wilson M (1972) J Chem Soc Dalton Trans 23:2617-2621

51 Migal P and Ivanov A (1967) J Gen Chem USSR 37:380-385

52 Murakami Y, Nakamura K and Tokunaga M (1963) Bull Soc Chem Jpn 36:669-675

53 Aydin R, Ozer U and Turkel N (1997) Tr J of Chemistry 21:428-436

54 Hansch C, Leo A and Taft RW (1991) Chem Rev 91:165-195

55 Hansch C and Gao H (1997) Chem Rev 97:2995-3059

56 Caroll F (2010) Perspectives on structure and mechanism in organic chemistry. John Wiley & Sons, Hoboken

57 Nematollahi D, Taherpour A, Jameh-Bozorghi S, Mansouri A and Dadpou B (2010) Int J Electrochem Sci 5:867-879

58 Ammal S, Mishima M and Yamataka H (2003) J Org Chem 68:7772-7778

59 Okamoto Y and Brown HC (1957) J Org Chem 22:485-494

60 Aparicio S and Alcalde R (2010) Eur J Chem 3:162-167

61 Takac M, Topic D and Govorcinovic T (2004) Acta Pharma 54:163-176

62 Ashizawa R and Noguchi T (2014) Phys Chem Chem Phys 16:11864-11876

63 Lee H, Lee BP and Messersmith PB (2007) Nature 448:338-341

64 Sandy M and Butler A (2011) J Nat Prod 74:1207-1212

65 Maier GP, Rapp MV, Waite JH, Israelachvili JN and Butler A (2015) Science 349:628-632

66 Danner EW, Kan Y, Hammer MU, Israelachvili JN and Waite JH (2012) Biochemistry 51:6511-6518

67 Van Laer K, Oliveira M, Wahni K and Messens J (2014) Protein Sci 23:238-242

APPENDIX A. KINETIC DATA FOR CATECHOL AND SUBSTITUTED CATECHOL AUTOXIDATION

Appendix A.1. Kinetic Data for Catechol *Autoxidation*

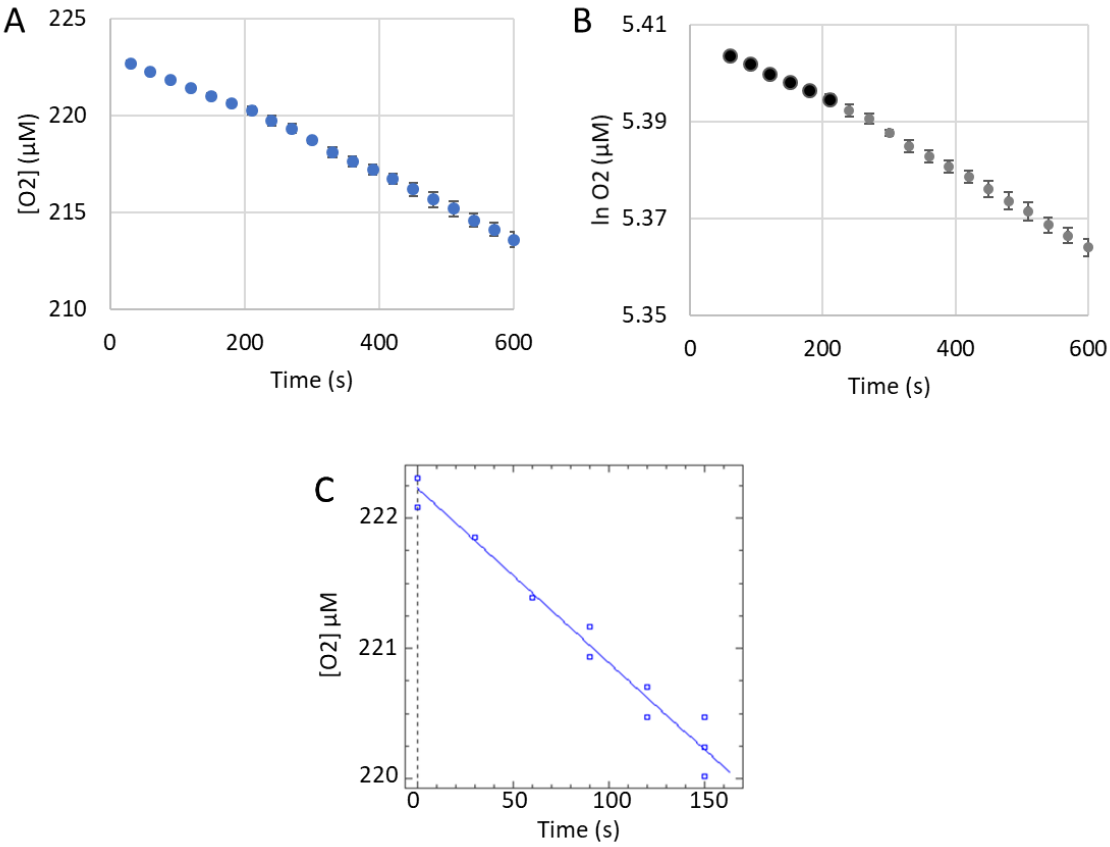

Figure A.1.1. pH 7.0 Autoxidation of 16.6 mM Catechol.

Reactions were carried out in triplicate under pseudo first-order conditions in 50 mM phosphate buffer pH 7.0 at 29.5°C with catechol in excess and an initial O_2 concentration of 223 µM. (A) A Clark-type oxygen electrode tracks the consumption of dissolved O_2 by catechol during the autoxidation process. (B) The initial linear portion (bold data points) of the plot of $\ln[O_2]$ versus time was used for the determination of pseudo first-order rate constant. The initial data point was not included to account for mixing upon the addition of catechol. (C) Non-linear least squares analysis was performed on the initial linear portion from (B) using Dynafit (version 4.05.087 software Biokin Ltd.), giving the pseudo first-order rate constant, standard error, and R^2 value (Table 4.1). Dioxygen consumption data for all three autoxidation reactions, rather than the average of these reactions, was included in the same plot when determining the pseudo first order rate constant.

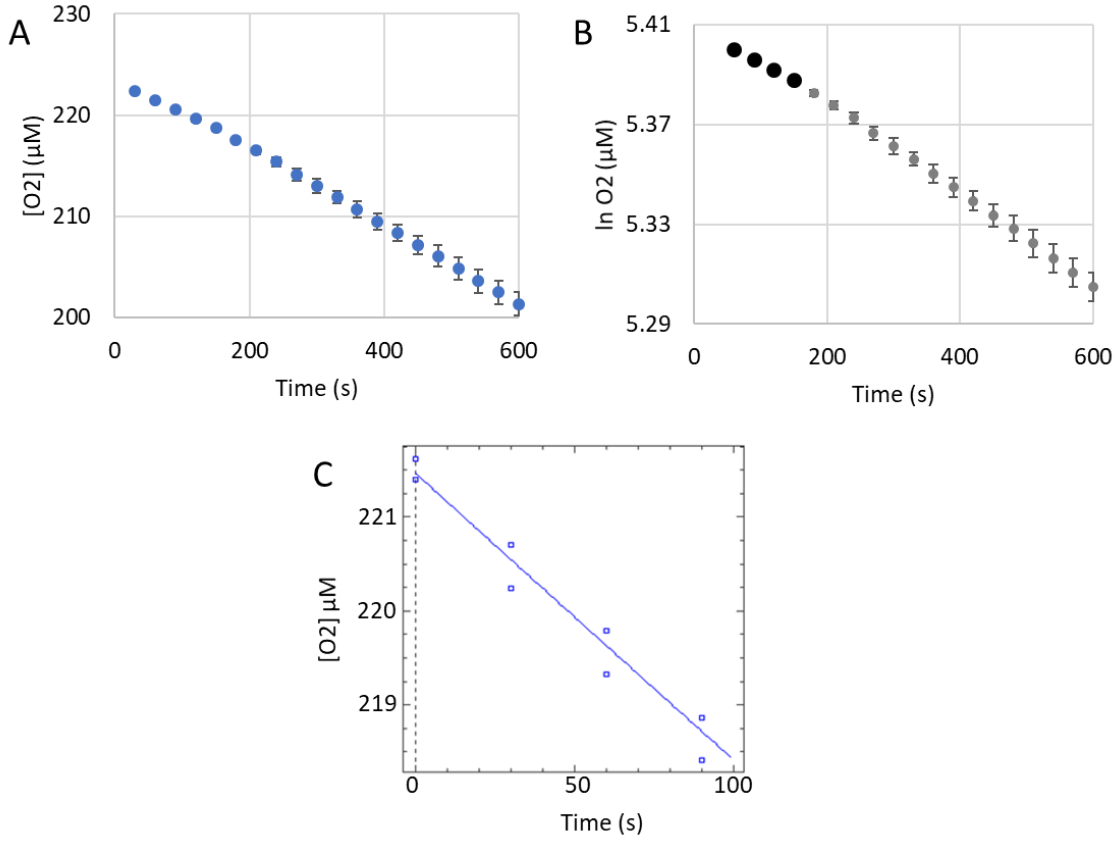

Figure A.1.2. pH 7.0 Autoxidation of 33.2 mM Catechol.

Reactions were carried out in triplicate under pseudo first-order conditions in 50 mM phosphate buffer pH 7.0 at 29.5°C with catechol in excess and an initial O_2 concentration of 223 µM. (A) A Clark-type oxygen electrode tracks the consumption of dissolved O_2 by catechol during the autoxidation process. (B) The initial linear portion (bold data points) of the plot of $\ln[O_2]$ versus time was used for the determination of pseudo first-order rate constant. The initial data point was not included to account for mixing upon the addition of catechol. (C) Non-linear least squares analysis was performed on the initial linear portion from (B) using Dynafit (version 4.05.087 software Biokin Ltd.), giving the pseudo first-order rate constant, standard error, and R^2 value (Table 4.1). Dioxygen consumption data for all three autoxidation reactions, rather than the average of these reactions, was included in the same plot when determining the pseudo first order rate constant.

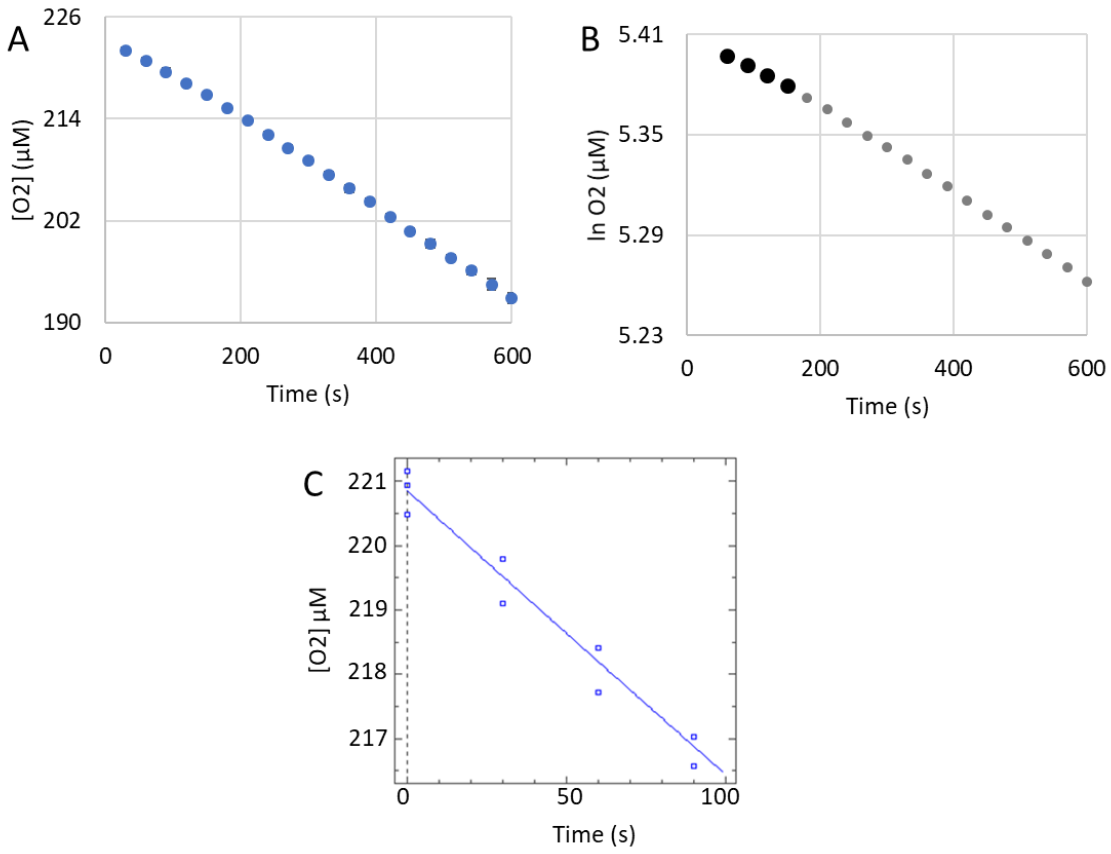

Figure A.1.3. pH 7.0 Autoxidation of 49.8 mM Catechol.

Reactions were carried out in triplicate under pseudo first-order conditions in 50 mM phosphate buffer pH 7.0 at 29.5°C with catechol in excess and an initial O_2 concentration of 223 µM. (A) A Clark-type oxygen electrode tracks the consumption of dissolved O_2 by catechol during the autoxidation process. (B) The initial linear portion (bold data points) of the plot of ln[O_2] versus time was used for the determination of pseudo first-order rate constant. The initial data point was not included to account for mixing upon the addition of catechol. (C) Non-linear least squares analysis was performed on the initial linear portion from (B) using Dynafit (version 4.05.087 software Biokin Ltd.), giving the pseudo first-order rate constant, standard error, and R^2 value (Table 4.1). Dioxygen consumption data for all three autoxidation reactions, rather than the average of these reactions, was included in the same plot when determining the pseudo first order rate constant.

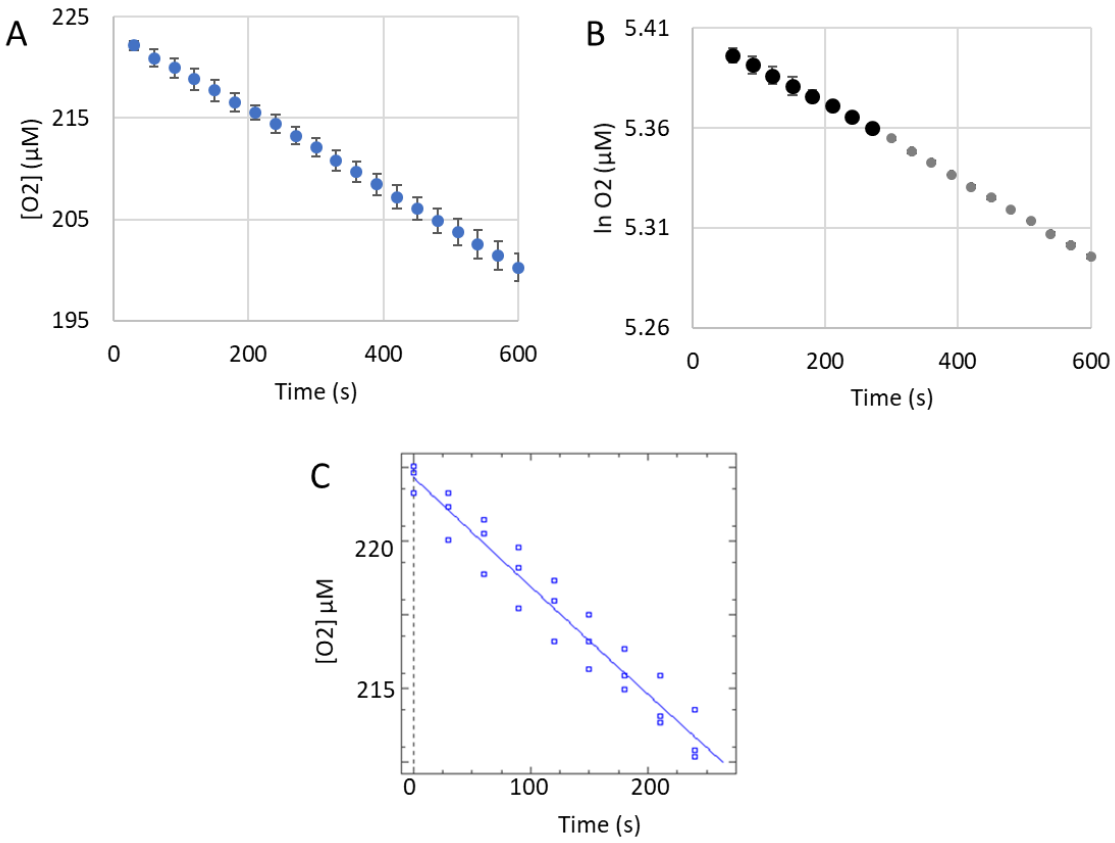

Figure A.1.4. pH 7.5 Autoxidation of 9.96 mM Catechol.

Reactions were carried out in triplicate under pseudo first-order conditions in 50 mM phosphate buffer pH 7.5 at 29.5°C with catechol in excess and an initial O_2 concentration of 223 µM. One of autoxidation reactions deviated from the average of the remaining two and was not included in the analysis. (A) A Clark-type oxygen electrode tracks the consumption of dissolved O_2 by catechol during the autoxidation process. (B) The initial linear portion (bold data points) of the plot of $\ln[O_2]$ versus time was used for the determination of pseudo first-order rate constant. The initial data point was not included to account for mixing upon the addition of catechol. (C) Non-linear least squares analysis was performed on the initial linear portion from (B) using Dynafit (version 4.05.087 software Biokin Ltd.), giving the pseudo first-order rate constant, standard error, and R^2 value (Table 4.1). Dioxygen consumption data for all three autoxidation reactions, rather than the average of these reactions, was included in the same plot when determining the pseudo first order rate constant.

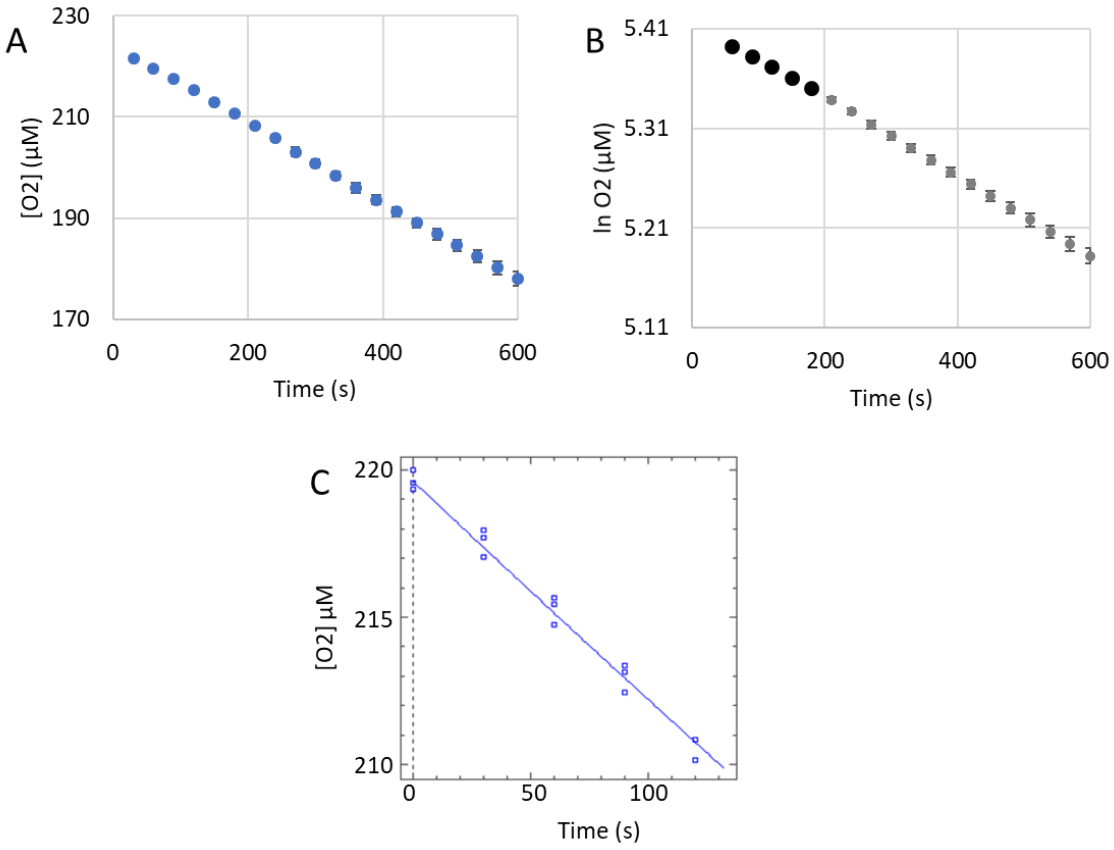

Figure A.1.5. pH 7.5 Autoxidation of 23.2 mM Catechol.

Reactions were carried out in triplicate under pseudo first-order conditions in 50 mM phosphate buffer pH 7.5 at 29.5°C with catechol in excess and an initial O_2 concentration of 223 µM. (A) A Clark-type oxygen electrode tracks the consumption of dissolved O_2 by catechol during the autoxidation process. (B) The initial linear portion (bold data points) of the plot of $\ln[O_2]$ versus time was used for the determination of pseudo first-order rate constant. The initial data point was not included to account for mixing upon the addition of catechol. (C) Non-linear least squares analysis was performed on the initial linear portion from (B) using Dynafit (version 4.05.087 software Biokin Ltd.), giving the pseudo first-order rate constant, standard error, and R^2 value (Table 4.1). Dioxygen consumption data for all three autoxidation reactions, rather than the average of these reactions, was included in the same plot when determining the pseudo first order rate constant.

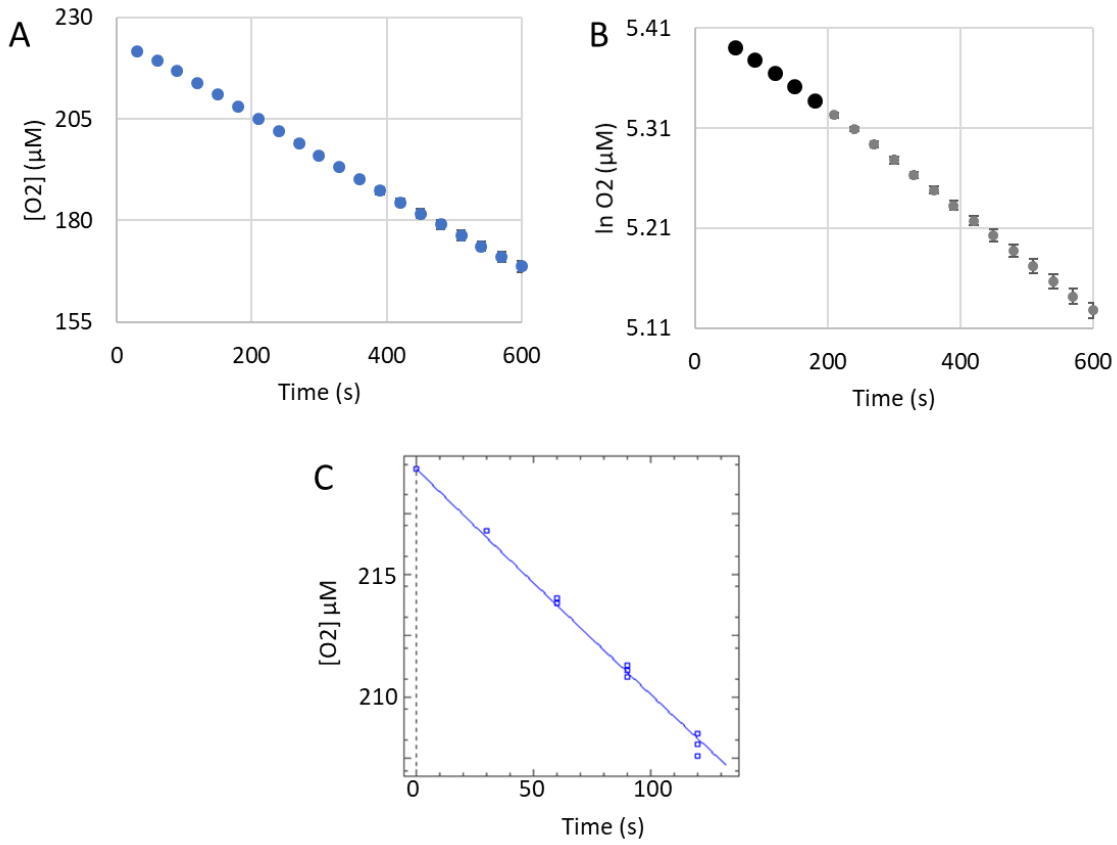

Figure A.1.6. pH 7.5 Autoxidation of 33.2 mM Catechol.

Reactions were carried out in triplicate under pseudo first-order conditions in 50 mM phosphate buffer pH 7.5 at 29.5°C with catechol in excess and an initial O_2 concentration of 223 µM. (A) A Clark-type oxygen electrode tracks the consumption of dissolved O_2 by catechol during the autoxidation process. (B) The initial linear portion (bold data points) of the plot of ln[O_2] versus time was used for the determination of pseudo first-order rate constant. The initial data point was not included to account for mixing upon the addition of catechol. (C) Non-linear least squares analysis was performed on the initial linear portion from (B) using Dynafit (version 4.05.087 software Biokin Ltd.), giving the pseudo first-order rate constant, standard error, and R^2 value (Table 4.1). Dioxygen consumption data for all three autoxidation reactions, rather than the average of these reactions, was included in the same plot when determining the pseudo first order rate constant.

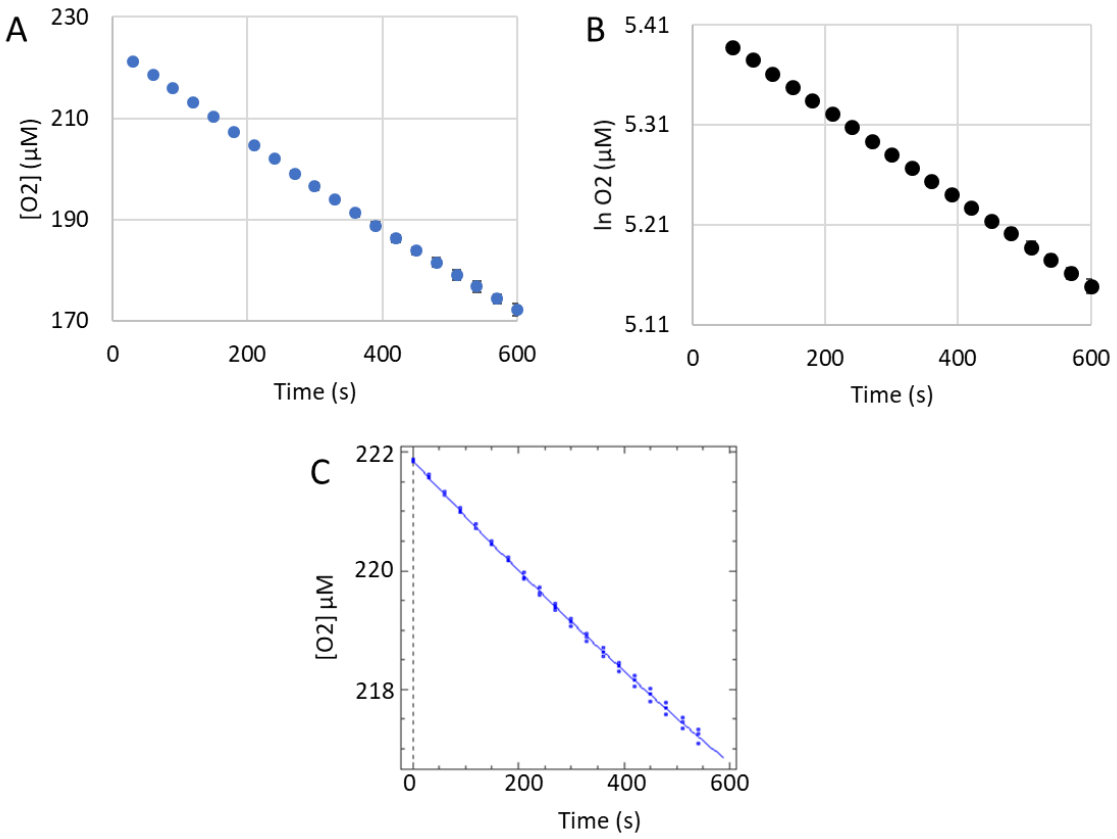

Figure A.1.7. pH 8.0 Autoxidation of 6.64 mM Catechol.

Reactions were carried out in triplicate under pseudo first-order conditions in 50 mM phosphate buffer pH 8.0 at 29.5°C with catechol in excess and an initial O_2 concentration of 223 µM. (A) A Clark-type oxygen electrode tracks the consumption of dissolved O_2 by catechol during the autoxidation process. (B) The initial linear portion (bold data points) of the plot of ln[O_2] versus time was used for the determination of pseudo first-order rate constant. The initial data point was not included to account for mixing upon the addition of catechol. (C) Non-linear least squares analysis was performed on the initial linear portion from (B) using Dynafit (version 4.05.087 software Biokin Ltd.), giving the pseudo first-order rate constant, standard error, and R^2 value (Table 4.1). Dioxygen consumption data for all three autoxidation reactions, rather than the average of these reactions, was included in the same plot when determining the pseudo first order rate constant.

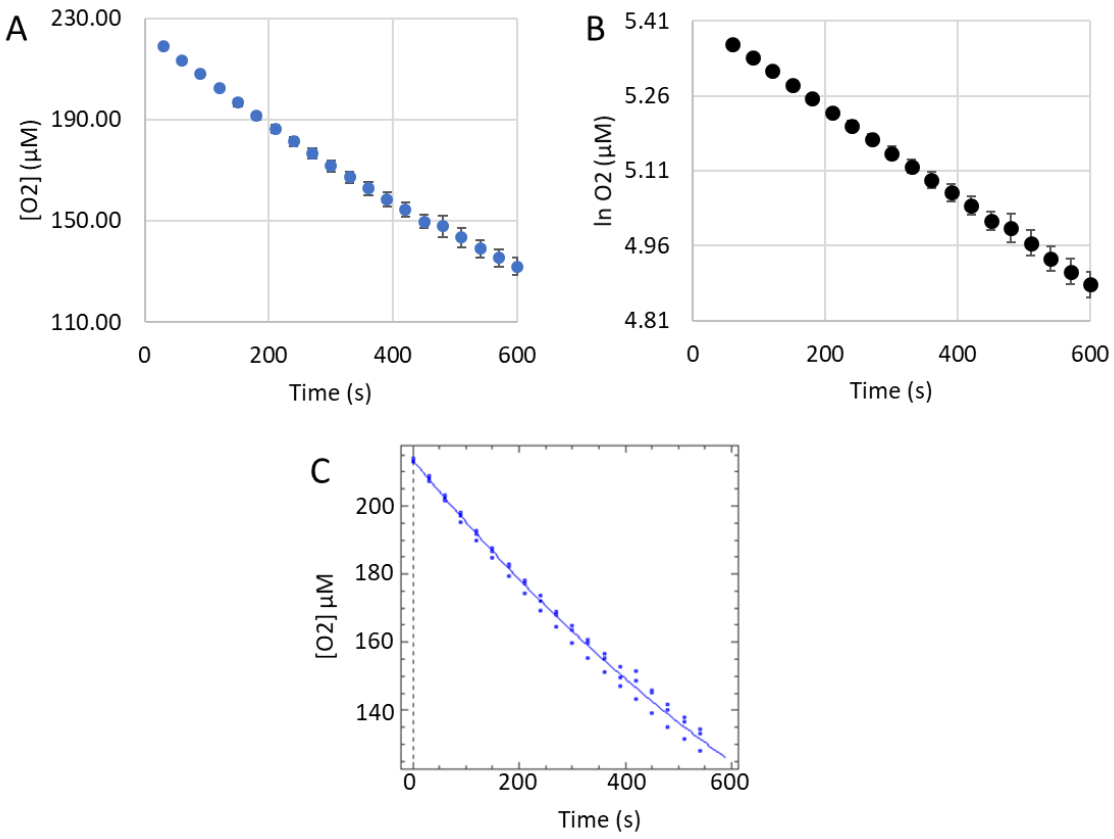

Figure A.1.8. pH 8.0 Autoxidation of 13.3 mM Catechol.

Reactions were carried out in triplicate under pseudo first-order conditions in 50 mM phosphate buffer pH 8.0 at 29.5°C with catechol in excess and an initial O_2 concentration of 223 µM. (A) A Clark-type oxygen electrode tracks the consumption of dissolved O_2 by catechol during the autoxidation process. (B) The initial linear portion (bold data points) of the plot of $\ln[O_2]$ versus time was used for the determination of pseudo first-order rate constant. The initial data point was not included to account for mixing upon the addition of catechol. (C) Non-linear least squares analysis was performed on the initial linear portion from (B) using Dynafit (version 4.05.087 software Biokin Ltd.), giving the pseudo first-order rate constant, standard error, and R^2 value (Table 4.1). Dioxygen consumption data for all three autoxidation reactions, rather than the average of these reactions, was included in the same plot when determining the pseudo first order rate constant.

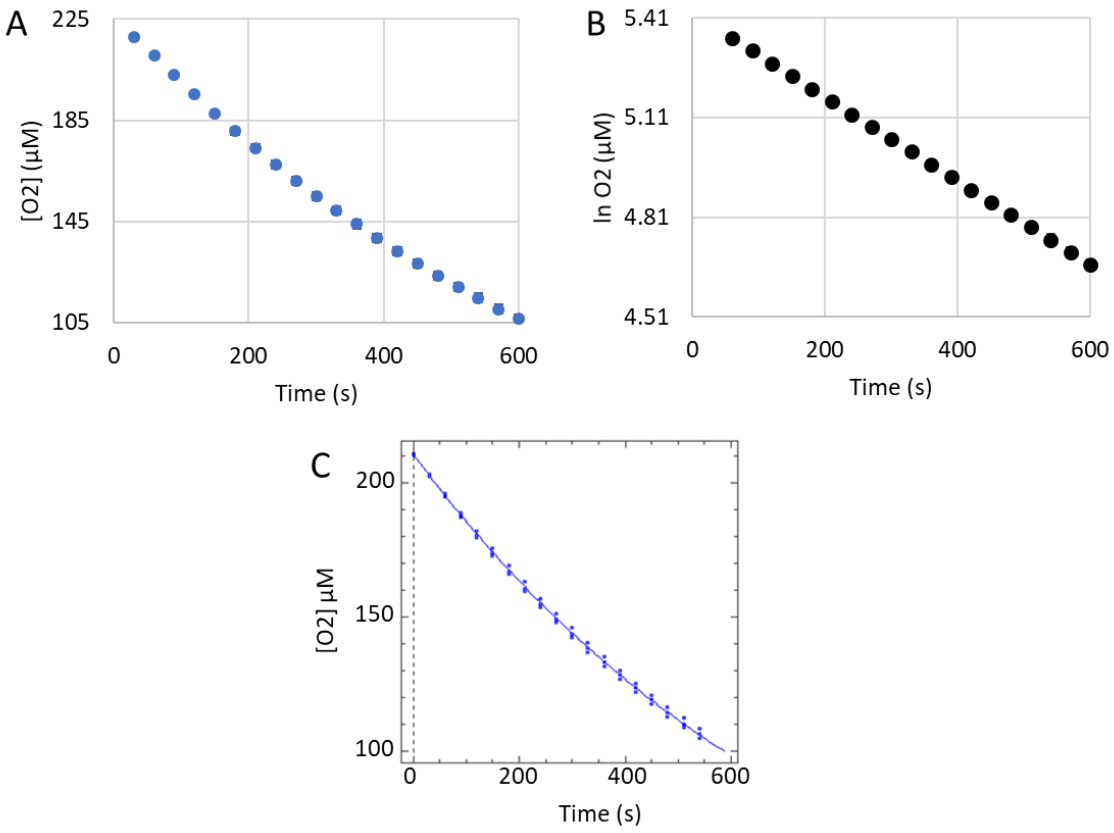

Figure A.1.9. pH 8.0 Autoxidation of 19.9 mM Catechol.

Reactions were carried out in triplicate under pseudo first-order conditions in 50 mM phosphate buffer pH 8.0 at 29.5°C with catechol in excess and an initial O_2 concentration of 223 µM. (A) A Clark-type oxygen electrode tracks the consumption of dissolved O_2 by catechol during the autoxidation process. (B) The initial linear portion (bold data points) of the plot of ln[O_2] versus time was used for the determination of pseudo first-order rate constant. The initial data point was not included to account for mixing upon the addition of catechol. (C) Non-linear least squares analysis was performed on the initial linear portion from (B) using Dynafit (version 4.05.087 software Biokin Ltd.), giving the pseudo first-order rate constant, standard error, and R^2 value (Table 4.1). Dioxygen consumption data for all three autoxidation reactions, rather than the average of these reactions, was included in the same plot when determining the pseudo first order rate constant.

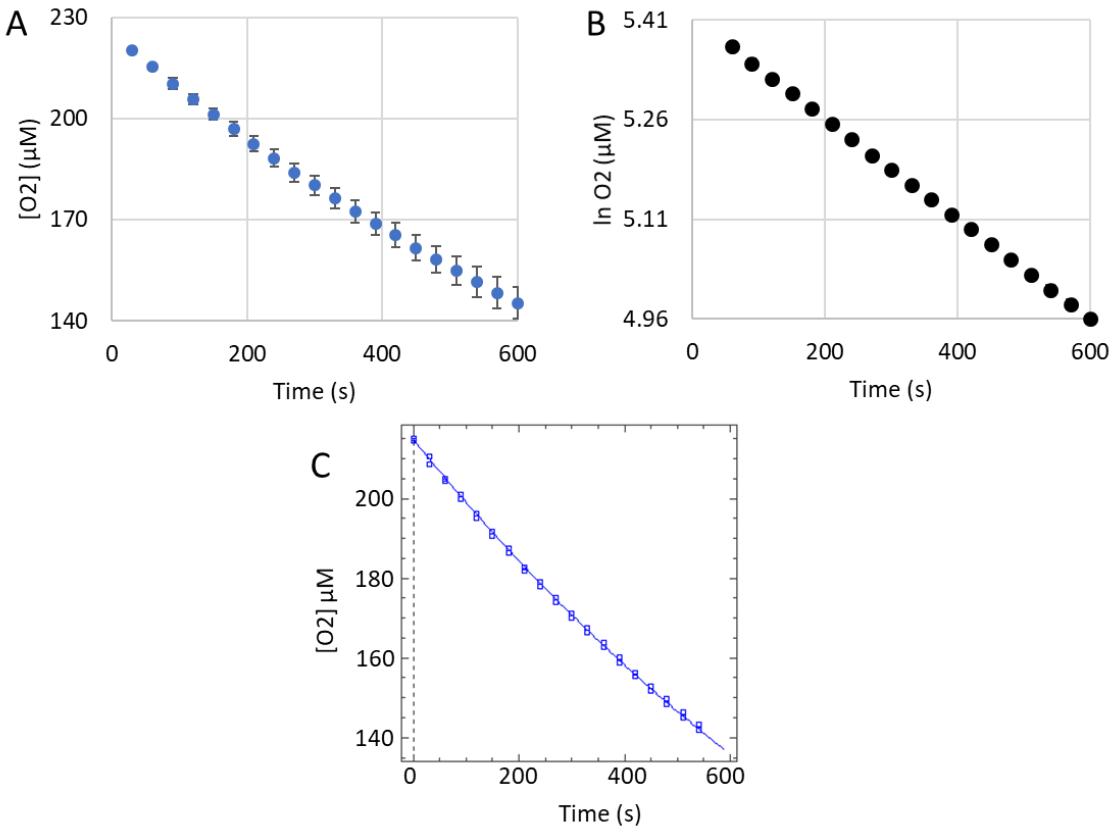

Figure A.1.10. pH 8.5 Autoxidation of 3.32 mM Catechol.

Reactions were carried out in triplicate under pseudo first-order conditions in 50 mM tricine buffer pH 8.5 at 29.5°C with catechol in excess and an initial O_2 concentration of 223 µM. One of autoxidation reactions deviated from the average of the remaining two and was not included in the analysis. (A) A Clark-type oxygen electrode tracks the consumption of dissolved O_2 by catechol during the autoxidation process. (B) The initial linear portion (bold data points) of the plot of $\ln[O_2]$ versus time was used for the determination of pseudo first-order rate constant. The initial data point was not included to account for mixing upon the addition of catechol. (C) Non-linear least squares analysis was performed on the initial linear portion from (B) using Dynafit (version 4.05.087 software Biokin Ltd.), giving the pseudo first-order rate constant, standard error, and R^2 value (Table 4.1). Dioxygen consumption data for all three autoxidation reactions, rather than the average of these reactions, was included in the same plot when determining the pseudo first order rate constant.

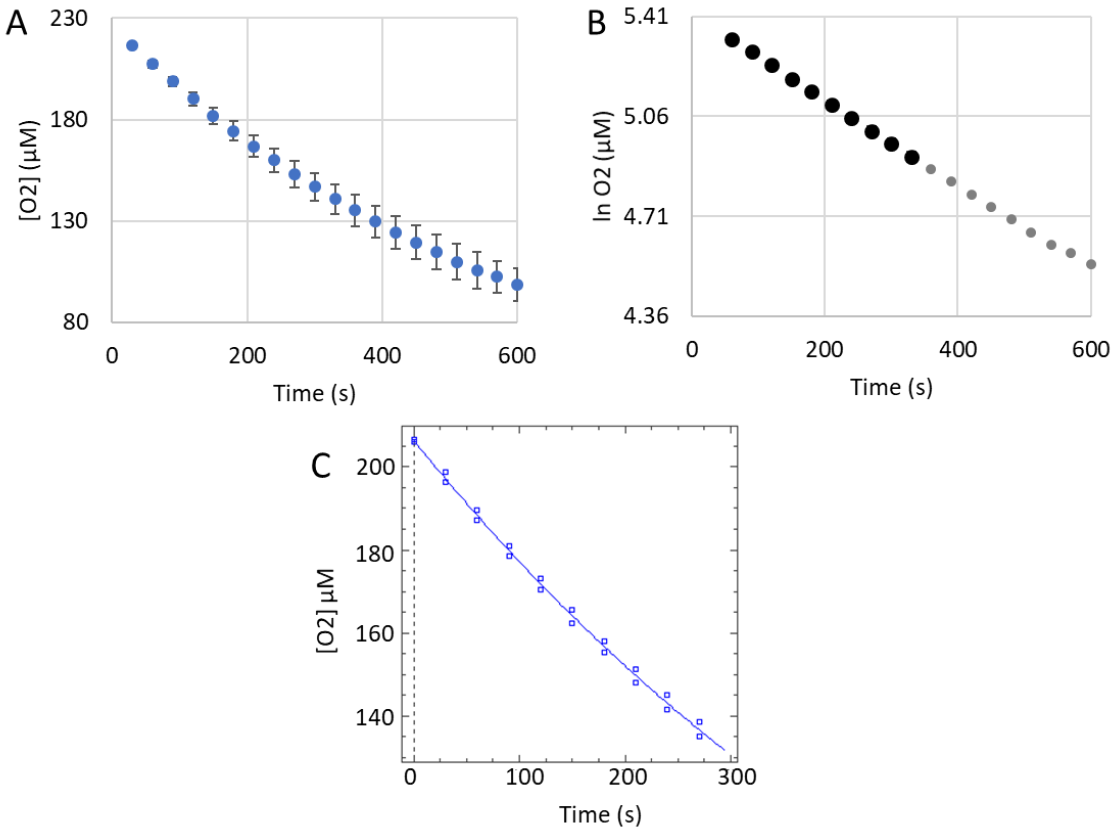

Figure A.1.12. pH 8.5 Autoxidation of 6.64 mM Catechol.

Reactions were carried out in triplicate under pseudo first-order conditions in 50 mM tricine buffer pH 8.5 at 29.5°C with catechol in excess and an initial O_2 concentration of 223 µM. One of autoxidation reactions deviated from the average of the remaining two and was not included in the analysis. (A) A Clark-type oxygen electrode tracks the consumption of dissolved O_2 by catechol during the autoxidation process. (B) The initial linear portion (bold data points) of the plot of $\ln[O_2]$ versus time was used for the determination of pseudo first-order rate constant. The initial data point was not included to account for mixing upon the addition of catechol. (C) Non-linear least squares analysis was performed on the initial linear portion from (B) using Dynafit (version 4.05.087 software Biokin Ltd.), giving the pseudo first-order rate constant, standard error, and R^2 value (Table 4.1). Dioxygen consumption data for all three autoxidation reactions, rather than the average of these reactions, was included in the same plot when determining the pseudo first order rate constant.

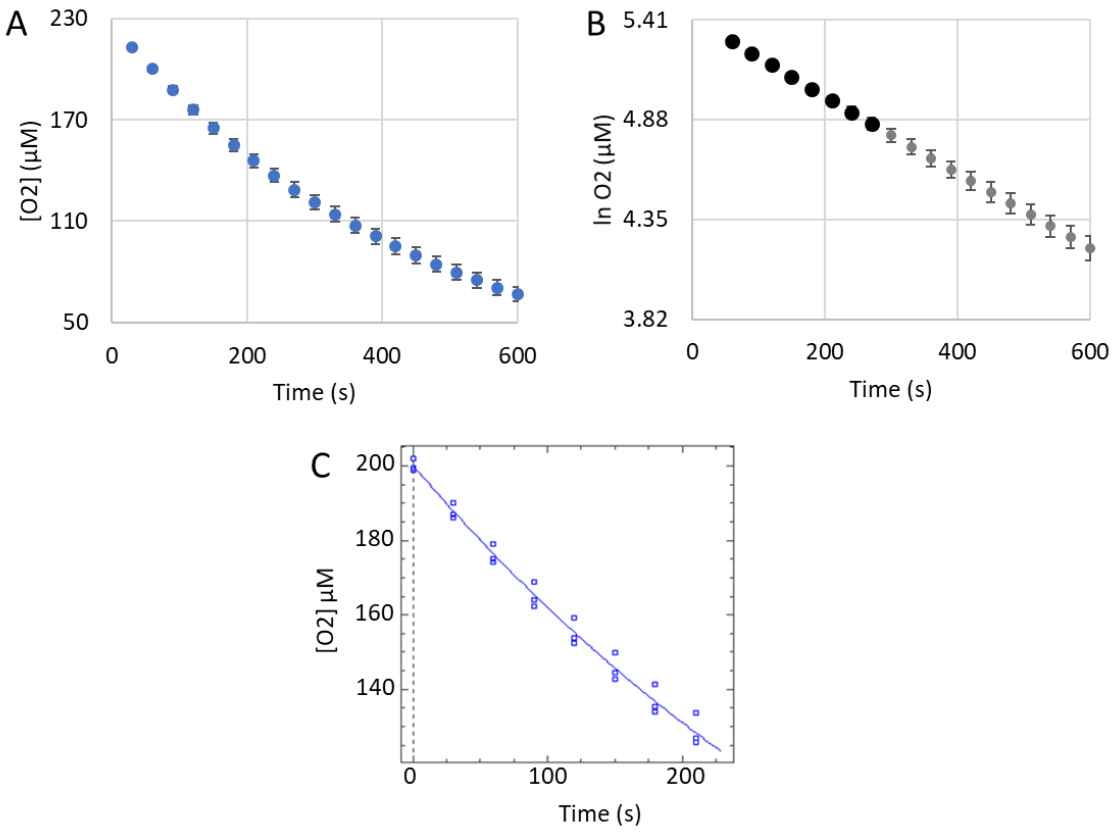

Figure A.1.13. pH 8.5 Autoxidation of 9.96 mM Catechol.

Reactions were carried out in triplicate under pseudo first-order conditions in 50 mM tricine buffer pH 8.5 at 29.5°C with catechol in excess and an initial O_2 concentration of 223 µM. (A) A Clark-type oxygen electrode tracks the consumption of dissolved O_2 by catechol during the autoxidation process. (B) The initial linear portion (bold data points) of the plot of $\ln[O_2]$ versus time was used for the determination of pseudo first-order rate constant. The initial data point was not included to account for mixing upon the addition of catechol. (C) Non-linear least squares analysis was performed on the initial linear portion from (B) using Dynafit (version 4.05.087 software Biokin Ltd.), giving the pseudo first-order rate constant, standard error, and R^2 value (Table 4.1). Dioxygen consumption data for all three autoxidation reactions, rather than the average of these reactions, was included in the same plot when determining the pseudo first order rate constant.

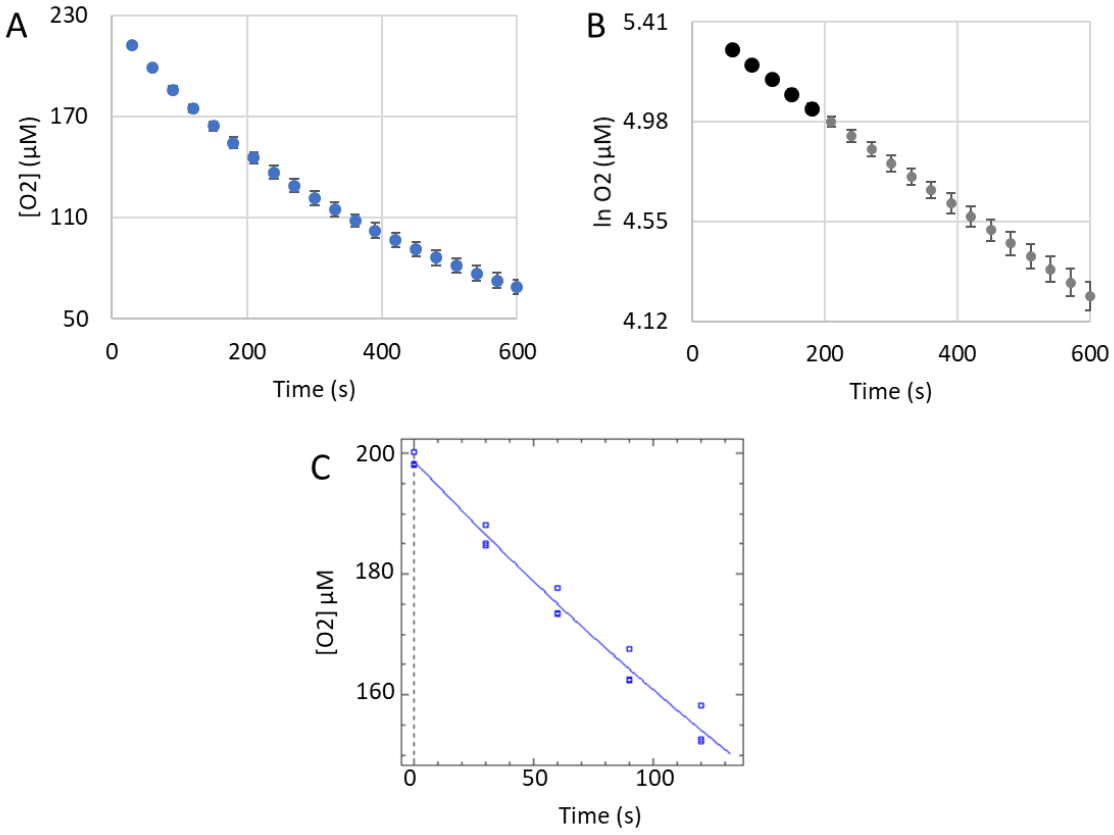

Figure A.1.14. pH 9.0 Autoxidation of 3.32 mM Catechol.

Reactions were carried out in triplicate under pseudo first-order conditions in 50 mM CAPSO buffer pH 9.0 at 29.5°C with catechol in excess and an initial O_2 concentration of 223 µM. (A) A Clark-type oxygen electrode tracks the consumption of dissolved O_2 by catechol during the autoxidation process. (B) The initial linear portion (bold data points) of the plot of ln[O_2] versus time was used for the determination of pseudo first-order rate constant. The initial data point was not included to account for mixing upon the addition of catechol. (C) Non-linear least squares analysis was performed on the initial linear portion from (B) using Dynafit (version 4.05.087 software Biokin Ltd.), giving the pseudo first-order rate constant, standard error, and R^2 value (Table 4.1). Dioxygen consumption data for all three autoxidation reactions, rather than the average of these reactions, was included in the same plot when determining the pseudo first order rate constant.

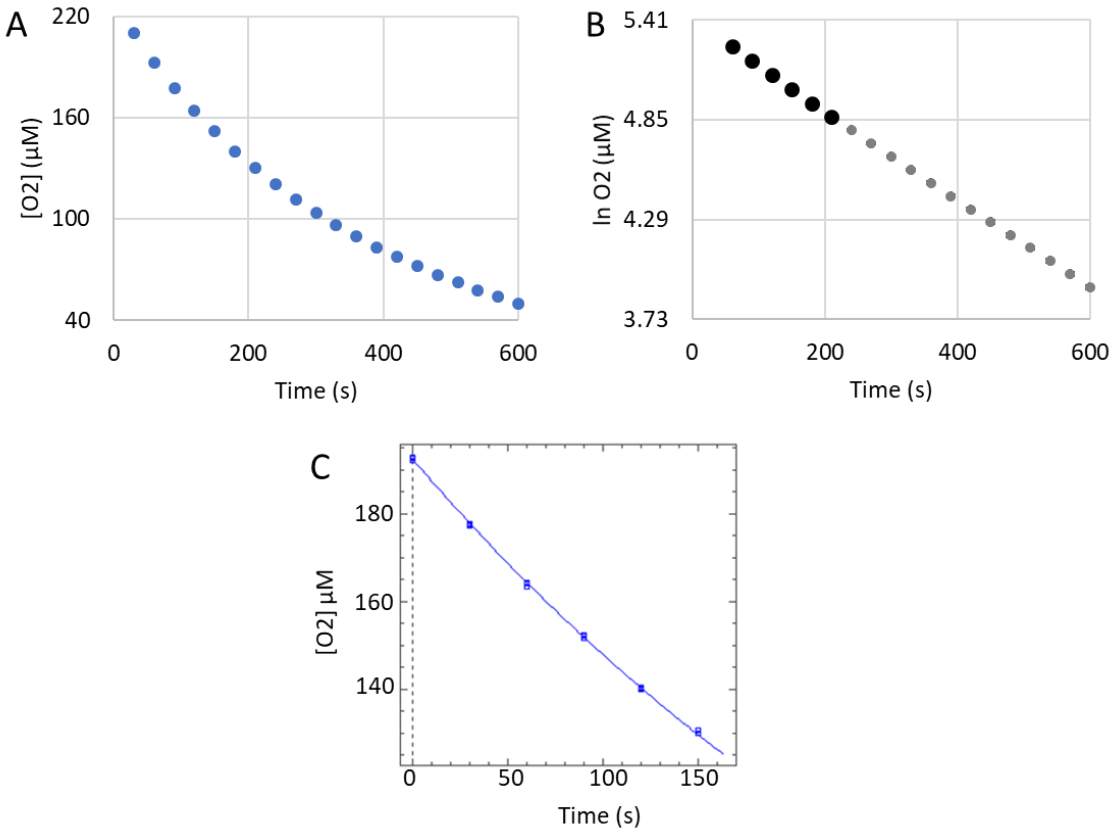

Figure A.1.15. pH 9.0 Autoxidation of 4.98 mM Catechol.

Reactions were carried out in triplicate under pseudo first-order conditions in 50 mM CAPSO buffer pH 9.0 at 29.5°C with catechol in excess and an initial O_2 concentration of 223 µM. (A) A Clark-type oxygen electrode tracks the consumption of dissolved O_2 by catechol during the autoxidation process. (B) The initial linear portion (bold data points) of the plot of ln[O_2] versus time was used for the determination of pseudo first-order rate constant. The initial data point was not included to account for mixing upon the addition of catechol. (C) Non-linear least squares analysis was performed on the initial linear portion from (B) using Dynafit (version 4.05.087 software Biokin Ltd.), giving the pseudo first-order rate constant, standard error, and R^2 value (Table 4.1). Dioxygen consumption data for all three autoxidation reactions, rather than the average of these reactions, was included in the same plot when determining the pseudo first order rate constant.

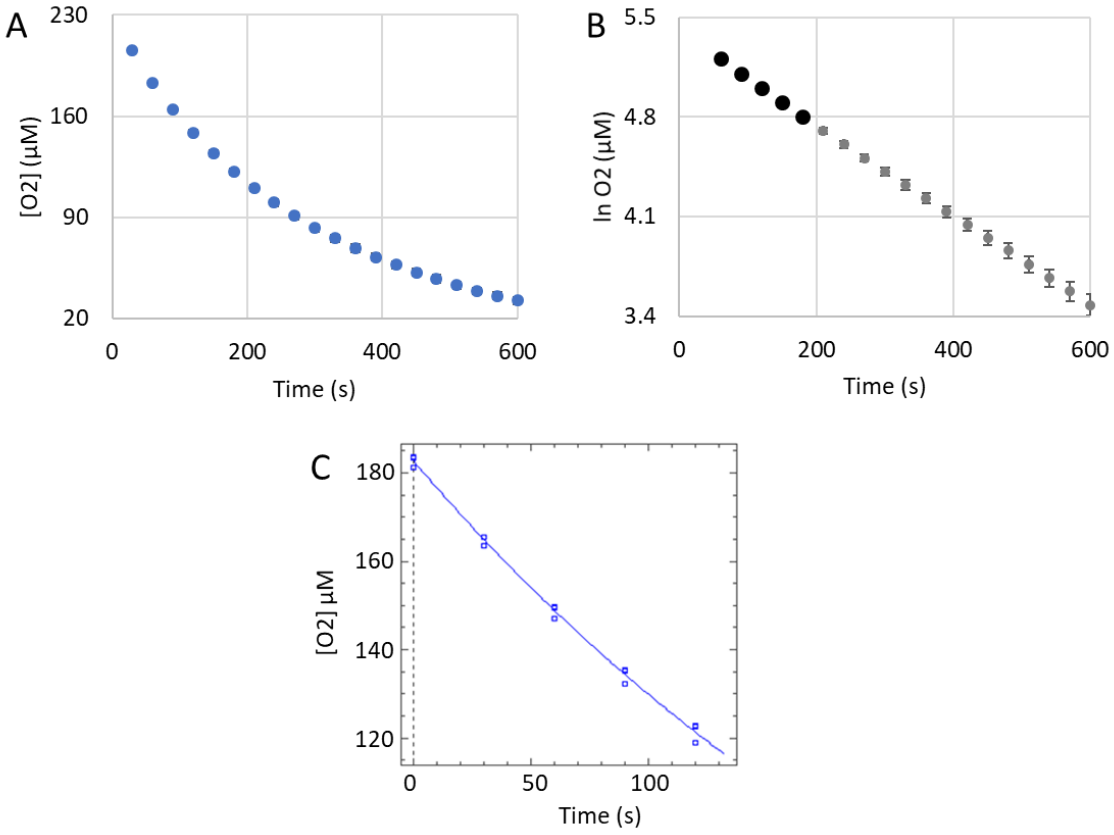

Figure A.1.16. pH 9.0 Autoxidation of 6.64 mM Catechol.

Reactions were carried out in triplicate under pseudo first-order conditions in 50 mM CAPSO buffer pH 9.0 at 29.5°C with catechol in excess and an initial O_2 concentration of 223 µM. (A) A Clark-type oxygen electrode tracks the consumption of dissolved O_2 by catechol during the autoxidation process. (B) The initial linear portion (bold data points) of the plot of ln[O_2] versus time was used for the determination of pseudo first-order rate constant. The initial data point was not included to account for mixing upon the addition of catechol. (C) Non-linear least squares analysis was performed on the initial linear portion from (B) using Dynafit (version 4.05.087 software Biokin Ltd.), giving the pseudo first-order rate constant, standard error, and R^2 value (Table 4.1). Dioxygen consumption data for all three autoxidation reactions, rather than the average of these reactions, was included in the same plot when determining the pseudo first order rate constant.

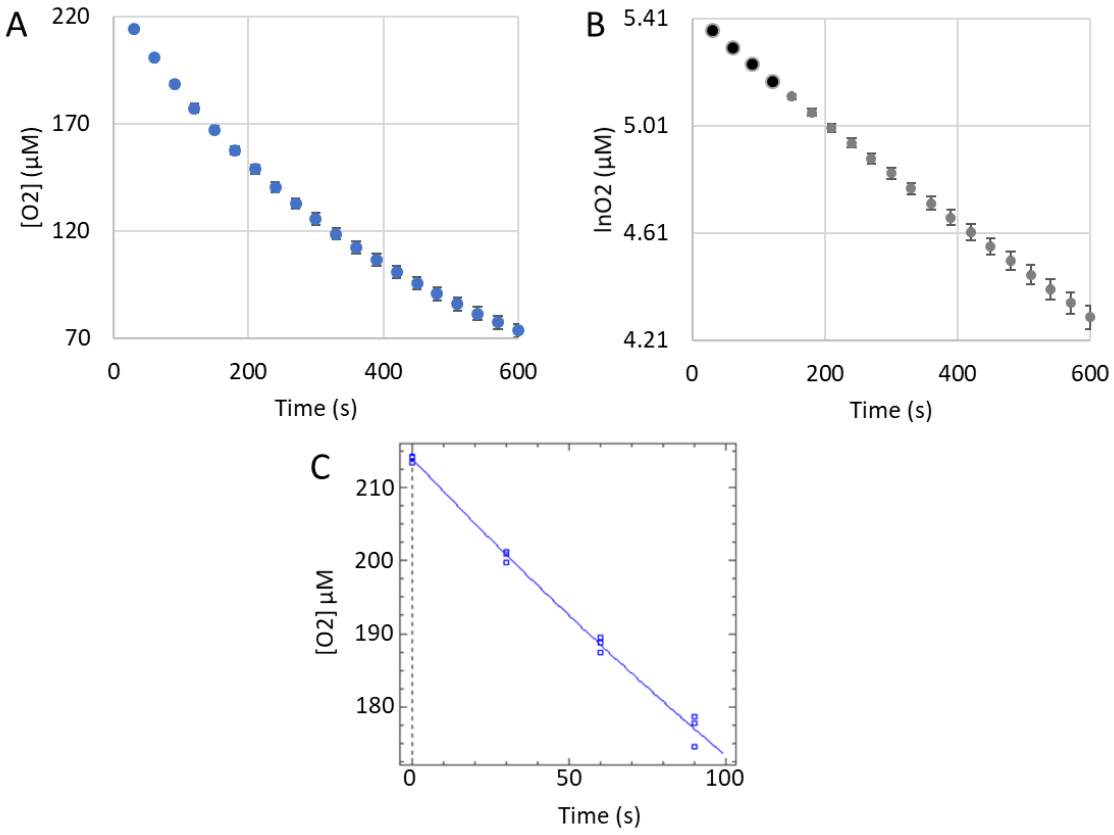

Figure A.1.17. pH 9.0 Autoxidation of 3.32 mM Catechol.

Reactions were carried out in triplicate under pseudo first-order conditions in 50 mM CAPSO buffer pH 9.0 at 29.5°C with catechol in excess and an initial O_2 concentration of 223 µM. (A) A Clark-type oxygen electrode tracks the consumption of dissolved O_2 by catechol during the autoxidation process. (B) The initial linear portion (bold data points) of the plot of ln[O_2] versus time was used for the determination of pseudo first-order rate constant. The initial data point was not included to account for mixing upon the addition of catechol. (C) Non-linear least squares analysis was performed on the initial linear portion from (B) using Dynafit (version 4.05.087 software Biokin Ltd.), giving the pseudo first-order rate constant, standard error, and R^2 value (Table 4.1). Dioxygen consumption data for all three autoxidation reactions, rather than the average of these reactions, was included in the same plot when determining the pseudo first order rate constant.

Appendix A.2. Kinetic Data for 4-Methylcatechol Autoxidation

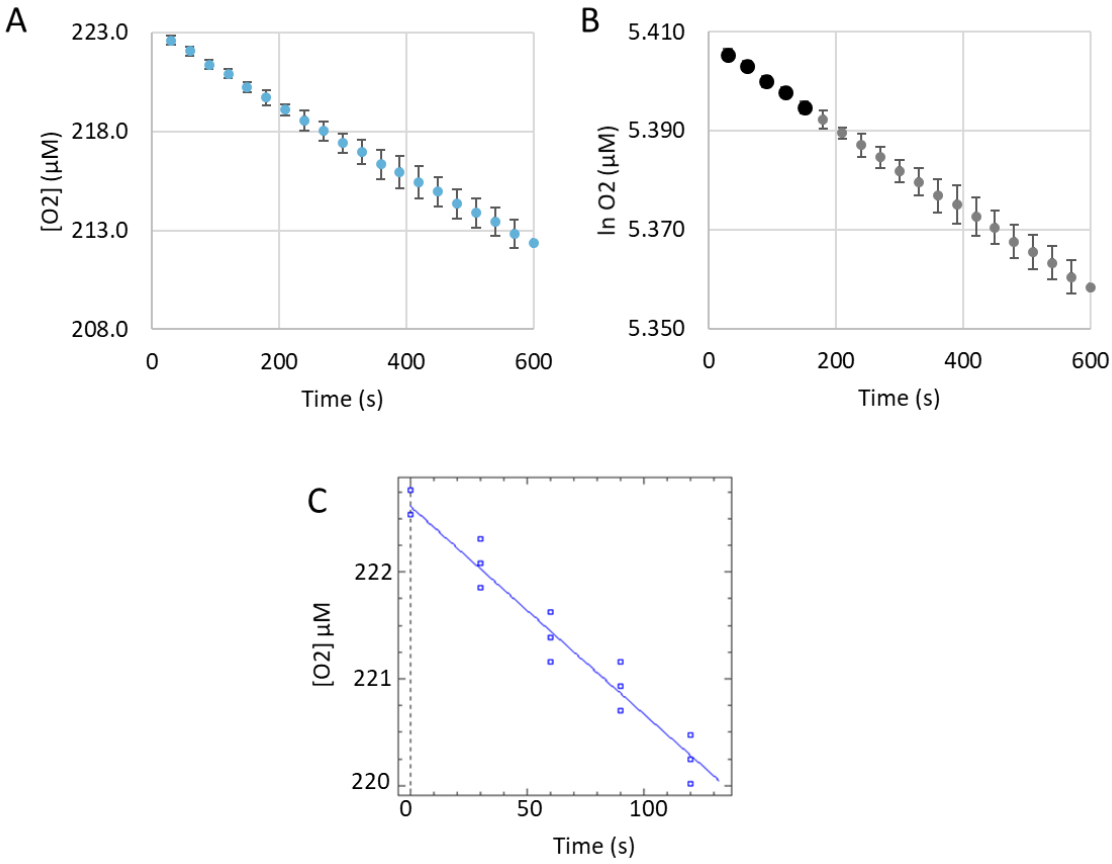

Figure A.2.1. pH 6.0 Autoxidation of 13.3 mM 4-Methylcatechol.

Reactions were carried out in triplicate under pseudo first-order conditions in 50 mM phosphate buffer pH 6.0 at 29.5°C with 4-methylcatechol in excess and an initial O_2 concentration of 223 µM. (A) A Clark-type oxygen electrode tracks the consumption of dissolved O_2 by catechol during the autoxidation process. (B) The initial linear portion (bold data points) of the plot of ln[O_2] versus time was used for the determination of pseudo first-order rate constant. The initial data point was not included to account for mixing upon the addition of catechol. (C) Non-linear least squares analysis was performed on the initial linear portion from (B) using Dynafit (version 4.05.087 software Biokin Ltd.), giving the pseudo first-order rate constant, standard error, and R^2 value (Table 4.3). Dioxygen consumption data for all three autoxidation reactions, rather than the average of these reactions, was included in the same plot when determining the pseudo first order rate constant.

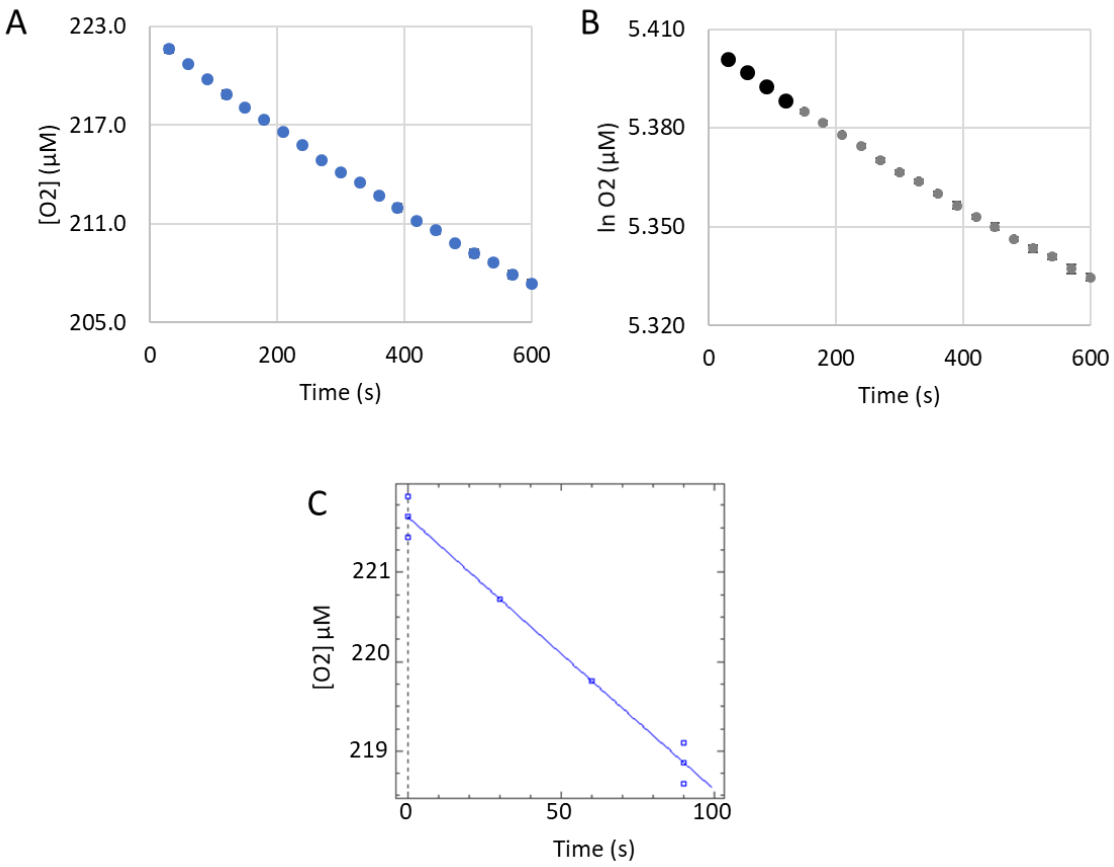

Figure A.2.2. pH 6.0 Autoxidation of 26.6 mM 4-Methylcatechol.

Reactions were carried out in triplicate under pseudo first-order conditions in 50 mM phosphate buffer pH 6.0 at 29.5°C with 4-methylcatechol in excess and an initial O_2 concentration of 223 µM. (A) A Clark-type oxygen electrode tracks the consumption of dissolved O_2 by catechol during the autoxidation process. (B) The initial linear portion (bold data points) of the plot of ln[O_2] versus time was used for the determination of pseudo first-order rate constant. The initial data point was not included to account for mixing upon the addition of catechol. (C) Non-linear least squares analysis was performed on the initial linear portion from (B) using Dynafit (version 4.05.087 software Biokin Ltd.), giving the pseudo first-order rate constant, standard error, and R^2 value (Table 4.3). Dioxygen consumption data for all three autoxidation reactions, rather than the average of these reactions, was included in the same plot when determining the pseudo first order rate constant.

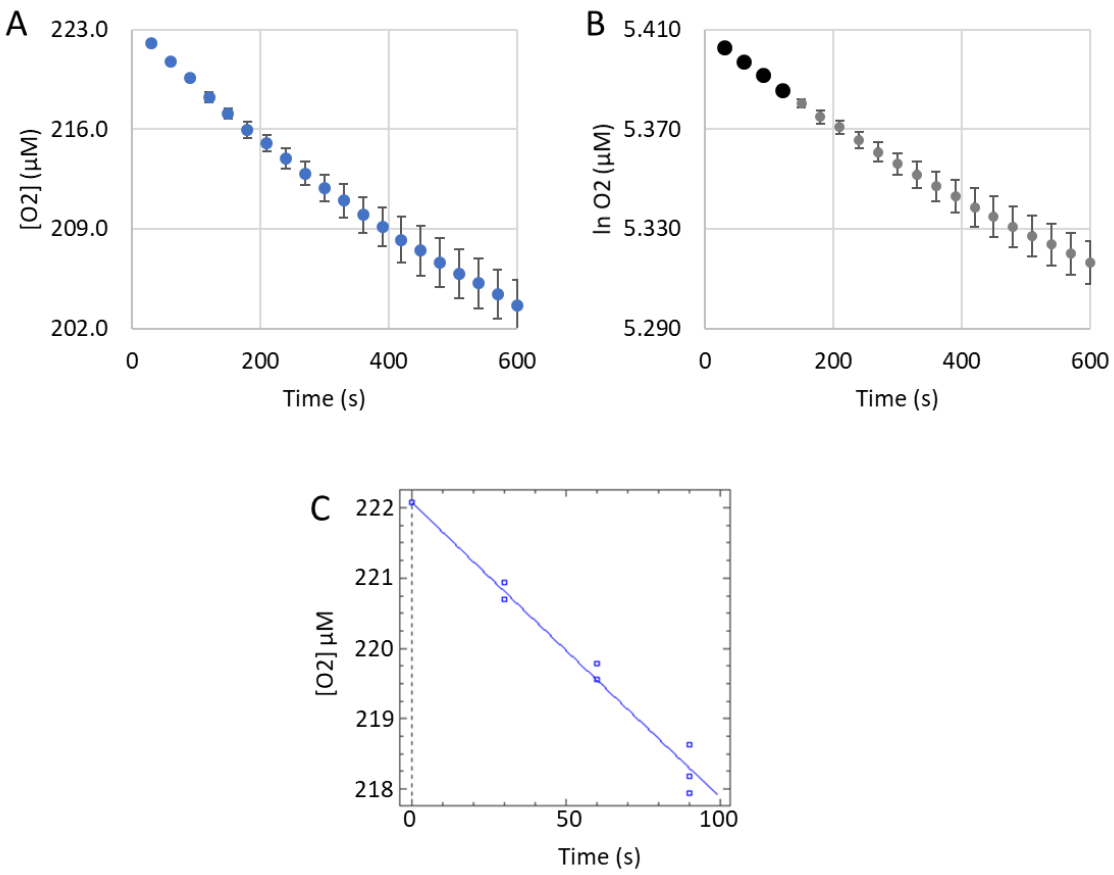

Figure A.2.3. pH 6.0 Autoxidation of 39.9 mM 4-Methylcatechol.

Reactions were carried out in triplicate under pseudo first-order conditions in 50 mM phosphate buffer pH 6.0 at 29.5°C with 4-methylcatechol in excess and an initial O_2 concentration of 223 µM. (A) A Clark-type oxygen electrode tracks the consumption of dissolved O_2 by catechol during the autoxidation process. (B) The initial linear portion (bold data points) of the plot of ln[O_2] versus time was used for the determination of pseudo first-order rate constant. The initial data point was not included to account for mixing upon the addition of catechol. (C) Non-linear least squares analysis was performed on the initial linear portion from (B) using Dynafit (version 4.05.087 software Biokin Ltd.), giving the pseudo first-order rate constant, standard error, and R^2 value (Table 4.3). Dioxygen consumption data for all three autoxidation reactions, rather than the average of these reactions, was included in the same plot when determining the pseudo first order rate constant.

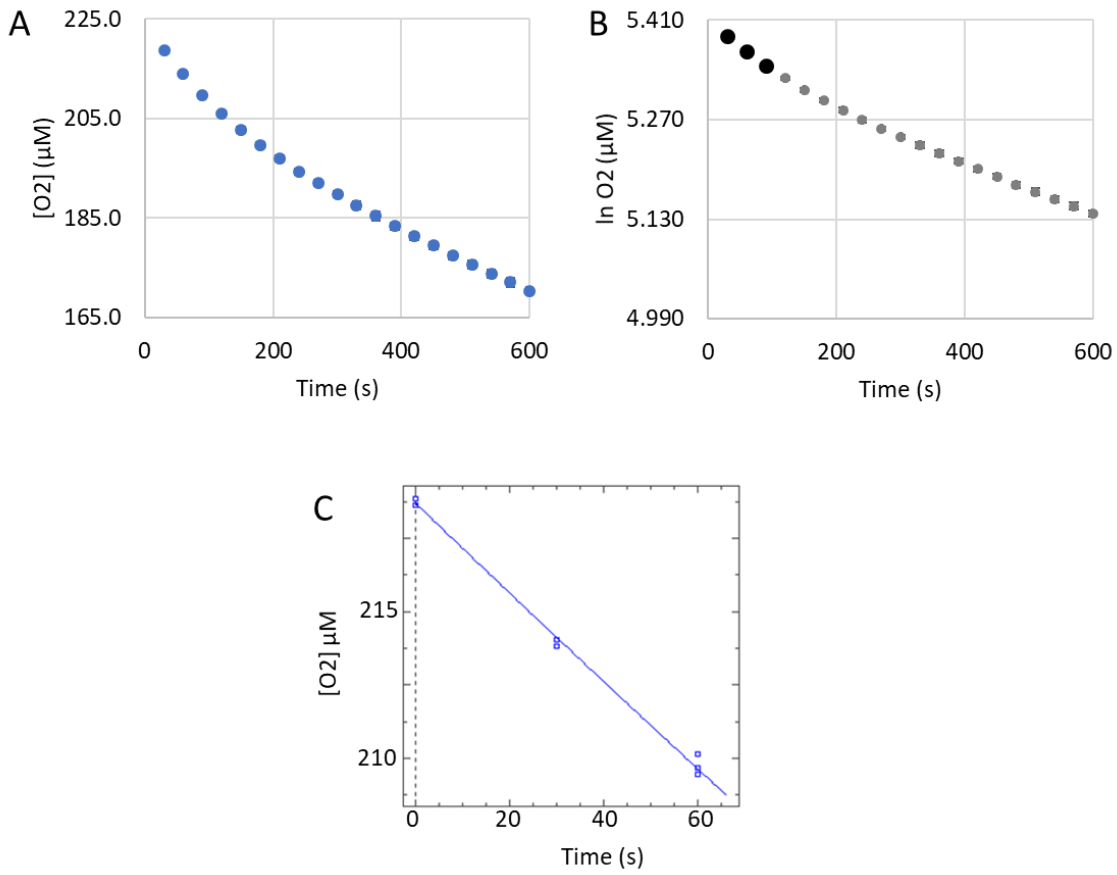

Figure A.2.4. pH 7.0 Autoxidation of 13.3 mM 4-Methylcatechol.

Reactions were carried out in triplicate under pseudo first-order conditions in 50 mM phosphate buffer pH 7.0 at 29.5°C with 4-methylcatechol in excess and an initial O_2 concentration of 223 µM. (A) A Clark-type oxygen electrode tracks the consumption of dissolved O_2 by catechol during the autoxidation process. (B) The initial linear portion (bold data points) of the plot of ln[O_2] versus time was used for the determination of pseudo first-order rate constant. The initial data point was not included to account for mixing upon the addition of catechol. (C) Non-linear least squares analysis was performed on the initial linear portion from (B) using Dynafit (version 4.05.087 software Biokin Ltd.), giving the pseudo first-order rate constant, standard error, and R^2 value (Table 4.3). Dioxygen consumption data for all three autoxidation reactions, rather than the average of these reactions, was included in the same plot when determining the pseudo first order rate constant.

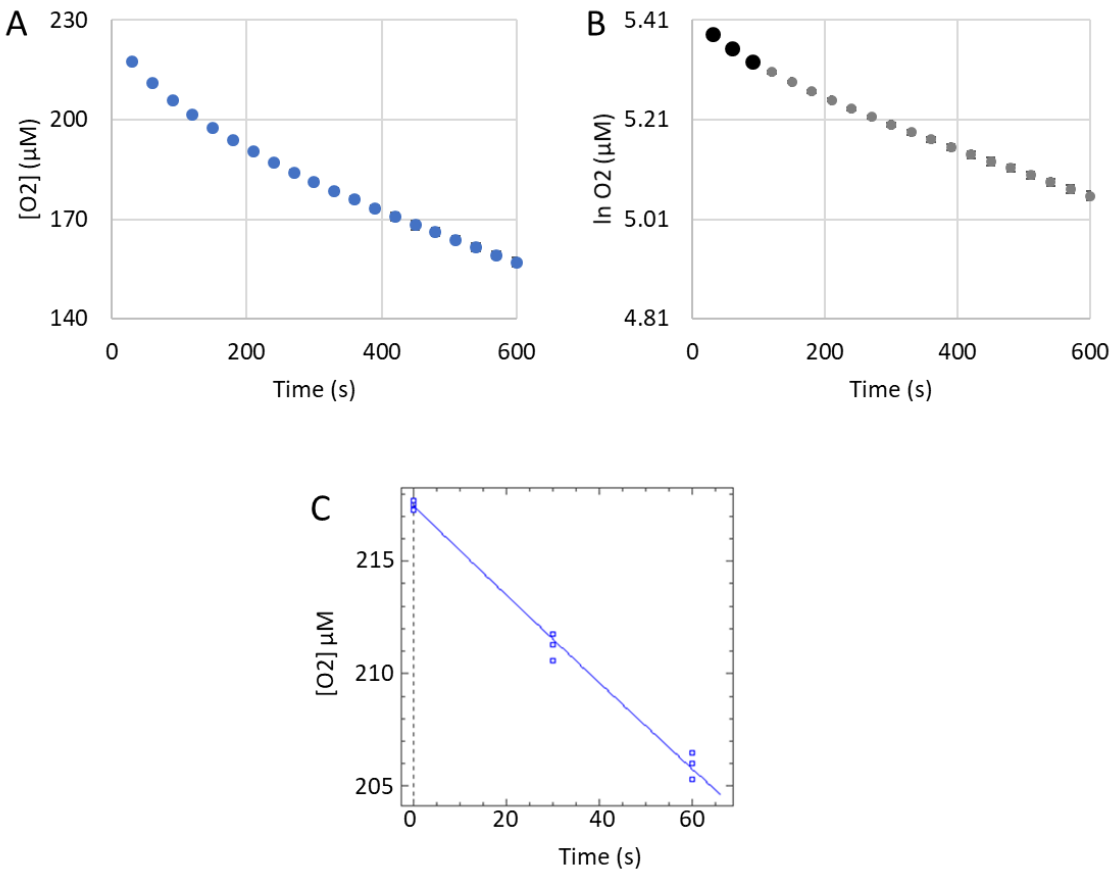

Figure A.2.5. pH 7.0 Autoxidation of 19.9 mM 4-Methylcatechol.

Reactions were carried out in triplicate under pseudo first-order conditions in 50 mM phosphate buffer pH 7.0 at 29.5°C with 4-methylcatechol in excess and an initial O_2 concentration of 223 µM. (A) A Clark-type oxygen electrode tracks the consumption of dissolved O_2 by catechol during the autoxidation process. (B) The initial linear portion (bold data points) of the plot of ln[O_2] versus time was used for the determination of pseudo first-order rate constant. The initial data point was not included to account for mixing upon the addition of catechol. (C) Non-linear least squares analysis was performed on the initial linear portion from (B) using Dynafit (version 4.05.087 software Biokin Ltd.), giving the pseudo first-order rate constant, standard error, and R^2 value (Table 4.3). Dioxygen consumption data for all three autoxidation reactions, rather than the average of these reactions, was included in the same plot when determining the pseudo first order rate constant.

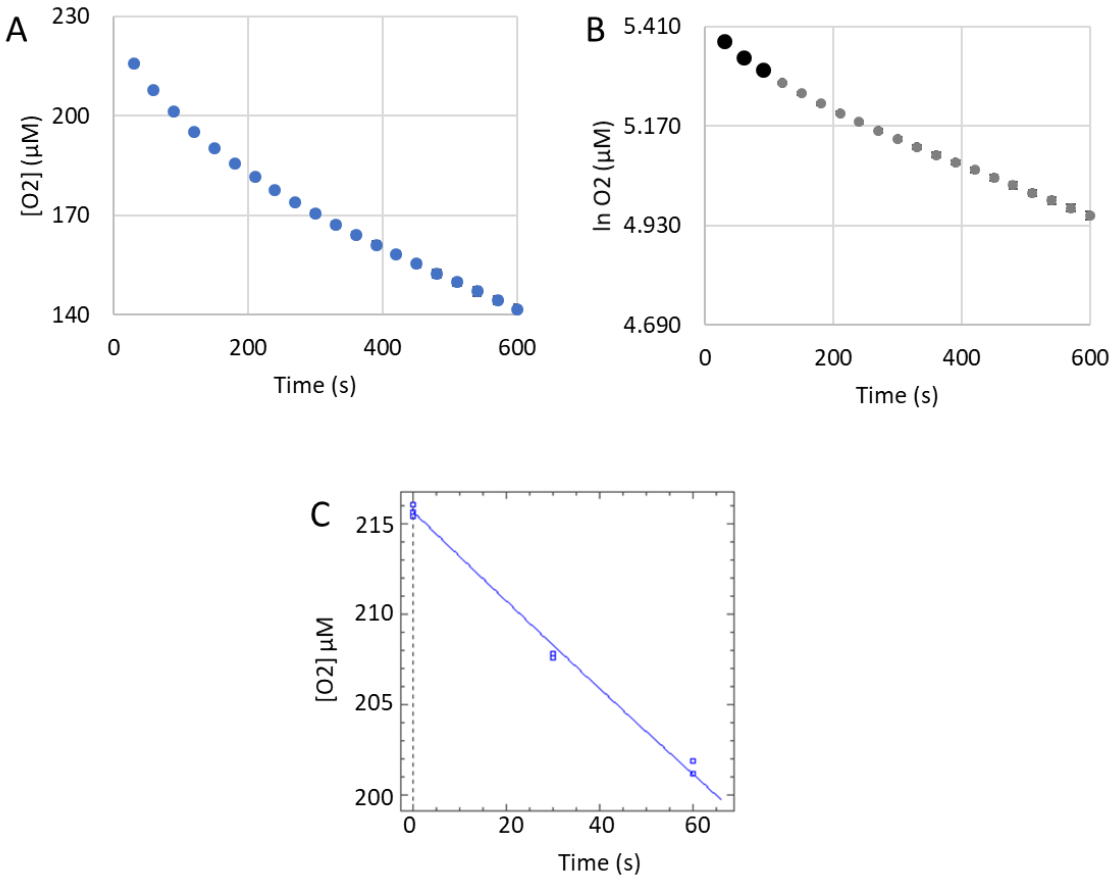

Figure A.2.6. pH 7.0 Autoxidation of 26.6 mM 4-Methylcatechol.

Reactions were carried out in triplicate under pseudo first-order conditions in 50 mM phosphate buffer pH 7.0 at 29.5°C with 4-methylcatechol in excess and an initial O_2 concentration of 223 µM. (A) A Clark-type oxygen electrode tracks the consumption of dissolved O_2 by catechol during the autoxidation process. (B) The initial linear portion (bold data points) of the plot of ln[O_2] versus time was used for the determination of pseudo first-order rate constant. The initial data point was not included to account for mixing upon the addition of catechol. (C) Non-linear least squares analysis was performed on the initial linear portion from (B) using Dynafit (version 4.05.087 software Biokin Ltd.), giving the pseudo first-order rate constant, standard error, and R^2 value (Table 4.3). Dioxygen consumption data for all three autoxidation reactions, rather than the average of these reactions, was included in the same plot when determining the pseudo first order rate constant.

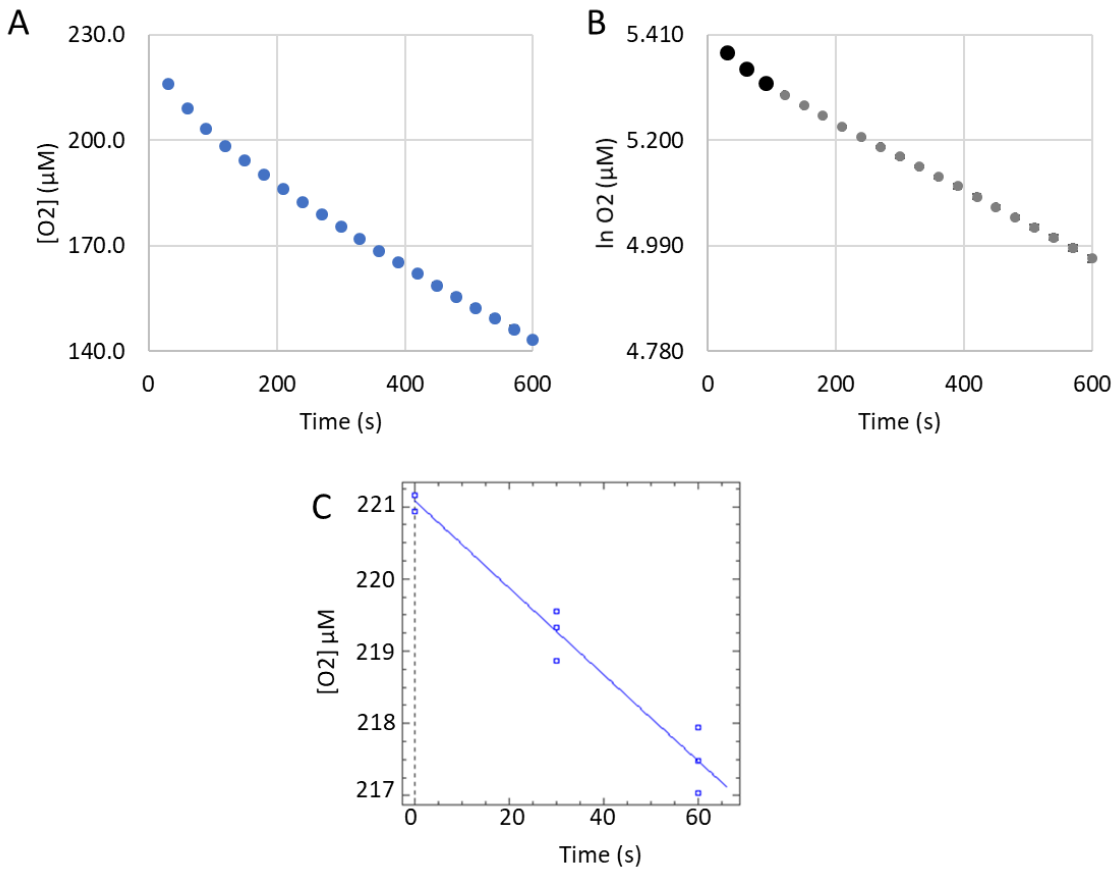

Figure A.2.7. pH 7.5 Autoxidation of 6.64 mM 4-Methylcatechol.

Reactions were carried out in triplicate under pseudo first-order conditions in 50 mM phosphate buffer pH 7.5 at 29.5°C with 4-methylcatechol in excess and an initial O_2 concentration of 223 µM. (A) A Clark-type oxygen electrode tracks the consumption of dissolved O_2 by catechol during the autoxidation process. (B) The initial linear portion (bold data points) of the plot of ln[O_2] versus time was used for the determination of pseudo first-order rate constant. The initial data point was not included to account for mixing upon the addition of catechol. (C) Non-linear least squares analysis was performed on the initial linear portion from (B) using Dynafit (version 4.05.087 software Biokin Ltd.), giving the pseudo first-order rate constant, standard error, and R^2 value (Table 4.3). Dioxygen consumption data for all three autoxidation reactions, rather than the average of these reactions, was included in the same plot when determining the pseudo first order rate constant.

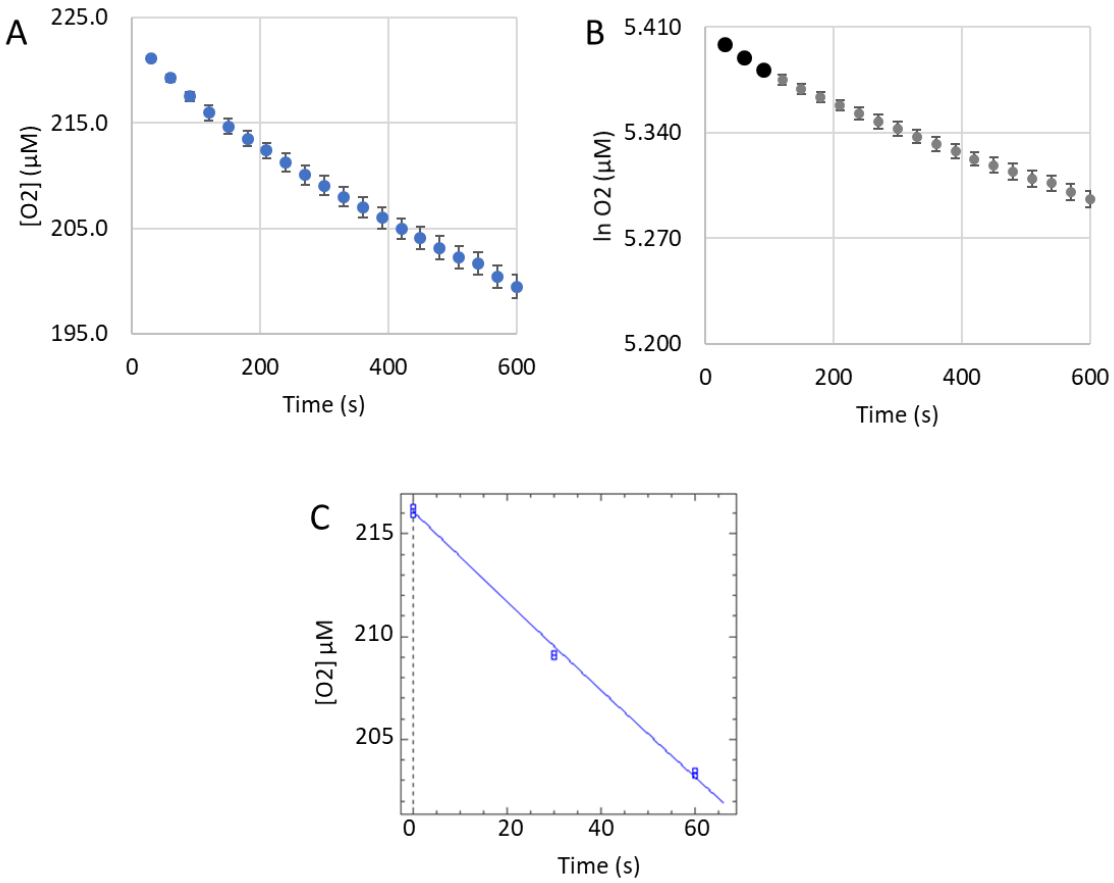

Figure A.2.8. pH 7.5 Autoxidation of 9.96 mM 4-Methylcatechol.

Reactions were carried out in triplicate under pseudo first-order conditions in 50 mM phosphate buffer pH 7.5 at 29.5°C with 4-methylcatechol in excess and an initial O_2 concentration of 223 µM. (A) A Clark-type oxygen electrode tracks the consumption of dissolved O_2 by catechol during the autoxidation process. (B) The initial linear portion (bold data points) of the plot of ln[O_2] versus time was used for the determination of pseudo first-order rate constant. The initial data point was not included to account for mixing upon the addition of catechol. (C) Non-linear least squares analysis was performed on the initial linear portion from (B) using Dynafit (version 4.05.087 software Biokin Ltd.), giving the pseudo first-order rate constant, standard error, and R^2 value (Table 4.3). Dioxygen consumption data for all three autoxidation reactions, rather than the average of these reactions, was included in the same plot when determining the pseudo first order rate constant.

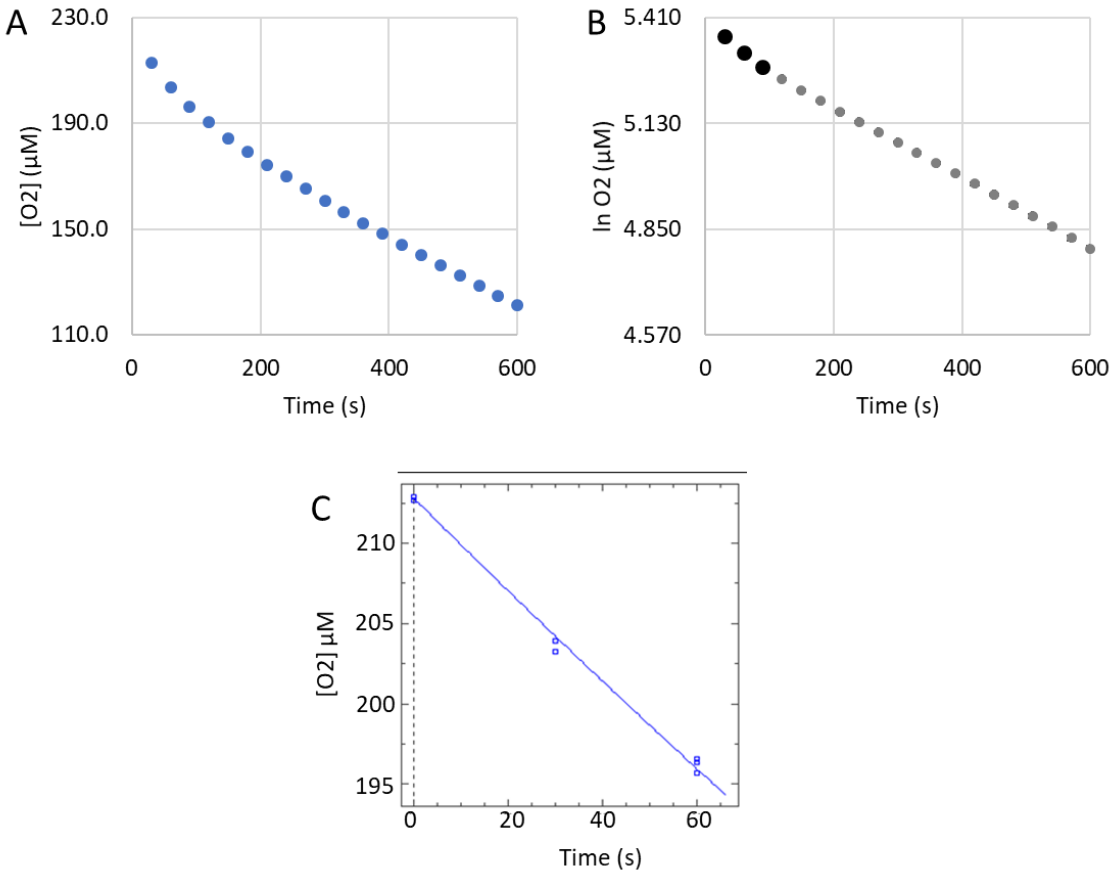

Figure A.2.9. pH 7.5 Autoxidation of 13.3 mM 4-Methylcatechol.

Reactions were carried out in triplicate under pseudo first-order conditions in 50 mM phosphate buffer pH 7.5 at 29.5°C with 4-methylcatechol in excess and an initial O_2 concentration of 223 µM. (A) A Clark-type oxygen electrode tracks the consumption of dissolved O_2 by catechol during the autoxidation process. (B) The initial linear portion (bold data points) of the plot of ln[O_2] versus time was used for the determination of pseudo first-order rate constant. The initial data point was not included to account for mixing upon the addition of catechol. (C) Non-linear least squares analysis was performed on the initial linear portion from (B) using Dynafit (version 4.05.087 software Biokin Ltd.), giving the pseudo first-order rate constant, standard error, and R^2 value (Table 4.3). Dioxygen consumption data for all three autoxidation reactions, rather than the average of these reactions, was included in the same plot when determining the pseudo first order rate constant.

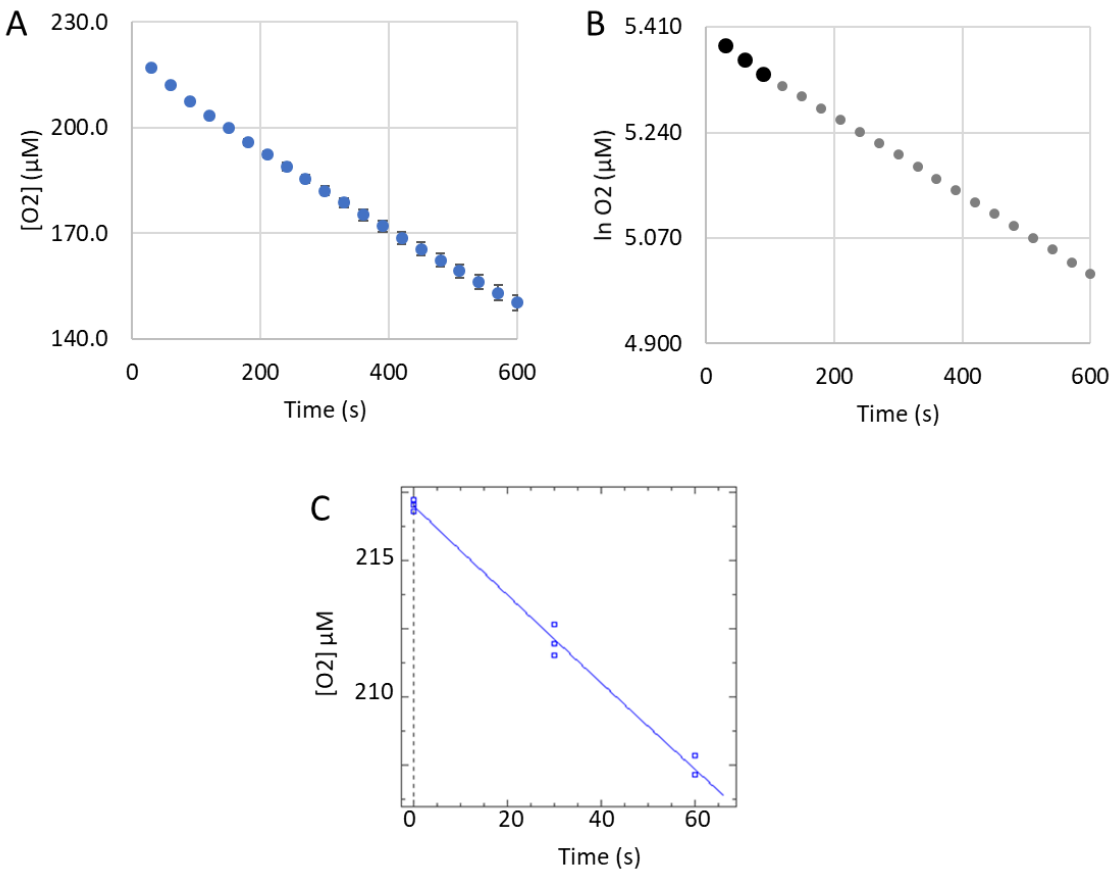

Figure A.2.10. pH 8.0 Autoxidation of 3.32 mM 4-Methylcatechol.

Reactions were carried out in triplicate under pseudo first-order conditions in 50 mM phosphate buffer pH 8.0 at 29.5°C with 4-methylcatechol in excess and an initial O_2 concentration of 223 µM. (A) A Clark-type oxygen electrode tracks the consumption of dissolved O_2 by catechol during the autoxidation process. (B) The initial linear portion (bold data points) of the plot of ln[O_2] versus time was used for the determination of pseudo first-order rate constant. The initial data point was not included to account for mixing upon the addition of catechol. (C) Non-linear least squares analysis was performed on the initial linear portion from (B) using Dynafit (version 4.05.087 software Biokin Ltd.), giving the pseudo first-order rate constant, standard error, and R^2 value (Table 4.3). Dioxygen consumption data for all three autoxidation reactions, rather than the average of these reactions, was included in the same plot when determining the pseudo first order rate constant.

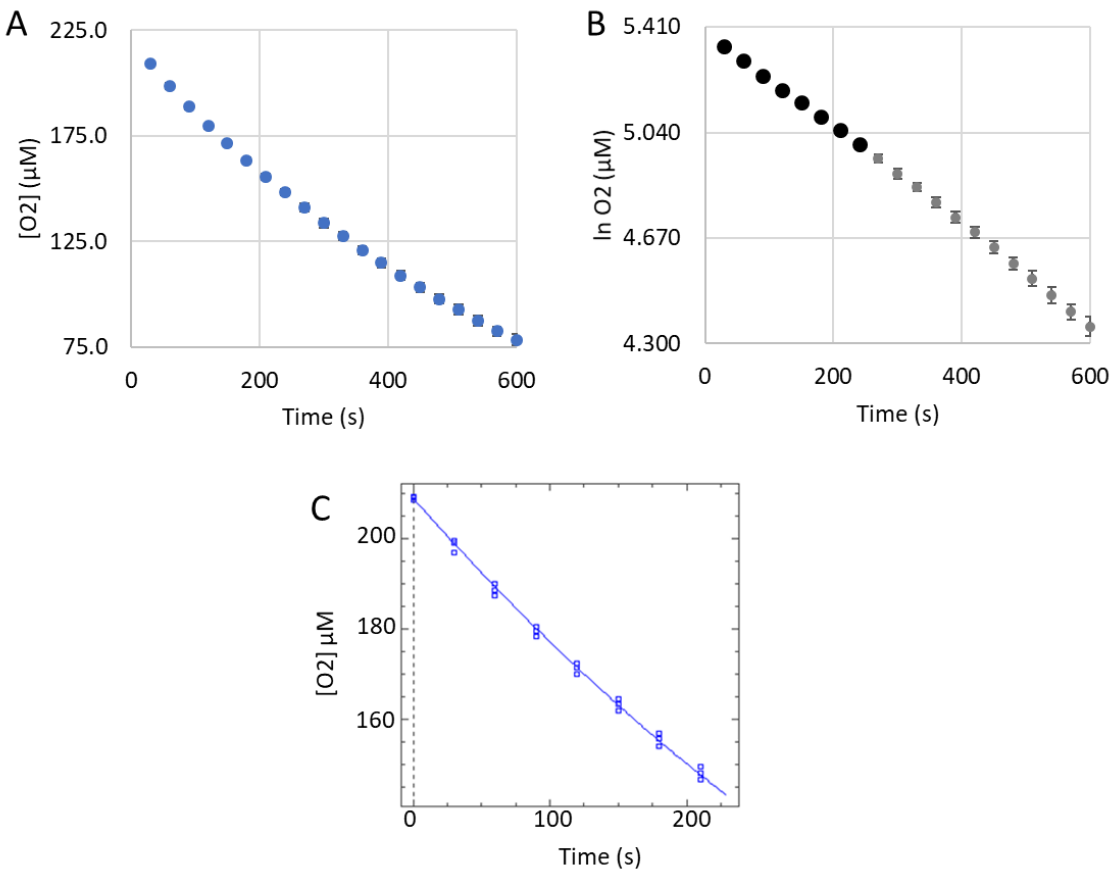

Figure A.2.11. pH 8.0 Autoxidation of 6.64 mM 4-Methylcatechol.

Reactions were carried out in triplicate under pseudo first-order conditions in 50 mM phosphate buffer pH 8.0 at 29.5°C with 4-methylcatechol in excess and an initial O_2 concentration of 223 µM. (A) A Clark-type oxygen electrode tracks the consumption of dissolved O_2 by catechol during the autoxidation process. (B) The initial linear portion (bold data points) of the plot of $\ln[O_2]$ versus time was used for the determination of pseudo first-order rate constant. The initial data point was not included to account for mixing upon the addition of catechol. (C) Non-linear least squares analysis was performed on the initial linear portion from (B) using Dynafit (version 4.05.087 software Biokin Ltd.), giving the pseudo first-order rate constant, standard error, and R^2 value (Table 4.3). Dioxygen consumption data for all three autoxidation reactions, rather than the average of these reactions, was included in the same plot when determining the pseudo first order rate constant.

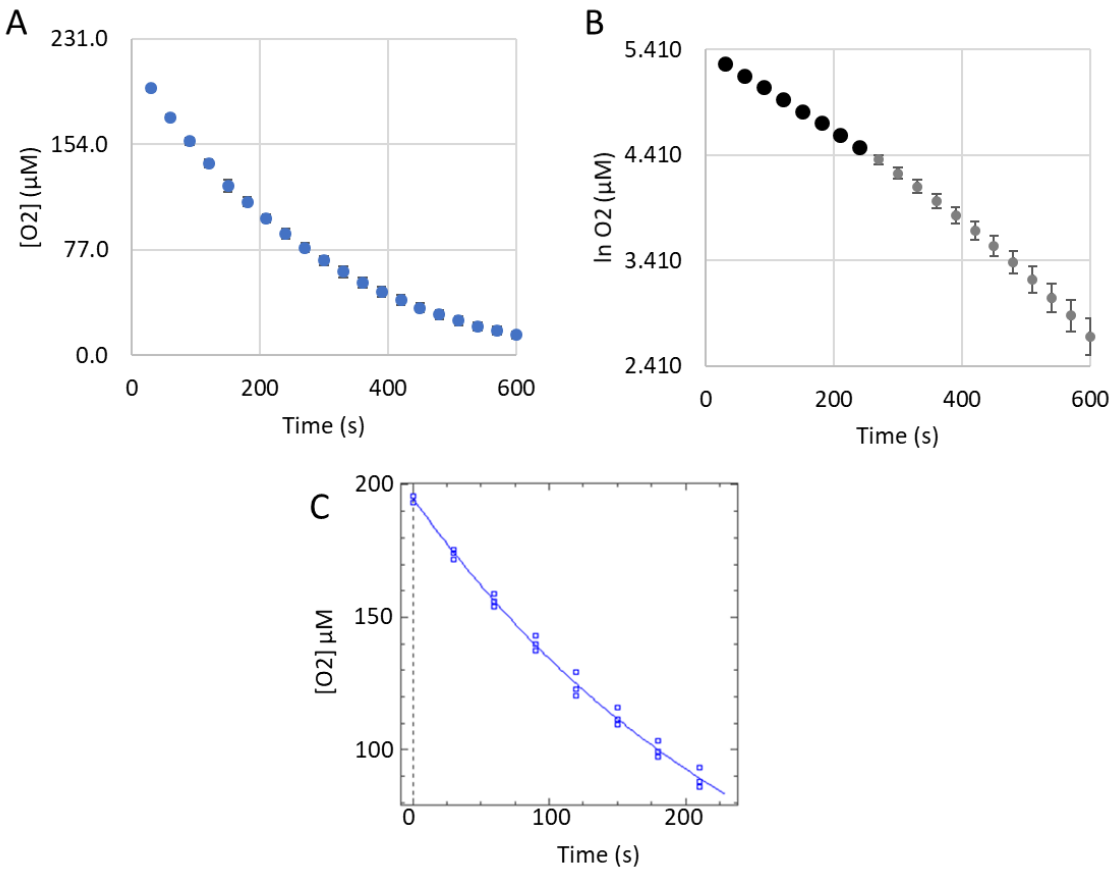

Figure A.2.12. pH 8.0 Autoxidation of 13.3 mM 4-Methylcatechol.

Reactions were carried out in triplicate under pseudo first-order conditions in 50 mM phosphate buffer pH 8.0 at 29.5°C with 4-methylcatechol in excess and an initial O_2 concentration of 223 µM. (A) A Clark-type oxygen electrode tracks the consumption of dissolved O_2 by catechol during the autoxidation process. (B) The initial linear portion (bold data points) of the plot of ln[O_2] versus time was used for the determination of pseudo first-order rate constant. The initial data point was not included to account for mixing upon the addition of catechol. (C) Non-linear least squares analysis was performed on the initial linear portion from (B) using Dynafit (version 4.05.087 software Biokin Ltd.), giving the pseudo first-order rate constant, standard error, and R^2 value (Table 4.3). Dioxygen consumption data for all three autoxidation reactions, rather than the average of these reactions, was included in the same plot when determining the pseudo first order rate constant.

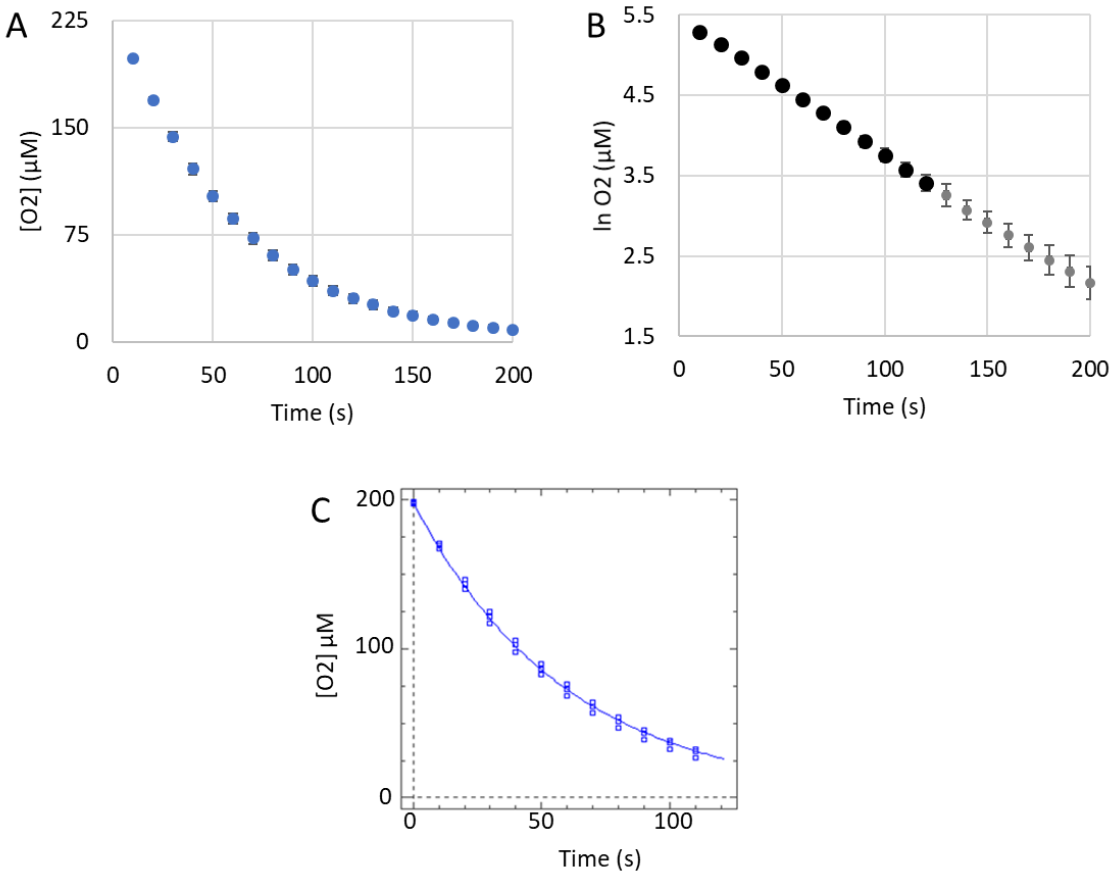

Figure A.2.13. pH 9.0 Autoxidation of 3.32 mM 4-Methylcatechol.

Reactions were carried out in triplicate under pseudo first-order conditions in 50 mM CAPSO buffer pH 9.0 at 29.5°C with 4-methylcatechol in excess and an initial O_2 concentration of 223 µM. (A) A Clark-type oxygen electrode tracks the consumption of dissolved O_2 by catechol during the autoxidation process. (B) The initial linear portion (bold data points) of the plot of ln[O_2] versus time was used for the determination of pseudo first-order rate constant. The initial data point was not included to account for mixing upon the addition of catechol. (C) Non-linear least squares analysis was performed on the initial linear portion from (B) using Dynafit (version 4.05.087 software Biokin Ltd.), giving the pseudo first-order rate constant, standard error, and R^2 value (Table 4.3). Dioxygen consumption data for all three autoxidation reactions, rather than the average of these reactions, was included in the same plot when determining the pseudo first order rate constant.

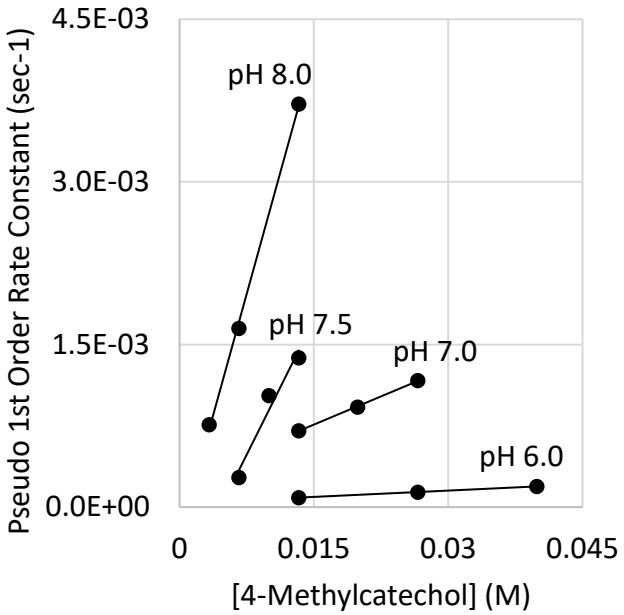

Figure A.2.14. pH-Dependence of 4-Methylcatechol Autoxidation.

Autoxidation of 4-methylcatechol was investigated at pH 6.0, 7.0, 7.5, 8.0, and 9.0.

Appendix A.3. Kinetic Data for 4-Ethylcatechol Autoxidation

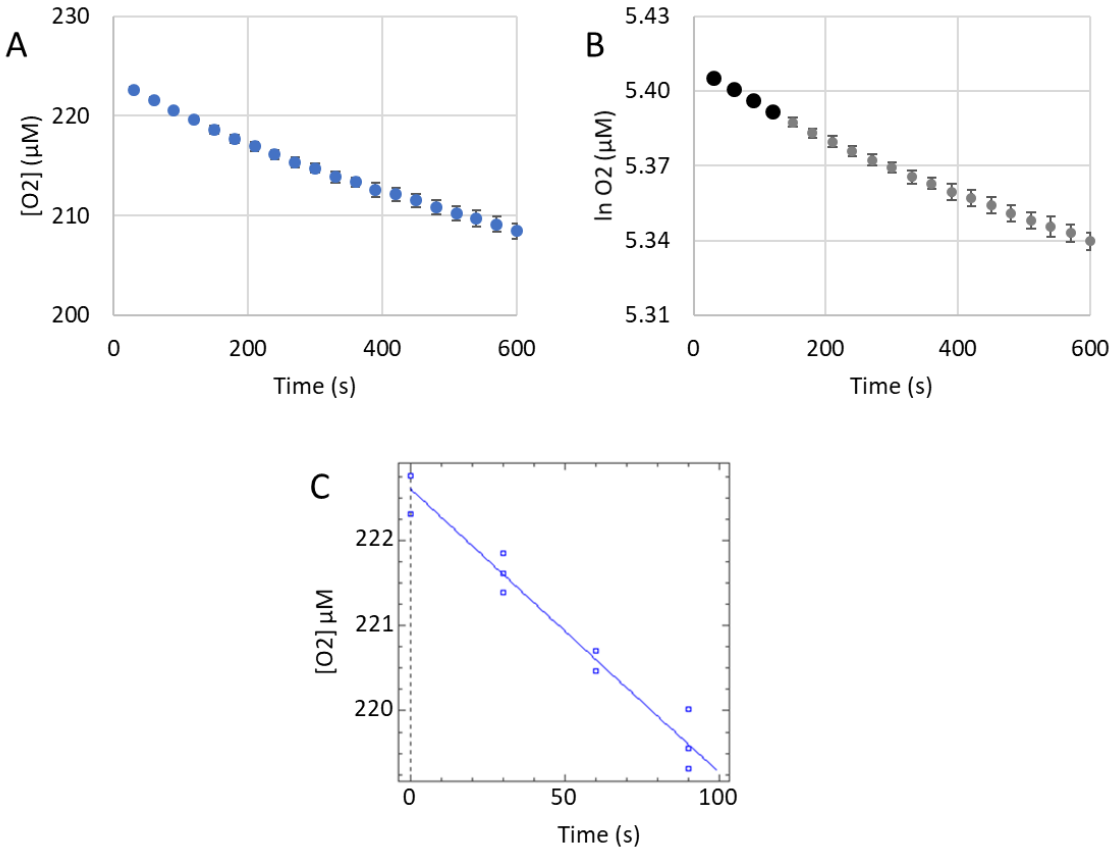

Figure A.3.1. pH 6.5 Autoxidation of 16.6 mM 4-Ethylcatechol.

Reactions were carried out in triplicate under pseudo first-order conditions in 50 mM phosphate buffer pH 6.5 at 29.5°C with 4-ethylcatechol in excess and an initial O_2 concentration of 223 µM. (A) A Clark-type oxygen electrode tracks the consumption of dissolved O_2 by catechol during the autoxidation process. (B) The initial linear portion (bold data points) of the plot of ln[O_2] versus time was used for the determination of pseudo first-order rate constant. The initial data point was not included to account for mixing upon the addition of catechol. (C) Non-linear least squares analysis was performed on the initial linear portion from (B) using Dynafit (version 4.05.087 software Biokin Ltd.), giving the pseudo first-order rate constant, standard error, and R^2 value (Table 4.3). Dioxygen consumption data for all three autoxidation reactions, rather than the average of these reactions, was included in the same plot when determining the pseudo first order rate constant.

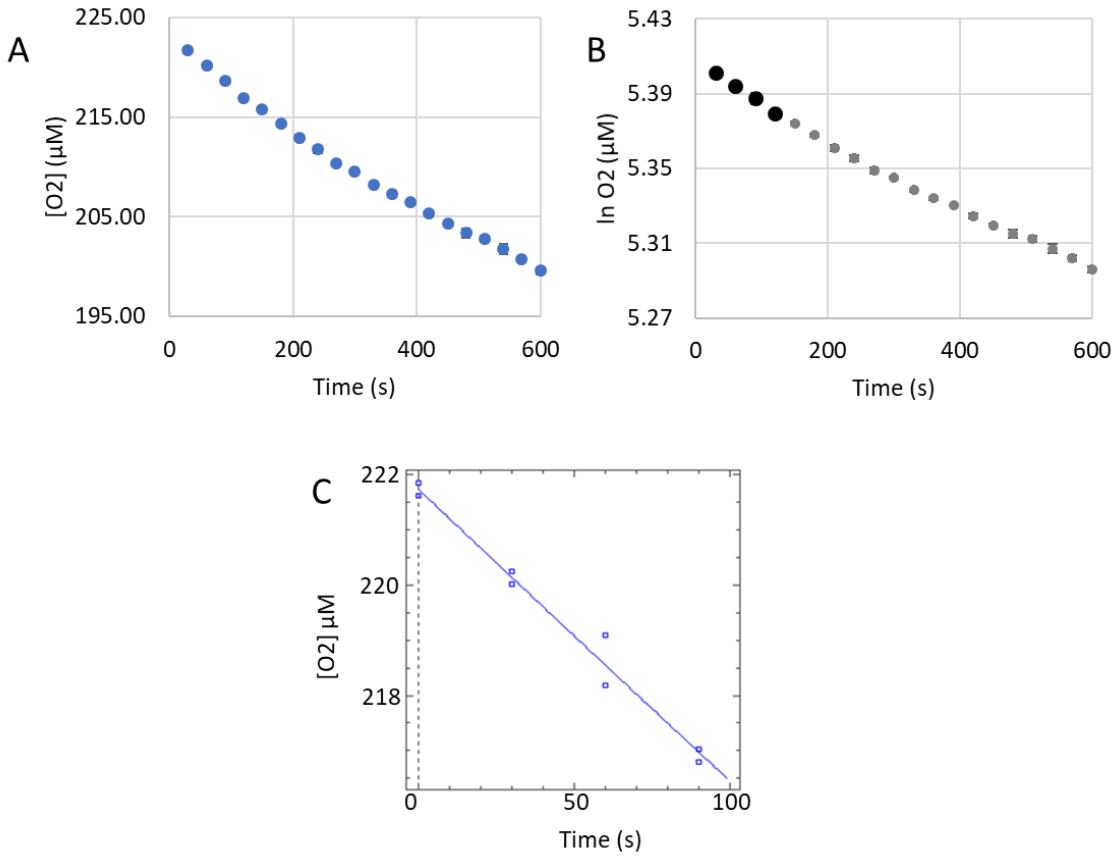

Figure A.3.2. pH 6.5 Autoxidation of 33.2 mM 4-Ethylcatechol.

Reactions were carried out in triplicate under pseudo first-order conditions in 50 mM phosphate buffer pH 6.5 at 29.5°C with 4-ethylcatechol in excess and an initial O_2 concentration of 223 µM. One of autoxidation reactions deviated from the average of the remaining two and was not included in the analysis. (A) A Clark-type oxygen electrode tracks the consumption of dissolved O_2 by catechol during the autoxidation process. (B) The initial linear portion (bold data points) of the plot of $\ln[O_2]$ versus time was used for the determination of pseudo first-order rate constant. The initial data point was not included to account for mixing upon the addition of catechol. (C) Non-linear least squares analysis was performed on the initial linear portion from (B) using Dynafit (version 4.05.087 software Biokin Ltd.), giving the pseudo first-order rate constant, standard error, and R^2 value (Table 4.3). Dioxygen consumption data for all three autoxidation reactions, rather than the average of these reactions, was included in the same plot when determining the pseudo first order rate constant.

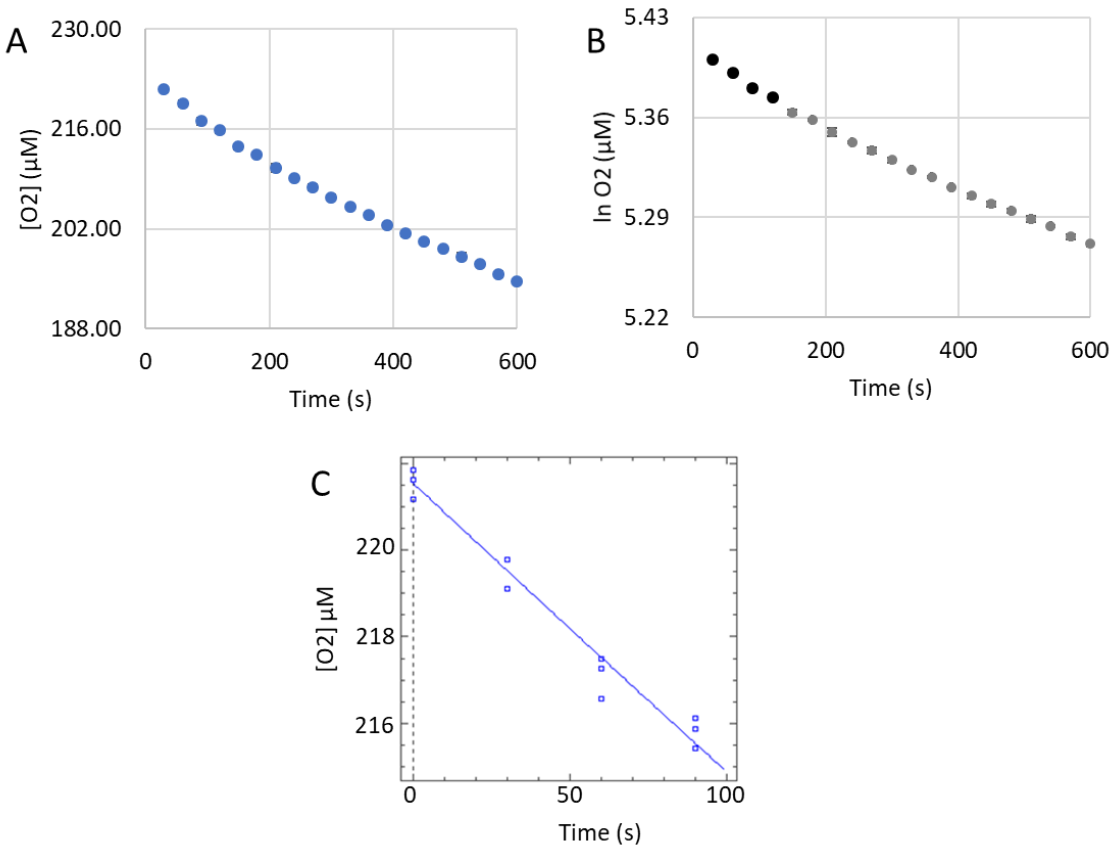

Figure A.3.3. pH 6.5 Autoxidation of 49.8 mM 4-Ethylcatechol.

Reactions were carried out in triplicate under pseudo first-order conditions in 50 mM phosphate buffer pH 6.5 at 29.5°C with 4-ethylcatechol in excess and an initial O_2 concentration of 223 µM. (A) A Clark-type oxygen electrode tracks the consumption of dissolved O_2 by catechol during the autoxidation process. (B) The initial linear portion (bold data points) of the plot of ln[O_2] versus time was used for the determination of pseudo first-order rate constant. The initial data point was not included to account for mixing upon the addition of catechol. (C) Non-linear least squares analysis was performed on the initial linear portion from (B) using Dynafit (version 4.05.087 software Biokin Ltd.), giving the pseudo first-order rate constant, standard error, and R^2 value (Table 4.3). Dioxygen consumption data for all three autoxidation reactions, rather than the average of these reactions, was included in the same plot when determining the pseudo first order rate constant.

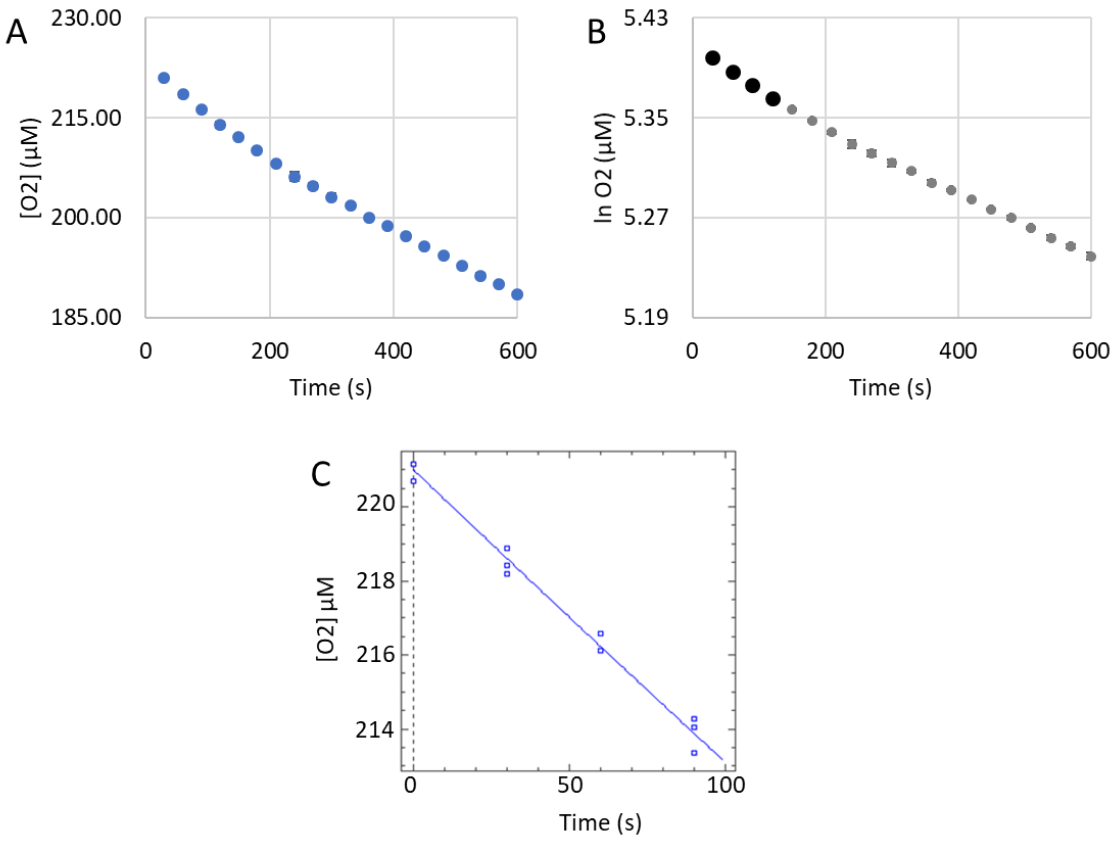

Figure A.3.4. pH 7.0 Autoxidation of 16.6 mM 4-Ethylcatechol.

Reactions were carried out in triplicate under pseudo first-order conditions in 50 mM phosphate buffer pH 7.0 at 29.5°C with 4-ethylcatechol in excess and an initial O_2 concentration of 223 µM. (A) A Clark-type oxygen electrode tracks the consumption of dissolved O_2 by catechol during the autoxidation process. (B) The initial linear portion (bold data points) of the plot of ln[O_2] versus time was used for the determination of pseudo first-order rate constant. The initial data point was not included to account for mixing upon the addition of catechol. (C) Non-linear least squares analysis was performed on the initial linear portion from (B) using Dynafit (version 4.05.087 software Biokin Ltd.), giving the pseudo first-order rate constant, standard error, and R^2 value (Table 4.3). Dioxygen consumption data for all three autoxidation reactions, rather than the average of these reactions, was included in the same plot when determining the pseudo first order rate constant.

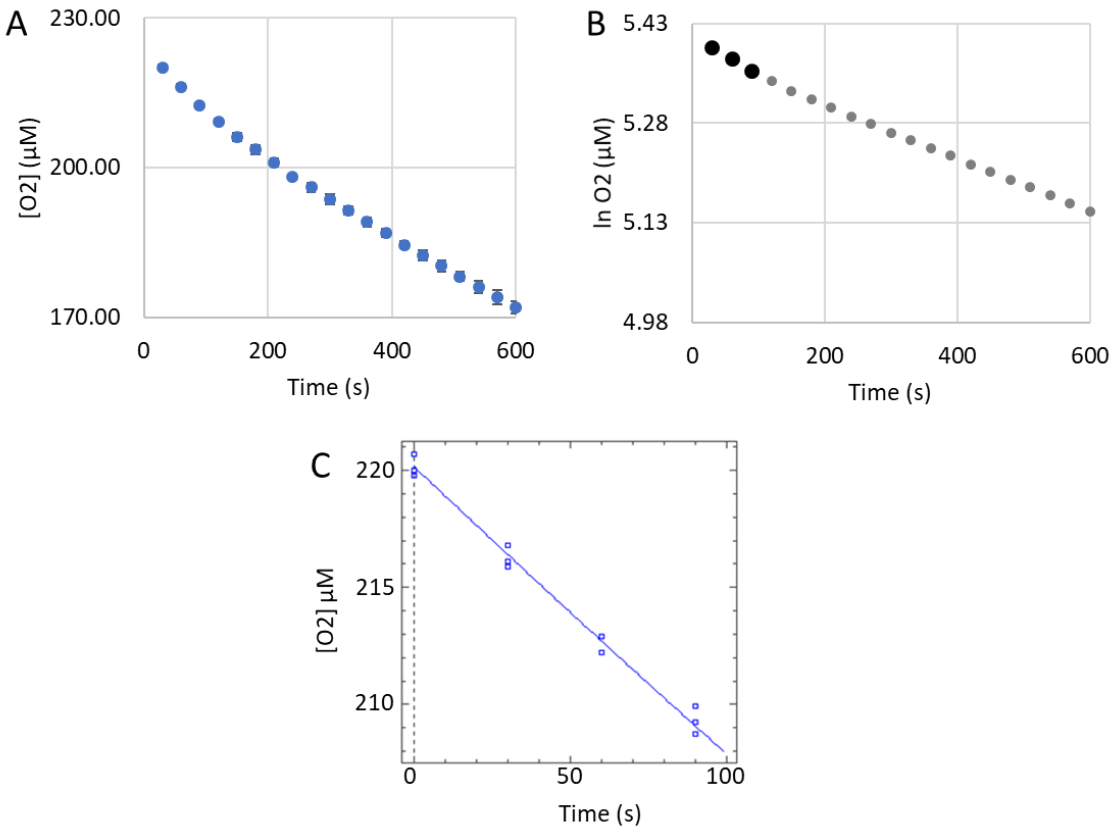

Figure A.3.5. pH 7.0 Autoxidation of 33.2 mM 4-Ethylcatechol.

Reactions were carried out in triplicate under pseudo first-order conditions in 50 mM phosphate buffer pH 7.0 at 29.5°C with 4-ethylcatechol in excess and an initial O_2 concentration of 223 µM. (A) A Clark-type oxygen electrode tracks the consumption of dissolved O_2 by catechol during the autoxidation process. (B) The initial linear portion (bold data points) of the plot of $\ln[O_2]$ versus time was used for the determination of pseudo first-order rate constant. The initial data point was not included to account for mixing upon the addition of catechol. (C) Non-linear least squares analysis was performed on the initial linear portion from (B) using Dynafit (version 4.05.087 software Biokin Ltd.), giving the pseudo first-order rate constant, standard error, and R^2 value (Table 4.3). Dioxygen consumption data for all three autoxidation reactions, rather than the average of these reactions, was included in the same plot when determining the pseudo first order rate constant.

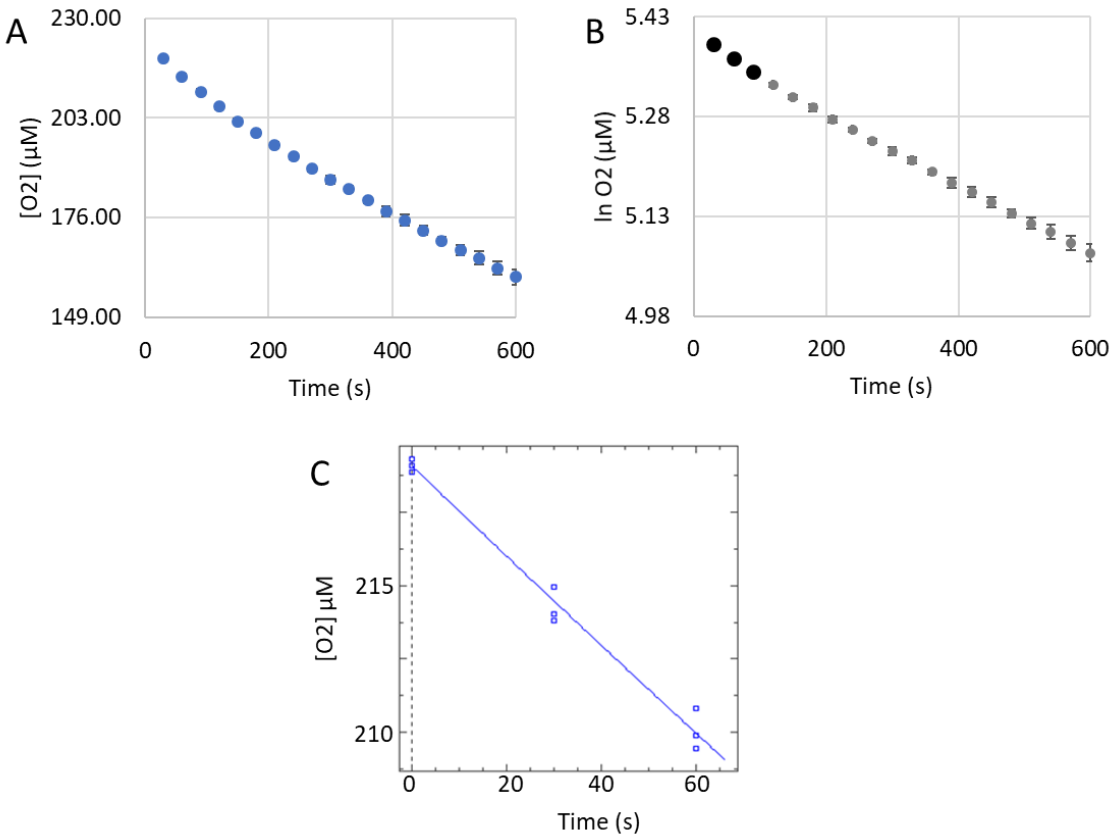

Figure A.3.6. pH 7.0 Autoxidation of 49.8 mM 4-Ethylcatechol.

Reactions were carried out in triplicate under pseudo first-order conditions in 50 mM phosphate buffer pH 7.0 at 29.5°C with 4-ethylcatechol in excess and an initial O_2 concentration of 223 µM. (A) A Clark-type oxygen electrode tracks the consumption of dissolved O_2 by catechol during the autoxidation process. (B) The initial linear portion (bold data points) of the plot of $\ln[O_2]$ versus time was used for the determination of pseudo first-order rate constant. The initial data point was not included to account for mixing upon the addition of catechol. (C) Non-linear least squares analysis was performed on the initial linear portion from (B) using Dynafit (version 4.05.087 software Biokin Ltd.), giving the pseudo first-order rate constant, standard error, and R^2 value (Table 4.3). Dioxygen consumption data for all three autoxidation reactions, rather than the average of these reactions, was included in the same plot when determining the pseudo first order rate constant.

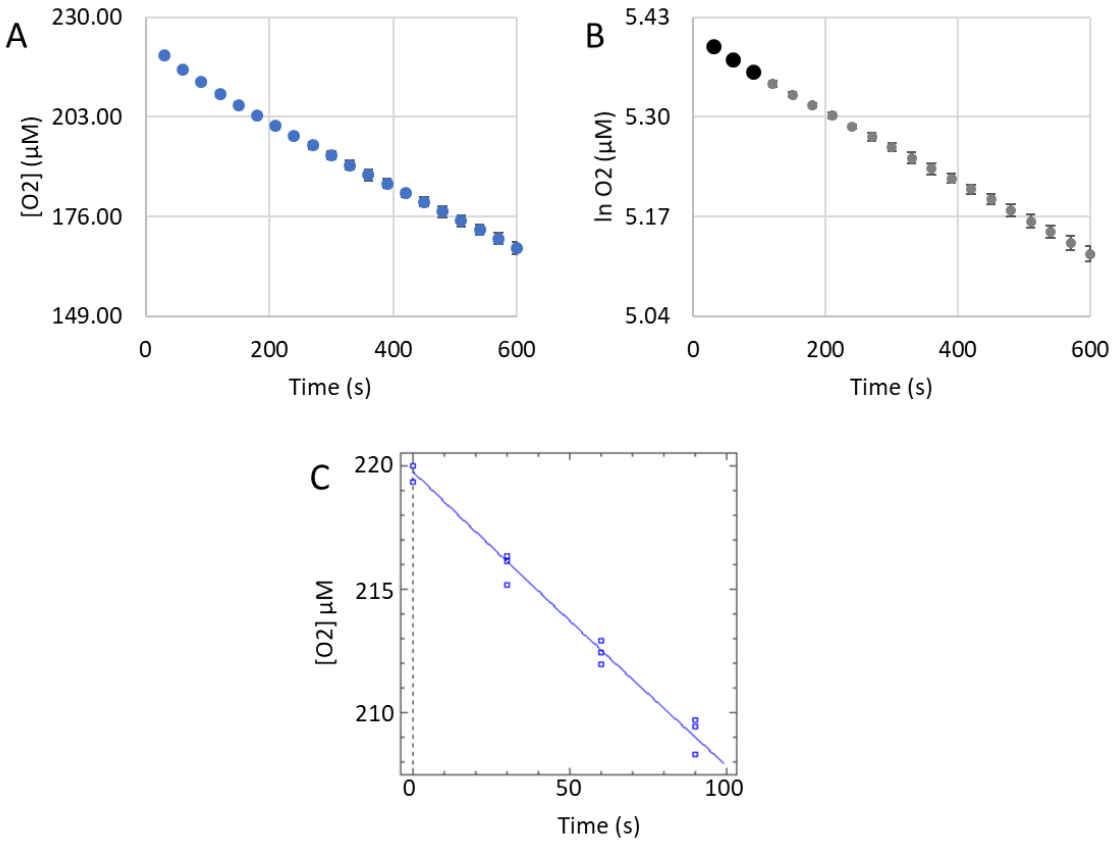

Figure A.3.7. pH 7.5 Autoxidation of 9.96 mM 4-Ethylcatechol.

Reactions were carried out in triplicate under pseudo first-order conditions in 50 mM phosphate buffer pH 7.5 at 29.5°C with 4-ethylcatechol in excess and an initial O_2 concentration of 223 µM. (A) A Clark-type oxygen electrode tracks the consumption of dissolved O_2 by catechol during the autoxidation process. (B) The initial linear portion (bold data points) of the plot of $\ln[O_2]$ versus time was used for the determination of pseudo first-order rate constant. The initial data point was not included to account for mixing upon the addition of catechol. (C) Non-linear least squares analysis was performed on the initial linear portion from (B) using Dynafit (version 4.05.087 software Biokin Ltd.), giving the pseudo first-order rate constant, standard error, and R^2 value (Table 4.3). Dioxygen consumption data for all three autoxidation reactions, rather than the average of these reactions, was included in the same plot when determining the pseudo first order rate constant.

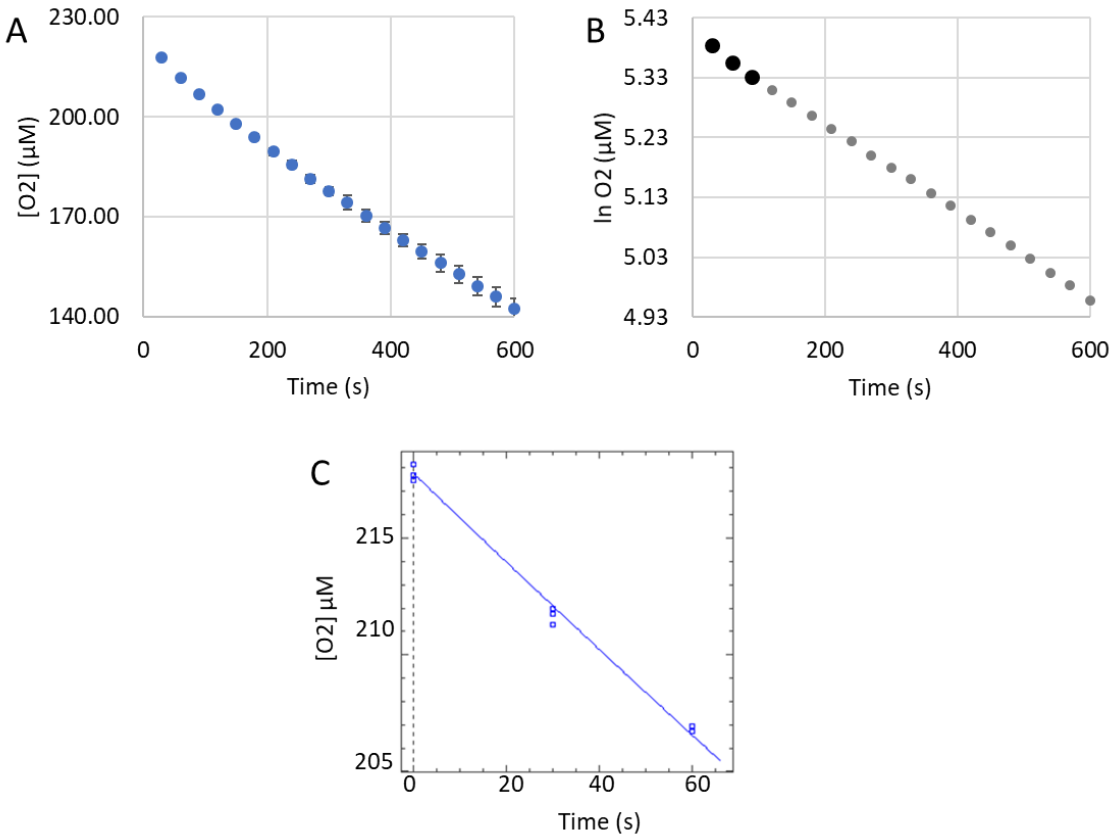

Figure A.3.8. pH 7.5 Autoxidation of 16.6 mM 4-Ethylcatechol.

Reactions were carried out in triplicate under pseudo first-order conditions in 50 mM phosphate buffer pH 7.5 at 29.5°C with 4-ethylcatechol in excess and an initial O_2 concentration of 223 µM. (A) A Clark-type oxygen electrode tracks the consumption of dissolved O_2 by catechol during the autoxidation process. (B) The initial linear portion (bold data points) of the plot of $\ln[O_2]$ versus time was used for the determination of pseudo first-order rate constant. The initial data point was not included to account for mixing upon the addition of catechol. (C) Non-linear least squares analysis was performed on the initial linear portion from (B) using Dynafit (version 4.05.087 software Biokin Ltd.), giving the pseudo first-order rate constant, standard error, and R^2 value (Table 4.3). Dioxygen consumption data for all three autoxidation reactions, rather than the average of these reactions, was included in the same plot when determining the pseudo first order rate constant.

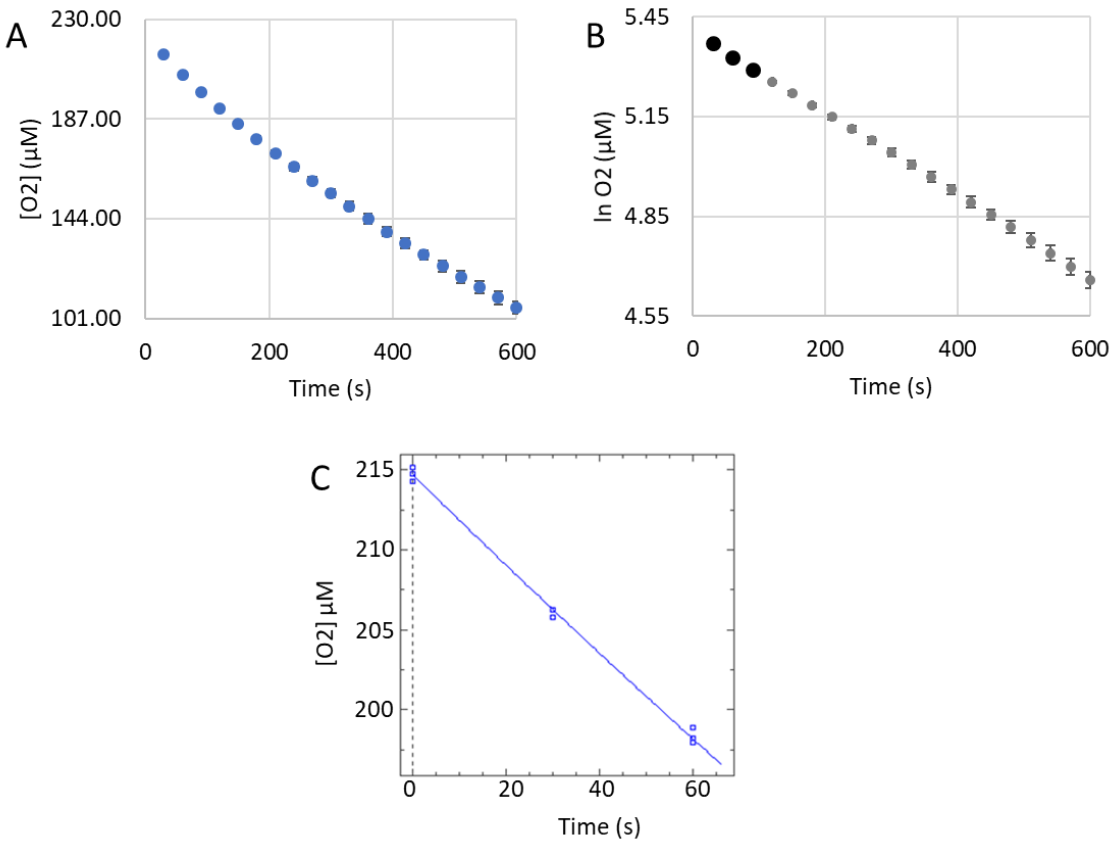

Figure A.3.9. pH 7.5 Autoxidation of 33.2 mM 4-Ethylcatechol.

Reactions were carried out in triplicate under pseudo first-order conditions in 50 mM phosphate buffer pH 7.5 at 29.5°C with 4-ethylcatechol in excess and an initial O_2 concentration of 223 µM. (A) A Clark-type oxygen electrode tracks the consumption of dissolved O_2 by catechol during the autoxidation process. (B) The initial linear portion (bold data points) of the plot of ln[O_2] versus time was used for the determination of pseudo first-order rate constant. The initial data point was not included to account for mixing upon the addition of catechol. (C) Non-linear least squares analysis was performed on the initial linear portion from (B) using Dynafit (version 4.05.087 software Biokin Ltd.), giving the pseudo first-order rate constant, standard error, and R^2 value (Table 4.3). Dioxygen consumption data for all three autoxidation reactions, rather than the average of these reactions, was included in the same plot when determining the pseudo first order rate constant.

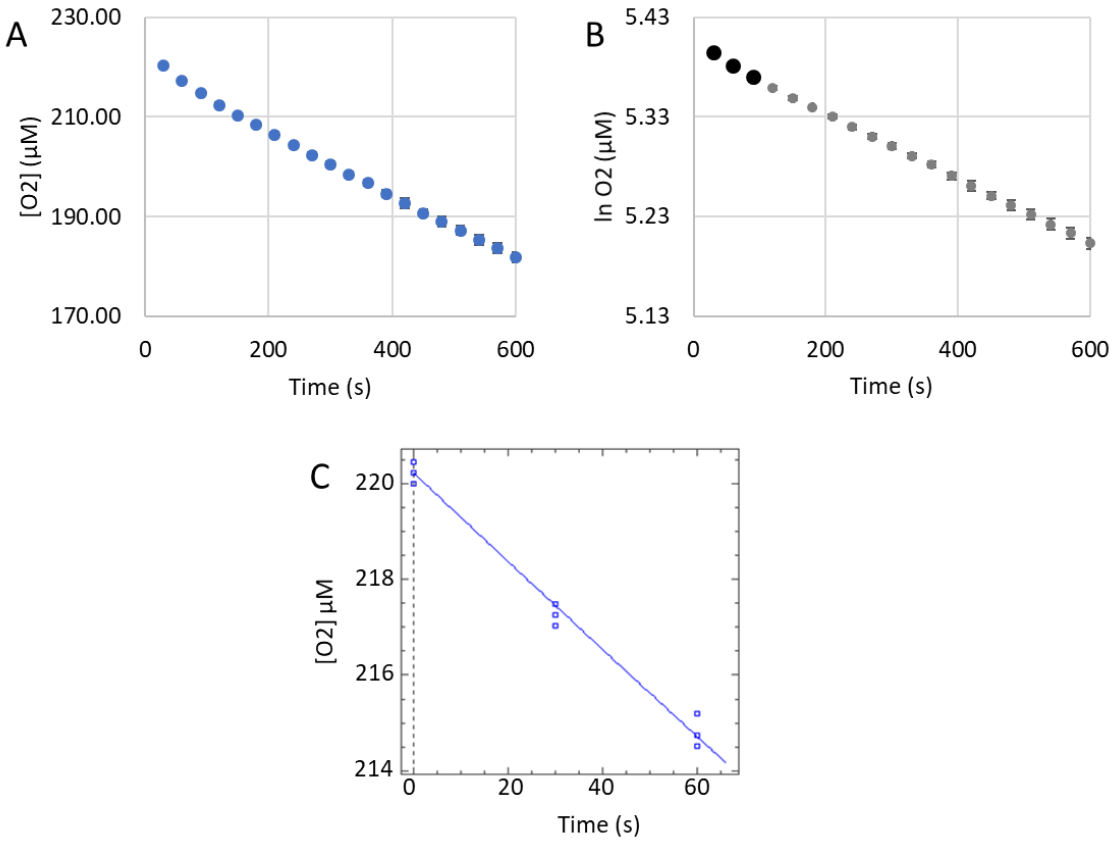

Figure A.3.10. pH 8.0 Autoxidation of 3.32 mM 4-Ethylcatechol.

Reactions were carried out in triplicate under pseudo first-order conditions in 50 mM phosphate buffer pH 8.0 at 29.5°C with 4-ethylcatechol in excess and an initial O_2 concentration of 223 µM. (A) A Clark-type oxygen electrode tracks the consumption of dissolved O_2 by catechol during the autoxidation process. (B) The initial linear portion (bold data points) of the plot of $\ln[O_2]$ versus time was used for the determination of pseudo first-order rate constant. The initial data point was not included to account for mixing upon the addition of catechol. (C) Non-linear least squares analysis was performed on the initial linear portion from (B) using Dynafit (version 4.05.087 software Biokin Ltd.), giving the pseudo first-order rate constant, standard error, and R^2 value (Table 4.3). Dioxygen consumption data for all three autoxidation reactions, rather than the average of these reactions, was included in the same plot when determining the pseudo first order rate constant.

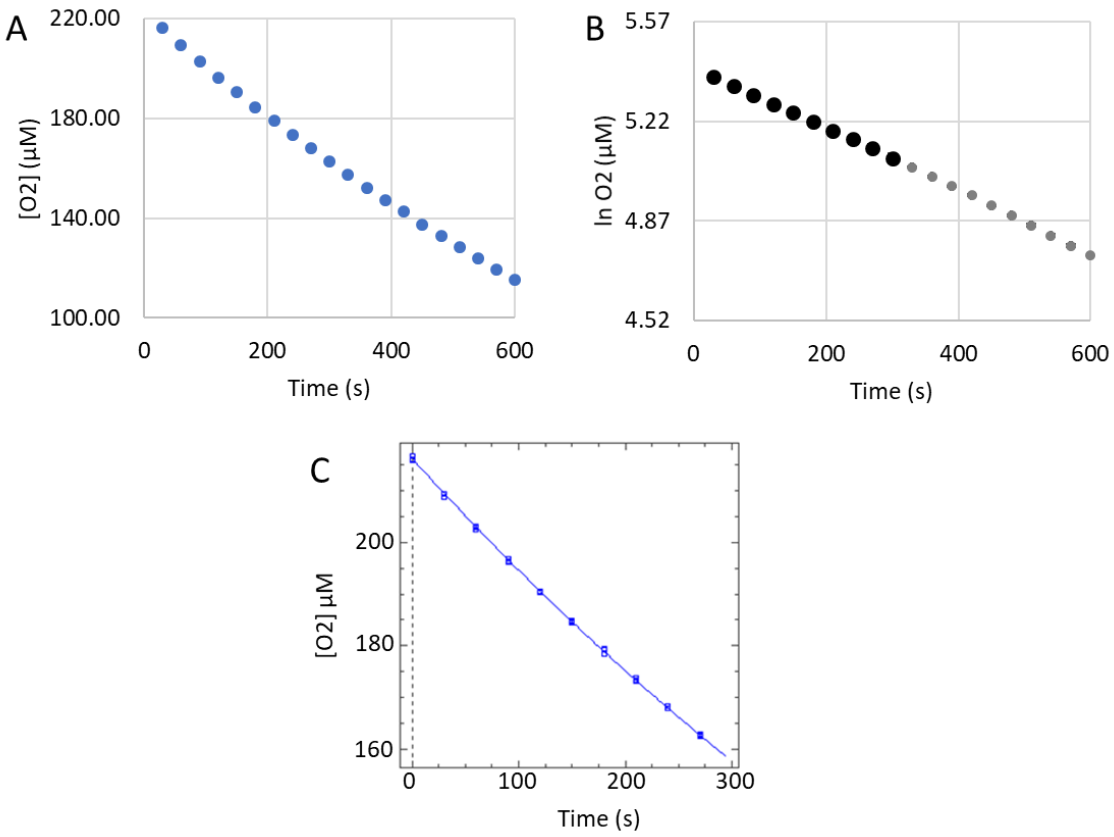

Figure A.3.11. pH 8.0 Autoxidation of 9.96 mM 4-Ethylcatechol.

Reactions were carried out in triplicate under pseudo first-order conditions in 50 mM phosphate buffer pH 8.0 at 29.5°C with 4-ethylcatechol in excess and an initial O_2 concentration of 223 µM. (A) A Clark-type oxygen electrode tracks the consumption of dissolved O_2 by catechol during the autoxidation process. (B) The initial linear portion (bold data points) of the plot of $\ln[O_2]$ versus time was used for the determination of pseudo first-order rate constant. The initial data point was not included to account for mixing upon the addition of catechol. (C) Non-linear least squares analysis was performed on the initial linear portion from (B) using Dynafit (version 4.05.087 software Biokin Ltd.), giving the pseudo first-order rate constant, standard error, and R^2 value (Table 4.3). Dioxygen consumption data for all three autoxidation reactions, rather than the average of these reactions, was included in the same plot when determining the pseudo first order rate constant.

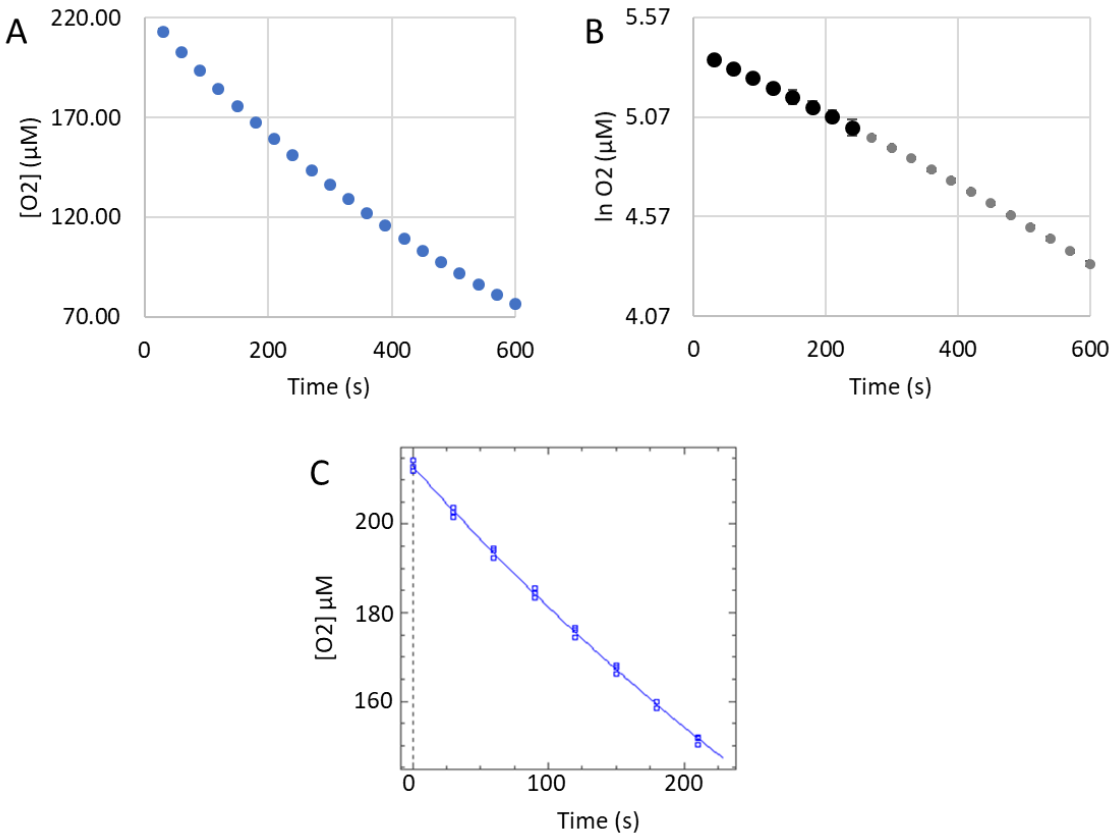

Figure A.3.12. pH 8.0 Autoxidation of 16.6 mM 4-Ethylcatechol.

Reactions were carried out in triplicate under pseudo first-order conditions in 50 mM phosphate buffer pH 8.0 at 29.5°C with 4-ethylcatechol in excess and an initial O_2 concentration of 223 µM. (A) A Clark-type oxygen electrode tracks the consumption of dissolved O_2 by catechol during the autoxidation process. (B) The initial linear portion (bold data points) of the plot of $\ln[O_2]$ versus time was used for the determination of pseudo first-order rate constant. The initial data point was not included to account for mixing upon the addition of catechol. (C) Non-linear least squares analysis was performed on the initial linear portion from (B) using Dynafit (version 4.05.087 software Biokin Ltd.), giving the pseudo first-order rate constant, standard error, and R^2 value (Table 4.3). Dioxygen consumption data for all three autoxidation reactions, rather than the average of these reactions, was included in the same plot when determining the pseudo first order rate constant.

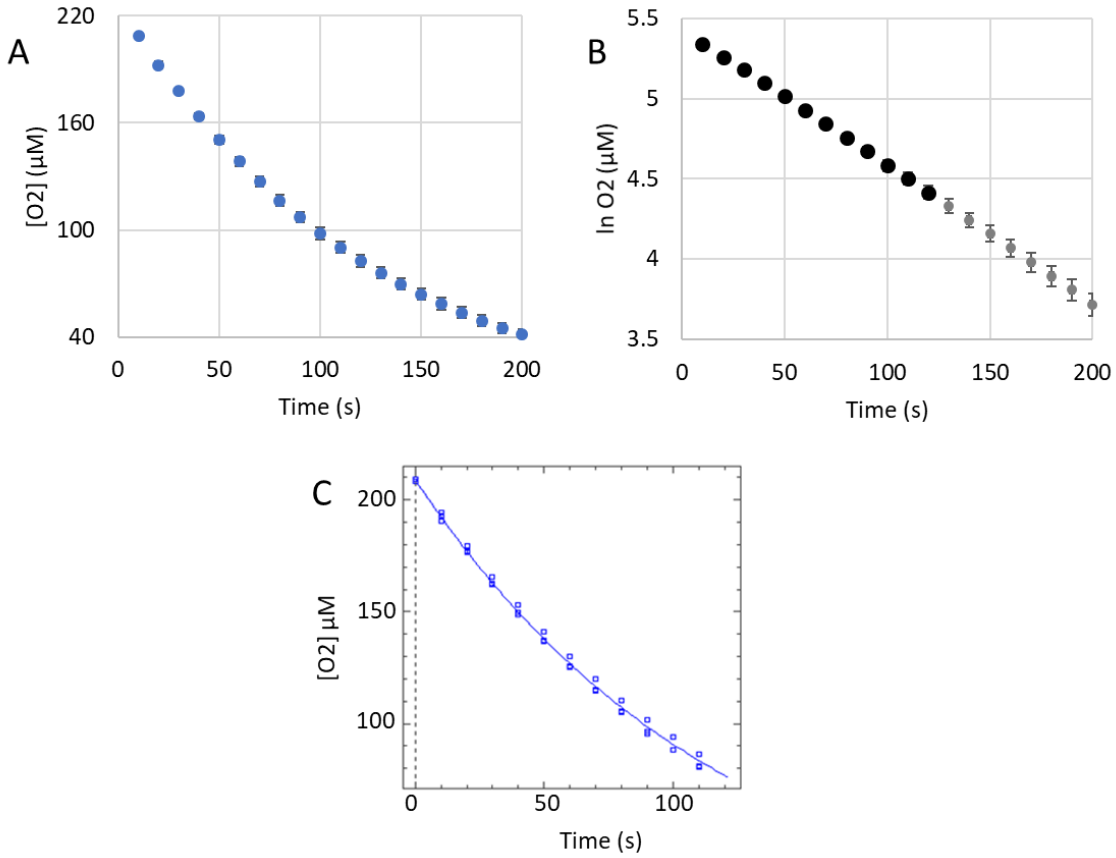

Figure A.3.13. pH 9.0 Autoxidation of 3.32 mM 4-Ethylcatechol.

Reactions were carried out in triplicate under pseudo first-order conditions in 50 mM CAPSO buffer pH 9.0 at 29.5°C with 4-ethylcatechol in excess and an initial O_2 concentration of 223 µM. (A) A Clark-type oxygen electrode tracks the consumption of dissolved O_2 by catechol during the autoxidation process. (B) The initial linear portion (bold data points) of the plot of ln[O_2] versus time was used for the determination of pseudo first-order rate constant. The initial data point was not included to account for mixing upon the addition of catechol. (C) Non-linear least squares analysis was performed on the initial linear portion from (B) using Dynafit (version 4.05.087 software Biokin Ltd.), giving the pseudo first-order rate constant, standard error, and R^2 value (Table 4.3). Dioxygen consumption data for all three autoxidation reactions, rather than the average of these reactions, was included in the same plot when determining the pseudo first order rate constant.

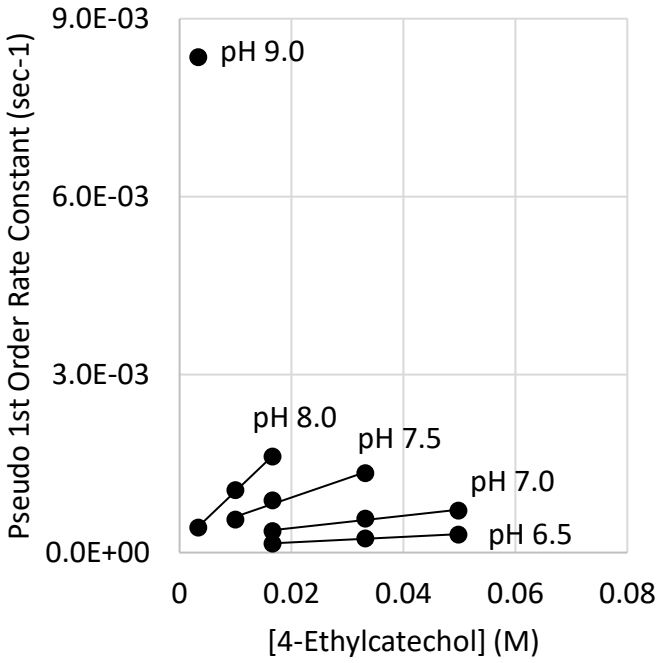

Figure A.3.14. pH-Dependence of 4-Ethylcatechol Autoxidation.

Autoxidation of 4-ethylcatechol was investigated at pH 6.5, 7.0, 7.5, 8.0, and 9.0.

Appendix A.4. Kinetic Data for 4-Chlorocatechol Autoxidation

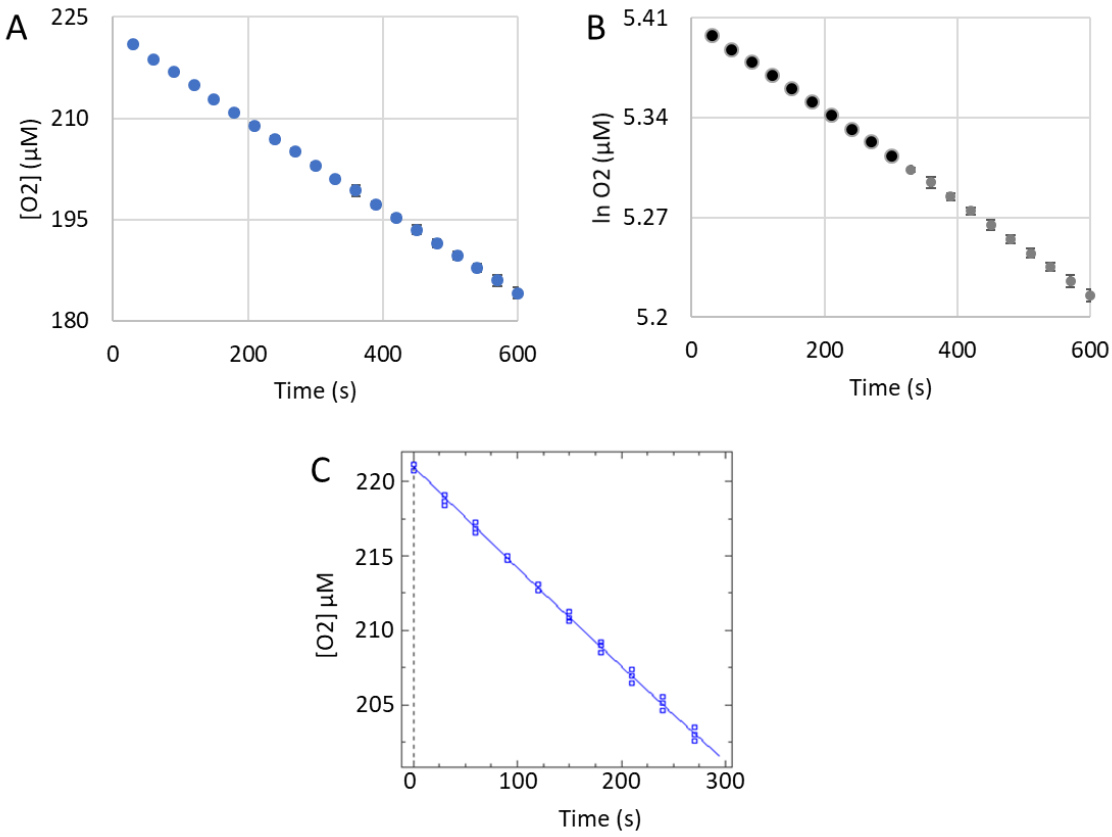

Figure A.4.1. pH 7.0 Autoxidation of 16.6 mM 4-Chlorocatechol.

Reactions were carried out in triplicate under pseudo first-order conditions in 50 mM phosphate buffer pH 7.0 at 29.5°C with 4-chlorocatechol in excess and an initial O_2 concentration of 223 µM. (A) A Clark-type oxygen electrode tracks the consumption of dissolved O_2 by catechol during the autoxidation process. (B) The initial linear portion (bold data points) of the plot of $\ln[O_2]$ versus time was used for the determination of pseudo first-order rate constant. The initial data point was not included to account for mixing upon the addition of catechol. (C) Non-linear least squares analysis was performed on the initial linear portion from (B) using Dynafit (version 4.05.087 software Biokin Ltd.), giving the pseudo first-order rate constant, standard error, and R^2 value (Table 4.3). Dioxygen consumption data for all three autoxidation reactions, rather than the average of these reactions, was included in the same plot when determining the pseudo first order rate constant.

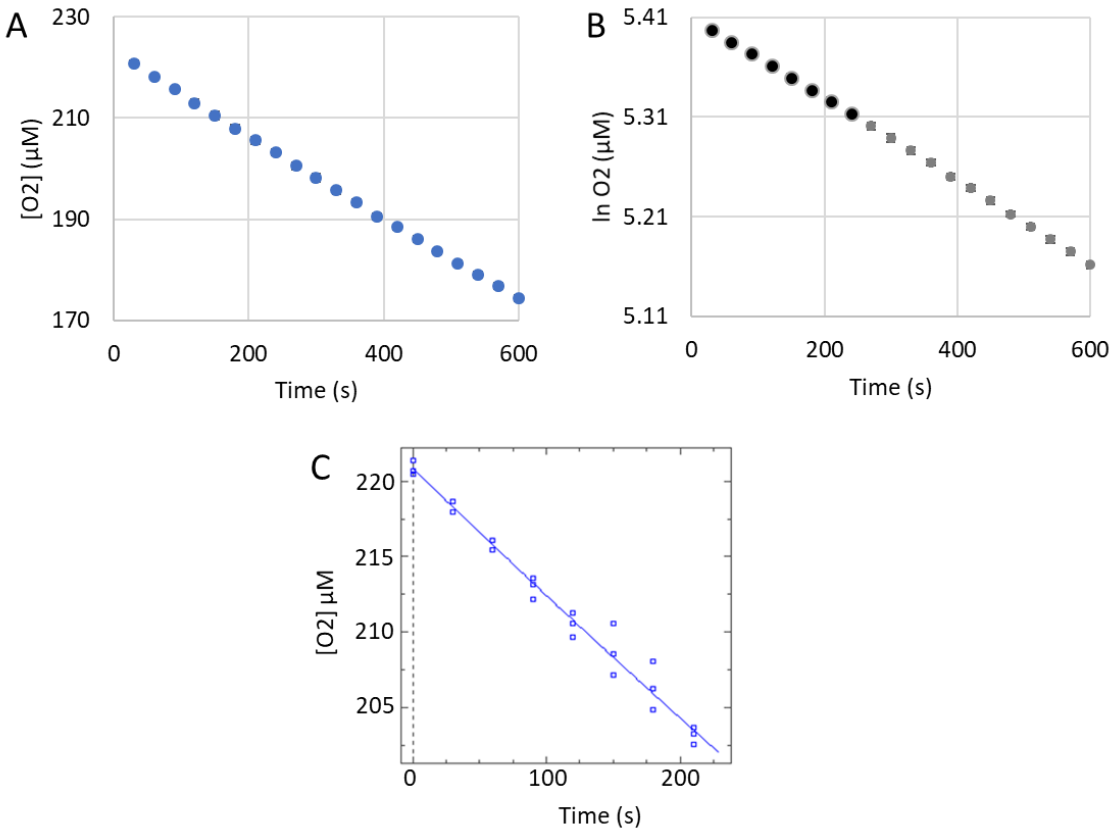

Figure A.4.2. pH 7.0 Autoxidation of 23.3 mM 4-Chlorocatechol.

Reactions were carried out in triplicate under pseudo first-order conditions in 50 mM phosphate buffer pH 7.0 at 29.5°C with 4-chlorocatechol in excess and an initial O_2 concentration of 223 µM. (A) A Clark-type oxygen electrode tracks the consumption of dissolved O_2 by catechol during the autoxidation process. (B) The initial linear portion (bold data points) of the plot of $\ln[O_2]$ versus time was used for the determination of pseudo first-order rate constant. The initial data point was not included to account for mixing upon the addition of catechol. (C) Non-linear least squares analysis was performed on the initial linear portion from (B) using Dynafit (version 4.05.087 software Biokin Ltd.), giving the pseudo first-order rate constant, standard error, and R^2 value (Table 4.3). Dioxygen consumption data for all three autoxidation reactions, rather than the average of these reactions, was included in the same plot when determining the pseudo first order rate constant.

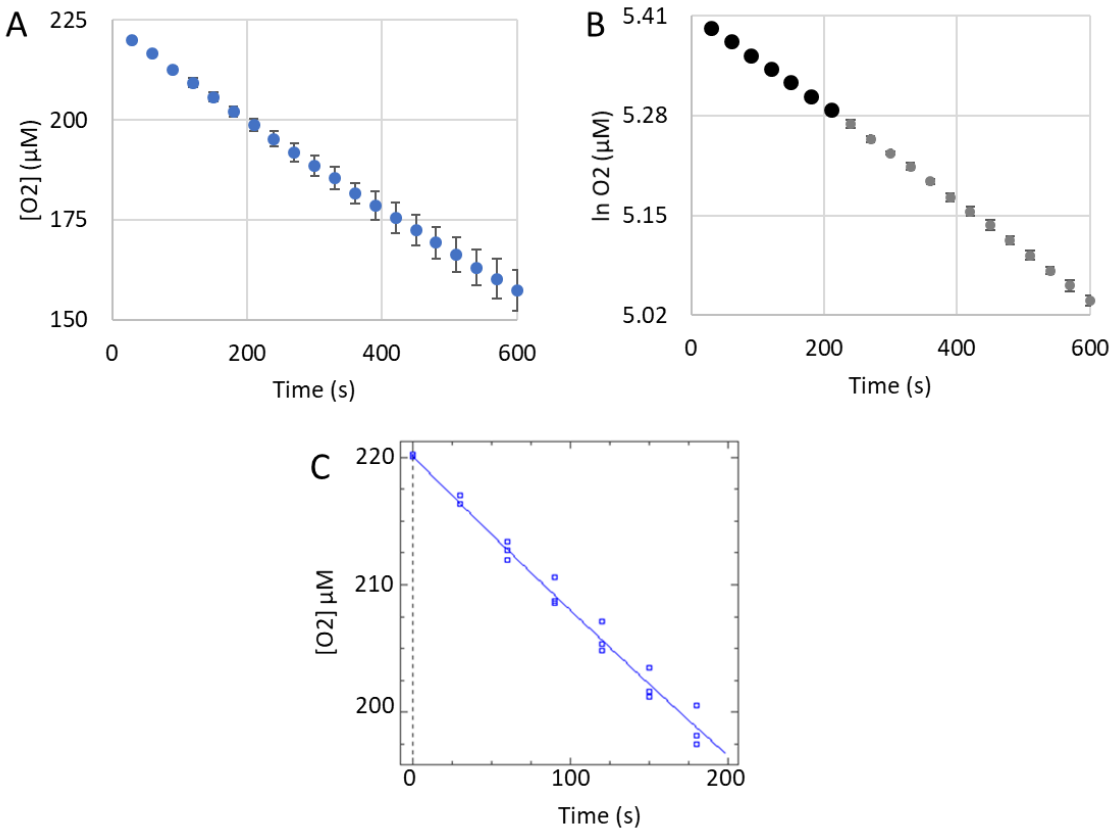

Figure A.4.3. pH 7.0 Autoxidation of 33.2 mM 4-Chlorocatechol.

Reactions were carried out in triplicate under pseudo first-order conditions in 50 mM phosphate buffer pH 7.0 at 29.5°C with 4-chlorocatechol in excess and an initial O_2 concentration of 223 µM. (A) A Clark-type oxygen electrode tracks the consumption of dissolved O_2 by catechol during the autoxidation process. (B) The initial linear portion (bold data points) of the plot of $\ln[O_2]$ versus time was used for the determination of pseudo first-order rate constant. The initial data point was not included to account for mixing upon the addition of catechol. (C) Non-linear least squares analysis was performed on the initial linear portion from (B) using Dynafit (version 4.05.087 software Biokin Ltd.), giving the pseudo first-order rate constant, standard error, and R^2 value (Table 4.3). Dioxygen consumption data for all three autoxidation reactions, rather than the average of these reactions, was included in the same plot when determining the pseudo first order rate constant.

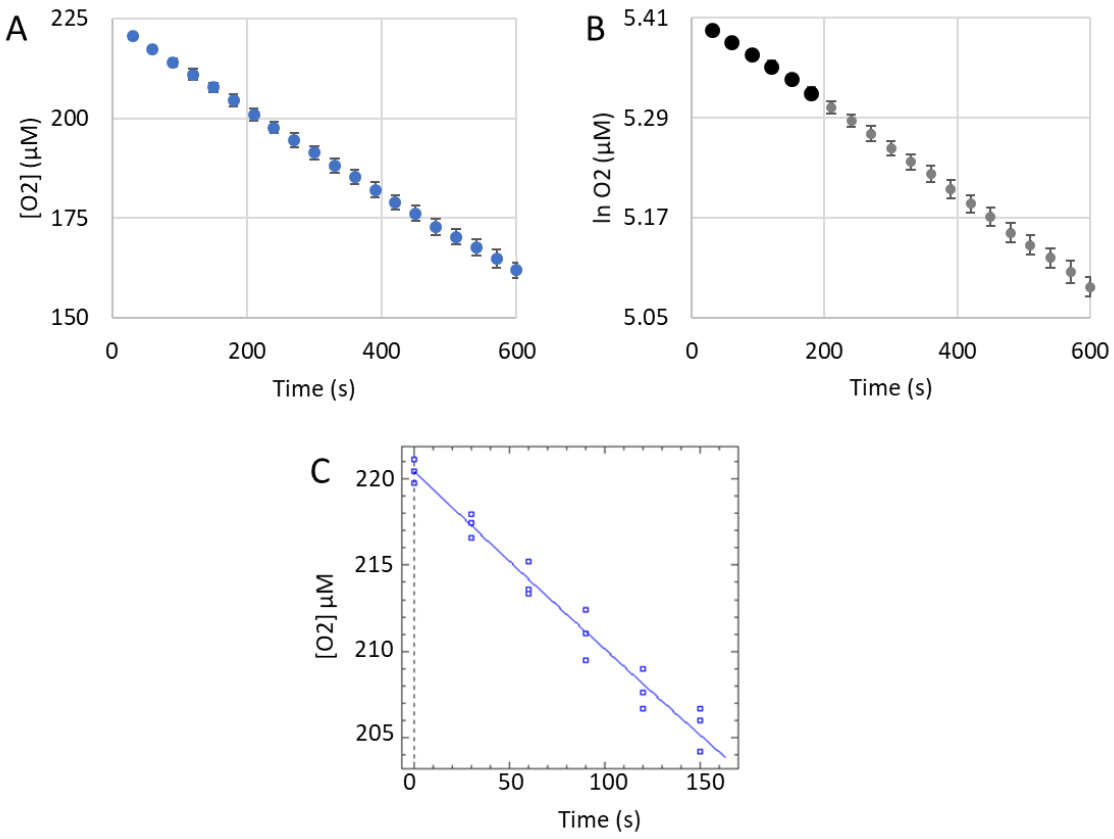

Figure A.4.4. pH 7.5 Autoxidation of 9.96 mM 4-Chlorocatechol.

Reactions were carried out in triplicate under pseudo first-order conditions in 50 mM phosphate buffer pH 7.5 at 29.5°C with 4-chlorocatechol in excess and an initial O_2 concentration of 223 µM. (A) A Clark-type oxygen electrode tracks the consumption of dissolved O_2 by catechol during the autoxidation process. (B) The initial linear portion (bold data points) of the plot of $\ln[O_2]$ versus time was used for the determination of pseudo first-order rate constant. The initial data point was not included to account for mixing upon the addition of catechol. (C) Non-linear least squares analysis was performed on the initial linear portion from (B) using Dynafit (version 4.05.087 software Biokin Ltd.), giving the pseudo first-order rate constant, standard error, and R^2 value (Table 4.3). Dioxygen consumption data for all three autoxidation reactions, rather than the average of these reactions, was included in the same plot when determining the pseudo first order rate constant.

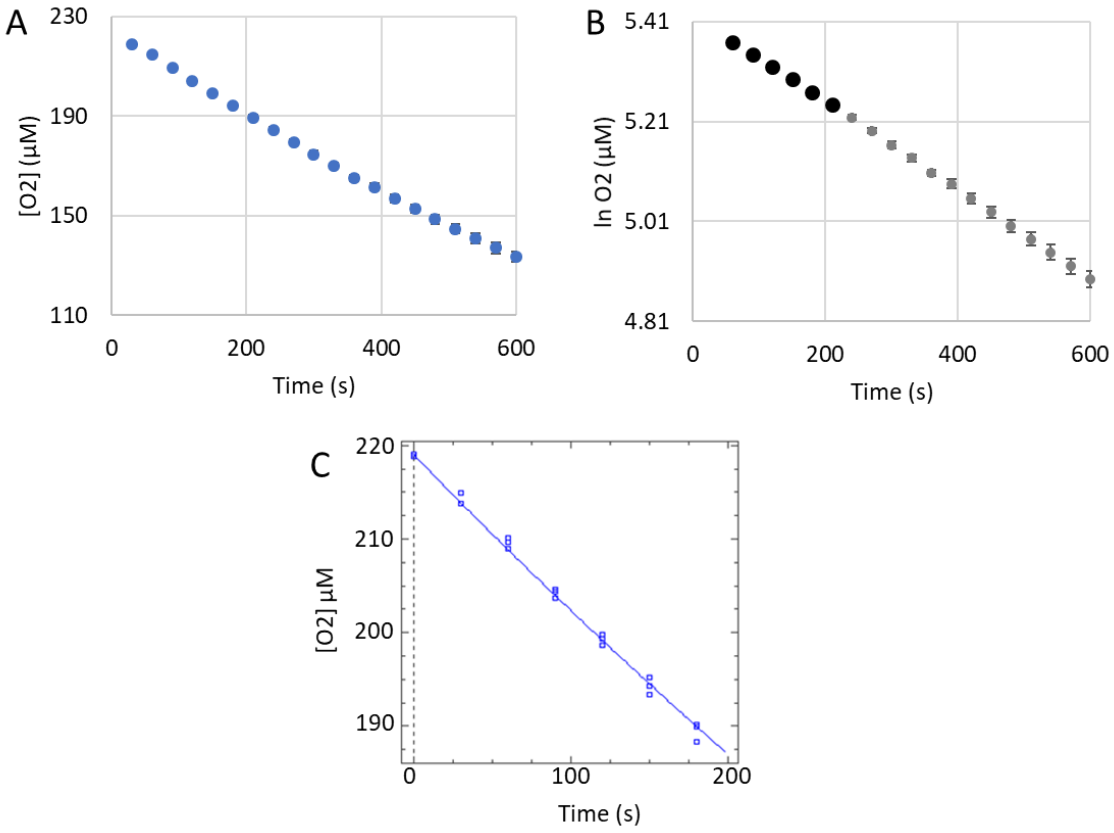

Figure A.4.5. pH 7.5 Autoxidation of 16.6 mM 4-Chlorocatechol.

Reactions were carried out in triplicate under pseudo first-order conditions in 50 mM phosphate buffer pH 7.5 at 29.5°C with 4-chlorocatechol in excess and an initial O_2 concentration of 223 µM. (A) A Clark-type oxygen electrode tracks the consumption of dissolved O_2 by catechol during the autoxidation process. (B) The initial linear portion (bold data points) of the plot of $\ln[O_2]$ versus time was used for the determination of pseudo first-order rate constant. The initial data point was not included to account for mixing upon the addition of catechol. (C) Non-linear least squares analysis was performed on the initial linear portion from (B) using Dynafit (version 4.05.087 software Biokin Ltd.), giving the pseudo first-order rate constant, standard error, and R^2 value (Table 4.3). Dioxygen consumption data for all three autoxidation reactions, rather than the average of these reactions, was included in the same plot when determining the pseudo first order rate constant.

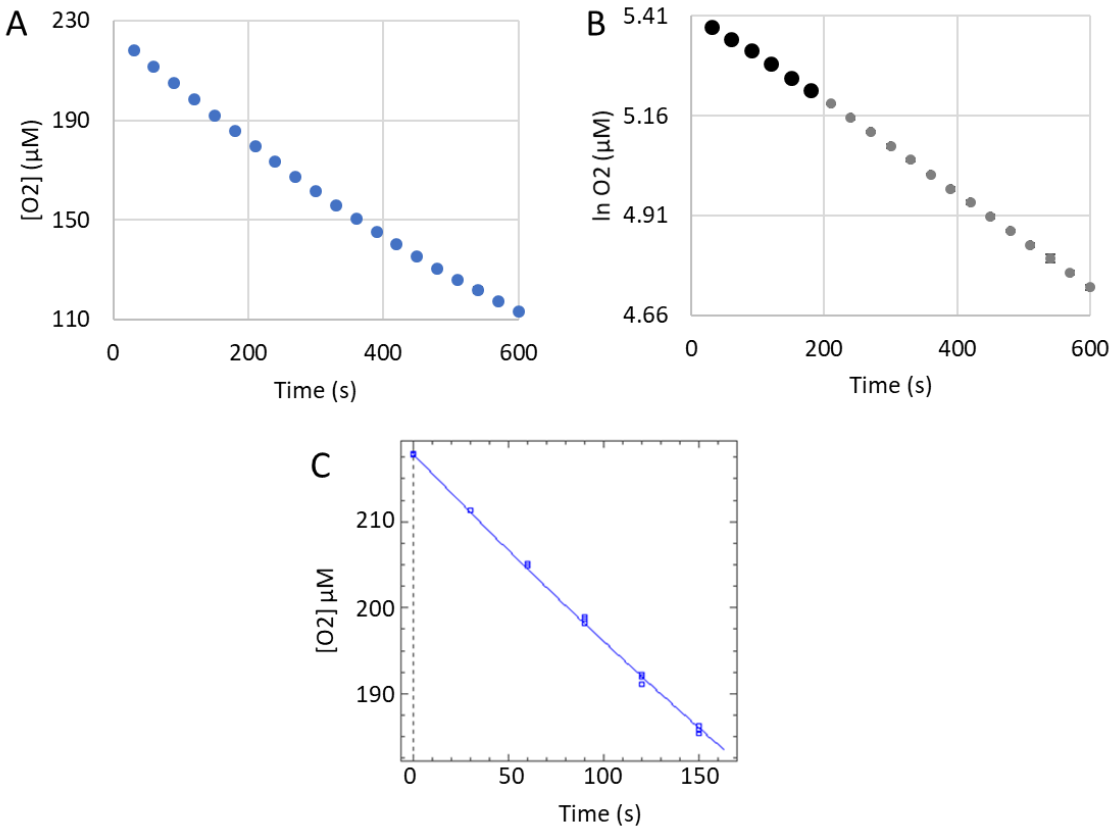

Figure A.4.6. pH 7.5 Autoxidation of 23.3 mM 4-Chlorocatechol.

Reactions were carried out in triplicate under pseudo first-order conditions in 50 mM phosphate buffer pH 7.5 at 29.5°C with 4-chlorocatechol in excess and an initial O_2 concentration of 223 µM. (A) A Clark-type oxygen electrode tracks the consumption of dissolved O_2 by catechol during the autoxidation process. (B) The initial linear portion (bold data points) of the plot of $\ln[O_2]$ versus time was used for the determination of pseudo first-order rate constant. The initial data point was not included to account for mixing upon the addition of catechol. (C) Non-linear least squares analysis was performed on the initial linear portion from (B) using Dynafit (version 4.05.087 software Biokin Ltd.), giving the pseudo first-order rate constant, standard error, and R^2 value (Table 4.3). Dioxygen consumption data for all three autoxidation reactions, rather than the average of these reactions, was included in the same plot when determining the pseudo first order rate constant.

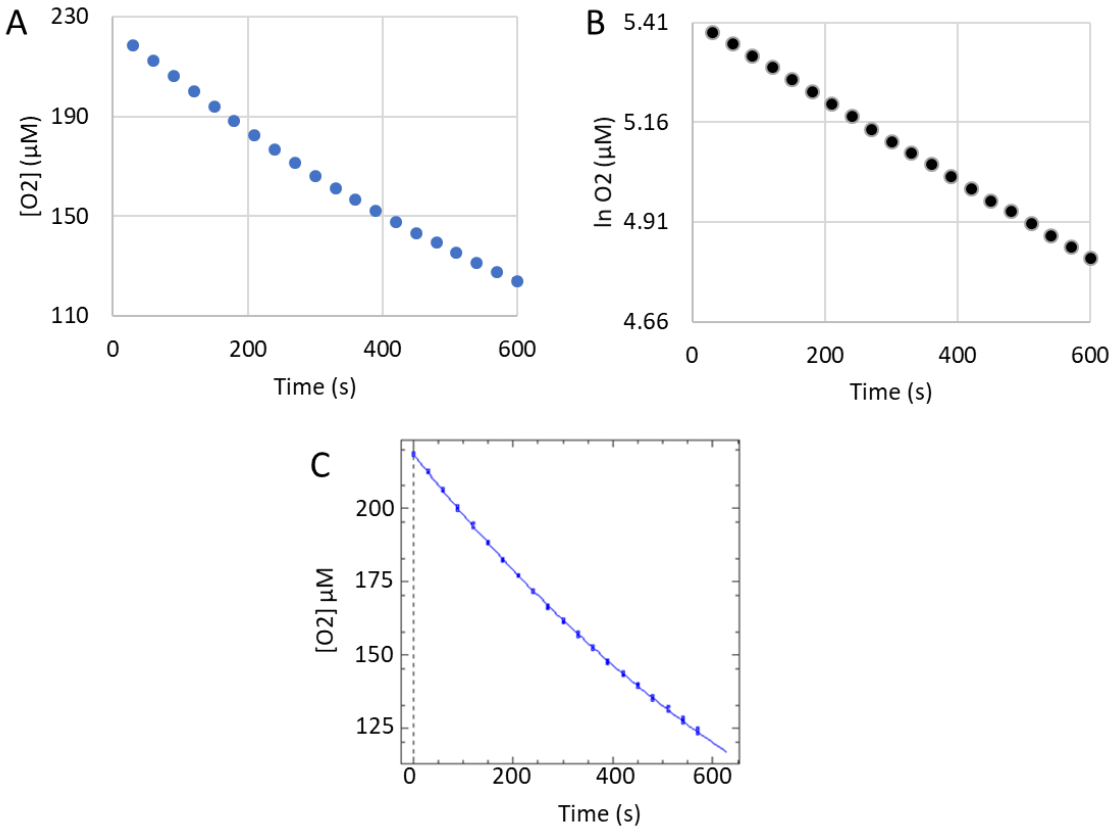

Figure A.4.7. pH 8.0 Autoxidation of 9.96 mM 4-Chlorocatechol.

Reactions were carried out in triplicate under pseudo first-order conditions in 50 mM phosphate buffer pH 8.0 at 29.5°C with 4-chlorocatechol in excess and an initial O_2 concentration of 223 µM. (A) A Clark-type oxygen electrode tracks the consumption of dissolved O_2 by catechol during the autoxidation process. (B) The initial linear portion (bold data points) of the plot of $\ln[O_2]$ versus time was used for the determination of pseudo first-order rate constant. The initial data point was not included to account for mixing upon the addition of catechol. (C) Non-linear least squares analysis was performed on the initial linear portion from (B) using Dynafit (version 4.05.087 software Biokin Ltd.), giving the pseudo first-order rate constant, standard error, and R^2 value (Table 4.3). Dioxygen consumption data for all three autoxidation reactions, rather than the average of these reactions, was included in the same plot when determining the pseudo first order rate constant.

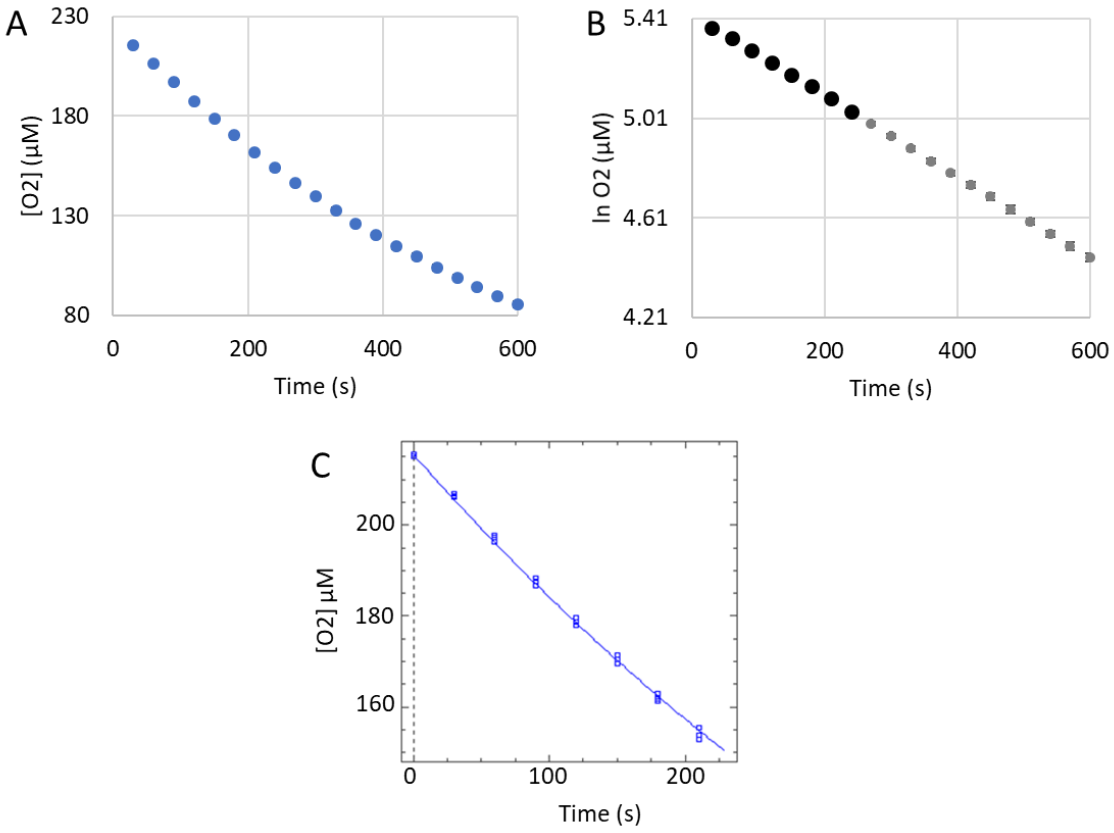

Figure A.4.8. pH 8.0 Autoxidation of 16.6 mM 4-Chlorocatechol.

Reactions were carried out in triplicate under pseudo first-order conditions in 50 mM phosphate buffer pH 8.0 at 29.5°C with 4-chlorocatechol in excess and an initial O_2 concentration of 223 µM. (A) A Clark-type oxygen electrode tracks the consumption of dissolved O_2 by catechol during the autoxidation process. (B) The initial linear portion (bold data points) of the plot of $\ln[O_2]$ versus time was used for the determination of pseudo first-order rate constant. The initial data point was not included to account for mixing upon the addition of catechol. (C) Non-linear least squares analysis was performed on the initial linear portion from (B) using Dynafit (version 4.05.087 software Biokin Ltd.), giving the pseudo first-order rate constant, standard error, and R^2 value (Table 4.3). Dioxygen consumption data for all three autoxidation reactions, rather than the average of these reactions, was included in the same plot when determining the pseudo first order rate constant.

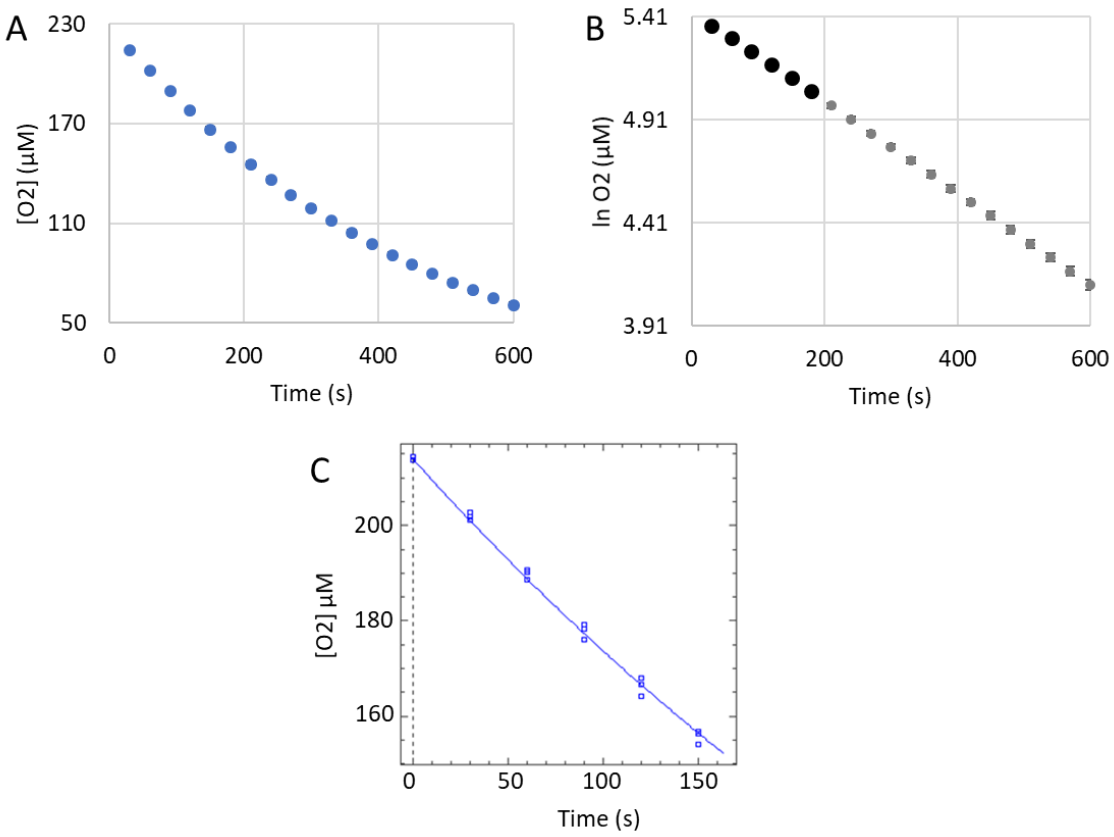

Figure A.4.9. pH 8.0 Autoxidation of 23.3 mM 4-Chlorocatechol.

Reactions were carried out in triplicate under pseudo first-order conditions in 50 mM phosphate buffer pH 8.0 at 29.5°C with 4-chlorocatechol in excess and an initial O_2 concentration of 223 µM. (A) A Clark-type oxygen electrode tracks the consumption of dissolved O_2 by catechol during the autoxidation process. (B) The initial linear portion (bold data points) of the plot of $\ln[O_2]$ versus time was used for the determination of pseudo first-order rate constant. The initial data point was not included to account for mixing upon the addition of catechol. (C) Non-linear least squares analysis was performed on the initial linear portion from (B) using Dynafit (version 4.05.087 software Biokin Ltd.), giving the pseudo first-order rate constant, standard error, and R^2 value (Table 4.3). Dioxygen consumption data for all three autoxidation reactions, rather than the average of these reactions, was included in the same plot when determining the pseudo first order rate constant.

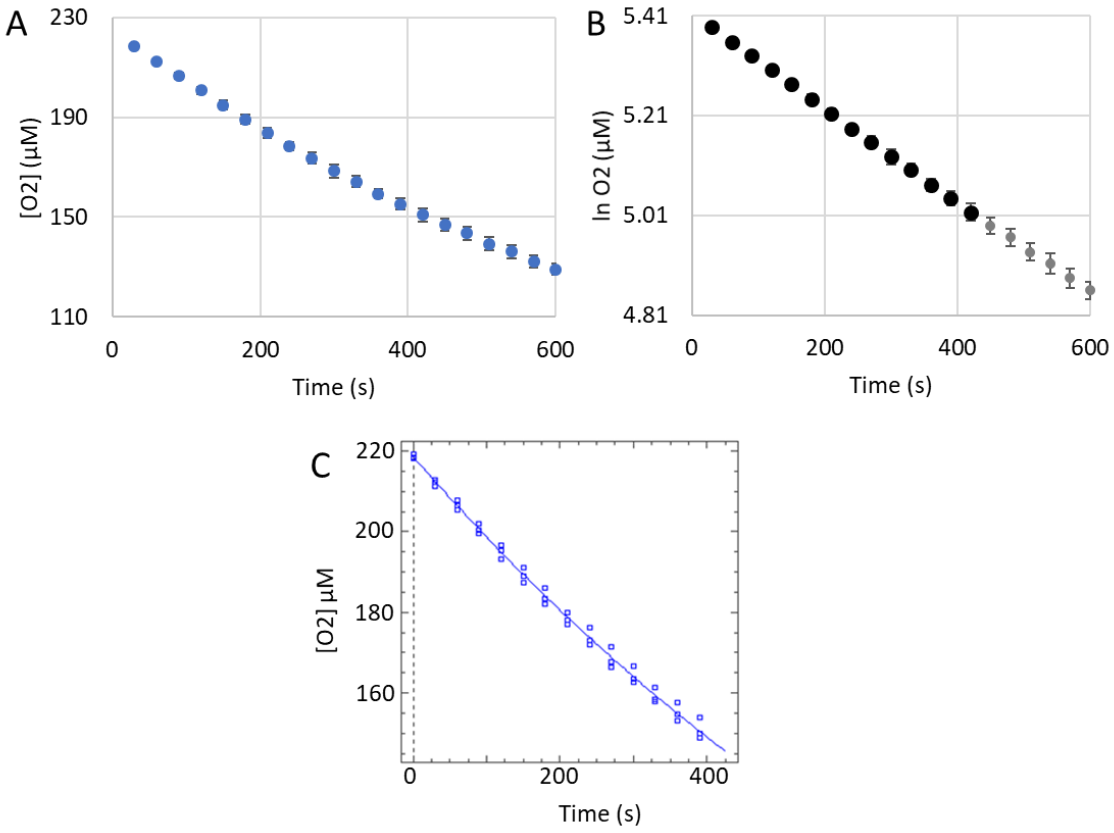

Figure A.4.10. pH 8.5 Autoxidation of 3.32 mM 4-Chlorocatechol.

Reactions were carried out in triplicate under pseudo first-order conditions in 50 mM tricine buffer pH 8.5 at 29.5°C with 4-chlorocatechol in excess and an initial O_2 concentration of 223 µM. (A) A Clark-type oxygen electrode tracks the consumption of dissolved O_2 by catechol during the autoxidation process. (B) The initial linear portion (bold data points) of the plot of ln[O_2] versus time was used for the determination of pseudo first-order rate constant. The initial data point was not included to account for mixing upon the addition of catechol. (C) Non-linear least squares analysis was performed on the initial linear portion from (B) using Dynafit (version 4.05.087 software Biokin Ltd.), giving the pseudo first-order rate constant, standard error, and R^2 value (Table 4.3). Dioxygen consumption data for all three autoxidation reactions, rather than the average of these reactions, was included in the same plot when determining the pseudo first order rate constant.

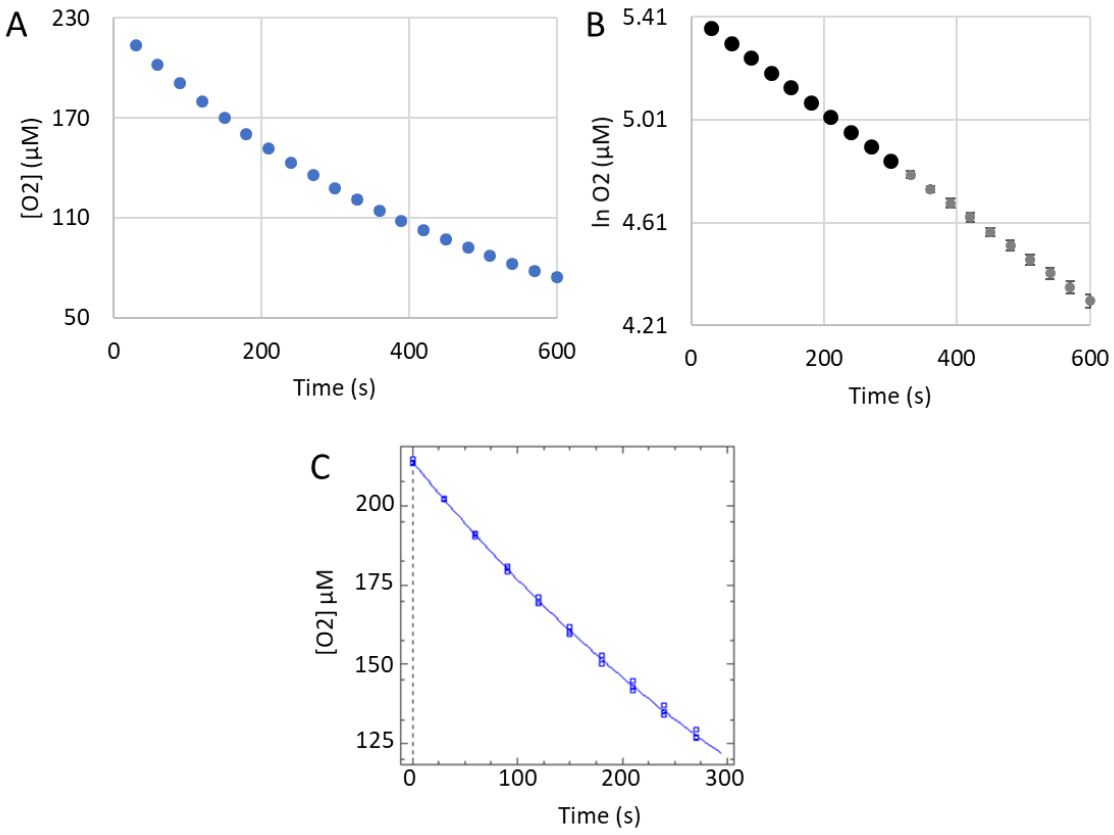

Figure A.4.11. pH 8.5 Autoxidation of 6.64 mM 4-Chlorocatechol.

Reactions were carried out in triplicate under pseudo first-order conditions in 50 mM tricine buffer pH 8.5 at 29.5°C with 4-chlorocatechol in excess and an initial O_2 concentration of 223 µM. (A) A Clark-type oxygen electrode tracks the consumption of dissolved O_2 by catechol during the autoxidation process. (B) The initial linear portion (bold data points) of the plot of ln[O_2] versus time was used for the determination of pseudo first-order rate constant. The initial data point was not included to account for mixing upon the addition of catechol. (C) Non-linear least squares analysis was performed on the initial linear portion from (B) using Dynafit (version 4.05.087 software Biokin Ltd.), giving the pseudo first-order rate constant, standard error, and R^2 value (Table 4.3). Dioxygen consumption data for all three autoxidation reactions, rather than the average of these reactions, was included in the same plot when determining the pseudo first order rate constant.

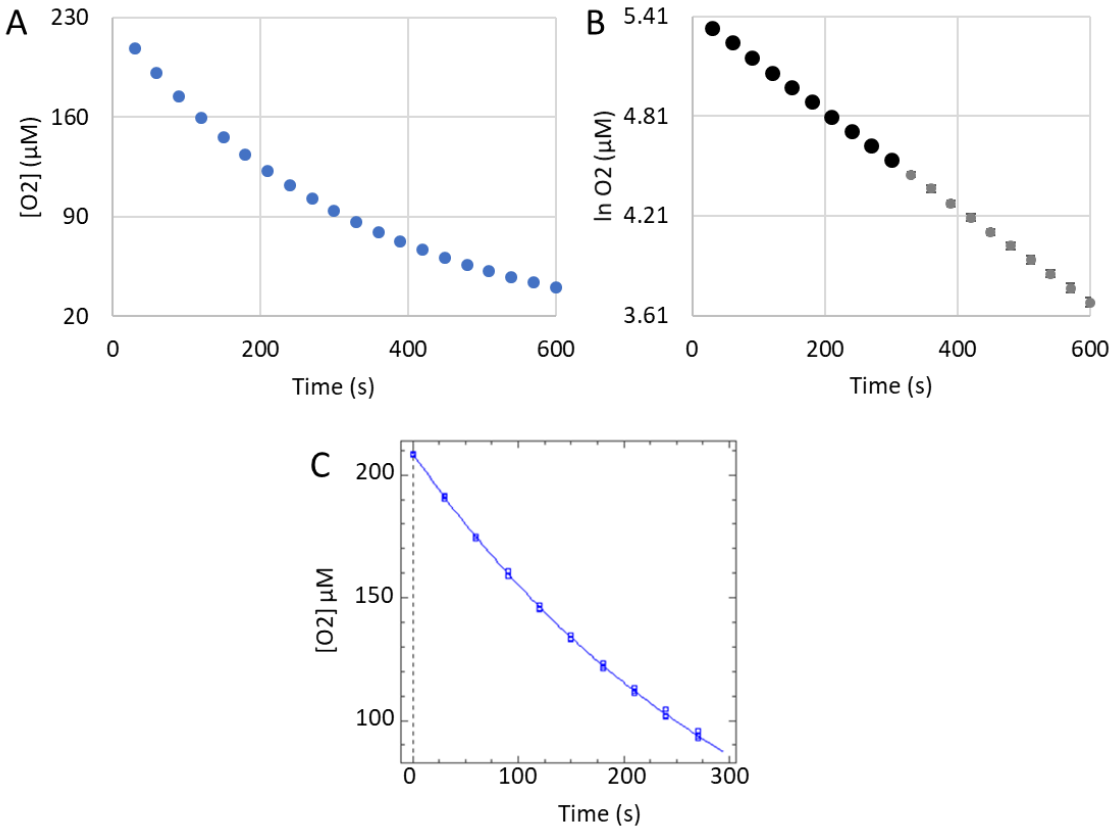

Figure A.4.12. pH 8.5 Autoxidation of 9.96 mM 4-Chlorocatechol.

Reactions were carried out in triplicate under pseudo first-order conditions in 50 mM tricine buffer pH 8.5 at 29.5°C with 4-chlorocatechol in excess and an initial O_2 concentration of 223 µM. (A) A Clark-type oxygen electrode tracks the consumption of dissolved O_2 by catechol during the autoxidation process. (B) The initial linear portion (bold data points) of the plot of ln[O_2] versus time was used for the determination of pseudo first-order rate constant. The initial data point was not included to account for mixing upon the addition of catechol. (C) Non-linear least squares analysis was performed on the initial linear portion from (B) using Dynafit (version 4.05.087 software Biokin Ltd.), giving the pseudo first-order rate constant, standard error, and R^2 value (Table 4.3). Dioxygen consumption data for all three autoxidation reactions, rather than the average of these reactions, was included in the same plot when determining the pseudo first order rate constant.

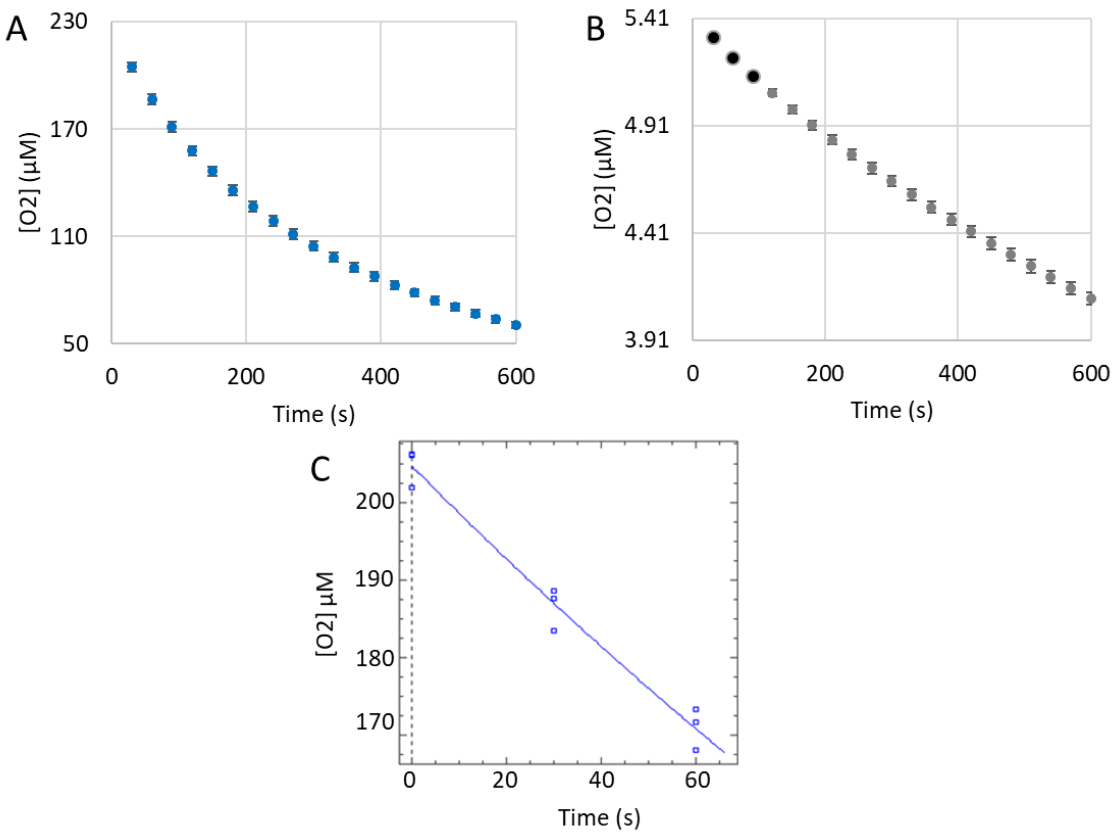

Figure A.4.13. pH 9.0 Autoxidation of 3.32 mM 4-Chlorocatechol.

Reactions were carried out in triplicate under pseudo first-order conditions in 50 mM CAPSO buffer pH 9.0 at 29.5°C with 4-chlorocatechol in excess and an initial O_2 concentration of 223 µM. (A) A Clark-type oxygen electrode tracks the consumption of dissolved O_2 by catechol during the autoxidation process. (B) The initial linear portion (bold data points) of the plot of $\ln[O_2]$ versus time was used for the determination of pseudo first-order rate constant. The initial data point was not included to account for mixing upon the addition of catechol. (C) Non-linear least squares analysis was performed on the initial linear portion from (B) using Dynafit (version 4.05.087 software Biokin Ltd.), giving the pseudo first-order rate constant, standard error, and R^2 value (Table 4.3). Dioxygen consumption data for all three autoxidation reactions, rather than the average of these reactions, was included in the same plot when determining the pseudo first order rate constant.

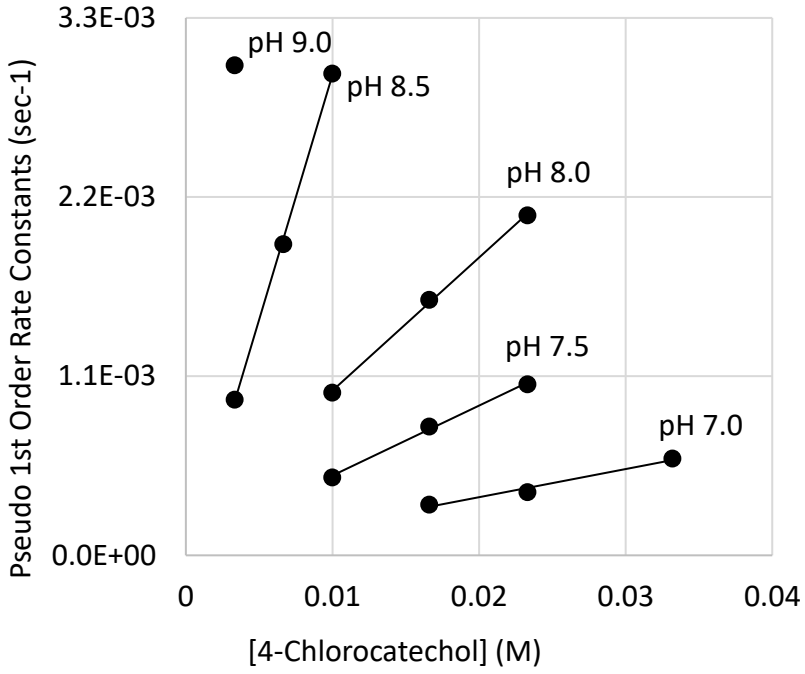

Figure A.4.14. pH-Dependence of 4-Chlorocatechol Autoxidation.

Autoxidation of 4-Chlorocatechol was investigated at pH 7.0, 7.5, 8.0, 8.5, and 9.0.

Appendix A.5. Kinetic Data for 3,4-DHBA Autoxidation

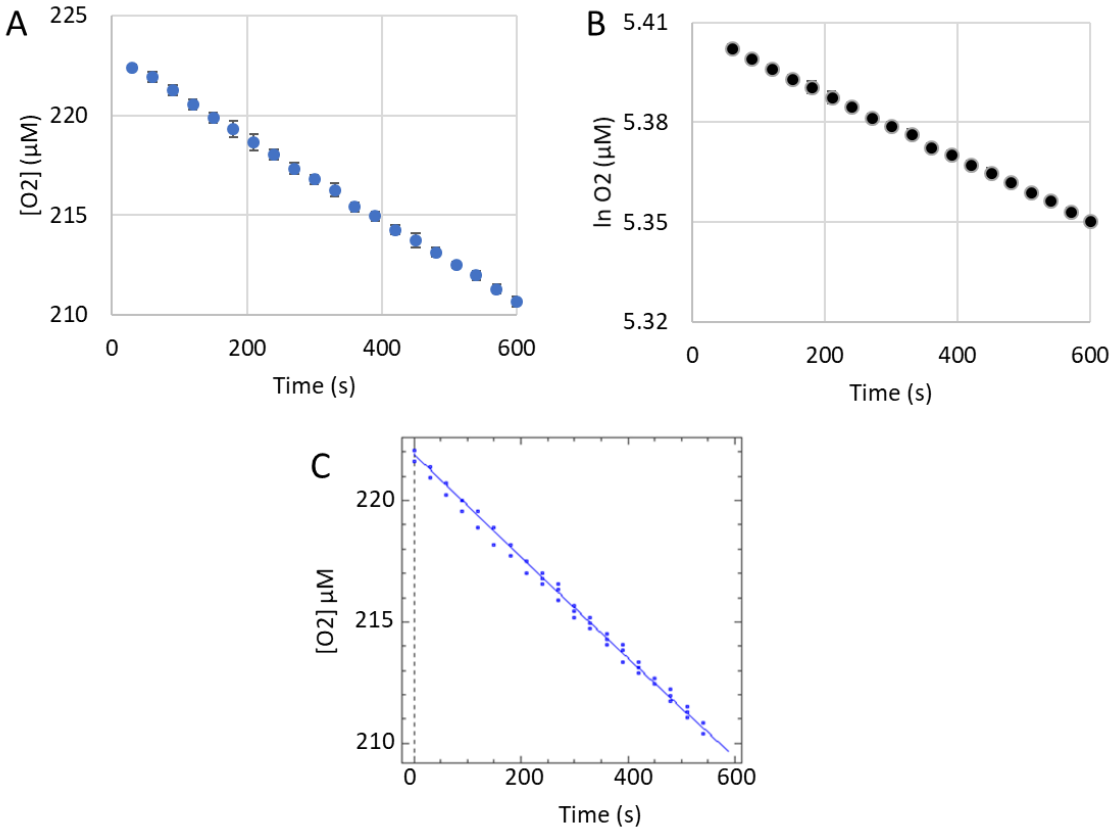

Figure A.5.1. pH 9.0 Autoxidation of 3.32 mM 3,4-DHBA.

Reactions were carried out in triplicate under pseudo first-order conditions in 50 mM CAPSO buffer pH 9.0 at 29.5°C with 3,4-DHBA in excess and an initial O_2 concentration of 223 µM. (A) A Clark-type oxygen electrode tracks the consumption of dissolved O_2 by catechol during the autoxidation process. (B) The initial linear portion (bold data points) of the plot of ln[O_2] versus time was used for the determination of pseudo first-order rate constant. The initial data point was not included to account for mixing upon the addition of catechol. (C) Non-linear least squares analysis was performed on the initial linear portion from (B) using Dynafit (version 4.05.087 software Biokin Ltd.), giving the pseudo first-order rate constant, standard error, and R^2 value (Table 4.3). Dioxygen consumption data for all three autoxidation reactions, rather than the average of these reactions, was included in the same plot when determining the pseudo first order rate constant.

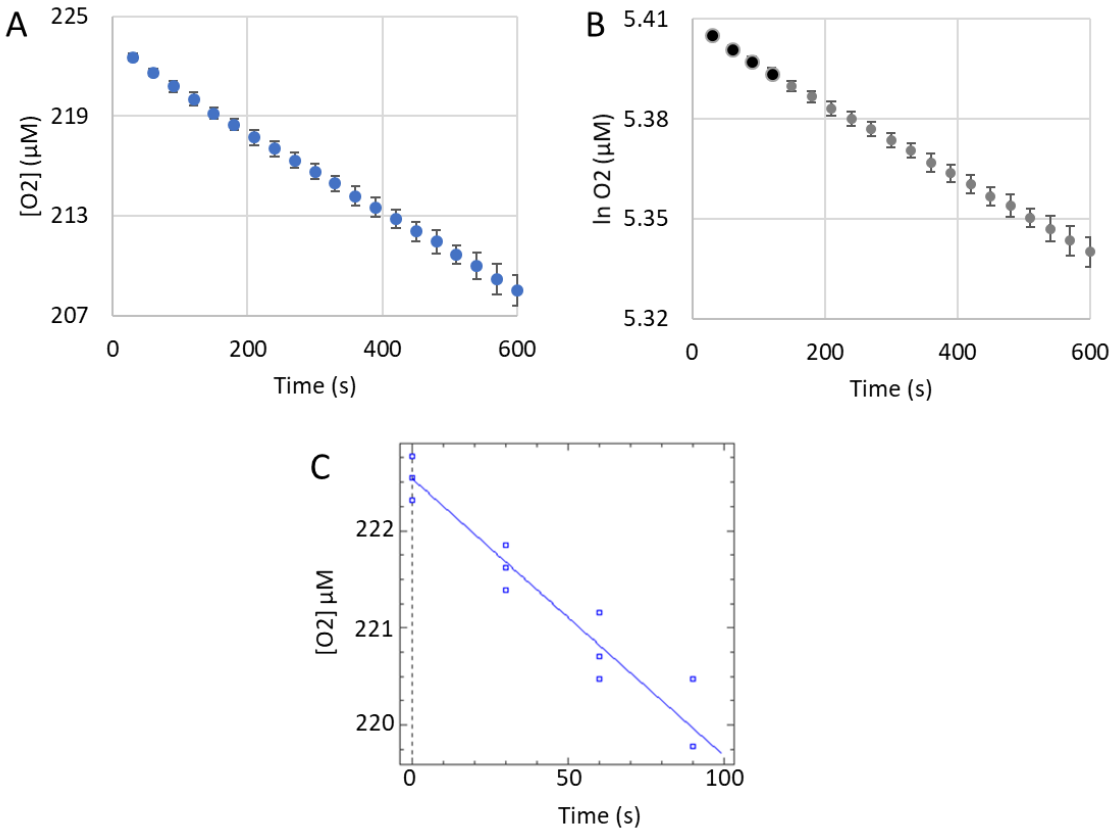

Figure A.5.2. pH 9.0 Autoxidation of 4.98 mM 3,4-DHBA.

Reactions were carried out in triplicate under pseudo first-order conditions in 50 mM CAPSO buffer pH 9.0 at 29.5°C with 3,4-DHBA in excess and an initial O_2 concentration of 223 µM. (A) A Clark-type oxygen electrode tracks the consumption of dissolved O_2 by catechol during the autoxidation process. (B) The initial linear portion (bold data points) of the plot of ln[O_2] versus time was used for the determination of pseudo first-order rate constant. The initial data point was not included to account for mixing upon the addition of catechol. (C) Non-linear least squares analysis was performed on the initial linear portion from (B) using Dynafit (version 4.05.087 software Biokin Ltd.), giving the pseudo first-order rate constant, standard error, and R^2 value (Table 4.3). Dioxygen consumption data for all three autoxidation reactions, rather than the average of these reactions, was included in the same plot when determining the pseudo first order rate constant.

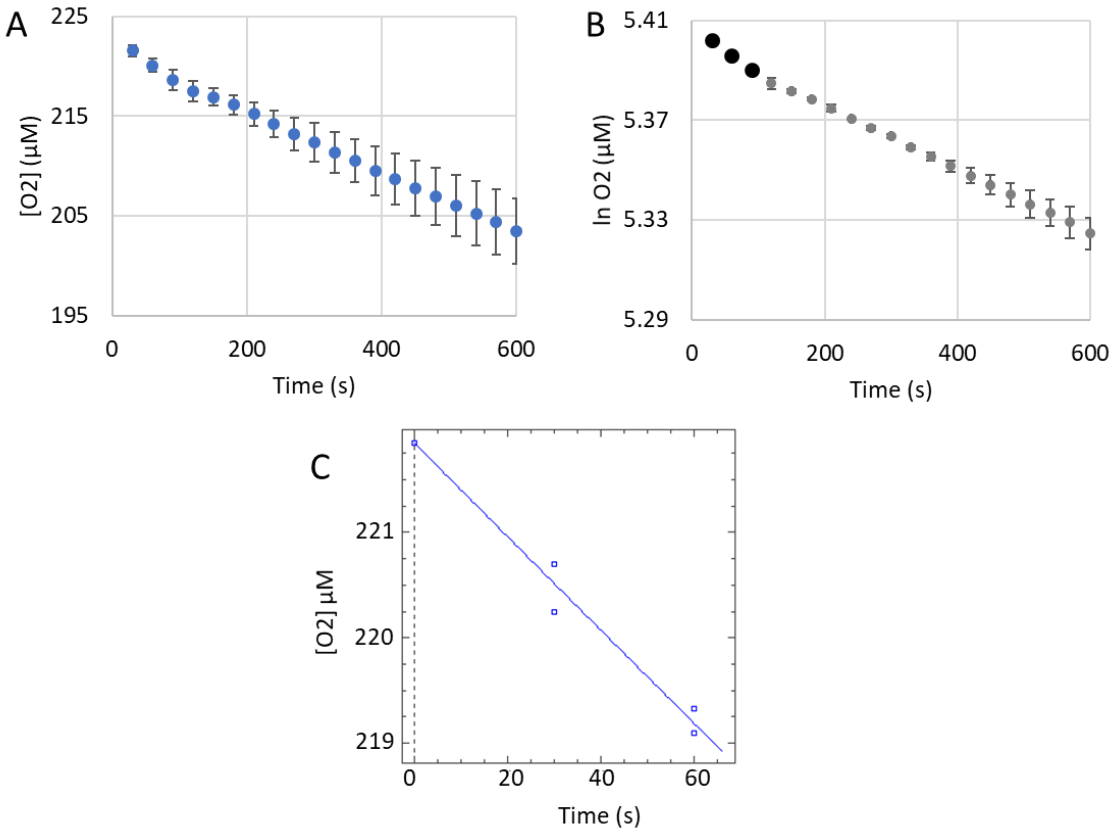

Figure A.5.3. pH 9.0 Autoxidation of 6.64 mM 3,4-DHBA.

Reactions were carried out in triplicate under pseudo first-order conditions in 50 mM CAPSO buffer pH 9.0 at 29.5°C with 3,4-DHBA in excess and an initial O_2 concentration of 223 µM. One of autoxidation reactions deviated from the average of the remaining two and was not included in the analysis. (A) A Clark-type oxygen electrode tracks the consumption of dissolved O_2 by catechol during the autoxidation process. (B) The initial linear portion (bold data points) of the plot of $\ln[O_2]$ versus time was used for the determination of pseudo first-order rate constant. The initial data point was not included to account for mixing upon the addition of catechol. (C) Non-linear least squares analysis was performed on the initial linear portion from (B) using Dynafit (version 4.05.087 software Biokin Ltd.), giving the pseudo first-order rate constant, standard error, and R^2 value (Table 4.3). Dioxygen consumption data for all three autoxidation reactions, rather than the average of these reactions, was included in the same plot when determining the pseudo first order rate constant.

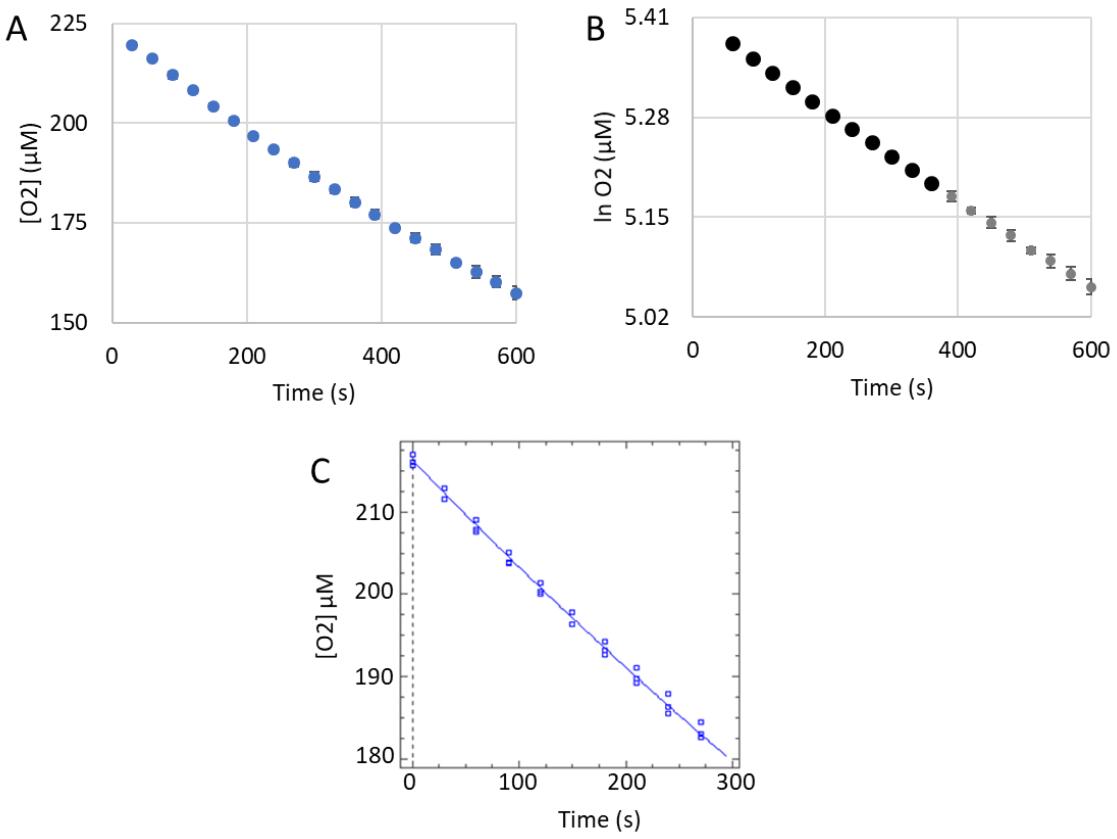

Figure A.5.4. pH 9.5 Autoxidation of 3.32 mM 3,4-DHBA.

Reactions were carried out in triplicate under pseudo first-order conditions in 50 mM CAPSO buffer pH 9.5 at 29.5°C with 3,4-DHBA in excess and an initial O_2 concentration of 223 µM. (A) A Clark-type oxygen electrode tracks the consumption of dissolved O_2 by catechol during the autoxidation process. (B) The initial linear portion (bold data points) of the plot of ln[O_2] versus time was used for the determination of pseudo first-order rate constant. The initial data point was not included to account for mixing upon the addition of catechol. (C) Non-linear least squares analysis was performed on the initial linear portion from (B) using Dynafit (version 4.05.087 software Biokin Ltd.), giving the pseudo first-order rate constant, standard error, and R^2 value (Table 4.3). Dioxygen consumption data for all three autoxidation reactions, rather than the average of these reactions, was included in the same plot when determining the pseudo first order rate constant.

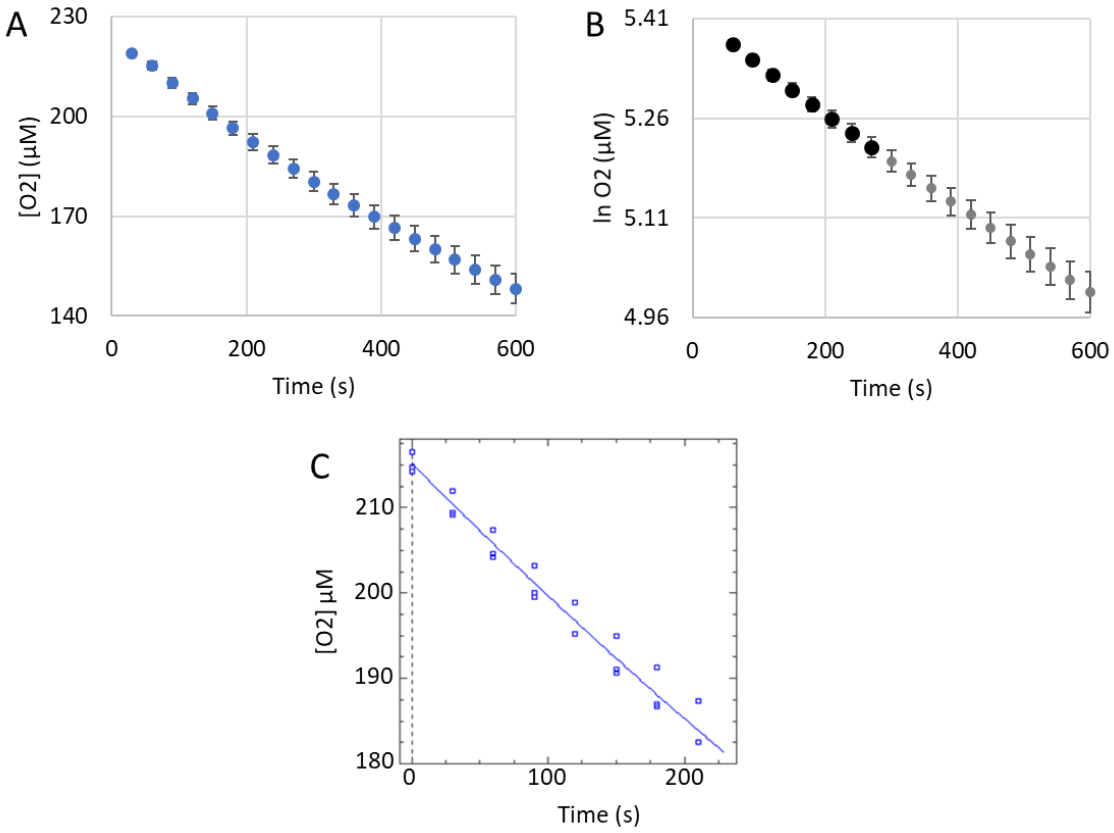

Figure A.5.5. pH 9.5 Autoxidation of 4.98 mM 3,4-DHBA.

Reactions were carried out in triplicate under pseudo first-order conditions in 50 mM CAPSO buffer pH 9.5 at 29.5°C with 3,4-DHBA in excess and an initial O_2 concentration of 223 µM. (A) A Clark-type oxygen electrode tracks the consumption of dissolved O_2 by catechol during the autoxidation process. (B) The initial linear portion (bold data points) of the plot of ln[O_2] versus time was used for the determination of pseudo first-order rate constant. The initial data point was not included to account for mixing upon the addition of catechol. (C) Non-linear least squares analysis was performed on the initial linear portion from (B) using Dynafit (version 4.05.087 software Biokin Ltd.), giving the pseudo first-order rate constant, standard error, and R^2 value (Table 4.3). Dioxygen consumption data for all three autoxidation reactions, rather than the average of these reactions, was included in the same plot when determining the pseudo first order rate constant.

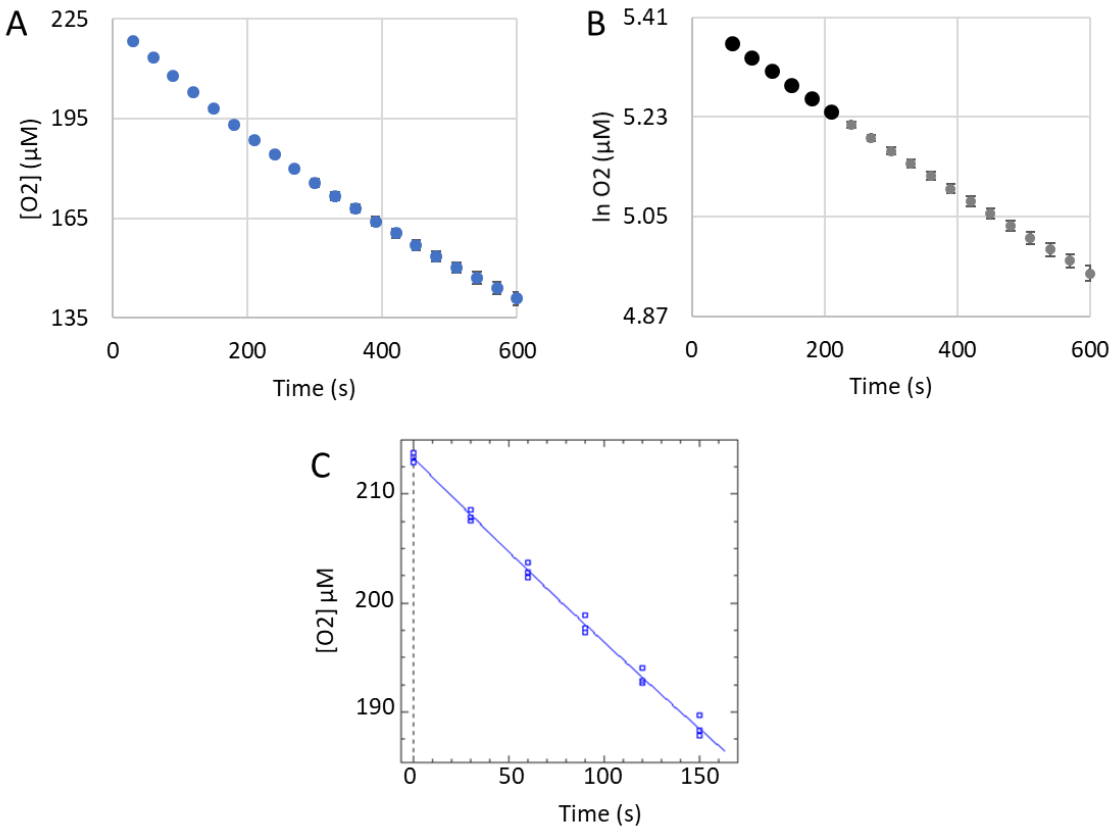

Figure A.5.6. pH 9.5 Autoxidation of 6.64 mM 3,4-DHBA.

Reactions were carried out in triplicate under pseudo first-order conditions in 50 mM CAPSO buffer pH 9.5 at 29.5°C with 3,4-DHBA in excess and an initial O_2 concentration of 223 µM. (A) A Clark-type oxygen electrode tracks the consumption of dissolved O_2 by catechol during the autoxidation process. (B) The initial linear portion (bold data points) of the plot of ln[O_2] versus time was used for the determination of pseudo first-order rate constant. The initial data point was not included to account for mixing upon the addition of catechol. (C) Non-linear least squares analysis was performed on the initial linear portion from (B) using Dynafit (version 4.05.087 software Biokin Ltd.), giving the pseudo first-order rate constant, standard error, and R^2 value (Table 4.3). Dioxygen consumption data for all three autoxidation reactions, rather than the average of these reactions, was included in the same plot when determining the pseudo first order rate constant.

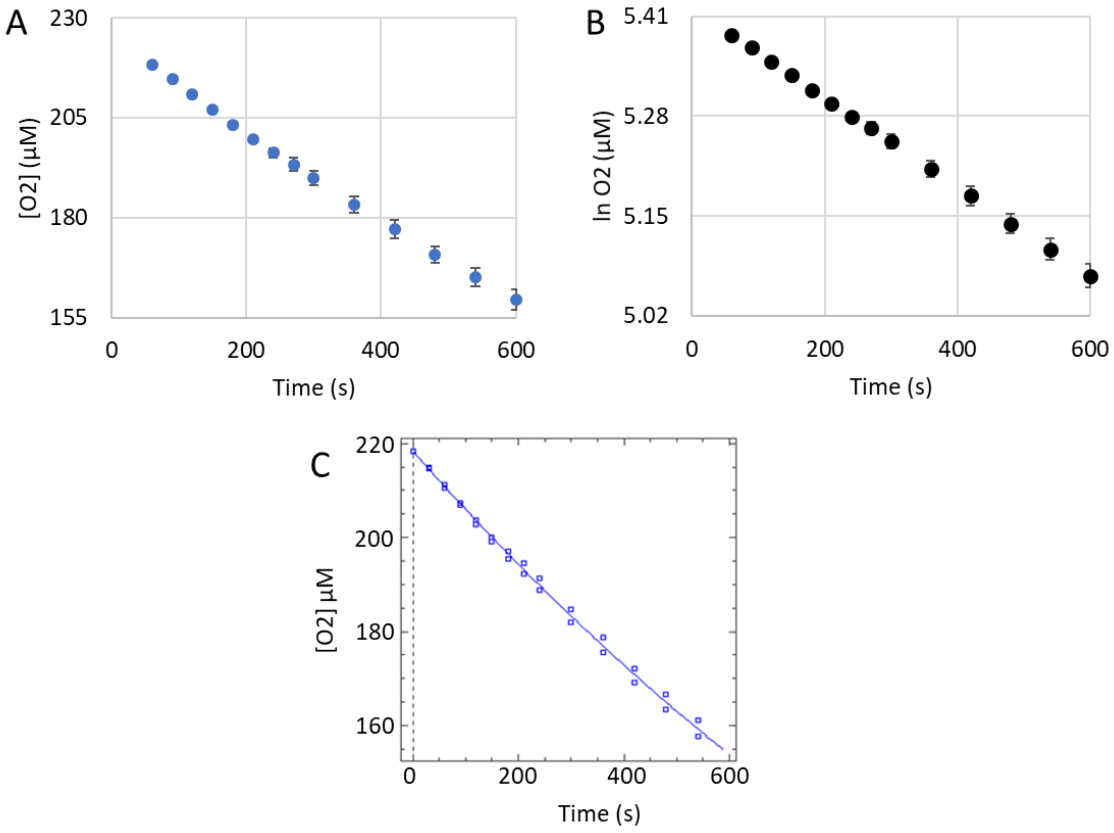

Figure A.5.7. pH 10.0 Autoxidation of 3.32 mM 3,4-DHBA.

Reactions were carried out in triplicate under pseudo first-order conditions in 50 mM CAPSO buffer pH 9.5 at 29.5°C with 3,4-DHBA in excess and an initial O_2 concentration of 223 µM. One of autoxidation reactions deviated from the average of the remaining two and was not included in the analysis. (A) A Clark-type oxygen electrode tracks the consumption of dissolved O_2 by catechol during the autoxidation process. (B) The initial linear portion (bold data points) of the plot of $\ln[O_2]$ versus time was used for the determination of pseudo first-order rate constant. The initial data point was not included to account for mixing upon the addition of catechol. (C) Non-linear least squares analysis was performed on the initial linear portion from (B) using Dynafit (version 4.05.087 software Biokin Ltd.), giving the pseudo first-order rate constant, standard error, and R^2 value (Table 4.3). Dioxygen consumption data for all three autoxidation reactions, rather than the average of these reactions, was included in the same plot when determining the pseudo first order rate constant.

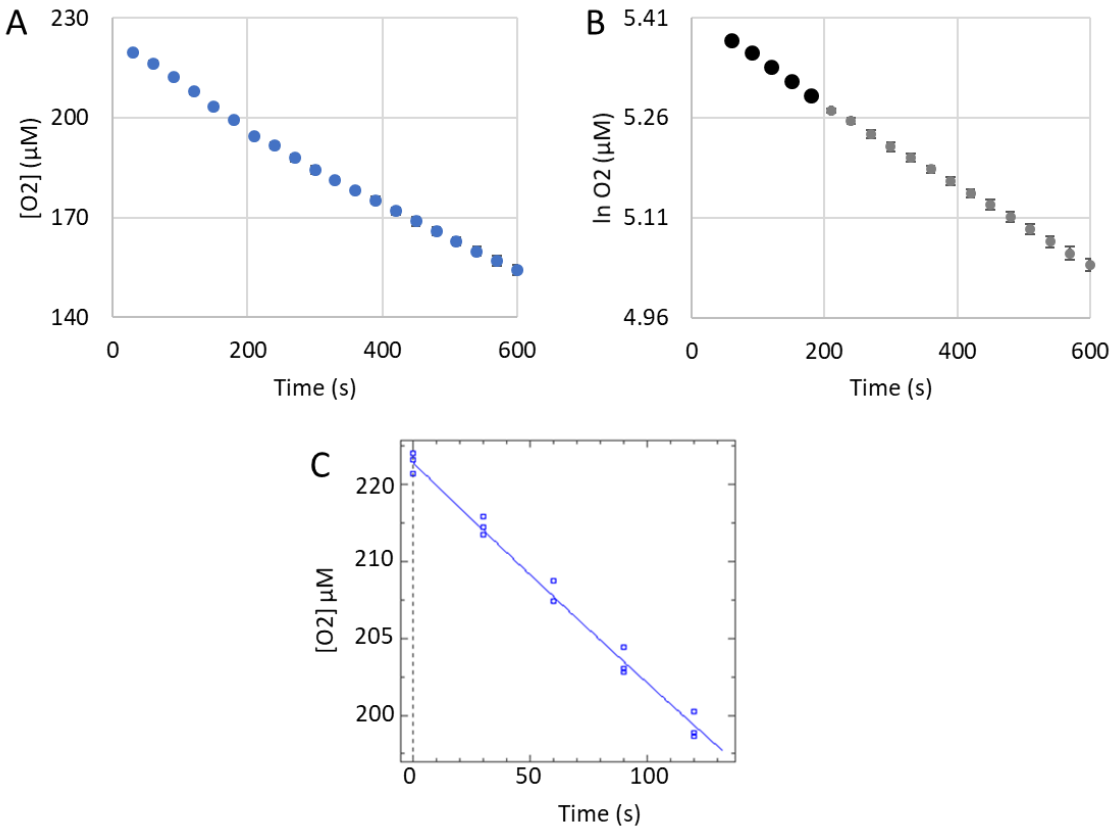

Figure A.5.8. pH 10.0 Autoxidation of 4.98 mM 3,4-DHBA.

Reactions were carried out in triplicate under pseudo first-order conditions in 50 mM CAPSO buffer pH 10.0 at 29.5°C with 3,4-DHBA in excess and an initial O_2 concentration of 223 µM. (A) A Clark-type oxygen electrode tracks the consumption of dissolved O_2 by catechol during the autoxidation process. (B) The initial linear portion (bold data points) of the plot of ln[O_2] versus time was used for the determination of pseudo first-order rate constant. The initial data point was not included to account for mixing upon the addition of catechol. (C) Non-linear least squares analysis was performed on the initial linear portion from (B) using Dynafit (version 4.05.087 software Biokin Ltd.), giving the pseudo first-order rate constant, standard error, and R^2 value (Table 4.3). Dioxygen consumption data for all three autoxidation reactions, rather than the average of these reactions, was included in the same plot when determining the pseudo first order rate constant.

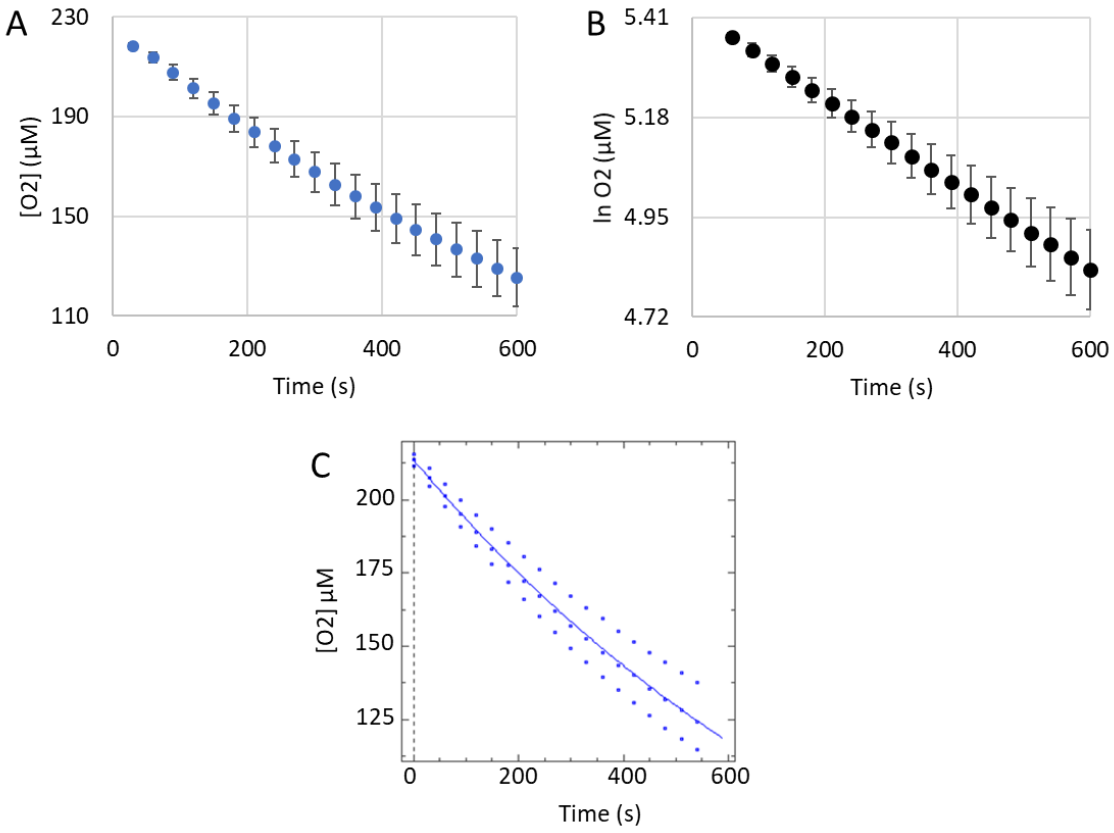

Figure A.5.9. pH 10.0 Autoxidation of 6.64 mM 3,4-DHBA.

Reactions were carried out in triplicate under pseudo first-order conditions in 50 mM CAPSO buffer pH 10.0 at 29.5°C with 3,4-DHBA in excess and an initial O_2 concentration of 223 µM. (A) A Clark-type oxygen electrode tracks the consumption of dissolved O_2 by catechol during the autoxidation process. (B) The initial linear portion (bold data points) of the plot of ln[O_2] versus time was used for the determination of pseudo first-order rate constant. The initial data point was not included to account for mixing upon the addition of catechol. (C) Non-linear least squares analysis was performed on the initial linear portion from (B) using Dynafit (version 4.05.087 software Biokin Ltd.), giving the pseudo first-order rate constant, standard error, and R^2 value (Table 4.3). Dioxygen consumption data for all three autoxidation reactions, rather than the average of these reactions, was included in the same plot when determining the pseudo first order rate constant.

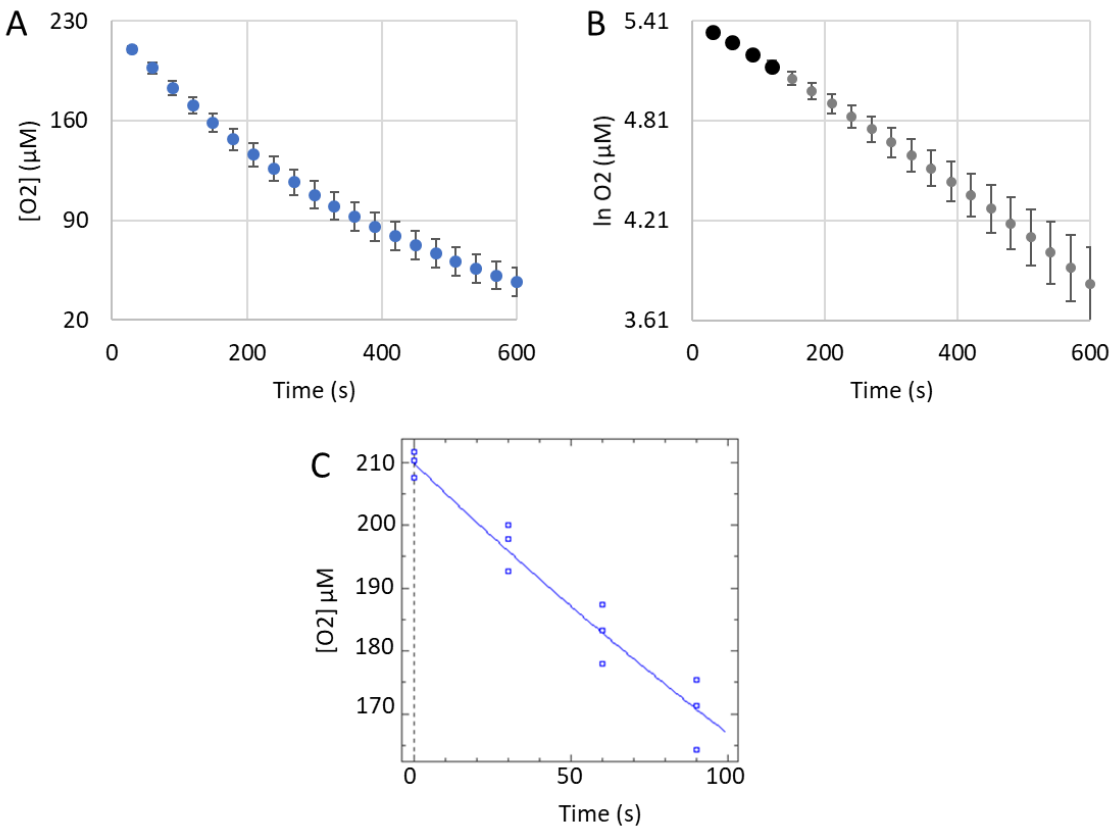

Figure A.5.10. pH 10.5 Autoxidation of 3.32 mM 3,4-DHBA.

Reactions were carried out in triplicate under pseudo first-order conditions in 50 mM CAPS buffer pH 10.5 at 29.5°C with 3,4-DHBA in excess and an initial O_2 concentration of 223 µM. (A) A Clark-type oxygen electrode tracks the consumption of dissolved O_2 by catechol during the autoxidation process. (B) The initial linear portion (bold data points) of the plot of $\ln[O_2]$ versus time was used for the determination of pseudo first-order rate constant. The initial data point was not included to account for mixing upon the addition of catechol. (C) Non-linear least squares analysis was performed on the initial linear portion from (B) using Dynafit (version 4.05.087 software Biokin Ltd.), giving the pseudo first-order rate constant, standard error, and R^2 value (Table 4.3). Dioxygen consumption data for all three autoxidation reactions, rather than the average of these reactions, was included in the same plot when determining the pseudo first order rate constant.

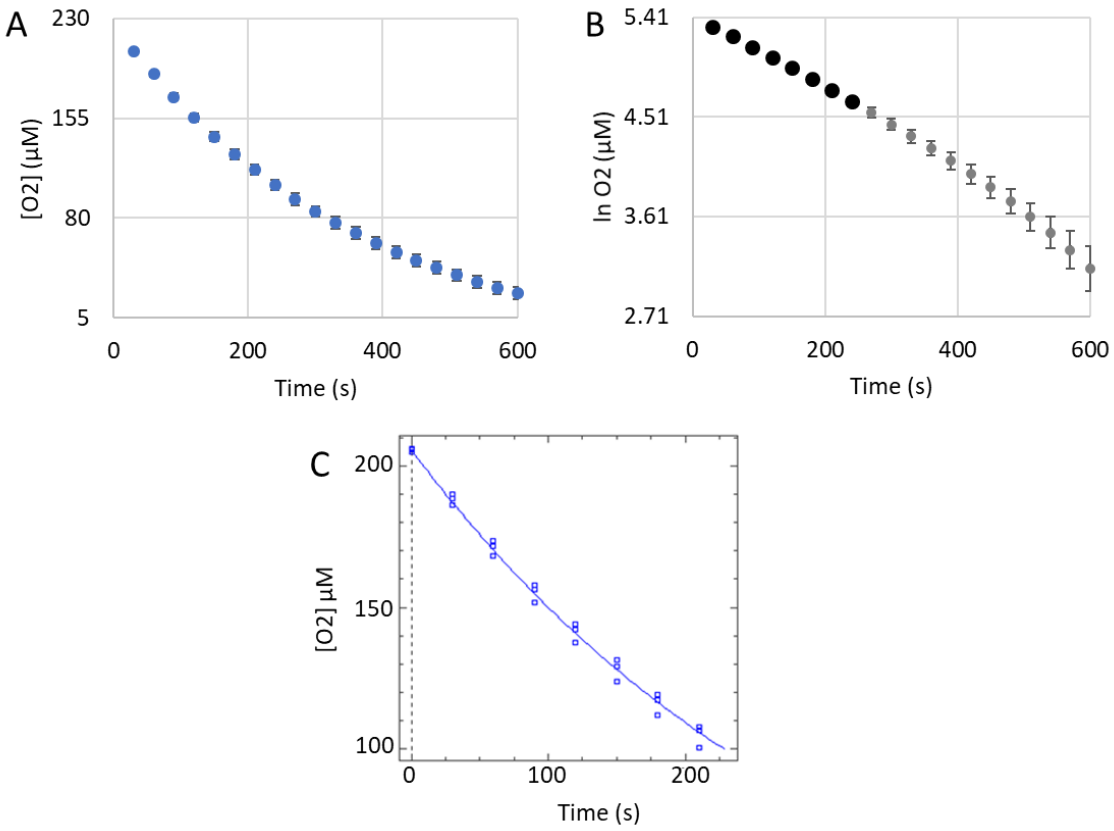

Figure A.5.11. pH 10.5 Autoxidation of 4.98 mM 3,4-DHBA.

Reactions were carried out in triplicate under pseudo first-order conditions in 50 mM CAPS buffer pH 10.5 at 29.5°C with 3,4-DHBA in excess and an initial O_2 concentration of 223 µM. (A) A Clark-type oxygen electrode tracks the consumption of dissolved O_2 by catechol during the autoxidation process. (B) The initial linear portion (bold data points) of the plot of $\ln[O_2]$ versus time was used for the determination of pseudo first-order rate constant. The initial data point was not included to account for mixing upon the addition of catechol. (C) Non-linear least squares analysis was performed on the initial linear portion from (B) using Dynafit (version 4.05.087 software Biokin Ltd.), giving the pseudo first-order rate constant, standard error, and R^2 value (Table 4.3). Dioxygen consumption data for all three autoxidation reactions, rather than the average of these reactions, was included in the same plot when determining the pseudo first order rate constant.

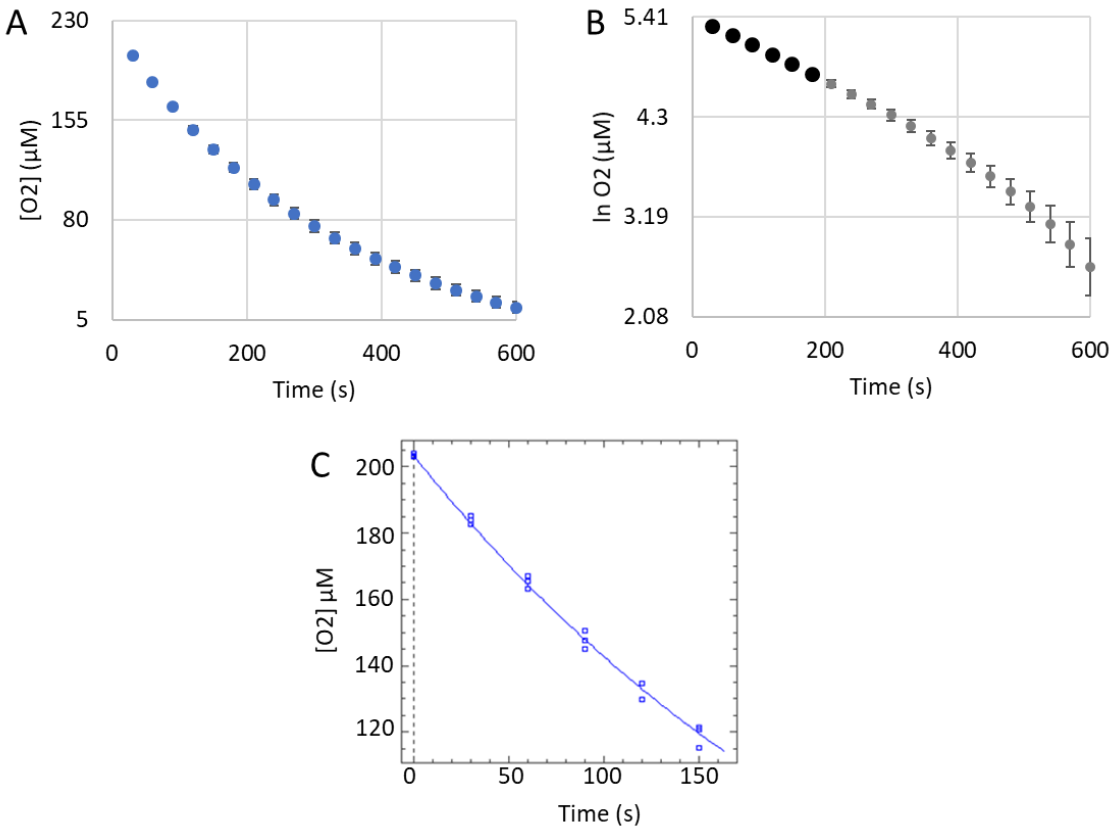

Figure A.5.12. pH 10.5 Autoxidation of 6.64 mM 3,4-DHBA.

Reactions were carried out in triplicate under pseudo first-order conditions in 50 mM CAPS buffer pH 10.5 at 29.5°C with 3,4-DHBA in excess and an initial O_2 concentration of 223 µM. (A) A Clark-type oxygen electrode tracks the consumption of dissolved O_2 by catechol during the autoxidation process. (B) The initial linear portion (bold data points) of the plot of $\ln[O_2]$ versus time was used for the determination of pseudo first-order rate constant. The initial data point was not included to account for mixing upon the addition of catechol. (C) Non-linear least squares analysis was performed on the initial linear portion from (B) using Dynafit (version 4.05.087 software Biokin Ltd.), giving the pseudo first-order rate constant, standard error, and R^2 value (Table 4.3). Dioxygen consumption data for all three autoxidation reactions, rather than the average of these reactions, was included in the same plot when determining the pseudo first order rate constant.

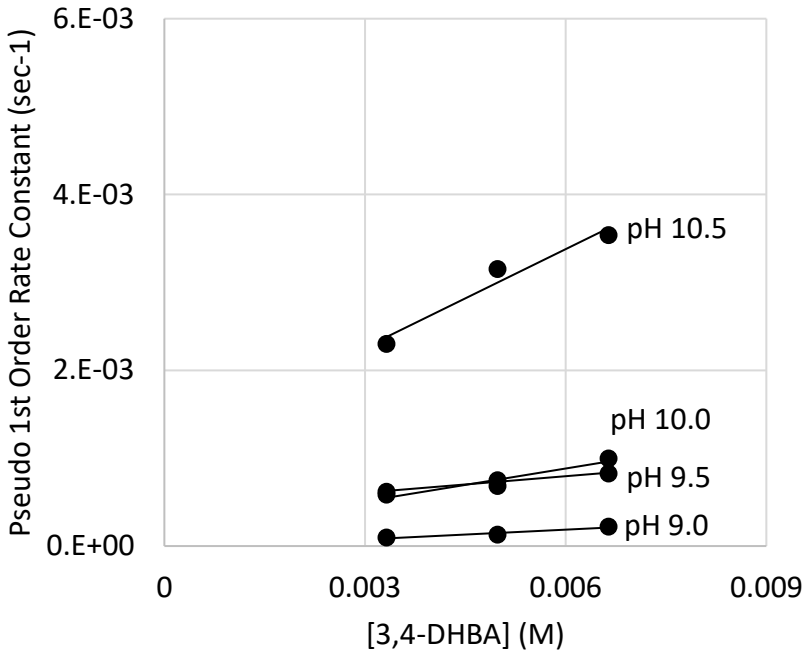

Figure A.5.13. pH-Dependence of 3,4-DHBA Autoxidation.

Autoxidation of 3,4-DHBA was investigated at pH 9.0, 9.5, 10.0, 10.5.

Appendix A.6. Kinetic Data for 2,4-DHBA Autoxidation

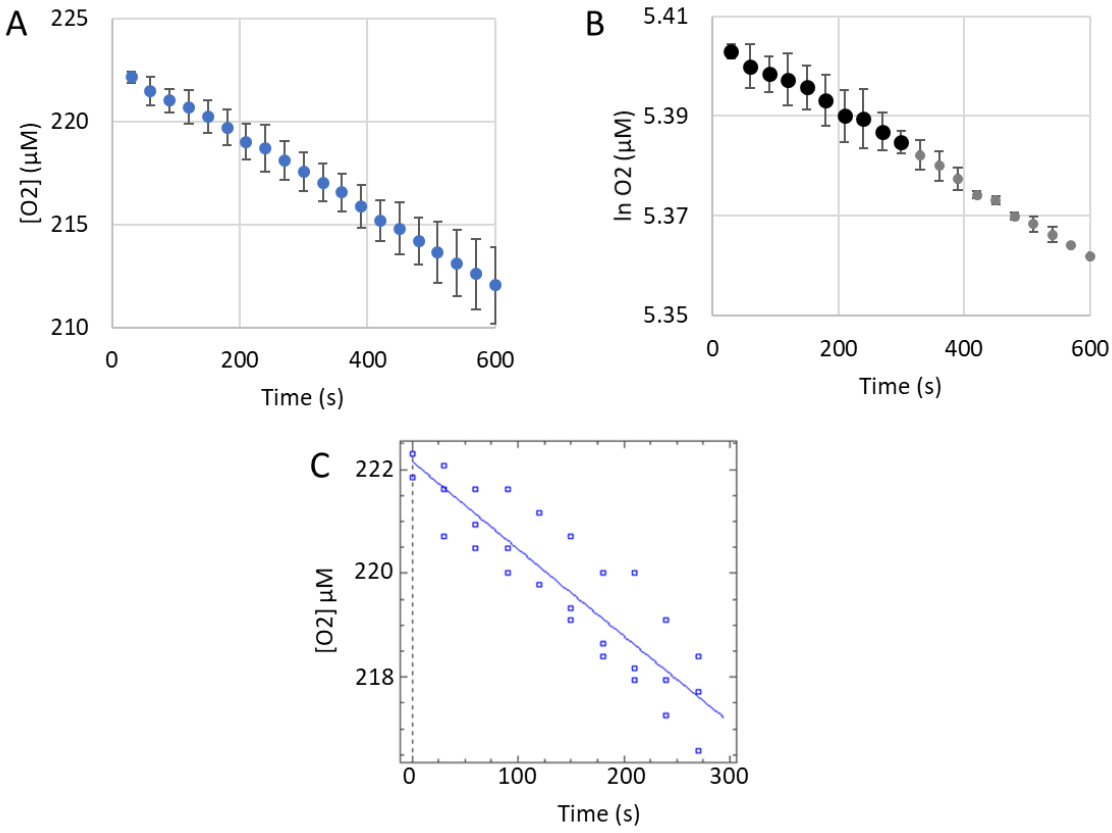

Figure A.6.1. pH 10.0 Autoxidation of 6.64 mM 2,3-DHBA.

Reactions were carried out in triplicate under pseudo first-order conditions in 50 mM CAPSO buffer pH 10.0 at 29.5°C with 2,3-DHBA in excess and an initial O_2 concentration of 223 µM. One of autoxidation reactions deviated from the average of the remaining two and was not included in the analysis. (A) A Clark-type oxygen electrode tracks the consumption of dissolved O_2 by catechol during the autoxidation process. (B) The initial linear portion (bold data points) of the plot of $\ln[O_2]$ versus time was used for the determination of pseudo first-order rate constant. The initial data point was not included to account for mixing upon the addition of catechol. (C) Non-linear least squares analysis was performed on the initial linear portion from (B) using Dynafit (version 4.05.087 software Biokin Ltd.), giving the pseudo first-order rate constant, standard error, and R^2 value (Table 4.3). Dioxygen consumption data for all three autoxidation reactions, rather than the average of these reactions, was included in the same plot when determining the pseudo first order rate constant

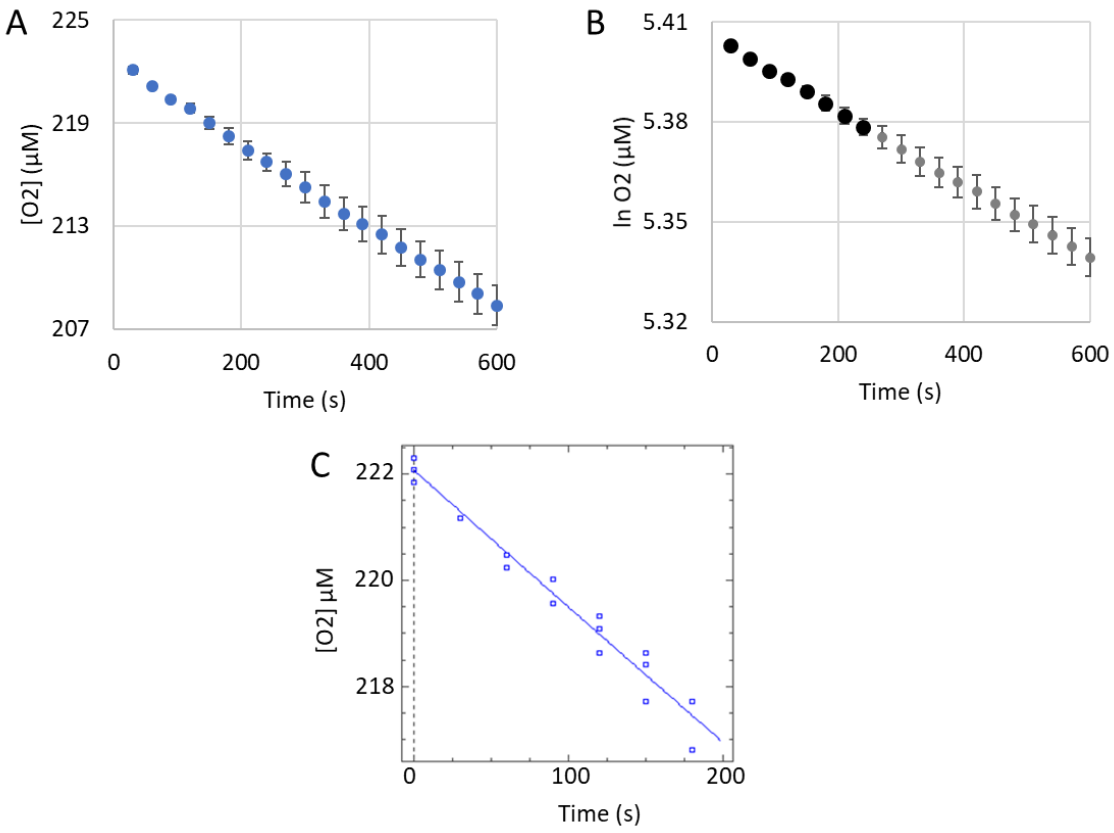

Figure A.6.2. pH 10.0 Autoxidation of 9.96 mM 2,3-DHBA.

Reactions were carried out in triplicate under pseudo first-order conditions in 50 mM CAPSO buffer pH 10.0 at 29.5°C with 2,3-DHBA in excess and an initial O_2 concentration of 223 µM. (A) A Clark-type oxygen electrode tracks the consumption of dissolved O_2 by catechol during the autoxidation process. (B) The initial linear portion (bold data points) of the plot of ln[O_2] versus time was used for the determination of pseudo first-order rate constant. The initial data point was not included to account for mixing upon the addition of catechol. (C) Non-linear least squares analysis was performed on the initial linear portion from (B) using Dynafit (version 4.05.087 software Biokin Ltd.), giving the pseudo first-order rate constant, standard error, and R^2 value (Table 4.3). Dioxygen consumption data for all three autoxidation reactions, rather than the average of these reactions, was included in the same plot when determining the pseudo first order rate constant

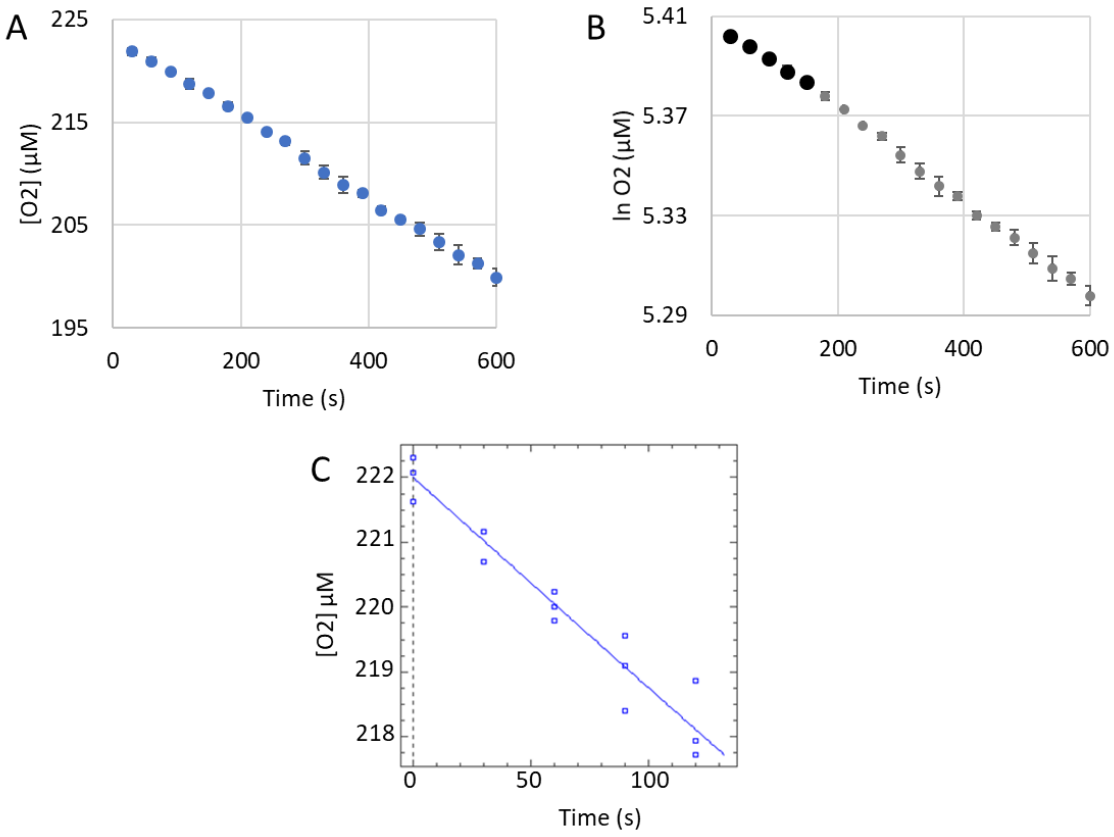

Figure A.6.3. pH 10.0 Autoxidation of 13.3 mM 2,3-DHBA.

Reactions were carried out in triplicate under pseudo first-order conditions in 50 mM CAPSO buffer pH 10.0 at 29.5°C with 2,3-DHBA in excess and an initial O_2 concentration of 223 µM. One of autoxidation reactions deviated from the average of the remaining two and was not included in the analysis. (A) A Clark-type oxygen electrode tracks the consumption of dissolved O_2 by catechol during the autoxidation process. (B) The initial linear portion (bold data points) of the plot of $\ln[O_2]$ versus time was used for the determination of pseudo first-order rate constant. The initial data point was not included to account for mixing upon the addition of catechol. (C) Non-linear least squares analysis was performed on the initial linear portion from (B) using Dynafit (version 4.05.087 software Biokin Ltd.), giving the pseudo first-order rate constant, standard error, and R^2 value (Table 4.3). Dioxygen consumption data for all three autoxidation reactions, rather than the average of these reactions, was included in the same plot when determining the pseudo first order rate constant

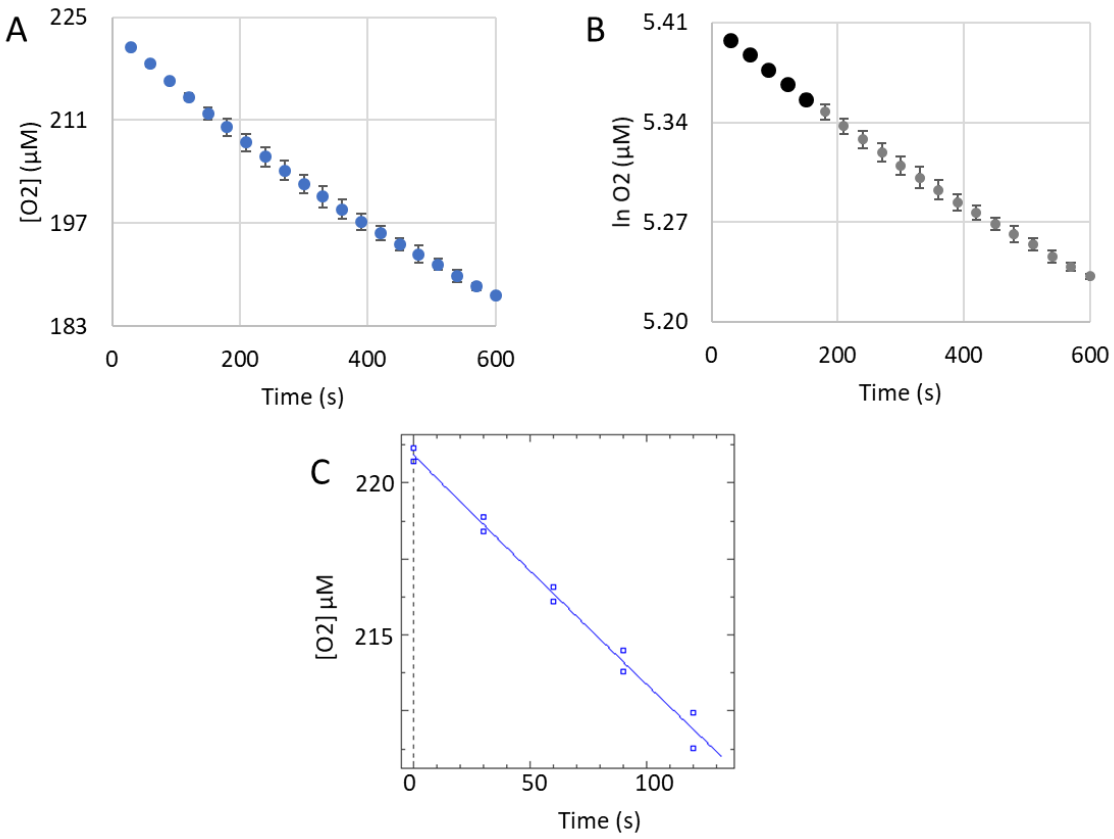

Figure A.6.4. pH 11.0 Autoxidation of 3.32 mM 2,3-DHBA.

Reactions were carried out in triplicate under pseudo first-order conditions in 50 mM CAPS buffer pH 11.0 at 29.5°C with 2,3-DHBA in excess and an initial O_2 concentration of 223 µM. One of autoxidation reactions deviated from the average of the remaining two and was not included in the analysis. (A) A Clark-type oxygen electrode tracks the consumption of dissolved O_2 by catechol during the autoxidation process. (B) The initial linear portion (bold data points) of the plot of ln[O_2] versus time was used for the determination of pseudo first-order rate constant. The initial data point was not included to account for mixing upon the addition of catechol. (C) Non-linear least squares analysis was performed on the initial linear portion from (B) using Dynafit (version 4.05.087 software Biokin Ltd.), giving the pseudo first-order rate constant, standard error, and R^2 value (Table 4.3). Dioxygen consumption data for all three autoxidation reactions, rather than the average of these reactions, was included in the same plot when determining the pseudo first order rate constant

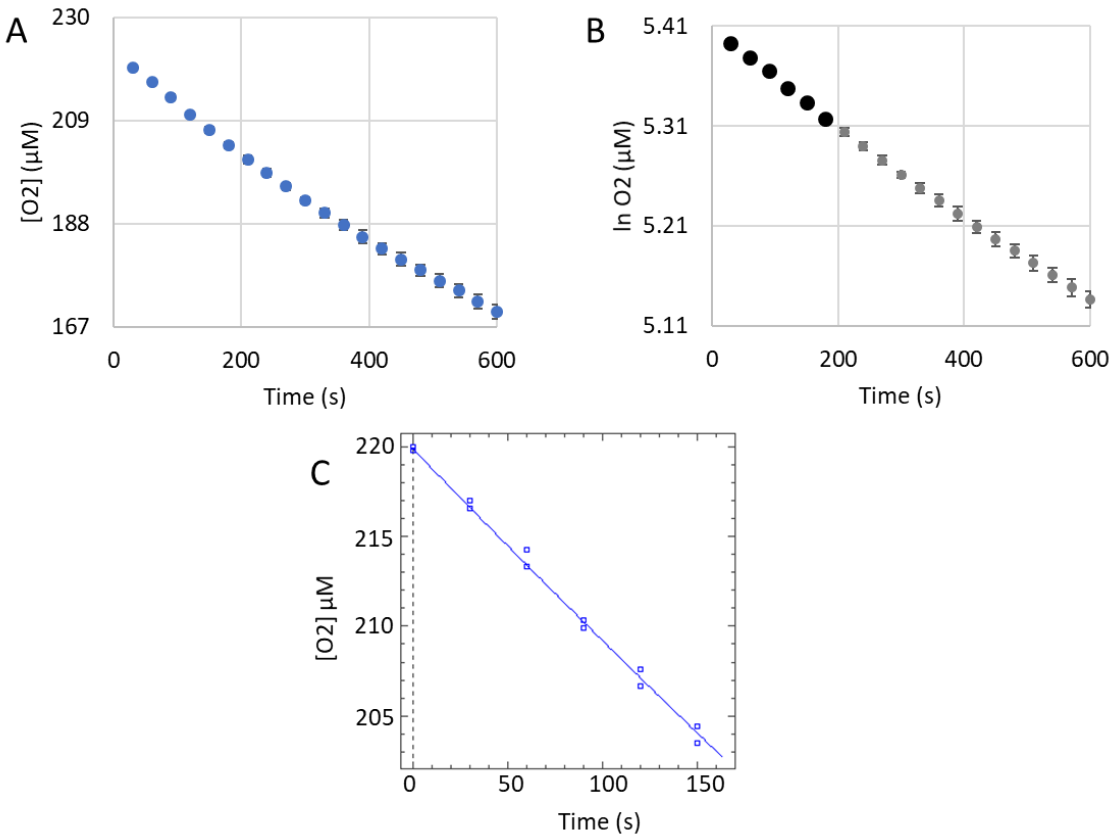

Figure A.6.5. pH 11.0 Autoxidation of 4.98 mM 2,3-DHBA.

Reactions were carried out in triplicate under pseudo first-order conditions in 50 mM CAPS buffer pH 10.0 at 29.5°C with 2,3-DHBA in excess and an initial O_2 concentration of 223 µM. One of autoxidation reactions deviated from the average of the remaining two and was not included in the analysis. (A) A Clark-type oxygen electrode tracks the consumption of dissolved O_2 by catechol during the autoxidation process. (B) The initial linear portion (bold data points) of the plot of ln[O_2] versus time was used for the determination of pseudo first-order rate constant. The initial data point was not included to account for mixing upon the addition of catechol. (C) Non-linear least squares analysis was performed on the initial linear portion from (B) using Dynafit (version 4.05.087 software Biokin Ltd.), giving the pseudo first-order rate constant, standard error, and R^2 value (Table 4.3). Dioxygen consumption data for all three autoxidation reactions, rather than the average of these reactions, was included in the same plot when determining the pseudo first order rate constant

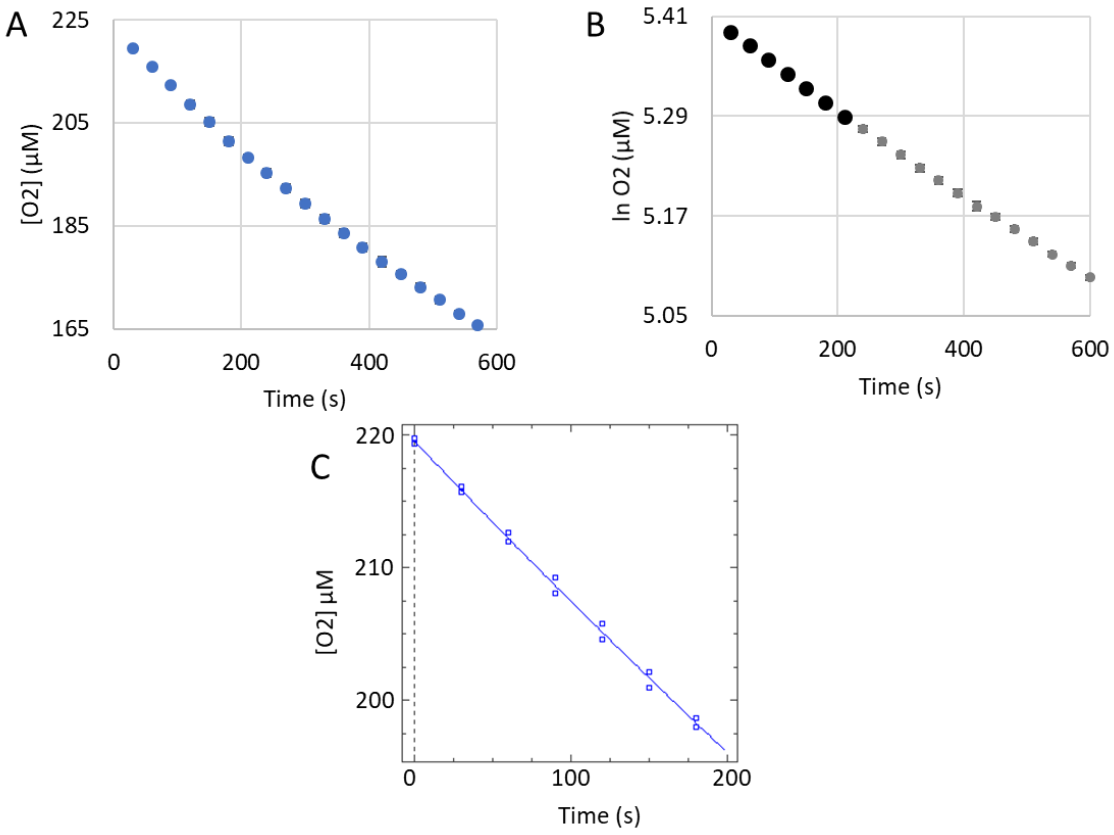

Figure A.6.6. pH 11.0 Autoxidation of 6.64 mM 2,3-DHBA.

Reactions were carried out in triplicate under pseudo first-order conditions in 50 mM CAPS buffer pH 11.0 at 29.5°C with 2,3-DHBA in excess and an initial O_2 concentration of 223 µM. One of autoxidation reactions deviated from the average of the remaining two and was not included in the analysis. (A) A Clark-type oxygen electrode tracks the consumption of dissolved O_2 by catechol during the autoxidation process. (B) The initial linear portion (bold data points) of the plot of $\ln[O_2]$ versus time was used for the determination of pseudo first-order rate constant. The initial data point was not included to account for mixing upon the addition of catechol. (C) Non-linear least squares analysis was performed on the initial linear portion from (B) using Dynafit (version 4.05.087 software Biokin Ltd.), giving the pseudo first-order rate constant, standard error, and R^2 value (Table 4.3). Dioxygen consumption data for all three autoxidation reactions, rather than the average of these reactions, was included in the same plot when determining the pseudo first order rate constant

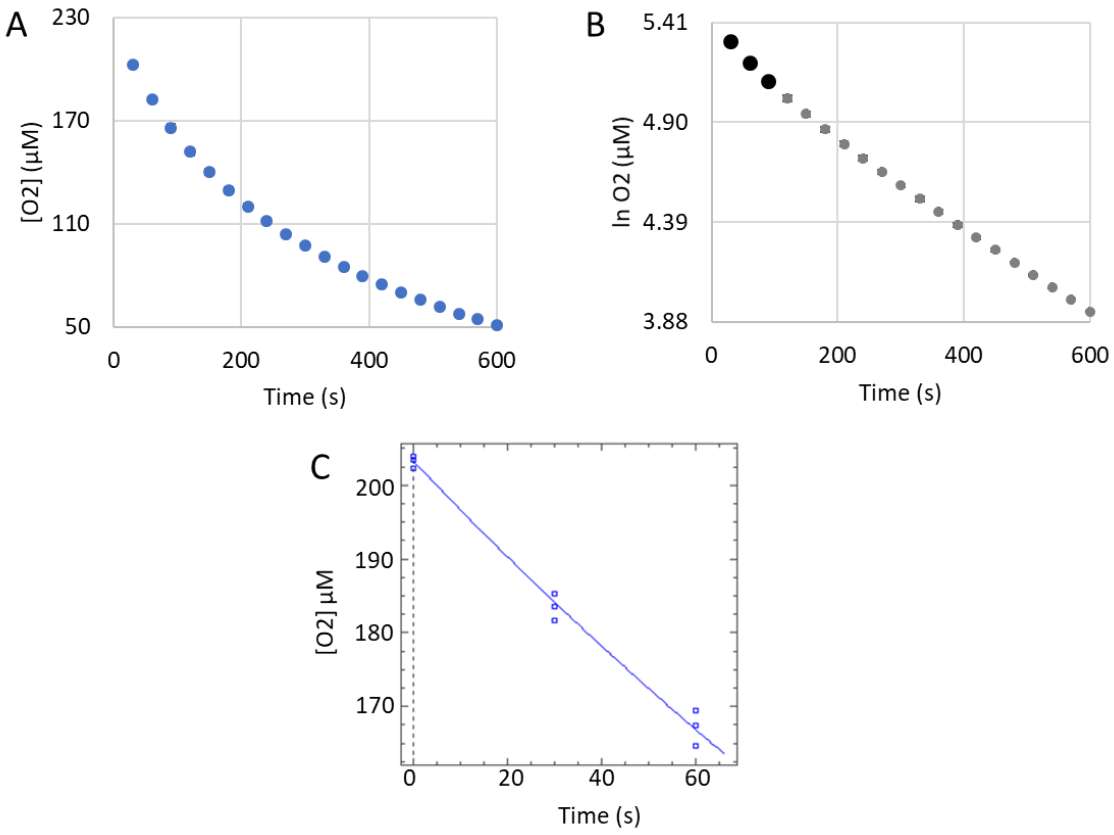

Figure A.6.7. pH 11.5 Autoxidation of 3.32 mM 2,3-DHBA.

Reactions were carried out in triplicate under pseudo first-order conditions in 50 mM phosphate buffer pH 11.5 at 29.5°C with 2,3-DHBA in excess and an initial O_2 concentration of 223 µM. One of autoxidation reactions deviated from the average of the remaining two and was not included in the analysis. (A) A Clark-type oxygen electrode tracks the consumption of dissolved O_2 by catechol during the autoxidation process. (B) The initial linear portion (bold data points) of the plot of ln[O_2] versus time was used for the determination of pseudo first-order rate constant. The initial data point was not included to account for mixing upon the addition of catechol. (C) Non-linear least squares analysis was performed on the initial linear portion from (B) using Dynafit (version 4.05.087 software Biokin Ltd.), giving the pseudo first-order rate constant, standard error, and R^2 value (Table 4.3). Dioxygen consumption data for all three autoxidation reactions, rather than the average of these reactions, was included in the same plot when determining the pseudo first order rate constant

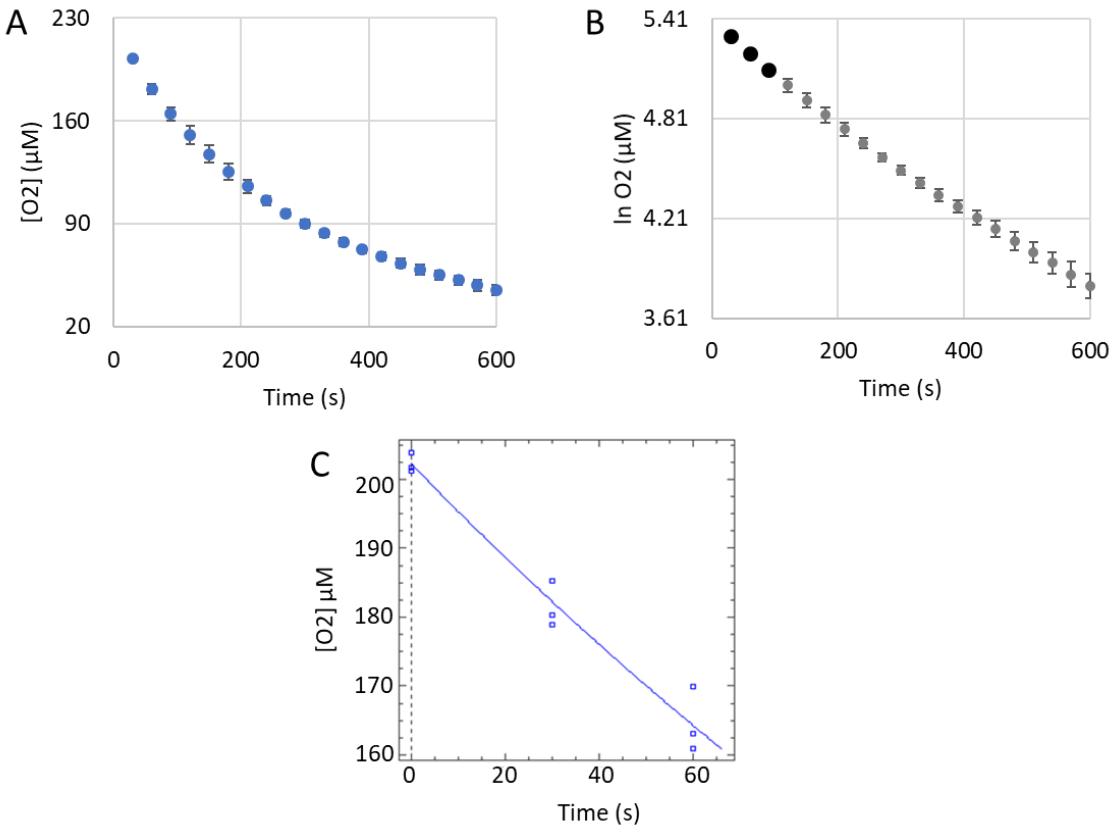

Figure A.6.8. pH 11.5 Autoxidation of 4.98 mM 2,3-DHBA.

Reactions were carried out in triplicate under pseudo first-order conditions in 50 mM phosphate buffer pH 11.5 at 29.5°C with 2,3-DHBA in excess and an initial O_2 concentration of 223 µM. (A) A Clark-type oxygen electrode tracks the consumption of dissolved O_2 by catechol during the autoxidation process. (B) The initial linear portion (bold data points) of the plot of ln[O_2] versus time was used for the determination of pseudo first-order rate constant. The initial data point was not included to account for mixing upon the addition of catechol. (C) Non-linear least squares analysis was performed on the initial linear portion from (B) using Dynafit (version 4.05.087 software Biokin Ltd.), giving the pseudo first-order rate constant, standard error, and R^2 value (Table 4.3). Dioxygen consumption data for all three autoxidation reactions, rather than the average of these reactions, was included in the same plot when determining the pseudo first order rate constant

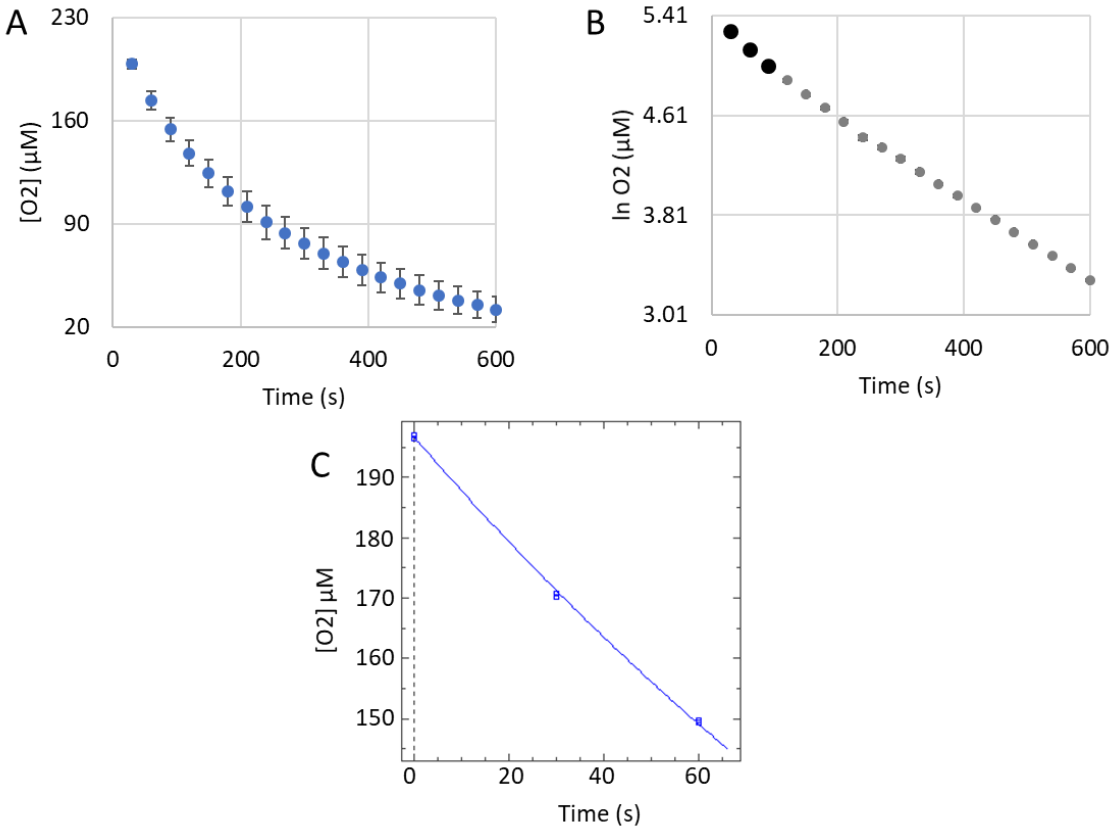

Figure A.6.9. pH 11.5 Autoxidation of 6.64 mM 2,3-DHBA.

Reactions were carried out in triplicate under pseudo first-order conditions in 50 mM phosphate buffer pH 11.5 at 29.5°C with 2,3-DHBA in excess and an initial O_2 concentration of 223 µM. One of autoxidation reactions deviated from the average of the remaining two and was not included in the analysis. (A) A Clark-type oxygen electrode tracks the consumption of dissolved O_2 by catechol during the autoxidation process. (B) The initial linear portion (bold data points) of the plot of ln[O_2] versus time was used for the determination of pseudo first-order rate constant. The initial data point was not included to account for mixing upon the addition of catechol. (C) Non-linear least squares analysis was performed on the initial linear portion from (B) using Dynafit (version 4.05.087 software Biokin Ltd.), giving the pseudo first-order rate constant, standard error, and R^2 value (Table 4.3). Dioxygen consumption data for all three autoxidation reactions, rather than the average of these reactions, was included in the same plot when determining the pseudo first order rate constant

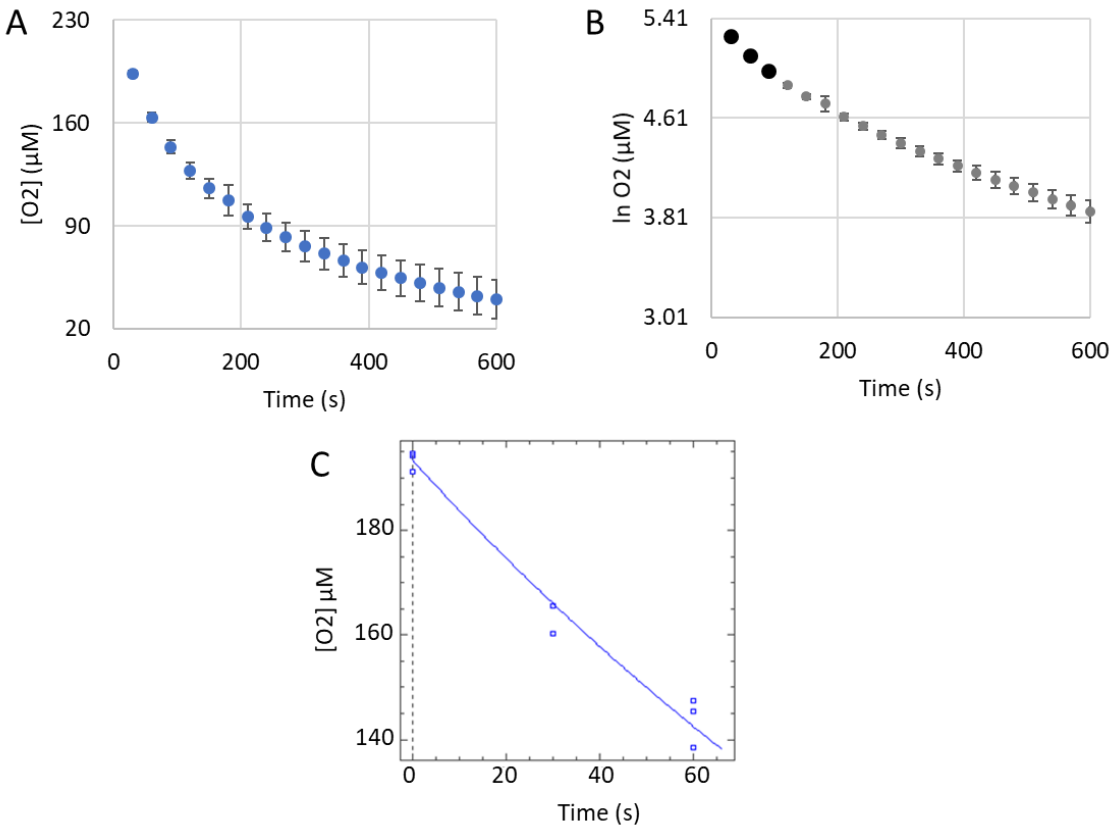

Figure A.6.10. pH 12.0 Autoxidation of 3.32 mM 2,3-DHBA.

Reactions were carried out in triplicate under pseudo first-order conditions in 50 mM phosphate buffer pH 12.0 at 29.5°C with 2,3-DHBA in excess and an initial O_2 concentration of 223 µM. One of autoxidation reactions deviated from the average of the remaining two and was not included in the analysis. (A) A Clark-type oxygen electrode tracks the consumption of dissolved O_2 by catechol during the autoxidation process. (B) The initial linear portion (bold data points) of the plot of $\ln[O_2]$ versus time was used for the determination of pseudo first-order rate constant. The initial data point was not included to account for mixing upon the addition of catechol. (C) Non-linear least squares analysis was performed on the initial linear portion from (B) using Dynafit (version 4.05.087 software Biokin Ltd.), giving the pseudo first-order rate constant, standard error, and R^2 value (Table 4.3). Dioxygen consumption data for all three autoxidation reactions, rather than the average of these reactions, was included in the same plot when determining the pseudo first order rate constant

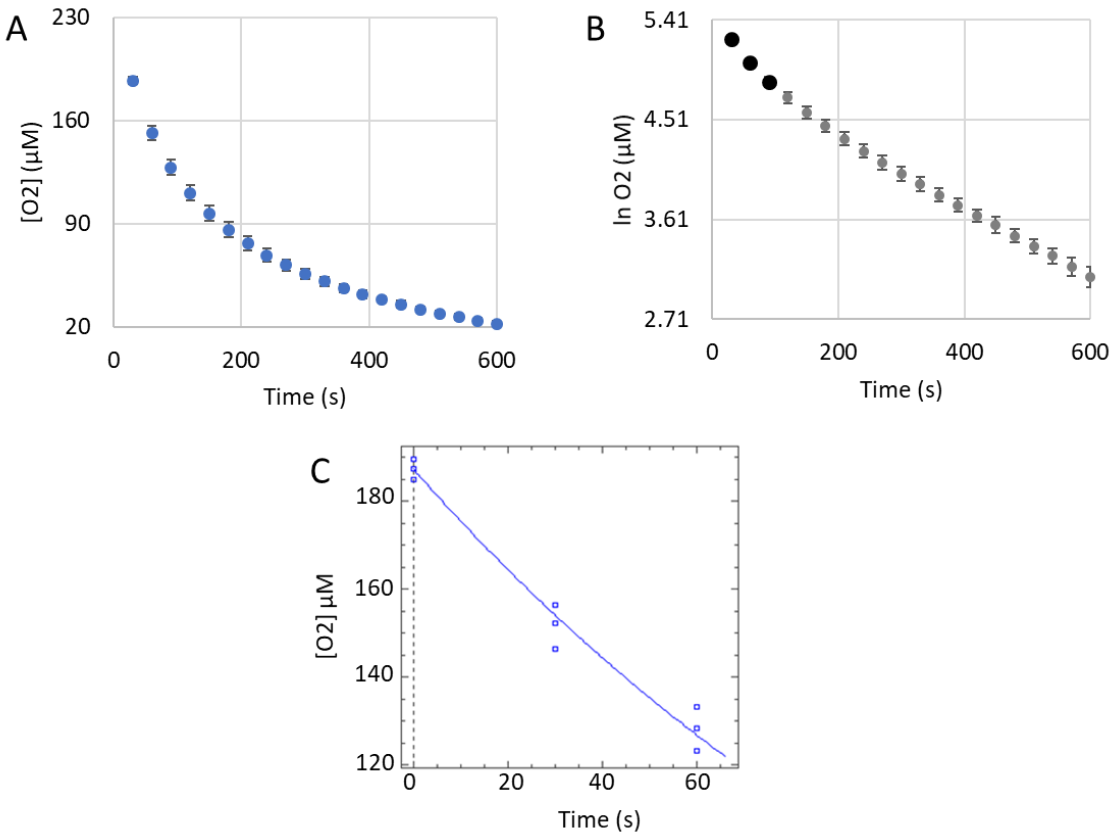

Figure A.6.11. pH 12.0 Autoxidation of 4.15 mM 2,3-DHBA.

Reactions were carried out in triplicate under pseudo first-order conditions in 50 mM phosphate buffer pH 12.0 at 29.5°C with 2,3-DHBA in excess and an initial O_2 concentration of 223 µM. (A) A Clark-type oxygen electrode tracks the consumption of dissolved O_2 by catechol during the autoxidation process. (B) The initial linear portion (bold data points) of the plot of ln[O_2] versus time was used for the determination of pseudo first-order rate constant. The initial data point was not included to account for mixing upon the addition of catechol. (C) Non-linear least squares analysis was performed on the initial linear portion from (B) using Dynafit (version 4.05.087 software Biokin Ltd.), giving the pseudo first-order rate constant, standard error, and R^2 value (Table 4.3). Dioxygen consumption data for all three autoxidation reactions, rather than the average of these reactions, was included in the same plot when determining the pseudo first order rate constant

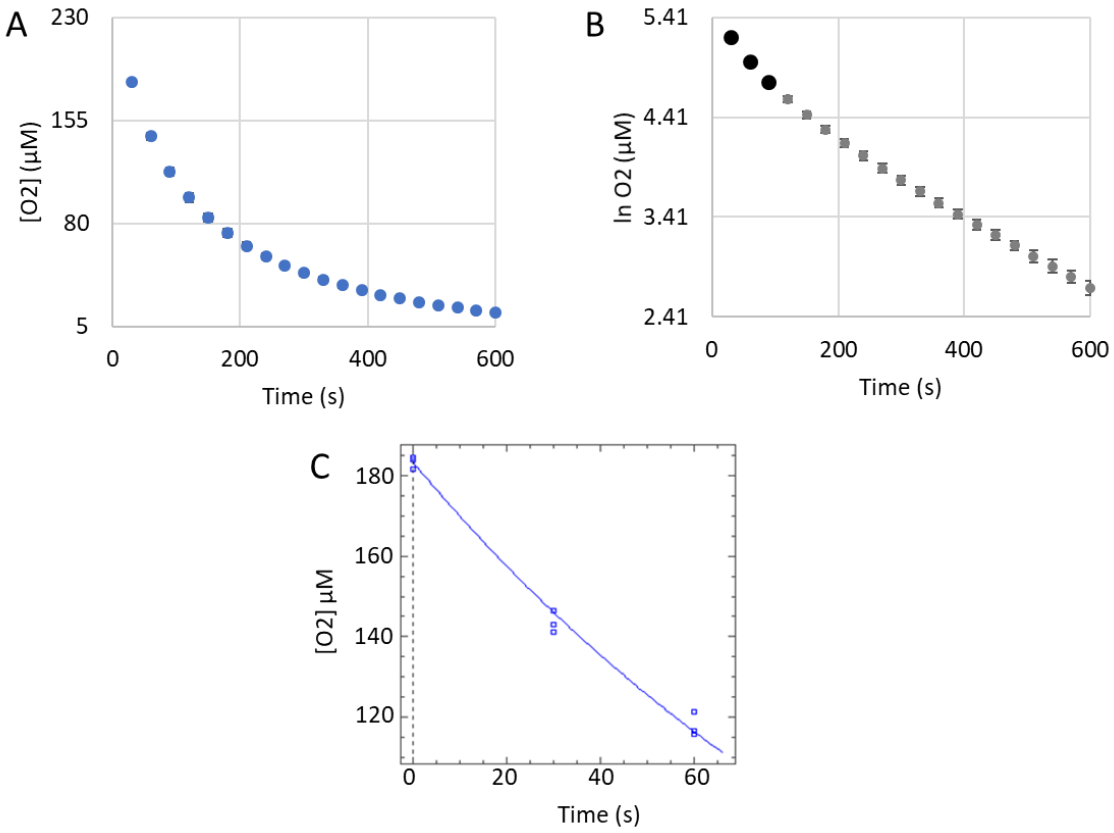

Figure A.6.12. pH 12.0 Autoxidation of 4.98 mM 2,3-DHBA.

Reactions were carried out in triplicate under pseudo first-order conditions in 50 mM phosphate buffer pH 12.0 at 29.5°C with 2,3-DHBA in excess and an initial O_2 concentration of 223 µM. (A) A Clark-type oxygen electrode tracks the consumption of dissolved O_2 by catechol during the autoxidation process. (B) The initial linear portion (bold data points) of the plot of ln[O_2] versus time was used for the determination of pseudo first-order rate constant. The initial data point was not included to account for mixing upon the addition of catechol. (C) Non-linear least squares analysis was performed on the initial linear portion from (B) using Dynafit (version 4.05.087 software Biokin Ltd.), giving the pseudo first-order rate constant, standard error, and R^2 value (Table 4.3). Dioxygen consumption data for all three autoxidation reactions, rather than the average of these reactions, was included in the same plot when determining the pseudo first order rate constant

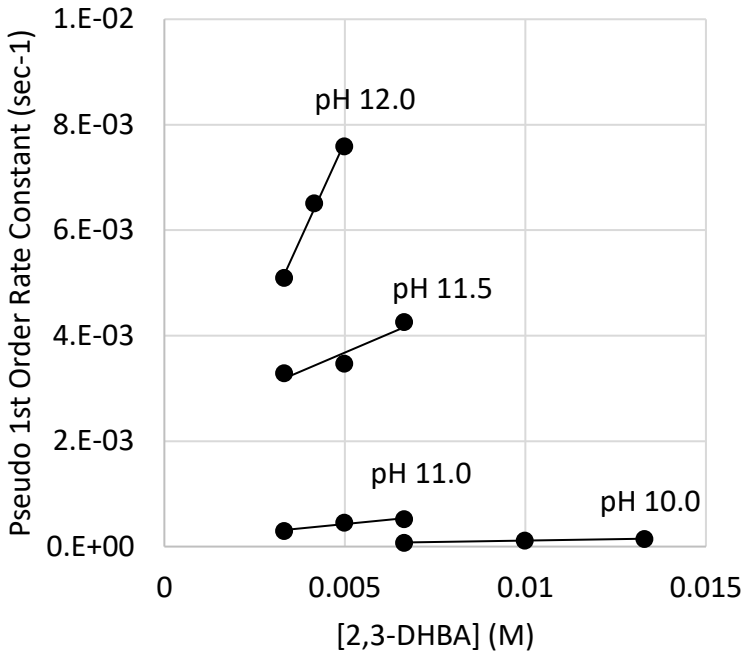

Figure A.6.13. pH-Dependence of 2,3-DHBA Autoxidation.

Autoxidation of 2,3-DHBA was investigated at pH 10.0, 11.0, 11.5, 12.0.

Appendix A.7. Kinetic Data for 5-Sulfo-2,3-DHBA Autoxidation

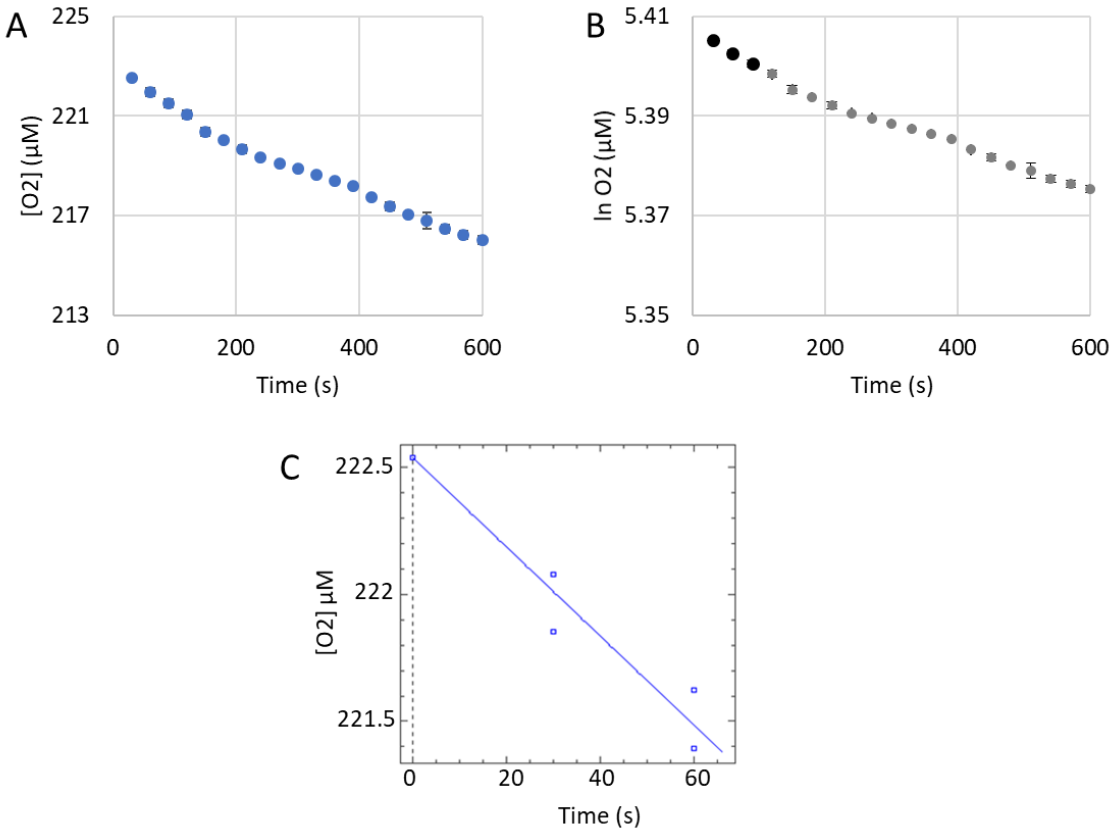

Figure A.7.1. pH 12.0 Autoxidation of 3.32 mM 5-Sulfo-2,3-DHBA.

Reactions were carried out in triplicate under pseudo first-order conditions in 50 mM phosphate buffer pH 12.0 at 29.5°C with 5-sulfo-2,3-DHBA in excess and an initial O_2 concentration of 223 µM. One of autoxidation reactions deviated from the average of the remaining two and was not included in the analysis. (A) A Clark-type oxygen electrode tracks the consumption of dissolved O_2 by catechol during the autoxidation process. (B) The initial linear portion (bold data points) of the plot of $\ln[O_2]$ versus time was used for the determination of pseudo first-order rate constant. The initial data point was not included to account for mixing upon the addition of catechol. (C) Non-linear least squares analysis was performed on the initial linear portion from (B) using Dynafit (version 4.05.087 software Biokin Ltd.), giving the pseudo first-order rate constant, standard error, and R^2 value (Table 4.3). Dioxygen consumption data for all three autoxidation reactions, rather than the average of these reactions, was included in the same plot when determining the pseudo first order rate constant

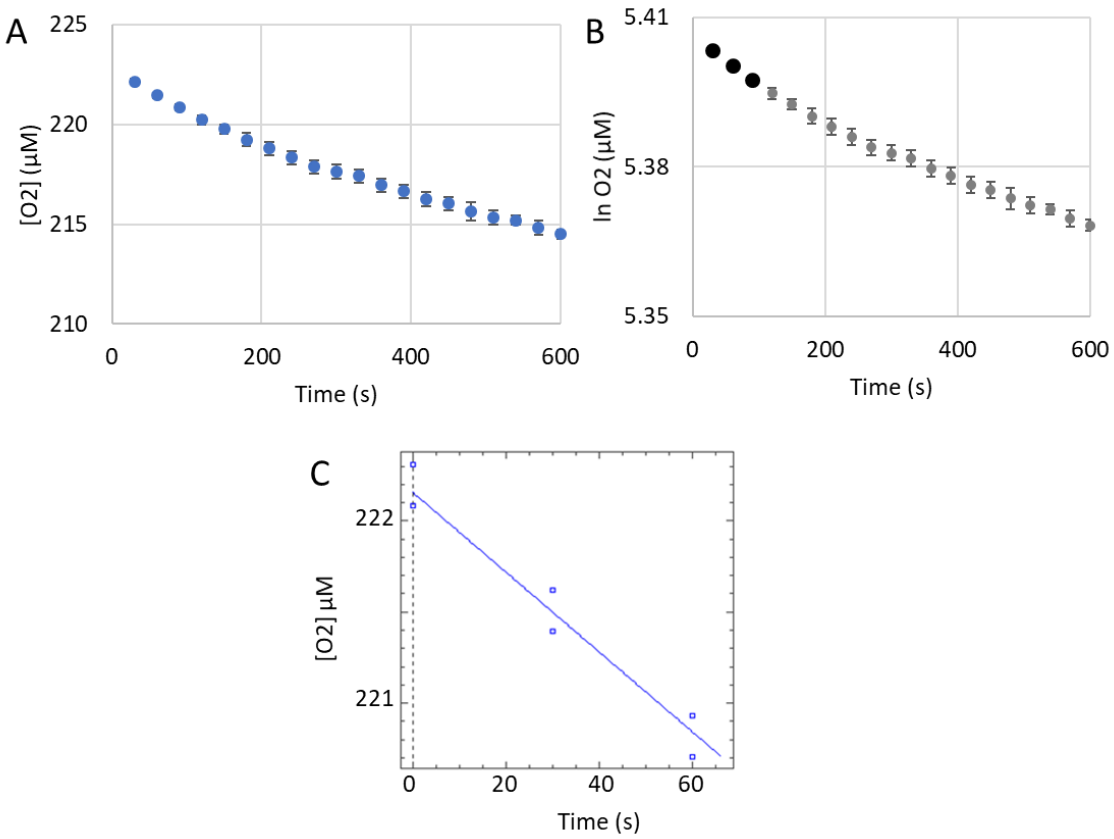

Figure A.7.2. pH 12.0 Autoxidation of 13.3 mM 5-Sulfo-2,3-DHBA.

Reactions were carried out in triplicate under pseudo first-order conditions in 50 mM phosphate buffer pH 12.0 at 29.5°C with 5-sulfo-2,3-DHBA in excess and an initial O_2 concentration of 223 µM. (A) A Clark-type oxygen electrode tracks the consumption of dissolved O_2 by catechol during the autoxidation process. (B) The initial linear portion (bold data points) of the plot of $\ln[O_2]$ versus time was used for the determination of pseudo first-order rate constant. The initial data point was not included to account for mixing upon the addition of catechol. (C) Non-linear least squares analysis was performed on the initial linear portion from (B) using Dynafit (version 4.05.087 software Biokin Ltd.), giving the pseudo first-order rate constant, standard error, and R^2 value (Table 4.3). Dioxygen consumption data for all three autoxidation reactions, rather than the average of these reactions, was included in the same plot when determining the pseudo first order rate constant

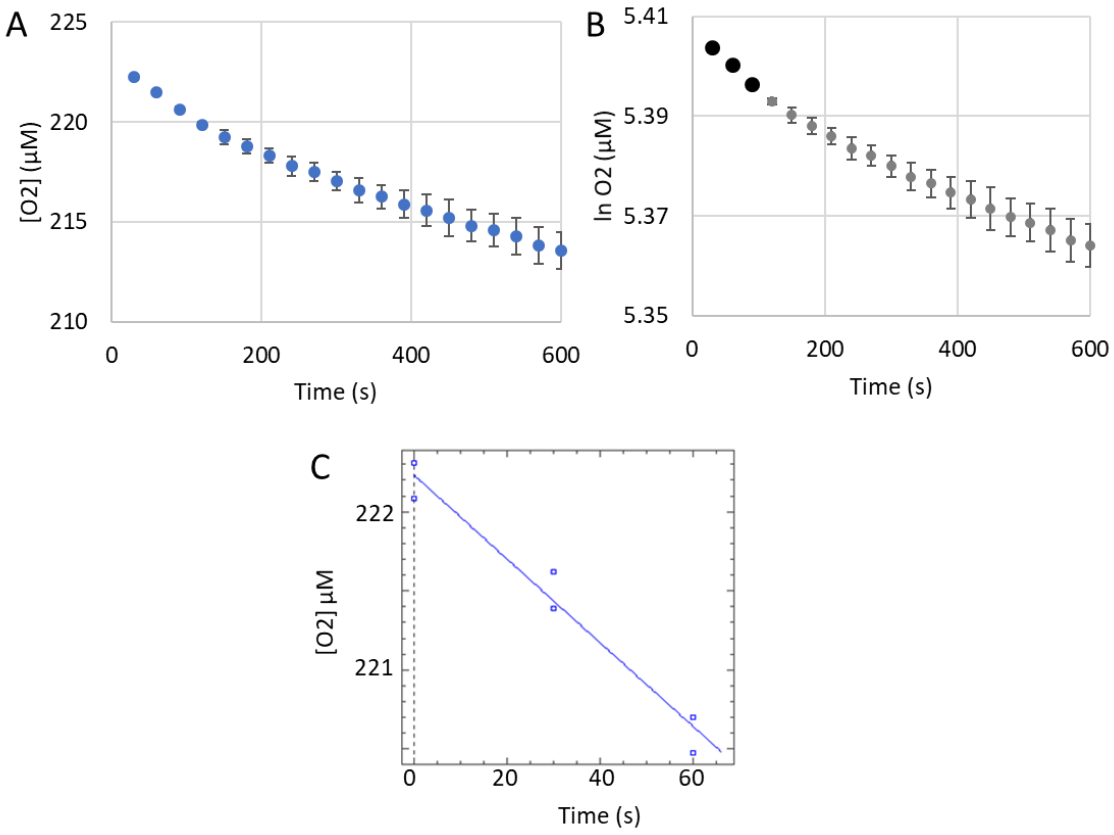

Figure A.7.3. pH 12.0 Autoxidation of 26.6 mM 5-Sulfo-2,3-DHBA.

Reactions were carried out in triplicate under pseudo first-order conditions in 50 mM phosphate buffer pH 12.0 at 29.5°C with 5-sulfo-2,3-DHBA in excess and an initial O_2 concentration of 223 µM. (A) A Clark-type oxygen electrode tracks the consumption of dissolved O_2 by catechol during the autoxidation process. (B) The initial linear portion (bold data points) of the plot of $\ln[O_2]$ versus time was used for the determination of pseudo first-order rate constant. The initial data point was not included to account for mixing upon the addition of catechol. (C) Non-linear least squares analysis was performed on the initial linear portion from (B) using Dynafit (version 4.05.087 software Biokin Ltd.), giving the pseudo first-order rate constant, standard error, and R^2 value (Table 4.3). Dioxygen consumption data for all three autoxidation reactions, rather than the average of these reactions, was included in the same plot when determining the pseudo first order rate constant

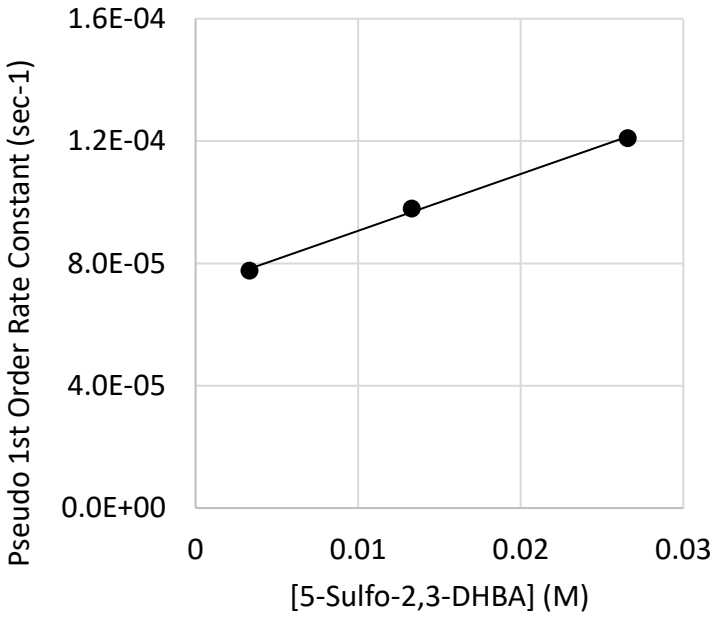

Figure A.7.4. Autoxidation of 5-Sulfo-2,3-DHBA at pH 12.0.